Ph.D. Thesis
Philosophiae Doctor

DTU Civil Engineering
Department of Civil Engineering

Mud-filtrate correction of sonic logs by fluid substitution

Modulus and pore-fluid coupling by pore-filling clay

Morten Kanne Sørensen

DTU

Kongens Lyngby 2015

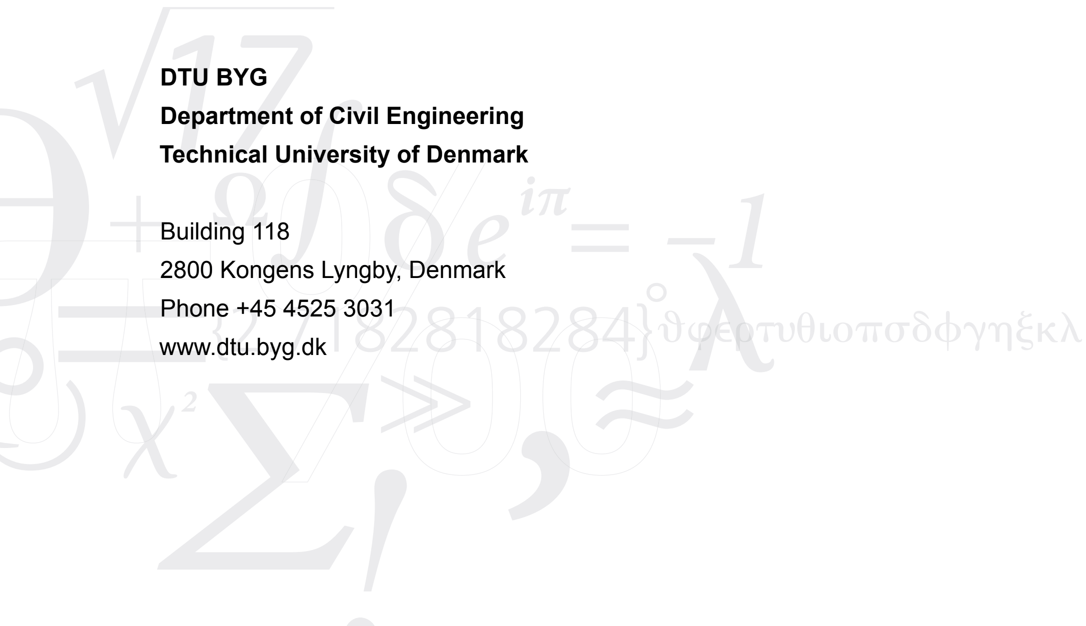

DTU BYG
Department of Civil Engineering
Technical University of Denmark

Building 118
2800 Kongens Lyngby, Denmark
Phone +45 4525 3031
www.dtu.byg.dk

Summary

The worlds hydrocarbons reserves have been exploited for over a century, and the amount of undiscovered reserves is dwindling, while the worlds need for energy is increasing (Owen et al., 2010). This pushes hydrocarbon exploration into unconventional reservoirs, often in complex geological structures. Making reliable discoveries in challenging conditions requires an increasing level of detail in seismic interpretation. Advanced seismic processing as Amplitude-Versus-Offset (AVO) analysis, have become commonplace in seismic interpretation. These techniques involves comparison with synthetic seismograms generated from velocity versus depth trends recorded as a sonic log in a borehole. Such a comparison is referred to as a well-tie. A high-quality well-tie requires a high-quality sonic log, but shallow depth of penetration makes sonic logs sensitive to invasion of mud-filtrate from the borehole. The pressure in the borehole is kept higher than in the surrounding formation to control fluid production from the borehole. The over pressure in the borehole drives fluid from the borehole into the formation, whereby a sonic log measures velocities at a different saturation than the formation saturation, which the seismic data probes. For a proper well-tie sonic logs therefore require correction.

Gassmann (1951) fluid substitution relates elastic velocities of a porous medium at one saturation to the elastic velocities at another saturation. Fluid substation can then predict a sonic log at the undisturbed formation saturation from the invaded saturation. Fluid substitution is exact for a uniform, high-permeable porous medium saturated by a single fluid. Rocks does not necessarily conform to these requirements, and both the formation saturation and invaded saturation involve two fluids. Sonic log correction therefore requires extension of Gassmann fluid substitution to the complex nature of an invaded rock formation.

Only sandstones are considered in the thesis. Measurements and model for fully saturated sandstones quantify divergences from fluid substitution arising from the first few percent of wetting phase saturation, and the clay content. When the water saturation is at the irreducible water saturation or higher only the effect of clay on the elastic velocities have a differential effect on the elastic velocities. Mixed saturations are fluid substituted using effective fluid moduli formulated as a set of bounds by Mavko and Mukerji (1998). Ultrasonic velocity data from the literature shows that these bounds applies most accurately to sandstones with a simple pore-space, as reflected in a high permeability and low clay fraction.

A classification for sandstones depending on the distribution of clay in the sandstone framework, is developed to facilitate incorporation of clay in fluid substitution correction of sonic logs. The classification consists of four groups: 1. clean sandstone, 2. sandstone with partial pore-filling clay, 3. sandstone with a pore-space homogeneously dominated by clay (critical shale concentration), and 4. load-bearing clay. Delineation of the groups involves comparing elastic moduli of the sandstone considered to a diagenetic trend between elastic moduli and porosity for lithified sandstones. From this, the true load-bearing porosity is by adding the volume of solid pore-filling clay to the measured porosity as suggested by Gal et al. (1999). Correspondence between this estimate of clay volume and petrographic data from image analysis determines the grouping. If the clay volumes are compatible clay is identified as pore-filling, if they are not compatible clay is identified as load-se bearing.

Fluid substitution under-predicts the bulk modulus for sandstones with clay. Saturation only slightly affects the shear moduli in sandstones with partial pore-filling clay; increases shear modulus in sandstones with complete pore-filling clay and reduce shear modulus in sandstones with load-bearing clay. Clean sandstones diverge from fluid substitution by effects associated with the first few percent of water saturation. The problem of sonic log correction therefore becomes equivalent with the problem of predicting the influence of clay on the saturated elastic moduli of a sandstone relative to the sandstone framework moduli.

The vast majority of sandstone reservoirs have some pore-filling clay whereby Group 2 is the natural focus of the study. Fluid flow from intra-clay porosity to the framework porosity was suggested by Best et al. (1994) as the cause of the increase in saturated elastic moduli, diverging from fluid substitution. Formulation of a model incorporating such flow, evaluates this proposition for homogeneously distributed clay. Comparison between model predictions and ultrasonic data shows the model to underestimate the saturated elastic bulk moduli in some sandstones. Divergence from the model is interpreted as the effect of heterogeneously distributed clay.

Diagenesis dictates clay distribution in a sandstone and there is no way to define a heterogeneous distribution without inadvertently biasing a model. Therefore, the investigation of heterogeneous distributed clay relies on laboratory measurements. Thorough characterization by conventional core analysis, X-Ray Diffraction (XRD), Mercury Injection Capillary Pressure (MICP), and low-field Nuclear Magnetic Resonance (NMR) identifies possible heterogeneously distribution of clay affecting the pore-space in a selected suited of sandstones with little clay (Group 1)or partially pore-filling clay (Group 2). Ultrasonic velocities measured in the dry, saturated, and partially saturated state, determines the effect of full and partial saturation on the elastic moduli. Comparison of ultrasonic velocities in the fully saturated state to those predicted by fluid substitution shows heterogeneous pore-fill to cause a larger discrepancy, than a uniform clay distribution. Sandstone with homogeneously distributed clay conform to the upper bound for fluid substitution by effective fluid moduli, while sandstone with a pore-space not affected by clay shift from the upper bound to the lower bound at a transition saturation.

Sandstones with heterogeneous clay have a larger effect introduced by saturation than expected from fluid substitution. This departure is associated with fluid saturation retained in clay-filled pores. Incorporation of these pores in the solid framework compose an effective set of framework moduli applicable to a fluid substitution of the effective porosity only.

Sonic log correction by fluid substitution reduces to an estimation of the distribution of clay. The critical evaluation is whether the clay distribution is heterogeneous. Distinction can be done by observation of the low-field NMR spectrum in the fully saturated state. A multi-modal T_2 spectrum signifies heterogeneous clay.

Load-bearing clay cause the saturated bulk modulus to increase relative to the dry and the saturated shear modulus to decrease relative to the dry. This split is different from the other groups whereby consideration of load-bearing clay is done separately. Ultrasonic velocity data recorded by Mondol et al. (2007) compose a data set in which isolating the effect induced by the clay. A normalization of the moduli to the load-bearing solid cross-section allows a comparing of the moduli in the dry and saturated state. This comparison shows the saturation of brine to decrease the shear modulus and increase the bulk modulus, qualitatively similar to the observations in sandstone albeit more pronounced. Interpretation of the effect suggests it to be the cause of water at the contacts between clay platelets, where it facilitates shear and oppose compression.

Sammenfatning

Fossile brændstoffer er blevet udvundet i over hundrede år og mængden er uopdagede reserver er svindende, mens verdens energibehov er stigende Owen et al. (2010). Dette driver eksploration efter fossile brændstoffer i ukonventionelle reservoirer, der ofte forekommer i komplekse geologiske strukturer. Opdagelse af nye reserver i sådanne udfordrende omgivelser kræver en stigende detalje rigdom i fortolkningen af seismisk data. Avancerede seismiske analysemetoder, som AVO analyse, har vundet mere og mere indpas. Sådanne analysemetoder kræver kalibrering ved syntetiske seismogrammer, bestemt ud fra hastigheder som funktion af dybde i form af en akustisk borehuls log. En sådan kalibrering kaldes et well-tie. Et well-tie af høj kvalitet kræver en akustisk log af høj kvalitet, men en akustisk log har en kort indtrængningsdybde og er følsomme overfor mudder filtrate invasion fra borehullet. Trykket i et borehul holdes højere end formationens trykket for at kontrollere produktionen af væske fra borehullet. Overtrykket i borehullet driver væske fra borehullet ud i formationen, hvorved en akustisk log måler hastigheder ved en anden væske mætning en den oplevet af en seismisk bølge. Et godt well-tie kræver derfor en korrektion af den akustiske log.

Gassmann (1951) fluid substitution knytter elastiske hastigheder for et porøst medie med en væske mætning til elastiske hastigheder ved en anden væske mætning. Fluid substitution gør det muligt at bestemme en akustisk log for den ufostyrrede formation fra målinger i den invadere formation. Fluid substitution er eksakt for et homogent, høj permeabelt porøst medie fuldkommen mættet med en væske. Bjergarter opfylder ikke nødvendigvis disse krav og dertil kommer at både den invadere zone og den uberørte formation er mættet med mere end en væske. Korrektion af en akustisk log kræver derfor en udvidelse af Gassman fluid substitution til den komplekse virkelighed, der hersker i en invaderet zone.

Kun sandsten er er behandlet i denne afhandling. Målinger og modellering af fuldt mættede sandsten kvantificerer afvigelser fra fluid substitution, der opstår som følge af de første få procents mætning af den vædende fase og ler indholdet. Når vandmætningen er lig med eller højere end den irreducibel vandmætning, er det kun ler der har en influerer de elastiske hastigheder forskelligt ved to mætninger. Blandede mætninger kan fluid substitueres med et effektivt væske modul som formuleret som et to grænser af Mavko and Mukerji (1998). Ultrasoniske hastigheds data fra litteraturen viser at for sandsten med et simpelt porerum er er disse grænser velegnede til beskrivelsen af de

elastiske hastigheder. Et simpelt porerum er karakteriseret ved en høj permeabilitet og et lavt ler indhold.

En klassificering af sandsten bestemt ved fordelingen af ler i sandstenens ramme bliver udviklet til at muligøre indarbejdelsen af ler indholdet i formulering af fluid substitution til korrektion af akustiske logs. Klassificeringen er inddelt i fire grupper: 1. rene sandsten, 2. sandsten med noget ler i porerne, 3. sandsten med et porerum domineret af ler, og 4. sandsten med bærende ler. Afgrænsningen af grupper opnås ved at sammenligne de elastiske moduli af en sandsten med en diagenetisk sammenhæng mellem porøsitet og elastisk moduli for en konsolideret sandsten. Fra denne sammenligning kan den sande porøsitet af den bærende ramme bestemmes ved at lægge volumenet af leret i porerne til den målte porøsitet, som foreslået af Gal et al. (1999). Overensstemmelse mellem dette estimat for ler indhold og ler indholdet bestemt ved petrografisk analyse definerer grupperingen. Hvis ler indholdet bestemt fra det elastiske modul stemmer med ler indholdet fra den petrografiske analyse er leret at finde i porerne og ikke bærende, er der ikke overensstemmelse er leret bærende.

Fluid substitution under estimerer kompressibilitetsmodulet for sandsten med ler. Mætningen af væske influerer kun forskydningsmodulet i begrænset omfang i sandsten med noget ler i porerne. I sandsten med et porerum domineret af ler bliver forskydningsmodulet froøget signifikant af en væskemætning. I sandsten medbærende ler reduceres forskydningsmodulet. Rene sandsten afviger fra fluid substitution ved effekter afledt af de første få procents mætning af den vædende fase. Problemet med korrektion af en akustisk log reducerer hermed til problemet i at forudsige indflydelsen af ler på de mættede moduli af en sandsten relativt til de umættede moduli.

Størstedelen af sandstens reservoir i verden har noget ler i porerne hvorved Gruppe 2 er det naturliglige fokus af dette studie. Væske strømninger fra porøsitet internt i leret og til sandstenens porøsitet blev foreslået af Best et al. (1994) som mekanismen bag det forøgede modul i den væske mættede tilstand. Formuleringen af en model der inkorporerer evaluerer denne ide for sandsten med homogent fordelt ler. En sammenligning af de modellered moduler og ultrasonisk data viser at modellen underestimerer de væske mættede moduler for sandsten i mange tilfælde. Afvigelser fra fluid substitution kan fortolkes som heterogent fordelt ler der influerer de elastiske moduler i en væske mættet tilstand.

Diagenese dikterer fordelingen af ler i en sandsten og der er ingen umiddelbar måde at inkorporere en heterogen fordeling af ler i en model uden at påvirke modellens forudsigelser. Derfor bliver de elastiske moduler af vandmættede sandsten målt i laboratoriet for at bestemme indflydelsen af heterogent fordelt ler. Ved en grundig karakterisering bestående af konventionel kerne analyse, XRD, MICP, og NMR med et lavt felt identificeres mulige heterogene fordelinger af ler i en udvalgt gruppe af sandsten med næsten ingen ler (Gruppe 1) eller noget ler i porerne (Gruppe 2). Ultrasoniske hastigheder målt tør, fuldt mættet og delvist mættet bestemmer indflydelsen af fuld og delvis mætning på de elastiske moduler. Sammenligning af de elastiske moduler i

fuldt mættet tilstand med modulerne bestemt ved fluid substitution viser at heterogent fordelt ler kan føre til større afvigelser en homogent fordelt ler. Sandsten med homogent fordelt ler knytter sig til den øvre grænse formuleret af Mavko and Mukerji (1998), men sandsten med et åbent porerum skifter fra den øvre til den nedre grænse ved en bestemt vandmætning. Sandsten med heterogent fordelt ler har en større effekt af væske mætning end forventet fra fluid substitution. Denne fravigelse er afledt af væske der bindes i ler fyldte porer. Kombinationen af de ler fyldte porer og det solide materiale kan betragtes som et effektivt solidt materiale of modulerne for dette er relevant til fluid substitution af den effektive porøsitet alene.

Korrektion af en akustisk log ved fluid substitution reducerer til et estimat af ler fordelingen. Den kritiske evaluering er om leret er heterogent fordelt. Identifikation kan opnåes gennem NMR T_2 spektra af fuldt vand mættede intervaller. Heterogent fordelt ler afstedkommer et multi-modalt T_2 spektrum.

Bærende ler fører til at det mættede kompressibilitetmodulus forøges i forhold til den tørre værdi, hvorimod forskydningsmodulet reduceres af en væske mætning. Denne observation er unik til gruppen med bærenden ler hvorfor denne behandles individuelt. Ultrasoniske hastigheder målt af Mondol et al. (2007) udgør et data sæt der kan isolere effekten induceret af ler. En normaliseing af modulerne til det bærende tværsnit af materiale tillader en sammenligning mellem modulerne i det tørre og mættede ler. Denne sammenligning viser at mætning med saltvand reducerer forskydningsmodulet of øger kompressibilitetsmodulet, kvalitativt sammenligneligt med observationerne i sandsten om end mere udtalt. Fortolkningen af denne effekt indikerer at den an skyldes vand, der er fanget i kontakterne mellem ler partiklerne .

Preface

This thesis was prepared at the Department of Civil Engineering of the Technical University of Denmark and submitted in partial fulfillment of the requirements for the Ph.D degree. The main supervisor is Professor Ida Lykke Fabricius at the Department of Civil Engineering of the Technical University of Denmark. The co-supervisor is Dr. Angus Ian Best at the National Oceanography Centre, Southampton. The project is funded by DONG Energy.

The work comprised in this thesis have resulted in four manuscripts submitted to peer-reviewed journals. Chapter 5, Chapter 6, Chapter 8, Chapter 9, and Chapter 10 closely reproduce the four manuscripts. The title and data for submission of the manuscripts is given in Appendix C along with the chapters corresponding to the content of the manuscripts. Five conference contributions have been based on the work, the abstracts for these are given in Appendix D.

Kongens Lyngby, March 8, 2015

Morten Kanne Sørensen

Acknowledgements

First and foremost I would like to express my appreciation and thanks to my supervisor Professor Dr. Ida Lykke Fabricius, and my co-supervisor Dr. Angus Best.

Many people have contributed greatly with help and advice during my journey, they are all deserving of a great deal of gratitude. From the laboratory at the Department of Environmental Engineering at the Technical University of Denmark I would like to thank Sinh Nguyen and Hector Diaz. From the Geological Survey of Denmark and Greenland I will like to thank Hans Jørgen Lorentzen, Dan Olsen, Marga Jørgensen, Niels Springer, and Claus Kjøller. From the laboratory at the Department of Civil Engineering I will thank Vita Larsen, and John Troelsen. From the laboratory at the National Oceanography Centre I will like to thank Jeremy Sothcott, and Laurence North. Finally from the laboratory at GEO I will like to thank Igor Loboda, and Niels Trads.

I will thank DONG energy for providing financially supporting the project. Tomas Hansen (formerly at DONG Energy) and Niels Christian van Gilse at DONG Energy deserve appreciation for valuable reality checks.

All the people at the Department of Civil Engineering have my deepest gratitude for making the years spend on this work good ones.

Finally, I will thank Lotte Ansgård Thomsen, and Storm Magne Kanne Thomsen, for their patience and wise advice.

Contents

Summary **i**

Sammenfatning **v**

Preface **ix**

Acknowledgements **xi**

Contents **xiii**

List of Figures **xvii**

List of Tables **xxi**

1 Introduction **1**
- 1.1 Motivation . . . 2
- 1.2 Problem statement . . . 2
- 1.3 Scope of study . . . 4

2 Mud-filtrate invasion and sonic logs **7**
- 2.1 Radial sensitivity of sonic logs . . . 8
- 2.2 Mud-filtrate invasion . . . 9

3 Sandstones framework and pore-space **13**
- 3.1 Grain-frame and pore-space coupling during invasion . . . 14
- 3.2 The effect of clay and the clean sandstone reference trend . . . 15

4 Velocities, elasticity, and fluid substitution in sandstone **17**
- 4.1 Elasticity of sandstone . . . 18
- 4.2 Gassmann fluid substitution . . . 19
- 4.3 Applicability of fluid substitution in sandstones . . . 19
- 4.4 Partial and mixed saturation . . . 24
- 4.5 Local sensitivity analysis of fluid substitution . . . 26
- 4.6 The iso-frame model . . . 27

5 **How sandstone-shale mixtures are reflected in dispersion of elastic moduli** **29**
5.1 The data-set . . . 31
5.2 Quantifying pore-filling clay and group delineation . . . 31
5.3 Permeability, shale morphology, and distribution . . . 37
5.4 Gassmann fluid substitution . . . 41
5.5 Distribution of shear residuals . . . 42
5.6 Distribution of bulk residuals . . . 42
5.7 Mechanisms: Gassmann limitation or physical reality . . . 45
5.8 Summary and conclusions . . . 52

6 **Modeling clay dispersion of bulk moduli in sandstone with a homogeneous clay distribution** **55**
6.1 Choice of mineral and frame parameters . . . 56
6.2 Gassmann and induced pore-pressure . . . 59
6.3 Frequency range . . . 61
6.4 Model formulation: Shale laminae . . . 61
6.5 Model formulation: Dispersed shale . . . 64
6.6 Results – Shale laminae . . . 64
6.7 Results – Dispersed shale . . . 65
6.8 Comparison with data . . . 67
6.9 Conclusions . . . 72

7 **Experimental procedures for sandstones with partial pore-filling clay** **75**
7.1 The samples . . . 76
7.2 Cleaning and routine core analysis . . . 77
7.3 Mercury intrusion capillary pressure, MICP . . . 77
7.4 X-ray diffraction, XRD . . . 78
7.5 Low-field NMR T_2 relaxation . . . 80
7.6 Saturation preparation . . . 80
7.7 Sample loading and ultrasonic measurement techniques . . . 81

8 **Characterization results: the influence of clay on the pore-space** **87**
8.1 X-ray diffraction and mineral moduli . . . 88
8.2 Porosity and permeability . . . 91
8.3 Mercury injection capillary pressure . . . 92
8.4 Low-field NMR spectra for fully saturated samples . . . 95

9 **Clay distribution effect on ultrasonic velocities and moduli** **101**
9.1 Dry and fully saturated velocities . . . 102
9.2 Moduli . . . 107
9.3 Moduli under evaporative drying . . . 110

10 **Effect of saturation on load-bearing clay** **121**

10.1 The data 122
10.2 Dry and saturated frameworks 123
10.3 Contact area: The iso-frame model 124
10.4 Discussion 126
10.5 Conclusion 127

11 Conclusion and future work 129
11.1 Recommendations for future work 132

Bibliography 134

A X-ray diffraction data 147

B Velocity data 154

C Journal manuscripts 159

D Conference contributions 161

List of Figures

2.1 Conventional Bore-Hole Compensated (BHC) monopole sonic log 8
2.2 Basic radial step profile saturations 10
2.3 Combination of the invasion and formation fluids 12

4.1 Difference between Brown and Korringa (1975) and Gassmann (1951) 21
4.2 Unaffected saturation of compliant porosity 23
4.3 Capillary entry pressure of compliant porosity 24
4.4 Local sensitivity of fluid substitution 26
4.5 Illustration of the iso-frame model 28

5.1 Correlation matrix of the basic parameters 32
5.2 Estimation of the clay fraction from the elastic moduli 34
5.3 Histogram of shale porosities 35
5.4 Delineation of the classification groups 36
5.5 Crossplot of porosity and permeability for the dataset 38
5.6 Illustration of flow in the groups 39
5.7 Comparison of specific surfaces 40
5.8 Difference between dry and saturated shear moduli 43
5.9 Difference between saturated and fluid substituted bulk moduli 44
5.10 Local flow compliant moduli ratios 46
5.11 Bulk modulus difference in Group 2 48
5.12 Effect of viscosity in Group 3 50
5.13 Viscoelatic moduli in Group 3 51

6.1 Choice of parameters for the sandframe 57
6.2 Choice of parameters for the clay frame 59
6.3 Induced pressure in a framework 60
6.4 Interaction of the framework and the induced pressure 61
6.5 Laminated clay model 62
6.6 Results for the laminated clay model as a function of χ 65
6.7 Results for the laminated clay model as a function of K_c 66
6.8 Results of the dispersed clay model as a function of χ 66
6.9 Overview of the dataset 68
6.10 Limits of a fluid clay suspension modulus 69

6.11 Comparison of data to the dispersed clay model 70
6.12 Comparison of data to the laminated clay model 71
6.13 Fitted clay moduli of the data conforming to the model 72
6.14 Porosity versus permeability for the data consistent with the model 73

7.1 Outcrop and well site locations. 76
7.2 Back-scatter SEM images of Colton, Bandera, Kentucky, and Scioto sandstones 78
7.3 Back-scatter SEM images of Kirby, Berea, Carbon tan, Stenlille, and Boise sandstones 79
7.4 Sketch of the rig used for loading and velocity measurements 82
7.5 Illustration of a loading path 83

8.1 Mineral composition of the solid framework from XRD 88
8.2 Solid clay fraction from XRD 89
8.3 VRH averaged mineral moduli 90
8.4 Cross-plot of porosity and permeability data 92
8.5 MICP curves for Colton, Bandera, Kentucky, and Scioto 93
8.6 MICP curves for Kirby, Berea, Carbon tan, Stenlille, and Boise 94
8.7 NMR spectra fully saturated samples 97
8.8 NMR spectra partially saturated samples 98
8.9 De-saturation models relevant to NMR 99

9.1 Dry V_p and V_s as a function of porosity 104
9.2 Saturated V_p versus V_s 105
9.3 Change in V_p versus V_s with $K0$ for a Berea sandstone 106
9.4 Saturated compressional moduli versus dry compressional moduli 107
9.5 Saturated shear moduli versus dry shear moduli 108
9.6 Relative error of the shear modulus and bulk modulus with fluid substitution 109
9.7 Compressional moduli at partial saturation 111
9.8 Shear moduli at partial saturation 112
9.9 Bulk moduli at partial saturation 114
9.10 Schematic of the effective porosity fluid substitution 115
9.11 Relative error of the shear modulus and bulk modulus with effective porosity fluid substitution 117

10.1 Porosity of clay powders as a function of smectite weight fraction 123
10.2 Poisson's ratio for clay mixtures as a function of axial stress 124
10.3 Fitted iso-frame values to the dry clay frames 125
10.4 Application of the dry frame iso-frame values to the saturated clay mixtures 126

A.1 XRD spectrum for Colton 148
A.2 XRD spectrum for Kentucky 149
A.3 XRD spectrum for Bandera 149
A.4 XRD spectrum for Scioto 150
A.5 XRD spectrum for Carbon tan 150

A.6 XRD spectrum for Berea 151
A.7 XRD spectrum for Kirby 151
A.8 XRD spectrum for Stenlille 152
A.9 XRD spectrum for Boise 152

List of Tables

2.1 The table shows the combinations of formation fluids and mud-filtrates. The arrows indicate the likely effect invasion will have on the elastic moduli. . . . 11

4.1 Mineral moduli used for determining the effective mineral modulus based on the semi-quantitative XRD analysis. 20

5.1 Data for the fluids composing the saturations 33
5.2 Criteria for the classification groups 35

6.1 Mineral moduli of clay minerals and quartz published in the literature. . . . 58

8.1 Mineral moduli from the literature 91
8.2 Effective mineral moduli determined as the average of the Hashin-Shtrikman bound based on the relative fractions determined by XRD analysis 91
8.3 $S_{w,ir}$ estimated from comparison of injected mercury volume and total pore-volume. 95

9.1 Fluid moduli used for distilled water and brine 108
9.2 Effective mineral moduli obtained by inversion of Equation 7.6a for the substitution illustrated in Figure 9.10 116

10.1 Contact moduli used in the model and their ratios. 126

A.1 Fractional composition of the solid frame by semi-quantitative XRD. 147
A.2 Fractional composition of the solid frame by semi-quantitative XRD. 148

Chapter 1

Introduction

1.1 Motivation

Seismic exploration uses elastic waves to extract information about the sub-surface. Increasing application of advanced seismic interpretation, as AVO analysis, increases the need for ties between synthetic seismograms from sonic logs and seismic data. High quality well-ties requires high quality sonic logs. Sonic logs are, however, often affected by mud-filtrate invasion, because of a shallow penetration depth in the formation. Invasion arises from an over-pressure in the borehole relative to the formation pressure to control fluid production from the borehole. Reliable well-ties require correction of sonic logs for the effects of mud-filtrate invasion.

1.2 Problem statement

The focus in this thesis is how to correct sonic logs in sandstone formations for the effect of mud-filtrate invasion. Evaluation of the need for correction is done depends on the relative magnitude of radius of the invaded annulus, and the radius of the annulus probed by a sonic logging tool. Sonic logging tools emit elastic waves in the sonic range (1 kHz – 40 kHz) that penetrate a formation to a depth governed by the frequency of the wave, the wave velocity in the formation, and the transmitter-receiver separation in the logging tool (Chi et al., 2006; Baker and Winbow, 1988). The penetration depth is universally shallow as sonic logs utilize refracted waves, or surface waves. A generic estimate argued in Section 2.1 limits the penetration depth to ≈ 20 cm.

The volume of mud-filtrate that invades a formation is chiefly determined by the properties of the mud. Minutes after the drill-bit penetrates a formation, filtration of solids at the borehole surface have formed a low permeable mud-cake, which determines the rate of invasion (Allen et al., 1991; Ferguson and Klotz, 1954; Abrams, 1977). The pore-space of the formation determines how the invaded mud-filtrate is distributed. Much of the difficulty concerning mud-filtrate invasion stems from the difficulty in determining the radial saturation profile for the mud-filtrate. Invasion displaces fluid in the effective porosity, always leaving the irreducible wetting saturation in place. Defining the radius of the invaded zone is ambiguous as the invasion saturation front is often sloping, so some regions are affected more than others. For sandstones of reservoir quality invasion affects the saturation deeper than the 20 cm, which is probed by the sonic log. The specifics of this analysis and the link between formation properties and filtrate distribution is presented in Section 2.2. Sonic logs, therefore require correction for invasion to provide the true formation velocities. Only immiscible invasion in the effective porosity cause a modulus contrast sufficient to affect the sonic log.

Correction of sonic logs is carried out by Gassmann (1951) fluid substitution, which quantifies the induced pressure in the pore-space of a saturated sandstone. Fluid substitution relies on assumptions that the sandstone framework is homogeneous, and do not differ at different fluid saturations. Fluid substitution also requires a uniform induced pressure. For a fully saturated sandstone the validity of these assumption and the effects of violation is considered in Section 4.3. Violations of the assumptions in fully saturated sandstones are related to the small fraction of compliant porosity in the framework, a wetting film on the grains, and clay in the pore-space. The effects of the first two violations are constant when the irreducible water saturation is kept in place, and therefore these effects does not cause a relative effect under mud-filtrate invasion. Clay may be found in the effective porosity and contribute differently depending on the saturation. Mixed saturation is incoporated in fluid substitution by a set of effective fluid moduli bounds formulated by Mavko and Mukerji (1998). The upper bound is where the fluid are dispersed as patches and fluid substitution is done in individual patches, and the lower bound is where the fluids have an average pressure determined by the Reuss average, and fluid substitution is done using this effective fluid modulus. These bounds does not include any evaluation of the pore-space affinity to the fluids, Any region of the pore-space are equally likely to be saturated by any fluid and any part of the pore-space contributes evenly to the saturated elastic moduli. A review of ultrasonic data in the literature, in Section 4.4, finds that fluid substitution using the bounds are accurate in sandstone with a simple pore-space (Gregory, 1976; King et al., 2000; Goertz and Knight, 1998), but less so in sandstone with a more complex pore-space. Low clay content and high permeability defines sandstone with a simple pore-space, while high clay content and low permeability defines sandstone with a complex pore-space. Klimentos (1991) found saturated elastic moduli to be more closely correlated with clay content than permeability and Han (1986) found clay content to be related to the departure of saturated elastic moduli from fluid substitution. The effects observed are thus likely associated with pore-filling clay affecting the pore-space. The nonconformity of sandstone with a complex pore-space to fluid substitution may arise from the fact than in a complex pore-space not all parts of the pore-space have the same affinity to any fluid. The fluid saturation is not a free parameter, but a function of how the saturation is achieved. Likewise this differential fluid affinity may affect the saturated moduli as observed for the fully saturated sandstones.

With this, the pertinent question in correction of sonic logs is how to incorporate clay in the description, including the effects of clay on the saturated elastic moduli, the fluid distribution under invasion and any links between these.

Any part of the pore-space that have an anomalous effect on the saturated elastic moduli, will always exert this effect if it is saturated. Therefore any contribution from possibly clay-filled in a state of mixed saturation will also be present at full saturation. [1]. Data for fully saturated sandstones are more abundant and better defined than for mixed saturation. Evaluation of how clay in the sandstone framework affects the saturated elastic moduli can be done using a data set of ultrasonic velocity data from the literature. This analysis of the contribution from clay results in a classification determined by the distribution of clay in the sandstones framework, presented in Chapter 5. Clay can affect the saturated elastic moduli by altering the interaction between the pore-space and the saturated framework moduli as the modulus of clay mixed with fluid is different from the the fluid (Marion et al., 1992). Clay only affect the elastic moduli of the unsaturated sandstone framework when in the load-bearing frame (Anstey, 1991; Minear, 1982). The often-stated notion that clay universally reduces the elastic moduli of a sandstone framework, originates from the implicit assumption that a measured porosity determinately specifies a sandstone framework. In this view, the effect of clay on the elastic framework moduli is determined by comparing a clean sandstone and a shaly sandstone at the same measured porosity. Gal et al. (1999) demonstrated how pore-filling clay causes an error in the measured porosity as the solid clay fills pores between the grains in sandstone framework. The measured porosity is then lower than the actual porosity of the load-bearing framework. The framework moduli are determined by the load-bearing framework porosity, so in the comparison it appears that clay have reduced the framework moduli. For some sandstones obviously clay do participate in the load-bearing framework, and reduce the framework moduli. The classification in develeoped in Chapter 5[Manuscript C] distinguishes these instances for a data set of ultrasonic velocities from collected from the literature (King, 1966; Han, 1986; Best, 1992; Khazanehdari and McCann, 2005). The clay distribution is determiened by estimating the clay fraction from the unsaturated compressional following the approach of Gal et al. (1999) and comparing this estimate to petrographic shale fraction (shale refer to the combination of clay and intra-clay porosity). If the clay fraction from the elastic framework moduli, agrees with the clay fraction from image analysis the clay is considered pore-filling, if not the clay is considered load-bearing.

---

[1] Assuming surface can be neglected as found by Tserkovnyak and Johnson (2002).

The classification in Chapter 5 divides the lithologies in the data-set into four groups; clean sandstone, sandstone with partial pore-filling clay, sandstone with pores dominated by clay, and sandstones with load-bearing clay. The clean sandstone groups is arbitrarily defined with a cutoff shale fraction of $\chi < 0.02$ to serve as reference group not affected by clay. Fluid substitution performs well in clean sandstones, with the discrepancies described in Section 4.3. For sandstone with pore-filling clay a divergence is observed on the bulk modulus, which is increased as pore-space becomes filled with clay. Load-bearing clay cause a reduction in shear modulus not seen by in other groups, while the bulk modulus is still increased beyond the prediction of fluid substitution. Sandstone reservoirs for the most part contain some fraction of clay, whereby Group 2 with partially pore-filling clay is the focus of the development in Chapter 6[Manuscript C],Chapter 8, and Chapter 9[Manuscript C], the aim is to define the mechanism responsible for the under-prediction of the saturated bulk moduli in this group and to consider a procedure to attain better prediction.

The effect of fluid saturation on the sandstones with load-bearing clay diverges from the other groups and warrants a separate analysis presented in Chapter 10[Manuscript C].

1.3 Scope of study

The analysis in this thesis is composed of five parts. In Chapter 2, Chapter 3, and Chapter 4 the concepts used in the analysis is developed along with the arguments for the focus on the effect of clay. The need for correcting sonic logs is addressed in Chapter 2, the treatment is limited to water-wet sandstones. In Section 2.2 different combinations of mud-filtrates and undisturbed saturation is presented. Sonic logs are only affected by invasion if the mud-filtrate have a fluid modulus significantly different from the fluid in place in the formation. Salinity gradients is associated with a modulus contrast, but this is too low to be be detected by a sonic log. Hereby invasion will refer to immiscible displacement only, meaning water invading an oil bearing formation or oil invading a water bearing formation.

Clay have a different effect and development in sandstones than other minerals. The development of a sandstone and the role of clay is presented in Chapter 3. The diagenetic trend relating porosity to the elastic moduli of a lithified sandstone framework, which is used for the classification in Chapter 5 is presented in 3.2, this trend takes the form of the Modified Upper Hashin-Shtrikman (MUHS) bound (Gal et al., 1999, 1998).

Gassmann (1951) fluid subsitution is the only model applied in this thesis to predict elastic moduli. Many other models exists, and are commonly applied in rock-physics of sandstone. Gassmann fluid substitution is the only purely phenomenological model, however, which gives it a broader application without the need to adjust it to a specific formation. Extensions to the basic formulation of fluid substitution is formulated in a way that, as far as possible, avoids parameters adapted to a specific lithology.

In 5[Manuscript Appendix C] the quantitative classification used to distinguish the distribution of clay is developed. A data set of ultrasonic velocities recorded at high stress ($\sigma - P_{pore} > 40$ MPa) in fully saturated sandstones serves to develop the classification, and subsequently analyze the application of Gassmann fluid substitution in the different classification groups. The data are collected from studies published in the literature (King, 1966; Han, 1986; Best, 1992; Khazanehdari and McCann, 2005). The classification divides the lithologies in groups of sandstones with: negligible pore-filling clay, partial pore-filling clay, homogeneous pore-filling clay, or load-bearing clay. The data set includes petrographic analysis of the volumetric shale fraction by image analysis used to verify the correction of porosity for pore-filing clay.

Fluid substitution under-predicts the bulk moduli of sandstones with pore-filling clay as gathered from the application of fluid substitution in the classification groups in Chapter 5. Best et al. (1994) suggested local flow from intra-clay porosity to the framework porosity to be the cause. This mechanism was dubbed clay-squirt by Best et al. (1994) and this denotion is also used in this study.

In Chapter 6 a model is formulated based on fluid substitution that quantifies the possible extend of clay-squirt on the bulk modulus in the case of homogeneously distributed clay. The model is restricted to the bulk modulus as the comparison of dry and saturated shear modulus in Section 5.5 does not show significant changes of the shear modulus, and to avoid assumptions of the geometry of clay inclusions.

Similarly heterogeneous distributions of clay are not easily modeled without introducing a bias in the model from the assumptions of the clay distribution. Experiments on sandstones with little or partly pore-filling clay therefore serve, to quantify the effect of heterogeneous clay. Selection of the sandstones focus on well-consolidated sandstones that have negligible, or partly pore-filling clay. A thorough characterization of the pore-space, described in Chapter 7, determines the distribution of clay in the pore-space. Ultrasonic velocities measured in dry, fully saturated, and partially saturated states yields the elastic moduli of the sandstones.

Load-bearing clay cause a shear modulus softened by saturation and bulk modulus stiffened by saturation according to the classification in Chapter 5. Elastic moduli of dry and saturated clay powders recorded by Mondol et al. (2007) provide a test of whether the effect may be ascribed to the clay or the interaction between clay and grains. A normalization is developed in Chapter 10 capable of normalizing the elastic moduli to a common basis for comparison. Softening of the shear modulus and stiffening of the bulk modulus characterize the clay data as the sandstone data. Clay between the contacts of clay platelets are suggested to cause this effect.

Chapter 2

Mud-filtrate invasion and sonic logs

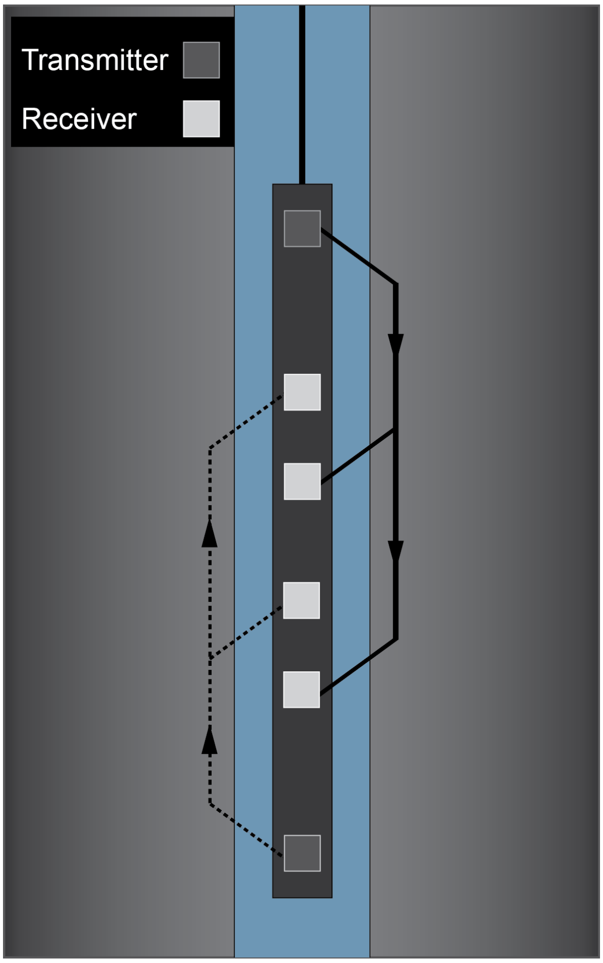

Figure 2.1: Illustration of a conventional BHC mono-pole sonic log. A mono-pole pressure pulse is emitted from the transmitters and recorded at the two receiver pairs. The resulting travel time for the formation is the averaged difference in travel-time between the two receiver pairs. This measurement compensates for bore-hole irregularities and tool orientation.

2.1 Radial sensitivity of sonic logs

Logging tools are naturally confined to the bore-hole, whereby no direct wave can be used to measure the formation velocities by a sonic log as illustrated in Figure 2.1.

Sonic logs therefore measure the travel times of waves traveling along the surface of the bore-hole. Conventional sonic log tools are the BHC mono-pole tools operating at a frequency of 10 to 40 kHz, newer tools involve multi-pole transmitters and receivers which operate at a lower frequency $1-12$ kHz (Close et al., 2009). Radial sensitivity of sonic logs depends on tool type, tool frequency, formation velocity, mud-filtrate invasion, drilling damage, and mud-cake thickness. As a rule of thumb for BHC mono-pole tools the sensitive depth in inches is equal to the transmitter-receiver separation in feet (Baker,

1984). Conventional BHC tools have transmitter-receiver distances of $3-6$ ft and therefore probe an annulus with a thickness of $3-6$ in (7 − 16 cm). Full-wave train inversion and multi-pole sonic tools can attain deeper penetration, and offer radially dependent inversion of the formation velocity (Haldorsen et al., 2006). Chi et al. (2006) demonstrated radial inversion of formation velocity using a multi-pole to applied to a layered model up to 50 cm. Multi-pole tools can have depth of penetration $3-4$ times larger than mono-pole tools, when the annulus affected by drilling and invasion have lower velocities than the virgin formation (Baker and Winbow, 1988).
Simulations by Xu et al. (2012) of a mono-pole sonic logging tool measuring at 8 kHz in a gas-bearing sandstone invaded by Oil Based Mud (OBM), showed the measured travel-time to be dominated by invasion after an invasion depth of 18 cm. The precise radial sensitivity profile of a sonic log changes depending on the properties of the log, the surrounding formation, and the bore-hole environment. Without radial inversion techniques however, the sensitivity of sonic logs is largely restricted to an annulus of 20 cm from the well-bore.

2.2 Mud-filtrate invasion

Drilling mud is circulated through a bore-hole to transport drill cuttings to the surface and to prevent influx of formation fluids into the bore-hole. Control of formation fluid is assured by keeping the pressure in the bore-hole higher than or equal to the formation pressure by adjusting the density of the mud. Mud density is controlled by adding solid weighting agents to the fluid base of the mud. The fluid base of a drilling mud can be either water (Water Based Mud (WBM)), or oil (OBM)[1]. The excess pressure in the bore-hole cause a radial pressure gradient forcing fluid from the mud to invade the formation replacing formation fluids. Solid particles suspended in the fluid are filtered from the mud at the bore-hole surface forming a mud-cake on the surface.

Invasion is an undesirable loss of drilling mud, and the invasion of small particles and chemicals added to the mud can damage the formation reducing the formation producibility (i.e. permeability) (Krueger, 1988). The size distribution of the solids added to the drilling mud is therefore designed to quickly form a low-permeable mud-cake, preventing a a large loss of mud to the formation (Abrams, 1977). Establishment of the mud-cake separates invasion into two regimes; spurt-loss and filtration loss (Black et al., 1985). Initially the drilled formation is open to invasion of both fluid and suspended particles. Invasion rates are governed by the formation permeability in this initial phase, known as spurt-loss, where the mud invades the exposed formation. Particles of comparable to slightly smaller size than the pore-sizes is deposited in a shallow annulus forming an internal mud-cake. With a proper size distribution of the suspended solids the internal mud-cake resides with the first mm of the formation (Bailey et al., 2000), and is established in seconds to minutes (Xie, 2001) after which filtration loss proceeds. During

---

[1] Emulsions are also common, but are omitted for simplicity of the concepts, WBM and OBM are considered to behave as extremes relative to emulsions.

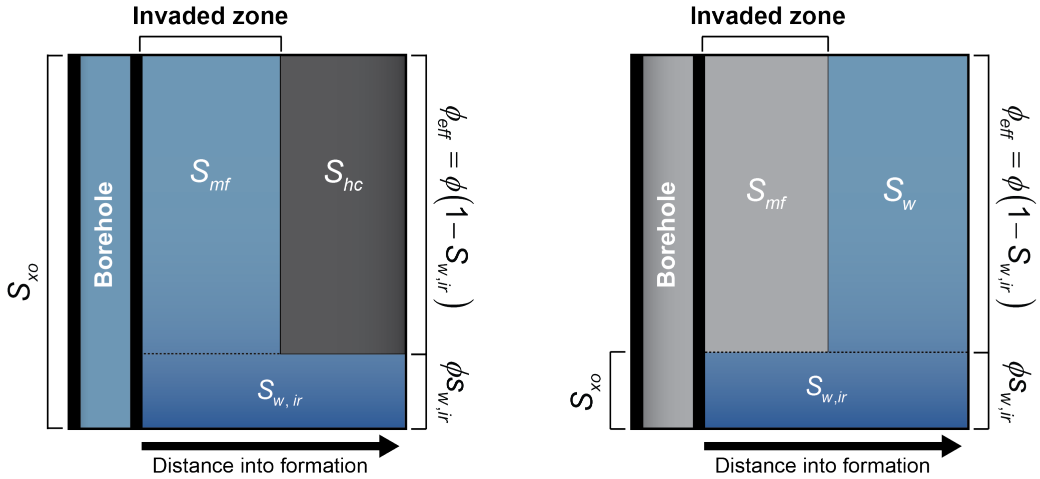

(a) WBM invading oil bearing sandstone

(b) OBM invading water saturated sandstone

Figure 2.2: Radial saturation step profiles. In the case of WBM invading an hydrocarbon bearing zone (a) the saturation is reduced to the residual oil saturation, for OBM invasion the water saturation is reduced to the irreducible water saturation. For cases the saturation is mixed in the effective porosity and the irreducible water saturation remains saturated with the wetting fluid, which is water in this case.

filtration loss solids are deposited on the bore-hole wall and only the fluid base invades the formation. Deposition of the solids creates a mud-cake on the bore-hole surface. The suspended solids are fine grained and the permeability of the mud-cake is low. Hereby most of the pressure gradient is absorbed over the mud-cake and the mud-cake determines the invasion rate (Dewan and Chenevert, 1993; Wu et al., 2005). While mud is circulated in the bore-hole the thickness of mud-cake is reduced by the shearing action of the circulating mud. Invasion while the drill pipe is in the bore-hole is referred to as dynamic filtration and accounts for the largest volume of invasion(Allen et al., 1991).

Invasion is a multiphase flow driven by the radial pressure gradient caused by the overpressure in the bore-hole. The most basic radial invasion profile is the step profile illustrated in Figure 2.2 for a water-wet formation. In a radial saturation step profile the invaded zone is completely flushed and the formation is unaffected beyond the invaded zone. Due to the difficulty of determining the actual invasion profile in-situ, this base case often serves. The applicability of the step profile depends on the depth of investigation of the tool in question, for long-spaced resistivity tools this invasion profile is very poor, for sonic logs it is often adequate (Head et al., 1992; Briceo and Peeters, 2005). The actual radial profile is determined by the balance between viscous and capillary forces (Phelps, 1995). The mud-cake dominates the rate of fluid flowing into the formation essentially decoupling the flow from the formation properties (Chenevert and Dewan, 2001; Wu et al., 2005). Capillary forces are generally dominant in high-permeable for-

	Formation fluids		
Mud base	Water	Water / Oil	Water / Gas
WBM	-	↑	↑
OBM	↓	-	↑

Table 2.1: The table shows the combinations of formation fluids and mud-filtrates. The arrows indicate the likely effect invasion will have on the elastic moduli.

mations, and viscous forces in low-permeable formations (Lenormand, 1990). Because of this, displacement in low-permeable formations are piston-like, flushing the effective porosity almost completely. In high-permeable formations the mud-filtrate saturation profiles are deeper, but more sloping (Phelps, 1995; Allen et al., 1991). Comparison of simulations conducted in several studies suggests that after a filtration time of 24 h an almost constant saturation is achieved in the region probed by sonic logs (Salazar and Torres-Verdín, 2008; Lane, 1993; Chenevert and Dewan, 2001).

Several combination of formation fluids and mud-filtrates are possible, in Table 2.1 the combinations are given and their probable effect on a sonic log reading relative to the virgin state. For a water wet system all combinations of formation fluids and mud-filtrate will have a water saturation larger or equal to the irreducible water saturation, $S_{w,ir}$, as illustrated in Figure 2.3. The irreducible water saturation is a property of the pore-space texture of the sandstone. The water saturation corresponding to the irreducible water saturation is therefore a practicable of reference for the correction of sonic logs.

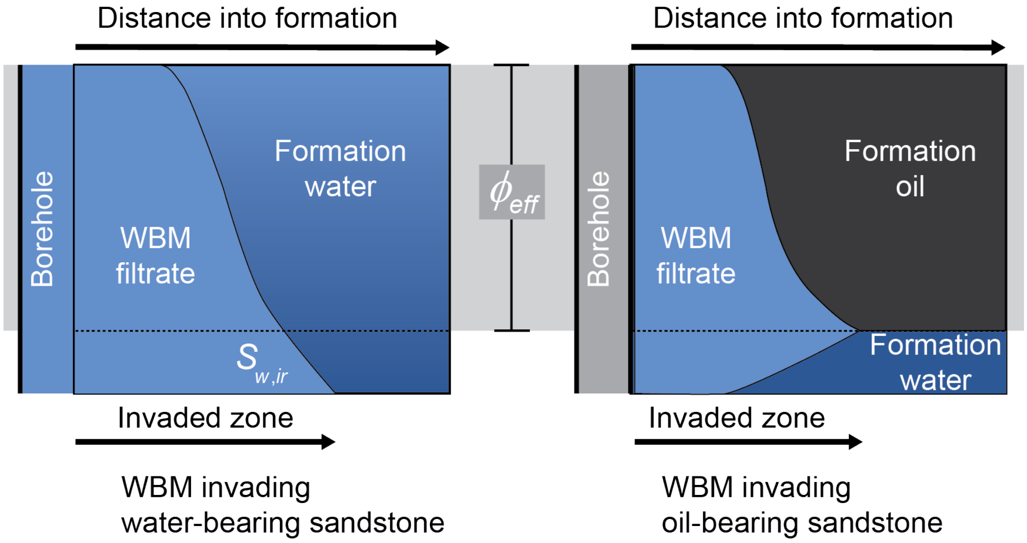
Distance into formation
Borehole
WBM
filtrate
Formation
water
$S_{w,ir}$
Invaded zone
WBM invading
water-bearing sandstone
ϕ_{eff}
Distance into formation
Borehole
WBM
filtrate
Formation
oil
Formation
water
Invaded zone
WBM invading
oil-bearing sandstone

(a) The qualitative radial saturation profiles from WBM filtrate invasion in a water-wet sandstone.

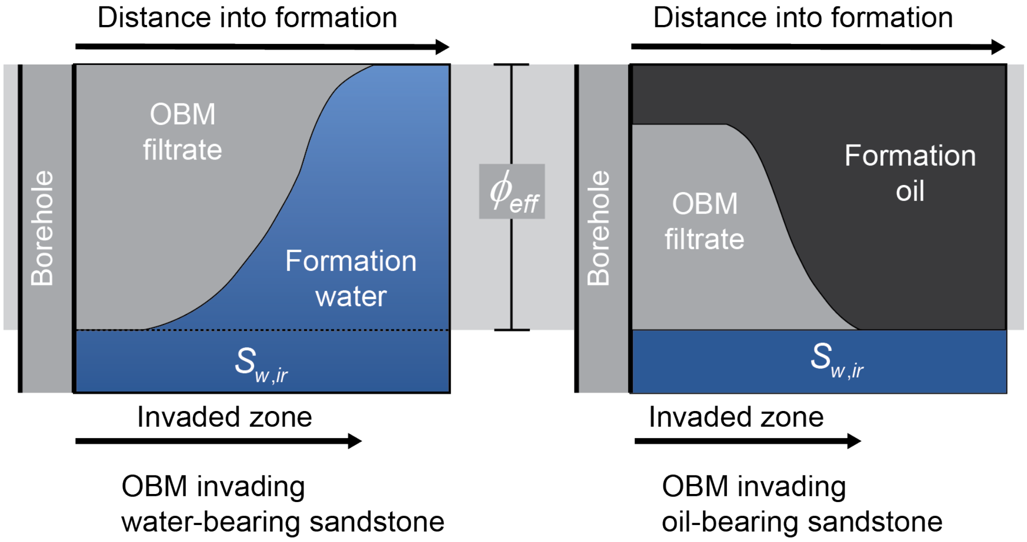
Distance into formation
Borehole
OBM
filtrate
Formation
water
$S_{w,ir}$
Invaded zone
OBM invading
water-bearing sandstone
ϕ_{eff}
Distance into formation
Borehole
OBM
filtrate
Formation
oil
$S_{w,ir}$
Invaded zone
OBM invading
oil-bearing sandstone

(b) The qualitative radial saturation profiles from OBM filtrate invasion in a water-wet sandstone.

Figure 2.3: Qualitative radial saturation profiles of mud-filtrate in a water-wet sandstone formation.

Chapter 3

Sandstones framework and pore-space

3.1 Grain-frame and pore-space coupling during invasion

Sandstones are the diagenetic product of a detrital sand, which is buried, compacted, and cemented (Burley and Worden, 2003). The measurable parameters of sandstone are the results of both the composition of the detrital sand-pack and the subsequent lithification. Complexity at micro-scale, and the amount of variables involved in diagenesis makes empirical regression models common in rock- and petro-physics. Within a single formation, porosity and permeability are often for instance well correlated (Nelson, 1994; Bloch, 1991). Most correlations are, however, only applicable within the specific geological unit in which it is determined. Correlations can be derived from measurements on the core-scale and be applicable to a formation of much larger scale, illustrating the homogeneity of the rock fabric arising from similar deposition and diagenesis (Scherer, 1987). The fabric and arrangement of solid material composing a sandstone are referred to by the texture property. Texture is primarily determined by the grains composing the load-bearing framework of the sandstone. The framework is composition of the detrital sand; grain-size, grain-sorting, grain-shape, and mineralogy, and secondly by diagenesis. An applied stress is projected through the sandstone framework of grains, whereby the elastic and mechanical response to an applied stress is governed by the texture of the sandstone framework. Between the grains is the porosity, which contains the fluid and facilitates the flow. Properties which involve flow through the pore-space (eg. permeability, and electrical resistivity) are determined by the texture of the pore-space, which is determined by the Pore-Size Distribution (PSD) of the sandstone framework, and any pore-filling material. often, and with the most pronounced implications, pore-filling material is composed of clay minerals. Clay grains (or platelets) are per definition at least an order of magnitude smaller than sand grains. Clay and sand are therefore not deposited simultaneously with the detrital sand (Blatt et al., 1980). Aggregates of clay minerals (floccules, aggregates, lithic remnants) may be deposited along with sand, but these are structurally weak and most often broken by mechanical compaction during burial. Hence clay whether detrital, authigenic, or allogenic is often pore-filling (Worden and Morad, 1999; Wilson and Pittman, 1977).

Since the pore-space is framed by the PSD of the sandstone framework the pore-space is coupled with to texture of the sandstone framework. Elastic or plastic compression of the grain-frame often cause a reduction in permeability (Davies and Davies, 2001; Gray and Fatt, 1963). Coupling between the pore-space and the sandstone framework occur when compression of the sandstone framework is projected to the pore-space causing an inducing a pressure (Biot, 1941, 1962). If the pressure can dissipate to unstressed areas, or the modulus of the pore-fill is low (eg. as for uncompressed gas), there is no coupling between non load-bearing pore-filling material and the sandstone framework (Anstey, 1991; Minear, 1982).

Klimentos (1991) investigated the correlation between elastic velocities and permeability, but only found a weak correlation, which was possibly a result of an underlying correlation between pore-filling clay, and permeability. Permeability is very sensitive to the texture of the pore-space, both the PSD of the sandstone framework (Nelson, 1994; Beard and Weyl, 1973), and the pore-filling material (Neasham, 1977; Wilson and Pittman, 1977). Mud-fitrate invasion affects sonic logs by a two-stage coupling of the pore-space and the sandstone framework. The fluid distribution resulting from invasion is determined by the pore-space texture as presented in Section 2.2, and the velocities measured by a sonic log is influenced by coupling with the pore-space texture through the induced pressure. In a homogeneous sandstone with little pore-filling material any region of the porosity is equally likely to be saturated and the fluid distribution is adequately described by the saturation. When the pore-space texture is affected by pore-filling material the distribution of invaded fluid becomes linked to the pore-space texture. In a homogeneous sandstone with a simple pore-space defined by the PSD of the quartz grain framework, all parts of the porosity is equally likely to be saturated during invasion and all parts of the porosity gives rise to the same induced pressure. In a sandstone with a more complex pore-space texture involving pore-filling clay the areas affected by the pore-filling clay will be more likely to be saturated by the wetting fluid and will have a higher induced pressure due to the increased pore-filling modulus (Marion et al., 1992). This effect is observed by Han (1986) when comparing dry measured elastic velocities with saturated velocities in sandstones with increasing clay content.

With these observations the problem of correcting sonic logs for invasion separates into two cases. In the first case, sandstone with a simple pore-space governed solely by the PSD of the grain framework. Here, the induced pressure is purely a relation between compression of the sandstone framework and the fluid. For this case sonic log correction requires only quantification of the induced pressure under compression characterized by the fluid saturation. For sandstones with simple pore-space texture the invasion mechanism does not favor specific pore entities and therefore there is no direct link between the invasion characteristics and the induced pressure. For the case of sandstone with a heterogeneous pore-space texture affected by pore-filling clay an invading fluid is not equally likely to be distributed in the entire pore-space. The elastic moduli of the saturated sandstone as addressed in correction of sonic logs will also be influenced by the non-uniform induced pressure which is directly related to the distribution of the invading fluids.

3.2 The effect of clay and the clean sandstone reference trend

Drained elastic moduli are determined by the texture of the sandstone framework. Detrital sands have porosity in the order of $\phi = 0.4$, mechanical compaction by burial and early cementation reduce the porosity to $\phi \approx 0.3$, after which chemical cementation reduces the porosity towards $\phi = 0$. This diagenesis results in a relation between porosity and elastic moduli consistent with the MUHS bound with a critical porosity in the range between $\phi_c = 0.4$ and $\phi_c = 0.45$. The critical porosity is the highest porosity where a sandstone retains rigidity i.e. the transition from solid to suspension. Gal et al. (1998) presented an analysis illustrating that the trend between moduli and porosity described by the MUHS was consistent with even cementation occurring in the pores leading to a uniform decrease in pore-space. The trend found for lithified sandstone therefore reflects the diagenetic consolidation of sandstone. Several authors have reported that relative to clean sandstone shaley sandstones have lower moduli at a given porosity (Han, 1986; Klimentos, 1991; Castagna et al., 1985; Best and McCann, 1995; Tosaya, 1982). This is sometimes reported in the literature as though clay reduces the elastic moduli of sandstone absolutely, while the observation is in fact restricted to a relative effect compared with a clean sandstone at a similar porosity. In this analysis all references to the effect of clay on elastic moduli will explicitly be done relative to the clean sandstone cementation trend described by the MUHS with a critical porosity of $\phi_c = 0.45$.

Chapter 4

Velocities, elasticity, and fluid substitution in sandstone

4.1 Elasticity of sandstone

Sonic logs measure the travel time, T, over a specified distance, L, from which formation velocity can be determined,

$$V = \frac{L}{T} \tag{4.1}$$

In a infinite isotropic elastic medium two waves can be excited polarized either parallel or perpendicular to the direction of propagation, compressional waves, V_p, and shear waves, V_s, respectively. The velocity of a wave in a sandstone is determined by the elastic moduli of the sandstone and the density,

$$V_p = \sqrt{\frac{M}{\rho}} \tag{4.2a}$$

$$V_s = \sqrt{\frac{G}{\rho}} \tag{4.2b}$$

Where, M, is the compressional modulus, G is the shear modulus, and ρ is the bulk density including solid material and pore-fill. The compressional modulus relates strain to stress when the medium is compressed without any lateral deformation. The compressional modulus is a combination of the bulk modulus, K, which relates volumetric strain to stress under isotropic compression and the shear modulus, G, which relates shear deformation to stress. The compressional modulus is given by,

$$M = K + \frac{4}{3}G \tag{4.3}$$

Isotropic elastic media are characterized by two independent moduli, in this treatment chosen to be the bulk and the shear modulus. Compressional moduli are included due to their natural relation to V_p. When the pore-fill have a negligible bulk modulus or is allowed to drain out under compression the moduli are a property of the grain-frame and quantified by the moduli $(M_{frame}, G_{frame}, K_{frame})$.

The frame moduli are lower than the moduli of the solids composing the frame, both because of the pores between the grains, but also because the structure of the grain-frame is imperfect. The entire solid cross-section given by $(1-\phi)$, does not support the load equally. The compression of the grain-frame is determined by both the minerals composing the grains and frame texture. The deformation not accomodated by the solid content is often referred to as the pore-compressibility, $Z_{phi} = 1/K_\phi$ (Mavko and Mukerji, 1995). Compressibility of a sandstone, $Z = 1/K_{frame}$ is thus the sum of mineral compressibility, $Z_0 = \frac{1}{K_0}$, and pore compressibility, $Z_{phi} = 1/K_\phi$,

$$\frac{1}{K_{frame}} = \frac{1}{K_0} + \frac{\phi}{K_\phi} \tag{4.4}$$

Where K_0 is the bulk modulus of the solid, and K_ϕ the apparent modulus of the pore-space.

4.2 Gassmann fluid substitution

Induced pressure, consequent of pore-compression, resists compression increasing the bulk modulus of the sandstone by reducing the pore-compression, relative to that observed in the drained case. Determining the un-drained frame bulk modulus, K_{sat}, therefore involves a feed-back between pore-compression and induced pressure. Gassmann (1951) derived relations between the drained bulk modulus and the un-drained bulk modulus, in terms of the mineral modulus, porosity and fluid modulus, K_f (Bourbié and Coussy, 1987),

$$K_{sat} = K_{frame} + \alpha^2 F, \tag{4.5a}$$

$$G_{sat} = G_{frame}, \tag{4.5b}$$

where

$$\alpha = 1 - \frac{K_{frame}}{K_0}, \quad 1/F = \frac{\alpha - \phi}{K_0} + \frac{\phi}{K_f}$$

Shear deformation involve no compression and therefore induce no pressure, whereby the drained frame shear modulus, G_{frame} is the same as the undrained frame shear modulus, G_{sat}. Underlying the derivation of Equation (4.5a) and Equation (4.5b) are three fundamental assumptions,

1. The solid frame is homogeneous
2. The undrained moduli are unaltered by saturation (i.e. no chemical alteration)
3. A uniform pore-pressure is induced under compression

The extend to which these assumptions apply to sandstones, and especially sandstones with mixed saturation, is the primary point addressed in this study.

Biot (1956a) formulated equivalent relations and extended them for high-frequency waves to include the coupling (or lack thereof) between the fluid and and solid. Dispersion occurs when inertia dominates the viscous coupling between fluid and solid (Biot, 1956b). While this dispersion mechanism is observed in glass beads (Berryman, 1980) and clean sandstones, it is generally found to be dominated by other mechanisms of dispersion (Winkler, 1985; Khazanehdari and McCann, 2005).

Fluid substitution between the drained frame modulus and the undrained frame modulus can be cast in a multitude of ways (Green and Wang, 1986; Gassmann, 1951; Bourbié and Coussy, 1987; Mavko et al., 2003). The basic notion is that a reduction of pore-space leads to induced pressure, which resists compression. The feedback in the system results in the complexity of F in Equation 4.5a which depends on both mineral, frame, and fluid properties.

Mineral	Bulk modulus K_0, [GPa]	Shear modulus G_0, [GPa]	Source
Quartz	38	45	(Koga et al., 1958)
K-feldspar (Perthite)	47	24	(Carmichael, 1989)
Plagioclase (Albite)	59	35	(Brown et al., 2006)
Calcite	70	29	(Peselnick and Robie, 1963)
Dolomite	95	45	(Humbert and Plicque, 1972)

Table 4.1: Mineral moduli used for determining the effective mineral modulus based on the semi-quantitative XRD analysis.

4.3 Applicability of fluid substitution in sandstones

Fluid substitution as formulated by Gassmann (1951) is exact when the medium comply with the assumptions. Sandstone does, however, often diverge from the assumptions. The compatibility of sandstone with the assumptions is presented along with possible extension to improve the application of fluid substitution.

Heterogeneous (poly-mineralic) frames

Sandstone contains significant fractions of feldspar, carbonate, clay, and other minerals, and are thus not mono-mineralic. Mineral moduli of these common minerals are however of same order of magnitude as seen in Table 4.1. Clays are also present, but the mineral moduli of clay are ambiguous (Vanorio et al., 2003; Mondol et al., 2008; Katahara, 1996; Chen and Evans, 2006). Clay minerals are by definition minute in size (< 3.9 µm) and are therefore more often found in the pores of the grain-frame.

Brown and Korringa (1975) extended Equation 4.5a to heterogeneous poly-mineralic frames introducing two additional moduli, K_s and $K_{\phi'}$ [1]. These moduli are defined as,

$$\frac{1}{K_s} = -\frac{1}{V}\left.\frac{\partial V}{\partial \sigma}\right|_{P_c - P} \tag{4.6a}$$

$$\frac{1}{K_{\phi'}} = -\frac{1}{V_\phi}\left.\frac{\partial V_\phi}{\partial \sigma}\right|_{P_c - P_P} \tag{4.6b}$$

These moduli denote the response of the solid to a change in stress keeping the difference between external pressure, P_c, and the pore-pressure, P_p, constant. In Figure 4.1 the different between Brown and Korringa (1975) and Gassmann (1951) is simply illustrated. In Gassmann's formulation $K_0 = K_{\phi'} = K_s$, and in the formulation of Brown and Korringa (1975) $K_0 \neq K_{\phi'} \neq K_s$. The extension of Brown and Korringa (1975) allows the pore-volume to change independent of the bulk volume as illustrated in Figure 4.1 in a test where the the external pressure equals the pore-pressure. Relative to Equation

---

[1] This moduli should not be confused with K_ϕ

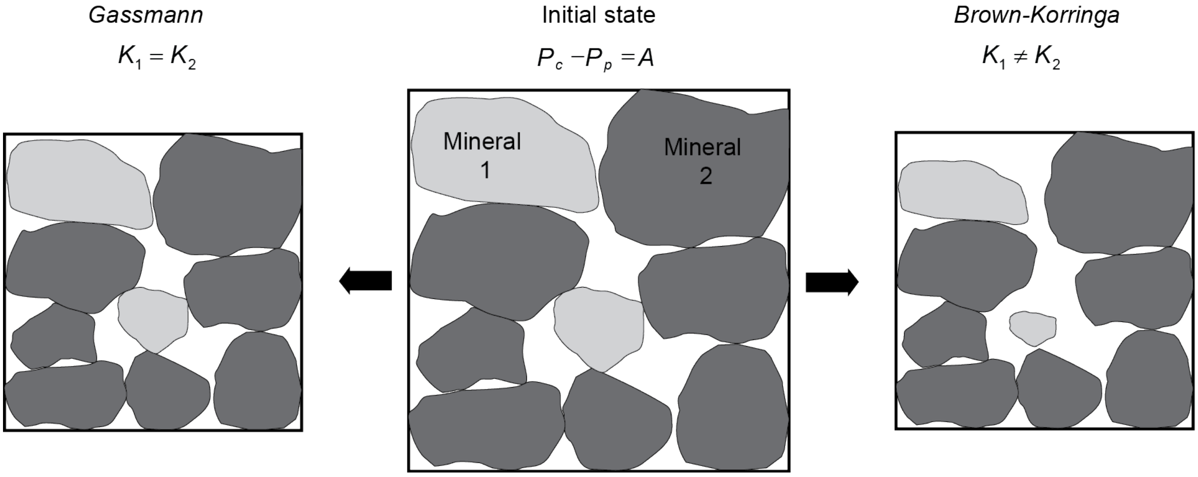

Figure 4.1: Sketch of the difference between Gassmann (1951) and Brown and Korringa (1975).

4.5a the difference introduced by Brown and Korringa (1975) is in F,

$$\frac{1}{F_{BK}} = \frac{\alpha}{K_s} - \frac{\phi}{K_{\phi'}} + \frac{\phi}{K_f} \tag{4.7}$$

The rest of Equation 4.5a is unchanged. Theoretical considerations (Ciz et al., 2008) and numerical simulations (Knackstedt et al., 2005; Makarynska et al., 2007) show that for randomly dispersed grains with different mineral modulus a Voight-Reuss-Hill (VRH) average of the mineral moduli is applicable to determine $K_{\phi'} \approx K_s$ and with this effective mineral modulus Equation 4.7 reverts to Equation 4.5a. Mavko and Mukerji (2013) found that if the minerals have a distinct structure, such as grain lining clay for instance, or the contrast between the mineral moduli is large (> 0.5), the effective mineral modulus yields significant error.

Fluid alteration of frame moduli

Fluid substitution assumes the moduli of the frame to be unaffected by saturation. The shear modulus provides a good test for this assumption as it should be completely unaltered by saturation according to Equation (4.5b). It is often observed that the shear modulus is reduced in the saturated state relative to the dry state (Murphy et al., 1984; Khazanehdari and Sothcott, 2003). Vo-Thanh (1995); Goertz and Knight (1998) found that the shear modulus increased from the saturated value towards the dry value when the saturation decreased below $S < 0.2$ in a drying experiment, at higher saturations the shear modulus varies only slightly. The effect observed was largest when the sandstone was saturated by water. Generally studies show reduction of shear modulus to occur in the first few percent of saturation (Gregory, 1976; Goertz and Knight, 1998). Clark et al. (1980); Pimienta et al. (2014) measured shear modulus as a function of water adsorption and found the modulus to decrease with water adsorption. These observations are explained by a reduction of the solid surface energy relative by wetting of a fluid (Spencer, 1981; Tittmann et al., 1980). The adsorption isotherm is related to the specific surface, whereby the corresponding saturation increases with decreasing permeability and porosity. Compared to the saturation achievable through immiscible displacement, the saturation associated with the adsorption isoterm is low. In the subsurface the wetting phase fluid will always be present ($S_{w,ir}$). This saturation incorporates the surface adsorbed saturation along with any capillary bound saturation. Any fluid substitution in the sub-surface therefore takes place from a wetted frame to a frame wetted by the same fluid if the wettability is unaltered. The large shear modulus reduction can thus be relegated to a set of effective wetted frame moduli. In comparison to laboratory data the effect may be significant. This is often remedied by measuring moduli on samples that have been allowed to absorb water.

Uniform induced pressure

Local-flow dispersion

The assumption of a single induced pressure relates directly to the coupling between the solid frame and the pore-fill. Most research have therefore been dedicated to this aspect (Paula and Pervukhina, 2012; Ravalec and Gueguen, 1996; Mavko and Jizba, 1991; Chapman et al., 2002; Sayers and Han, 2002; Adelinet et al., 2011; Gurevich et al., 2010). Induced pressure gradients may arise from a non-uniform compression, or a non-uniform saturation, and combinations of the two. Gradients of the induced pressure arising from differences in frame compliance leads to dispersion relative to the predictions by fluid substitution. Such dispersion is referred to as local-flow dispersion or squirt flow dispersion. The concept is illustrated in Figure 5.10, a large pressure is induced a compliant part of the porosity. If the fluid relaxation time of this excitation is large compared to the frequency of the deformation the saturated frame is going to act different than predicted by fluid substitution, because the effective frame modulus of the compliant porosity is much lower than the sample average, therefore the compliant porosity is affected to a much higher degree by the fluid. Compliant porosity is ascribed to weaknesses in the grain frame, in the form of micro-cracks (Walsh, 1965; O'Connell and Budiansky, 1974) or other defects associated with grain contacts in the frame (Winkler et al., 1986; Sayers and Kachanov, 1991). Comparison of the stress dependency of sandstone porosity and sandstone elastic moduli, suggests that compliant porosity makes up only a small fraction of the total porosity (Khaksar et al., 1999; MacBeth, 2004). Compliant porosity is modeled as inclusions in a uniform medium characterized by an aspect ratio, $\xi = \frac{a}{b}$, where a is the aperture of the pore and b the length, as illustrated in Figure 5.10. Inversion of the stress dependency of elastic moduli shows the aspect ratio to be very small, on the order of $\xi = 10^{-4}$ to $\xi = 10^{-3}$ (Cheng and Toksöz, 1979; Tao et al., 2006). The length of the pore is therefore $10^3 - 10^4$ longer than the aperture, whereby the time needed for fluid to evacuate such a crack is significant. Pore length is constrained by the size scale as the compliant porosity is linked to contacts between grains. Mavko and

Jizba (1991) derived a phenomenological expression relating the pressure dependency of the elastic moduli to a compliant pore population causing induced pressure gradients. Shear deformation is polarized while compaction is not, leading to a difference in the effect of elongated compliant porosity on shear and bulk modulus. Through solid angle averaging assuming a random orientation of compliant porosity Mavko and Jizba (1991) predicted that the ratio of the change in bulk compliance $1/K_{frame} - 1/K_{HF}$, where K_{HF} denotes the unrelaxed frame bulk modulus, and the difference in shear compliance $1/G_{frame} - 1/G_{HF}$, where G_{Hf} applies to the unrelaxed frame, is directly correlated,

$$\frac{1}{K_{frame}} - \frac{1}{K_{HF}} = \frac{4}{15}\frac{1}{G_{frame}} - \frac{1}{G_{HF}} \tag{4.8}$$

Gurevich et al. (2009) achieved the same correlation with a different formulation and Berryman et al. (2002) found the 4/15 to be an upper limit for the correlation.
The transition frequency between unrelaxed and relaxed compliant porosity can be expressed in terms of the aspect ratio and the bulk modulus of the background material material, K_{ma}, (Jones, 1986)

$$f_{lf} \approx \frac{K_{ma}}{\eta}\xi^3 \tag{4.9}$$

The unrelaxed frame moduli are determined by the properties of the compliant porosity and the fluid in the compliant porosity. Figure 4.2 illustrates that the unrelaxed frame moduli is unchanged by an invading non-wetting phase, as the saturation of the compliant porosity remains the same. Since the compliant porosity have low mobility, so it must be assumed that this porosity is saturated by the wetting phase. The influence of squirt flow on the fluid substitution from fully saturated to mixed saturated depends on whether the saturation of the compliant porosity changes. Figure 4.3 depicts estimated capillary entry pressure of the compliant porosity based on Equation (4.9) using the Washburn (1921) equation to evaluate the entry pressure. The aperture of the compliant porosity decreases with decreasing frequency as the time for equilibration increases, $T = 1/f$. Even at high frequencies the entry pressure necessary to affect the compliant porosity is high. In the sonic range the capillary entry pressure is very high compared to pressure gradient driving invasion after the mud-cake as treated in Section 2.2. Squirt flow is therefore not likely to be affected by mud-filtrate invasion and may therefore be included in an effective frame modulus.

The first few percent of water saturation fills the framework weaknesses. The effect of both local flow and any softening of the frame is then fully developed (at least) at the irreducible water saturation. Fluid substitution from one saturated state to another is therefore not directly influenced by these effect as they are implicitly incorporated in the saturated frame. Rasolofosaon et al. (2009) found a linear relation between fluid bulk moduli and the elastic moduli of a large dataset. Fluid substitution in these sandstones was achieved by extrapolation to $K_f = 0$ and using the elastic moduli from this extrapolation as the framework moduli. This is equivalent to the arguments presented here, as the effects of the mechanisms discussed are incorporated in an effective framework.

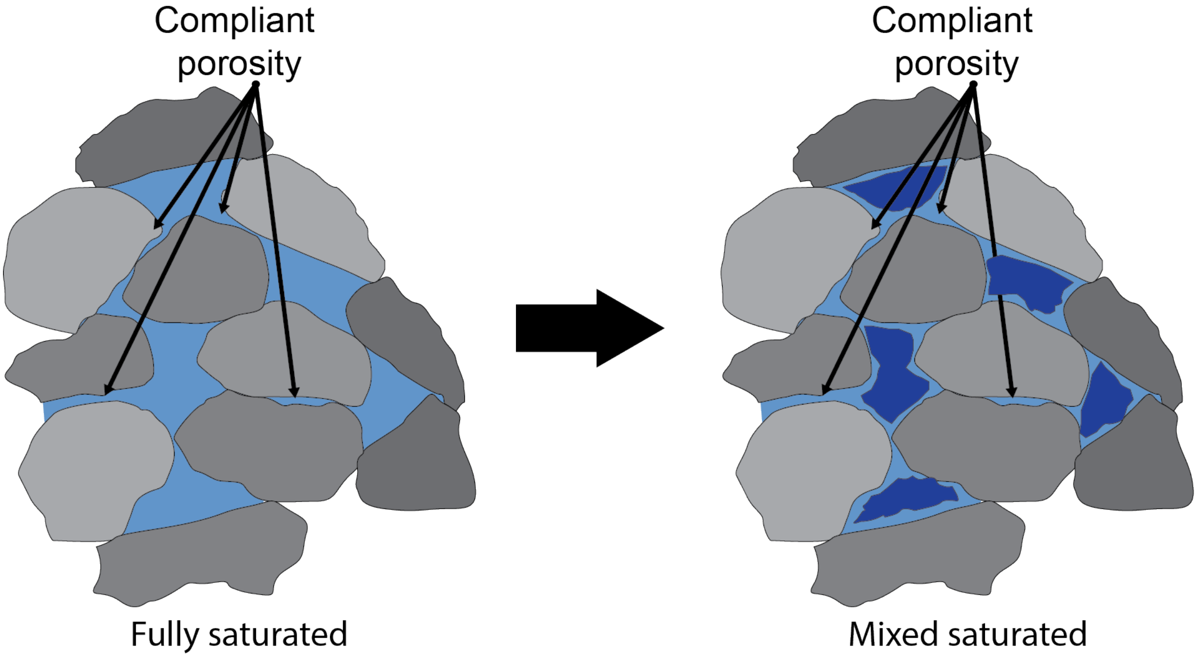

Figure 4.2: The compliant porosity has high capillary entry pressures and therefore remain saturated by the wetting phase.

4.4 Partial and mixed saturation

Saturation of more than one fluid departs from the assumption of a uniform fluid. Equilibration can occur between the fluid if sufficient time is allowed. Mavko and Mukerji (1998) formulates upper and lower bounds for the elastic moduli of porous media saturated with more than one fluid. The bounds are formulated by the distribution of the fluids in the pore-space. Patchy saturation, where continuous patches of one fluid is large enough to prevent equilibration of pressure between the fluids compose the upper bound. Assuming that the shear modulus of the frame does not depend on saturation the modulus in of the patchy saturation can be calculated by the expression formulated by Hill (1963),

$$\frac{1}{M_{patchy}} = \left\langle \frac{S_i}{M_i} \right\rangle . \tag{4.10}$$

Where S_i refer to the saturation of fluid i and M_i is the compressional modulus of the frame saturated by fluid i. The lower bound is realized when the fluids are dispersed finely enough for pressure to be equilibrated. Characteristic length scale for patches to be unequilibrated can be estimated by the pressure diffusion length, (Johnson, 2001)

$$L_c \approx \sqrt{\frac{kK_f}{\eta f}}. \tag{4.11}$$

Where η denotes the dynamic viscosity of the most viscous phase, and k the permeability.

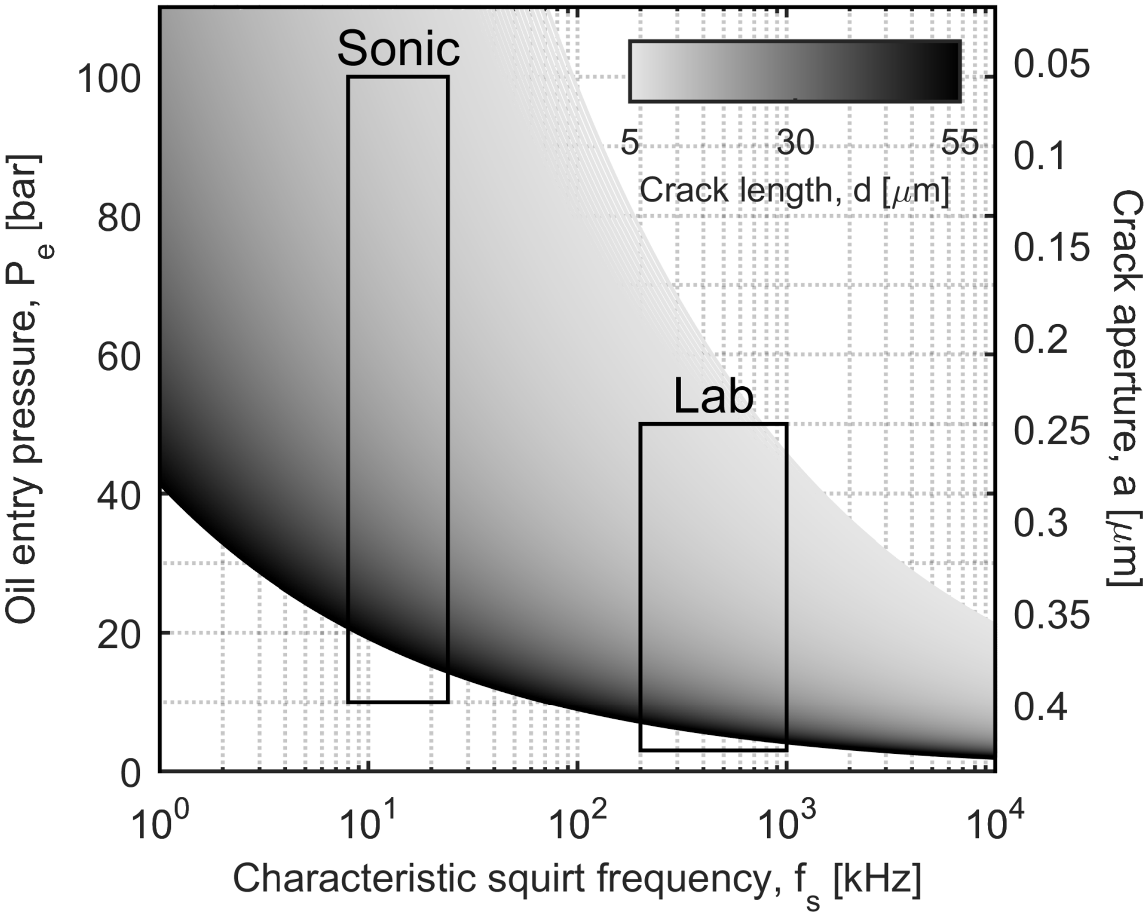

Figure 4.3: Capillary entry pressure of crack like compliant porosity as a function of transition frequency. Porosity is assumed to be saturated by water and invaded by oil.

Murphy (1984) measured velocities of a high porosity, high permeability Massilon sandstone at low frequency (560 Hz) and found them to be consistent with the lower bound. Measuring on limestones, Cadoret (1993) found partial saturations prepared by drainage (drying at constant humidity) to comply with the upper bound and partial saturations prepared by imbibition to conform to the lower bound. Gregory (1976) found the development with saturation to be grouped by porosity at ultrasonic frequency, in partial saturation prepared by drying. Sandstone with medium porosity ($0.1 < \phi < 0.25$) exhibited ultrasonic moduli consistent with the lower bound, high porosity sandstone ($\phi > 0.25$) showed ultrsonic moduli similar to the lower bound, but with a significant weakening introduced at very low saturation. Low porosity sandstones ($\phi < 0.1$) had a transitional behavior with a decrease in velocity at high saturation, a plateau at intermediate saturation, and a decrease again at low saturation. King et al. (2000) measured ultrasonic velocities in partially saturated sandstones with porosity in the narrow range

$0.23 < \phi < 0.28$. The data by King et al. (2000) was qualitatively similar to tho those of by Gregory (1976), but the separation was more closely linked to permeability than porosity. King et al. (2000) found the compressional velocity of highly permeable sandstones to decrease to an almost constant level at a saturation above $S_w = 0.6$, while less permeable sandstones decreased to an intermediate plateau before decreasing further at a saturation below $S_w = 0.4$ to ultimately coincide with the measurements done in the dry state. Shear velocities for the same sandstones was consistent with the predictions of a constant shear modulus from Equation 4.5b except for a increase in velocity at saturation below $S_w = 0.2$.
Lebedev et al. (2009) used CT imaging simultaneously with ultrasonic measurements while flushing a unsaturated sandstone ($\phi = 0.167$, $k = 7.26$ mD) with water. Two flush rates were tried 10 mL/h and a quasi-static flow. For both flow rates the compressional velocity complied with the lower bound at low saturation, before transitioning to the upper bound over a saturation range of 0.1 for the fast flow rate and 0.2 for the low flow rate. The transition to the upper bound also occur at a higher saturation for the low flow rate relative to the high flow rate. The transition saturations where $S_w \approx 0.4$ for the high flow rate and $S_w \approx 0.55$ for the low flow rate. CT imaging showed clustering of fluid patches at the saturation where the transition started from the lower to the upper bound.

4.5 Local sensitivity analysis of fluid substitution

Determination the appropriate extension to Gassmann fluid substitution is aided by observing the sensitivity of Equation 4.5a to the input parameters. The local sensitivity of the fluid substitution equations to the mineral bulk modulus, the fluid bulk modulus, and the porosity is evaluated. Local sensitivity analysis involve evaluation of the partial derivatives of Equation 4.5a with respect to the different parameters. Sensitivity of fluid substitution to mineral bulk modulus, fluid modulus, and porosity is depicted in Figure 4.4(a), 4.4(b), and 4.4(c) respectively.

Increasing the mineral bulk modulus increases the effect of a fluid on the bulk moduli, as seen from Figure 4.4(a). The mineral bulk modulus is most influential at low porosity, as more of the compression adhere from the mineral frame. The bulk modulus of a sandstone is due to compression of the mineral and the frame structure. Keeping the frame bulk modulus constant and increasing the mineral modulus, decreases the mineral compression increasing the compression from the frame structure, whereby the fluid effect increases. Practical extensions of fluid substitution often involves an effective mineral moduli. Figure 4.4(a) illustrates that to explain an under estimated saturated bulk modulus the mineral modulus must be increased. This has the implication that en underestimated saturated bulk modulus cannot be explained by a reduction in the mineral bulk modulus by clay in the framework.

Increasing the fluid modulus inadvertently increases the fluid effect as seen in Figure 4.4(b). The relative effect of increasing the fluid modulus increase as the frame

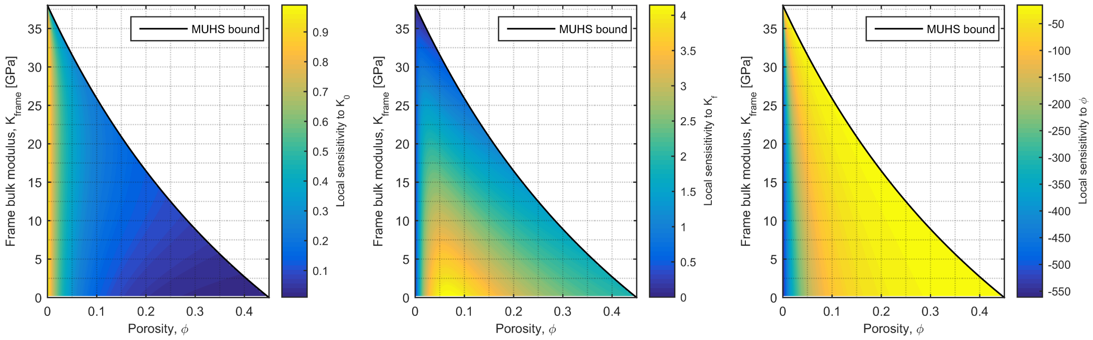

(a) $\frac{\partial}{\partial K_0}\left(K_{sat} - K_{frame}\right)$ **(b)** $\frac{\partial}{\partial K_f}\left(K_{sat} - K_{frame}\right)$ **(c)** $\frac{\partial}{\partial \phi}\left(K_{sat} - K_{frame}\right)$

Figure 4.4: Local sensitivity analysis of Equation 7.6a.

modulus depart from the MUHS as the frame structure experience more compression. Figure 4.4(b) illustrates the rather obvious fact that increasing the fluid modulus increases the induced pressure and the contribution of the fluid to the sandstone bulk modulus.

Increasing the porosity decreases the relative compression of the pore-space as the frame compression is unchanged and the pore-volume is larger. Therefore the sensitivity to porosity is negative in Figure 4.4(c). Extensions of fluid substitution with an decrease in porosity increases the predicted effect of the fluid on the bulk modulus. This is applicable to fluid substitution of the effective porosity. Such a fluid substitution involves a smaller porosity and therefore increase the predicted effect of fluid on the saturated bulk modulus.

This analysis serves to estimate the effect that may be expected by altering fluid substitution by effective parameters in the following chapters.

4.6 The iso-frame model

The iso-frame model, formulated by Fabricius et al. (2010, 2007) will be used to relate a elastic modulus to the porosity in Chapter 6 and Chapter 10. The iso-frame model allows for a fraction of the solid cross-section to not participate in the load-bearing frame. The basic assumptions of the model is illustrated in Figure 4.5. The iso-frame moel rests on the assumption that the moduli of a granular frame comply with the upper Hashin-Shtrikman (HS) bound. Moduli below this bound, as depicted in Figure 4.5, have only a part of the solid cross-section $(1 - \phi)$ participating in the load-bearing framework. The solid cross-section, $1 - \phi$, is adjusted by a factor, x_{IF}, and so that for the adjusted solid cross-section $(1 - \phi)\, x_{IF}$ the moduli does comply with the upper HS bound. The remainder of the solid cross-section $(1 - \phi)(1 - x_{IF})$ are in an effective suspension. The HS is corrected to rely on the suspension modulus of the fluid and the non load-bearing

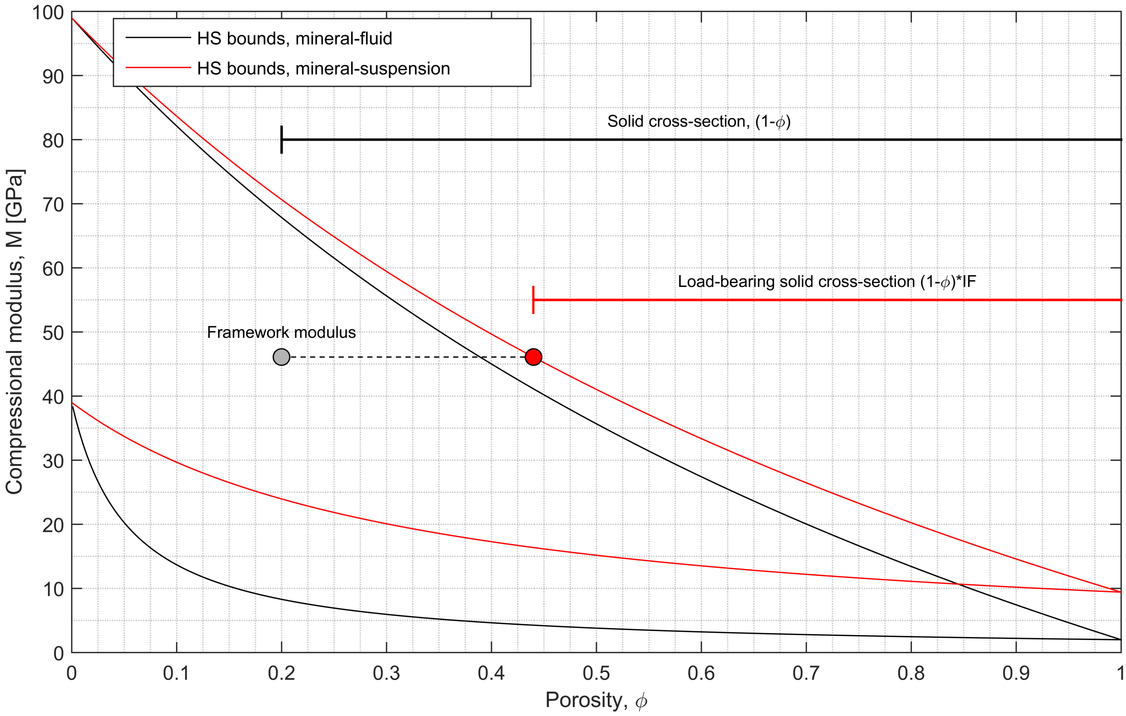

Figure 4.5: The iso-frame model assumes that the load-bearing frame complies with the upper HS bound. Only a fraction of the solid cross-section, X_{IF}, participates in the load-bearing frame the rest of the solid cross-section $(1 - x_{IF})(1 - \phi)$ is effectively in suspension.

solid and not the fluid modulus. This model is consistent with the HS bounds and the (ϕ, x_{if}) space is equivalent to the area spanned by the HS bounds, which is used in Chapter 6. The model also allows for the determination of the moduli on the basis of the cross-section of solid participating in the load-bearing frame as exploited in Chapter 10.

Chapter 5

How sandstone-shale mixtures are reflected in dispersion of elastic moduli

Models proposed to account for dispersion relative to fluid substitution performs well in clean quartz sandstone(Paula and Pervukhina, 2012), but less so in complex pore textures with pore-filling clay. Han (1986) found that moduli residuals in sandstone increase with increasing shale content. Attempts to model these observations have not been entirely satisfactory (Marketos and Best, 2010; Paula and Pervukhina, 2012). Furthermore, the data of Han (1986) and others (Mann and Fatt, 1960; Best, 1992; Gist, 1994; Shatilo et al., 1998; Diallo et al., 2003) show a larger scatter in velocity residuals at higher shale fractions that are both negative (softening) and positive (stiffening). Han et al. (2011) found a transition in the relation between pore-space texture quantified by resistivity and elastic moduli at intermediate shale fractions. When combined with the observation that elastic moduli residuals increase both with shale fraction in sandstones and with sand fraction in shales, this suggests that there is a transition at an intermediate shale fraction.

A barrier to the identification of the mechanisms responsible for moduli residuals in shaly sandstones is the difficulty in quantifying the texture of the granular frame in terms of suitable model parameters. The effect of shale on the granular frame depends strongly on the distribution of shale (Minear, 1982; Anstey, 1991; Sams and Andrea, 2001). Measurable characteristics used for identifying texture in clean sandstones become ambiguous in shaly sandstones. Porosity is commonly used as an indicator of the texture of the granular frame in clean sandstones (e.g., high porosity is indicative of low inter-granular cement and loose grain packing), but in shaly sandstones, pore-filling shale affects the measured porosity, thus giving different porosity for similar frames (Gal et al., 1999).

We wish to evaluate how far into the continuum from clean quartz arenites to shale the models applied to quartz arenites can be extended. To do this we must firstly define quantitative measures of sandstone texture. We do this by defining a classification based on the volumetric shale fraction, measured total rock porosity, and elastic moduli of the dry frame. The classification relies on two assumptions; elastic moduli of a clean quartz arenite frame are related to porosity by the modified upper Hashin-Shtrikman (MUHS) bound, and shale in sandstones is predominantly authigenic and pore-filling. Based on these two assumptions, we first interpret divergence of the dry elastic moduli from the MUHS bound as the result of the measured porosity being different from the frame porosity due to the presence of pore-filling shale. We then adjust the dry elastic moduli to the MUHS bound and hence quantify the amount of solid shale in the pore space. If the divergence from the MUHS bound is too large relative to the measured volumetric shale fraction (obtained from image analysis), the assumption of pore-filling shale is rejected and the lithology is classified as having load-bearing shale. As a second approach, we make the assumption that the entire measured porosity is in the shale fraction, and from this calculate the porosity of the shale fraction. We then compare this value to the value obtained by adjusting the dry moduli to the MUHS bound. If the two shale porosities are similar we interpret it as though the pore-space is dominated by shale, called the critical shale fraction by Marion et al. (1992). Based on these considerations, we quantify four groups: clean sandstones having less than 2 % shale by volume; sandstones with partial pore-filling shale; sandstones at the critical shale fraction; and sandstones with load-bearing shale.

We then evaluate the fluid saturated moduli relative to the quasi-static Gassmann prediction for each group. Comparison to the Gassmann predicted moduli isolates mechanisms acting on top of the induced pressures. Observing the behavior of the moduli residuals in each group allows the evaluation of the dispersion mechanisms for similar texture rocks.

In this section the data set is presented and then the classification procedure starting with fitting of the dry compressional modulus to the clean sandstone reference composed by the MUHS bound. The obtained porosity is compared to measured porosity to define the four groups. As the grouping relies solely on volumetrically averaged quantitities, an investigation into the permeability of the groups is added to evaluate mesoscopic homogeneity. The adaptation of fluid substitution to account for the clay fraction is presented, before the discussion of the accuracy of fluid substitution in the four groups.

5.1 The data-set

The data used in the analysis is a combination of data sets collected from the literature (King, 1966; Han, 1986; Best, 1992; Khazanehdari and McCann, 2005). The data set covers a wide range of lithologies from clean quartz arenites to greywackes, and sandy shales. A data point is comprised of dry compressional velocity, V_p^{dry}, dry shear velocity, V_s^{dry} , saturated compressional velocity, V_p^{sat}, saturated shear velocity, V_s^{sat} , porosity, ϕ, grain density, ρ_0, and volumetric shale fraction, χ. All data sets, except the one by Han (1986), also include permeability. In Figure 5.1 crossplots of the parameters along with Pearson's correlation coefficient are shown. The correlation between the dry velocities is very strong and the correlations between velocities, porosity, and clay fraction are also significant as noted by the authors King (1966); Han (1986); Best (1992); Khazanehdari and McCann (2005). The scatter plots between the velocities and the clay fraction show that the correlation is strongest at low shale fractions. Figure 5.1 shows that the combined dataset conforms to the findings for sandstone in the literature without any apparent bias.

In Table 5.1 the fluids used for saturation in the different data sets are listed. The majority of the data are recorded with either distilled water or brine. Some samples are saturated with non-polar hydrocarbons (hexane, kerosene, dead oil) and some with highly viscous polar mixtures of water and glycerol. All velocities are measured at ultrasonic frequencies. The data of Han (1986) and King (1966) are measured using the pulse-transmission method (Birch, 1960) at 1 MHz and 0.5 MHz for compressional waves respectively and 0.6 MHz and 0.5 MHz for shear waves. The data of Best (1992) and Khazanehdari and McCann (2005) are measured using the pulse-echo method (Winkler and Plona, 1982) at 0.6 MHz to 0.9 MHz for compressional waves and shear waves.

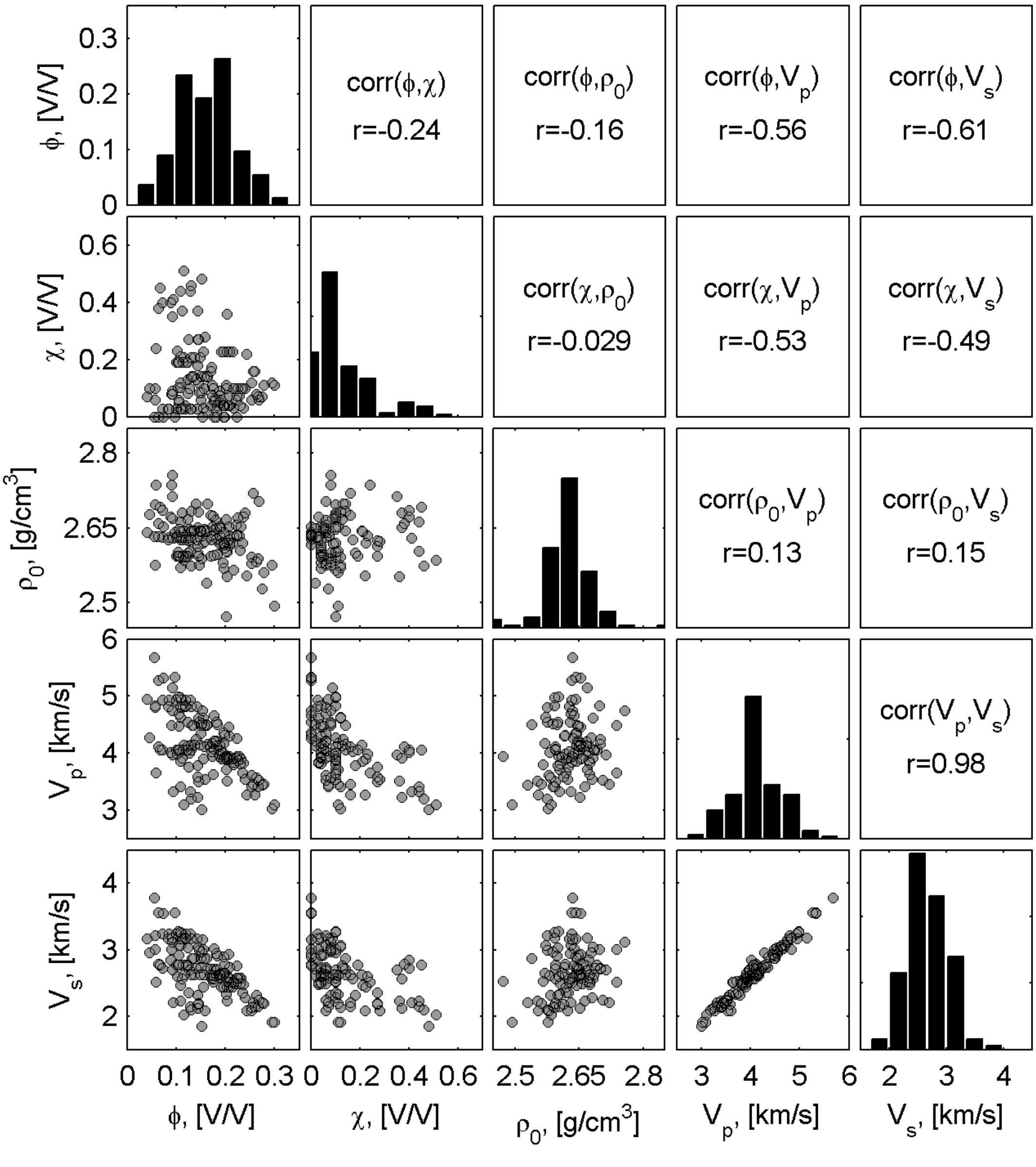

Figure 5.1: Correlation matrix showing the relation between V_s^{dry}, V_p^{dry}, ρ_0, χ, and ϕ. The lower half shows the scatter plot while the upper gives the correlation strength by Pearson's correlation coefficient. The diagonal gives the distribution of the parameter. A strong correlation is seen between V_p^{dry} and V_s^{dry}, velocities are also seen to decrease with porosity and clay fraction.

Table 5.1: The fluid used in the data sets with their respective viscosity, η, and bulk modulus, K_f. The high viscosity fluids used in the data set of Best (1992) should be noted.

Fluid	Viscosity η, $[cP]$	Bulk modulus K_f, [GPa]	Data set
Brine 2M NaCl	1.12	2.8	[1]
Kerosene	2.25	1.6	[1,2]
Distilled water	1	2	[3,4]
Hexane	0.33	1.6	[3]
Water/glycol mixture 1	20	3.7	[3]
Water/glycol mixture 2	70	4	[3]
Water/glycol mixture 3	450	4.3	[3]
Water/glycol mixture 4	950	4.4	[3]
Synthetic brine 1	1.03	2.56	[2]
Synthetic brine 2	1.14	3.15	[2]
Dead oil	7.5	1.6	[2]

Data set 1: (King, 1966)
Data set 2: (Khazanehdari and McCann, 2005)
Data set 3: (Best, 1992)
Data set 4: (Han, 1986)

5.2 Quantifying pore-filling clay and group delineation

Figure 5.2a shows dry compressional moduli cross-plotted with porosity and shaded by volumetric shale fraction. The solid line is the MUHS bound with a critical porosity of 0.45 and a compressional mineral modulus of $M_0 = 99$ GPa corresponding to pure quartz (Koga et al., 1958). The MUHS compose the reference clean sandstone diagenetic trend for compressional modulus of grain supported sandstones (i.e., porosity reduces from the critical porosity as diagenetic quartz cement fills the pores) as presented in Section 3.2. Authigenic clay is deposited in the pores increasing the modulus of the pore-fill, but not affecting the frame modulus (Marion, 1990; Anstey, 1991). A comparison between frame moduli and cementation trends involves a correction of the porosity (total porosity) to the frame porosity (Gal et al., 1999),

$$\phi_{frame} = \phi + \chi \left(1 - \phi_{sh}\right) \tag{5.1}$$

where, χ, denotes the volumetric shale fraction, ϕ_{sh}, the shale porosity, and, ϕ_{frame} the frame porosity. Gal et al. (1999) demonstrated the value of this approach assuming constant shale porosity for each data set observed. Given the deposition and diagenesis of authigenic shale in sandstones, there is, however, no a priori basis for assuming constant shale porosity. We treat the shale porosity as a free parameter and adjust it in order to

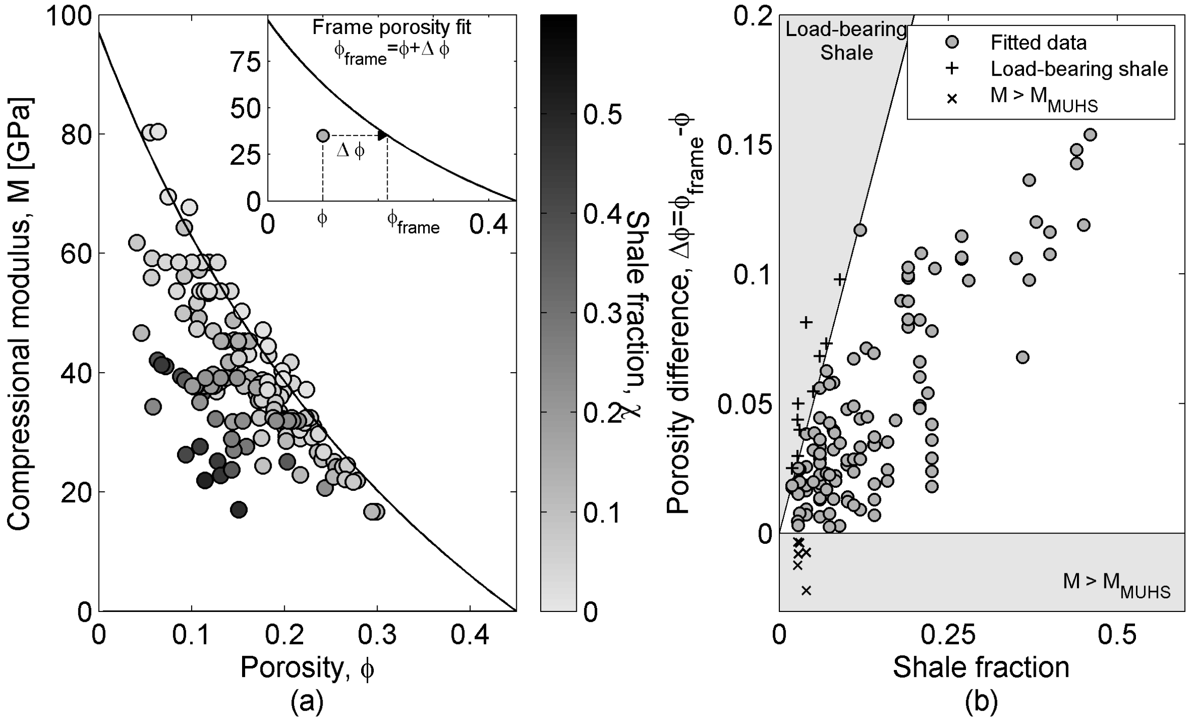

Figure 5.2: Dry compressional elastic modulus versus porosity (a) shaded to volumetric shale fraction. The solid line shows the modified-Upper-Hashin-Shtrikman bound (MUHS) as a trend between clean quartz frame and porosity. The inset in (a) shows the correction of the porosity when shale fills the pores. Some samples cannot be fitted by to the MUHS trend due to load-bearing shale or a too high compressional modulus (b).

make the dry compressional moduli coincide with the MUHS trend. The results for the frame porosity fit versus shale fraction are seen in Figure 5.2b. Figure 5.2a shows that few samples fall above the MUHS trend and cannot be fitted by correcting the frame porosity. Compressional modulus above the MUHS trend may be caused the presence of feldspar or calcite with larger modulus than quartz. The difference between the MUHS trend and the high-modulus samples is small and all have very low shale content, so they all fall in the clean sandstone group. Figure 5.2b also shows that some samples have compressional moduli too low to be fitted to the MUHS trend. These samples are interpreted as having load-bearing shale. Because load-bearing shales influence the compressional modulus, no information can be extracted regarding the shale porosity and samples are delegated to the group with load-bearing shale without further analysis. Figure 5.3 shows the distribution of the fitted shale porosities. The distribution is negatively skewed with a mean of 0.59. The total span of the distribution, from about 0.2 to 0.9, is consistent with observations of shale porosity by Hurst and Nadeau (1995). The distribution of shale porosities has a maximum at about 0.7 agreeing with values of micro-porosities extracted for sandstones with pore-filling clays by thin section image

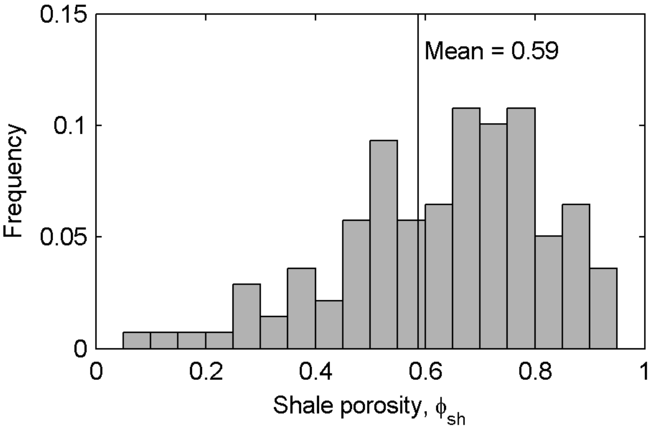

Figure 5.3: Histogram of the shale porosities achieved from fitting the dry compressional moduli to the MUHS trend. The mean of 0.59 corresponds well with observations on sandstone thin sections by Vernik (1994).

Table 5.2: The quantified delineation of the classification. A limit of 0.1 is set on the difference between the fitted shale porosity and the shale porosity observed assuming the pore-space to be completely dominated by shale.

Clay distribution	Group 1 Clean	Group 2 Heterogeneous	Group 3 Homogeneous	Group 4 Load-bearing
Lower limit	-	$\chi > 0.02$	$\frac{\phi}{\chi} > \phi_c^M - 0.1$	$\frac{\phi}{\chi} > \phi_c^M + 0.1$
Upper limit	$\chi < 0.02$	$\frac{\phi}{\chi} < \phi_c^M - 0.1$	$\frac{\phi}{\chi} < \phi_c^M + 0.1$	-

analysis (Vernik, 1994).

In order to evaluate whether the obtained shale porosities are realistic, we compare them to the measured porosity normalized to the volumetric shale fraction. To do this we observe the porosity of the pore-filling material, ϕ_{pf} (Marion et al., 1992):

$$\phi_{pf} = \frac{\phi_{frame} - \chi(1 - \phi_{sh})}{\phi_{frame}} \tag{5.2}$$

We have no direct measure of ϕ_{frame}, but we can observe three distinct cases:

- Partial pore-fill, sand frame: $\chi < \phi_{frame}$ and therefore, $\phi_{pf} > \phi_{sh}$
- Critical shale fraction, sand frame: $\chi \approx \phi_{frame}$ whereby, $\phi_{pf} \approx \phi_{sh} = \frac{\phi}{\chi}$
- Load-bearing shale, shale frame: $\chi > \phi_{frame}$ whereby, $\phi_{sh} = \frac{\phi}{\chi}$

If the shale porosity obtained by fitting of the elastic moduli is lower than the pore-filling porosity, then the lithology is interpreted as having a pore-space partially filled with shale. If the porosity achieved by fitting is comparable to the pore-filling porosity, then the pore-space is at the critical shale fraction. Finally, if the porosity achieved by fitting of the elastic moduli is much larger than the value determined by Equation 5.2, then the lithology does not comply with the MUHS trend because of load-bearing shale weakening the frame. A cross-plot of the shale porosity obtained from moduli fitting and Equation 5.2 is shown in Figure 5.4. Based on Figure 5.4 and the shale fraction, we define the four groups with the delineations given in Table 5.2. Group 1 is clean sandstones with a shale fraction less than 2 %; Group 2 has a sand frame and partial pore-filling clay, identified as samples with smaller shale porosity from mineral fitting than obtained from Equation 5.2. Group 3 has a sand frame and a homogeneous shale pore-fill with similar shale porosity from fitting of the moduli and from the porosity. Group 4 has load-bearing shale with dispersed sand grains and significantly lower shale porosity determined from equation 5.2 than from the modulus fitting.

5.3 Permeability, shale morphology, and distribution

We expect velocity dispersion in sandstones to be related to textural features affecting the relaxation of transient elastic waves. The grouping scheme introduced above relies on an evaluation of volumetrically averaged texture. Permeability depends on the spatial distribution of the shale and therefore provides further information about the texture within the groups (Revil and Cathles, 1999). Figure 5.5 shows permeability versus measured porosity for the samples where permeability is available. No permeability data is available for Group 1, so data from Bourbié and Zinszner (1985) for Fontainebleau sandstones are included as reference for clean sandstones.

The relation between shale morphology and permeability is illustrated by the regions in Figure 5.5, suggested by Neasham (1977). At similar shale fraction and porosity, pore-bridging clay mineralogies, such as illite, have a much larger effect on the permeability than pore-lining, and pore-body filling.

Revil and Cathles (1999) modeled the permeability of sand-shale mixtures based on Kozeny's equation (Kozeny, 1927), supplemented by electrical measurements in groups conceptually similar to the ones presented in this study. Flow in the different groups is illustrated in Figure 5.6. If the pore-filling shale fraction is significantly less than critical shale fraction (Group 1 and Group 2) Revil and Cathles (1999) attributes flow to the effective porosity,

$$\phi_{eff} = \phi - \chi\phi_{sh} = \phi_{frame} - \chi \tag{5.3}$$

When the shale fraction exceeds the critical shale fraction, flow occurs through the shale matrix with imbedded sand grains blocking the flow (Group 3 and Group 4). Using Kozeny's equation the apparent specific surface of the samples can be determined and compared to literature values for the constituent minerals. Apparent specific surfaces

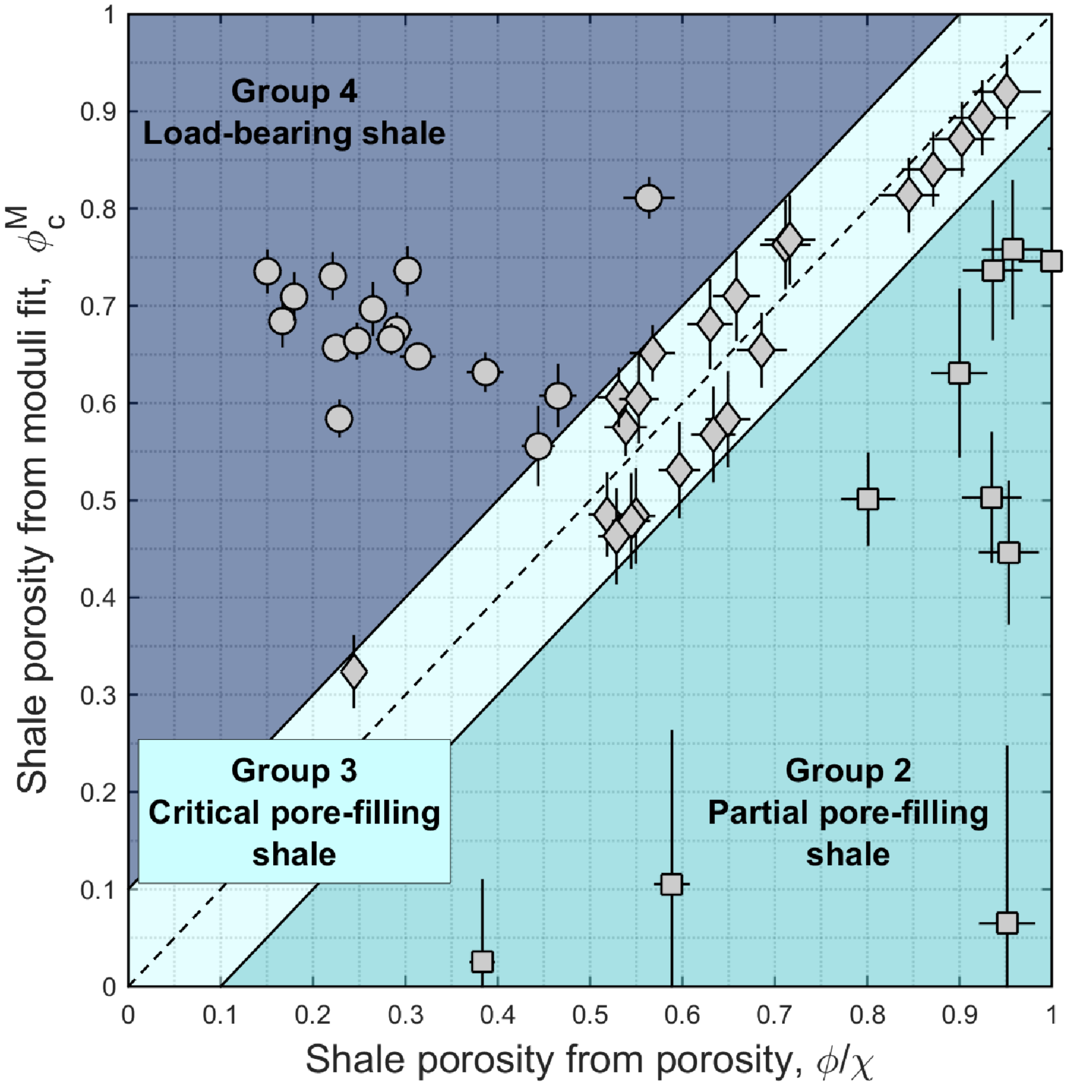

Figure 5.4: Fitted shale porosity compared to measured porosity normalized to the shale fraction. The group delineation is shown in the figure for Group 2 to Group 4. Samples with $\phi/\chi > 1$ are omitted.

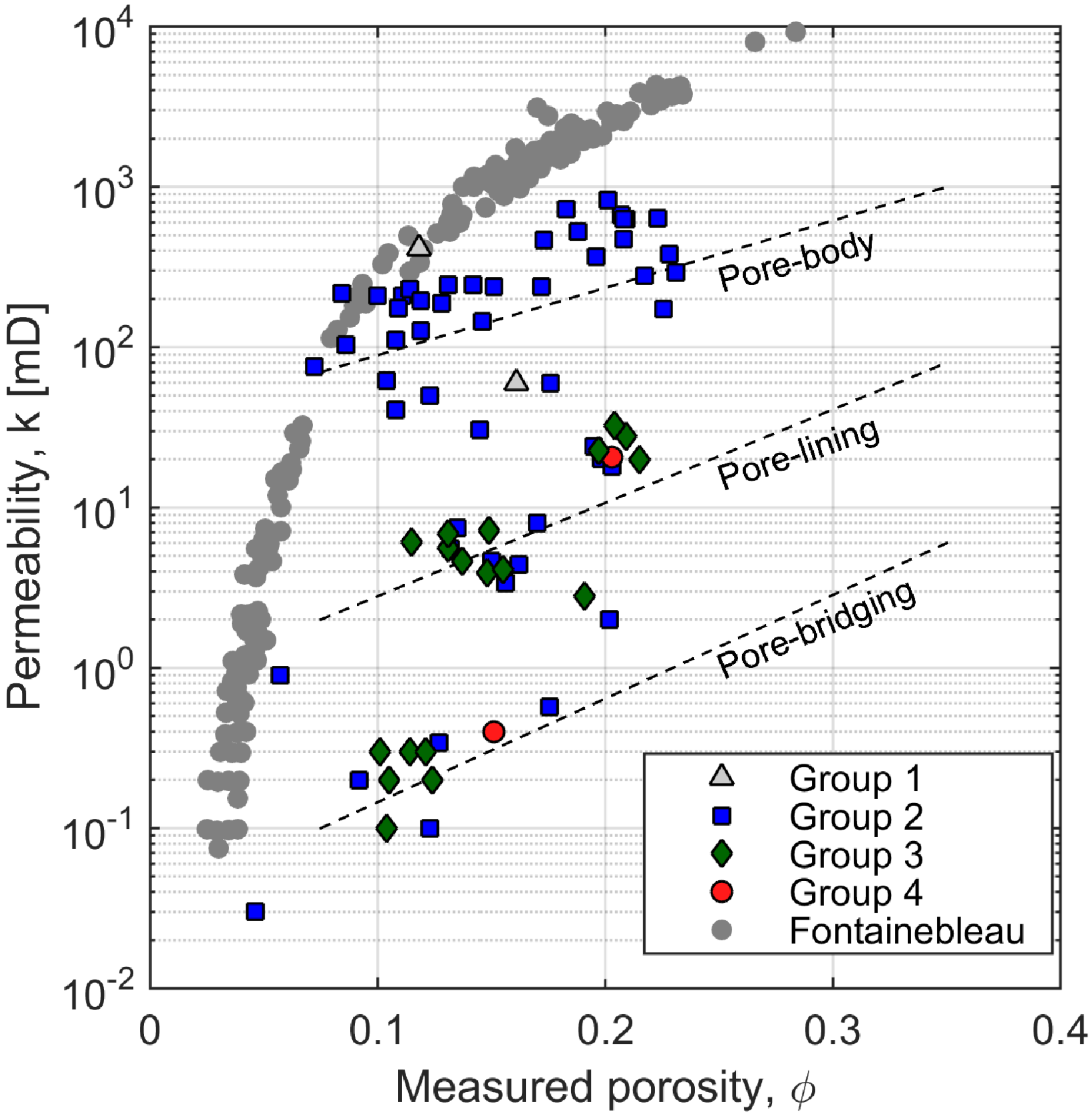

Figure 5.5: Permeability versus measured porosity with morphology zones suggested by Neasham (1977). Group 2 is spread over all zones while group 3 and 4 appear to have pore-lining and pore-bridging shale morphologies.

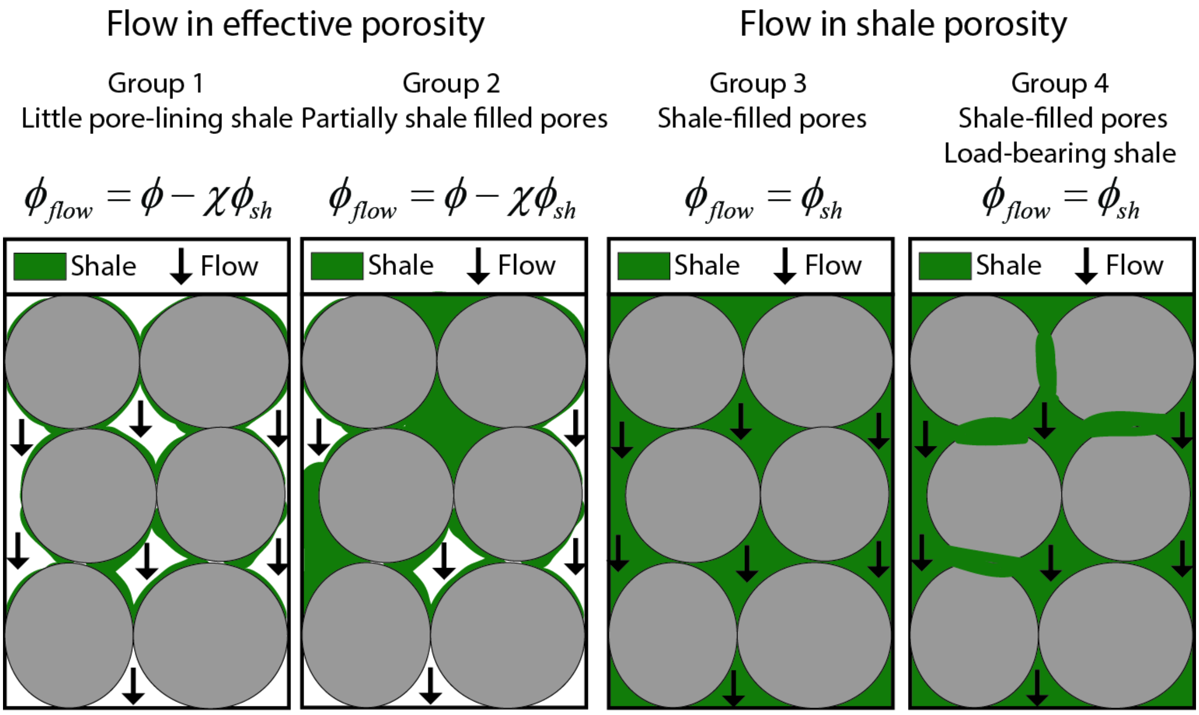
Flow in effective porosity
Flow in shale porosity
Group 1
Little pore-lining shale
Group 2
Partially shale filled pores
Group 3
Shale-filled pores
Group 4
Shale-filled pores
Load-bearing shale
$\phi_{flow} = \phi - \chi\phi_{sh}$
$\phi_{flow} = \phi - \chi\phi_{sh}$
$\phi_{flow} = \phi_{sh}$
$\phi_{flow} = \phi_{sh}$
Shale
Flow

Figure 5.6: Flow characteristics differ between the four groups as different parts of the porosity conduct the flow. Grain dominated groups (Group 1 and Group 2) have flow predominantly in the large inter-granular quartz pores. While the shale dominated groups (Group 3 and Group 4) have flow in the shale micro-porosity.

relative to the pore volume, S_p, are determined from (Kozeny, 1927)

$$k = c(\phi)\frac{\phi}{S_p^2} \tag{5.4}$$

The function $c(\phi)$ accounts for the granular nature of the rock as given by Mortensen et al. (1998). In the grain supported groups, the flow is in the effective porosity and the specific surface relative to effective pore-space is given by,

$$S_p = \sqrt{c(\phi_{eff})\frac{\phi_{eff}}{k}} \tag{5.5}$$

In the shale dominated groups, flow is in the shale porosity and the specific surface per pore volume of the shale is determined by,

$$S_p = \frac{\sqrt{c(\phi)\frac{\phi}{k}}}{\chi} \tag{5.6}$$

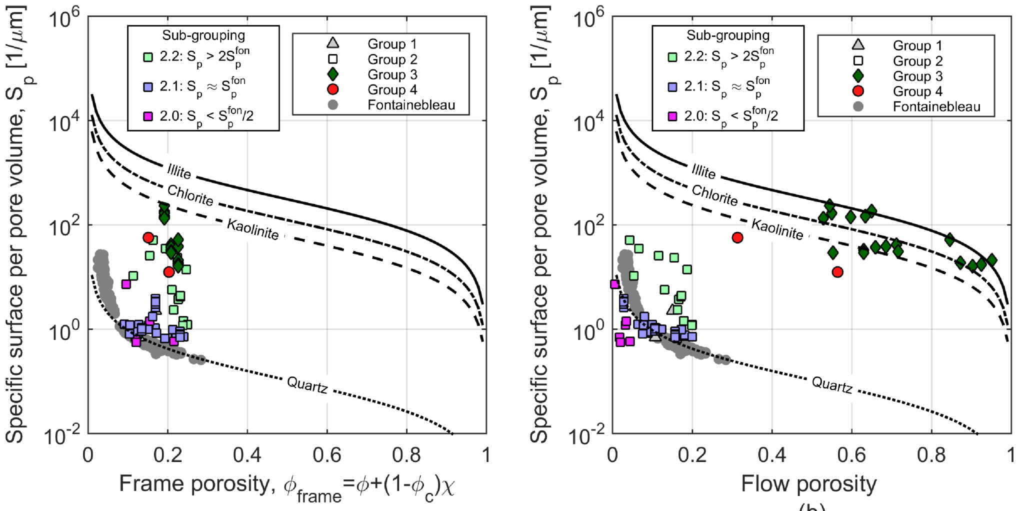

(a) (b)

Figure 5.7: Comparison of specific surface per pore volume to literature values in the groups. The comparison based on the frame porosity (a) shows an increase of the specific surface with shale fraction, but no distinction. Correcting the specific surface to the flow medium (b), as illustrated in Figure 5.6, shows good agreement with literature data for Group 3. Group 2 is divided into 3 subgroups denoted 2.0, 2.1, and 2.2, depending on the lithology's behavior relative to the Fontainebleau trend. Subgroup 2.0 has lower S_p than the Fontainebleau trend, subgroup 2.1 complies with the trend, and 2.2 lies above the trend.

The numerator in Equation 5.6 determines the observed specific surface per pore-volume in the sample. This specific surface is normalized to unity volume by the shale fraction per bulk volume to facilitate comparison with measurements of specific surface in mono-mineralic state. Specific surfaces can be measured by BET (Brunauer-Emmet-Teller) adsorption giving a comparison to the values obtained from Equation (5.5) and Equation (5.6). BET measurements of quartz grains are sensitive to grain size and are often over predicted (Kendall et al., 1975). For quartz minerals we therefore use the apparent specific surfaces calculated by Equation 5.4 for the Fontainebleau sandstone data set of Bourbié and Zinszner (1985), shown in Figure 5.5.

Figure 5.7a shows the specific surface per pore volume by using Equation 5.5 and Equation 5.6 versus frame porosity. Figure 5.7b shows the specific surface per pore volume of the flow medium i.e. the effective porosity for the grain dominated groups and the shale porosity for the shale dominated groups. The shale dominated samples show specific surfaces in good agreement with the values obtained by BET for clay minerals. The few samples from Group 4 with permeability data falls at a lower specific surface. These samples are greensand samples with structural glauconite pellets. Greensand does have load-bearing structural clay, but need not have a completely shale dominated frame. Therefore it tends to have unusual high porosity and permeability for a given shale fraction. The members of Group 2 fall on and around the Kozeny trend derived from the Fontainebleau data. To address this we define three subgroups: Subgroup 2.0 has lower specific surfaces than the Kozeny trend, Subgroup 2.1 complies with the Kozeny trend, and Subgroup 2.2 has higher specific surface than the Kozeny trend. For Subgroup 2.1 the assumption of flow dominated by the effective porosity appears valid. The flow medium mimics clean sandstone with a porosity less than that measured because shale occupies some of the porosity (Figure 5.6). The agreement with the Fontainebleau trend suggests that the lithologies in this Subgroup are homogeneous at the mesoscopic scale. Subgroup 2.0 has lower specific surface than expected from the Fontainebleau trend. This means that the porosity fraction assigned to the shale by the analysis is not omitted from the flow. This could either suggest that the shale porosity was over-predicted, due to some load-bearing shale reducing the dry moduli beyond the porosity effect, or that the shale porosity contributes to the net flow. The former cause would mean that Subgroup 2.0 resembles Group 4 and could be seen as a transition state between Group 2 and Group 4. Subgroup 2.2 has higher specific surface than expected from the Fontainebleau trend. This implies that there is something obstructing the flow which is not found in a frame composed solely of grains. This is interpreted as a heterogeneous distribution of shale in the pore-space; some pores are dominated by shale causing flow blockage and an apparently increased specific surface. Pores dominated by shale are the definition of Group 3 so Subgroup 2.2 is intermediate between Group 2 and Group 3.

5.4 Gassmann fluid substitution

We are only interested in effects occuring on the time-scale of a passing wave whereby we determine the quasi-static baseline moduli by using Gassmann fluid substitution from elastic moduli measured in the dry state. Pore-filling shale will act to stiffen the pore-fluid. This effect has to be accounted for in the application of Gassmann fluid substitution. With the mineral bulk modulus, K_0, frame bulk modulus, K_{fr}, frame shear modulus, G_{fr} ,and the porosity, ϕ, the Gassmann predicted moduli are,

$$K_{gass} = K_{fr} + \frac{\alpha^2}{\frac{\phi}{K_{fl}} + \frac{1-\phi}{K_0} - \frac{K_{fr}}{K_0^2}} \tag{5.7a}$$

$$G_{gass} = G_{dry} \tag{5.7b}$$

Shear moduli are not affected by fluid saturation because shearing does not cause compression of the pore space. The moduli residuals caused by transients for the bulk and shear moduli are,

$$\Delta K = K_{sat} - K_{gass} \tag{5.8a}$$

$$\Delta G = G_{sat} - G_{dry} \tag{5.8b}$$

The shear residual is uniquely defined by the measured modulus in the dry and saturated states whereas the bulk residual requires further input. Load-bearing shale can be incorporated into Equation 5.7a by determining an effective mineral modulus (Knackstedt et al., 2005). Since the mineral bulk moduli of clay and quartz are of the same order of magnitude (Vanorio et al., 2003), a reasonable estimate of the effective mineral modulus may be achieved by the Voigt-Reuss-Hill average (Vanorio et al., 2003). Pore-filling shale stiffens the pore-fluid without affecting the frame mineral modulus. This can be incorporated by replacing the fluid modulus with the modulus of shale suspended in the pore-fluid (Marion et al., 1992),

$$\frac{1}{K_f^{eff}} = \frac{1 - S_{sh}}{K_0^{sh}} + \frac{S_{sh}}{K_f} \tag{5.9}$$

where $S_{sh} = \chi \left(1 - \phi_{sh}\right) / \phi$ is the fraction of the pore-space occupied by solid shale and K_0^{sh} is the mineral bulk modulus of the shale. Group 3 is treated in the same manner as Group 2.

5.5 Distribution of shear residuals

The distributions of the shear modulus residuals for all four groups are given in Figure 5.8. Different distributions are seen in each group:

- **Group 1 - Clean sandstones:** All shear residuals are within ±2 GPa . There are two peaks in the distribution, one at very small negative residuals and another larger one at low positive residuals.
- **Group 2 - Partial pore-filling shale:** This group has a symmetric distribution around 0 with a particular peak at 0. All shear residuals are between ±2 GPa. Color-coding based on the subgroups found in Figure 5.7 shows Subgroup 2.1 (compliant to effective porosity modeling) to have a symmetric spread around 0, while the transition Subgroup 2.2 to Group 3 (too high specific surface) have positive moduli residuals and the transition Subgroup 2.0 to Group 4 (too low specific surface) have negative shear residuals.
- **Group 3 - Homogenous pore-fill:** The shear residuals in Groups 3 strongly favors positive values indicating a larger saturated shear modulus than dry shear modulus (stiffening). The distribution is slightly peaked at 0.5 GPa and decreases towards the maximum at 5 GPa. The lack of symmetry in the distribution discredits uncertainties as the explanation.
- **Group 4 - Load-bearing shale:** The shear residuals in Group 4 strongly favors negative values, meaning that the saturated shear modulus is less than the dry shear modulus (softening). The lack of symmetry in the distribution discredits the notion of random fluctuations being the cause.

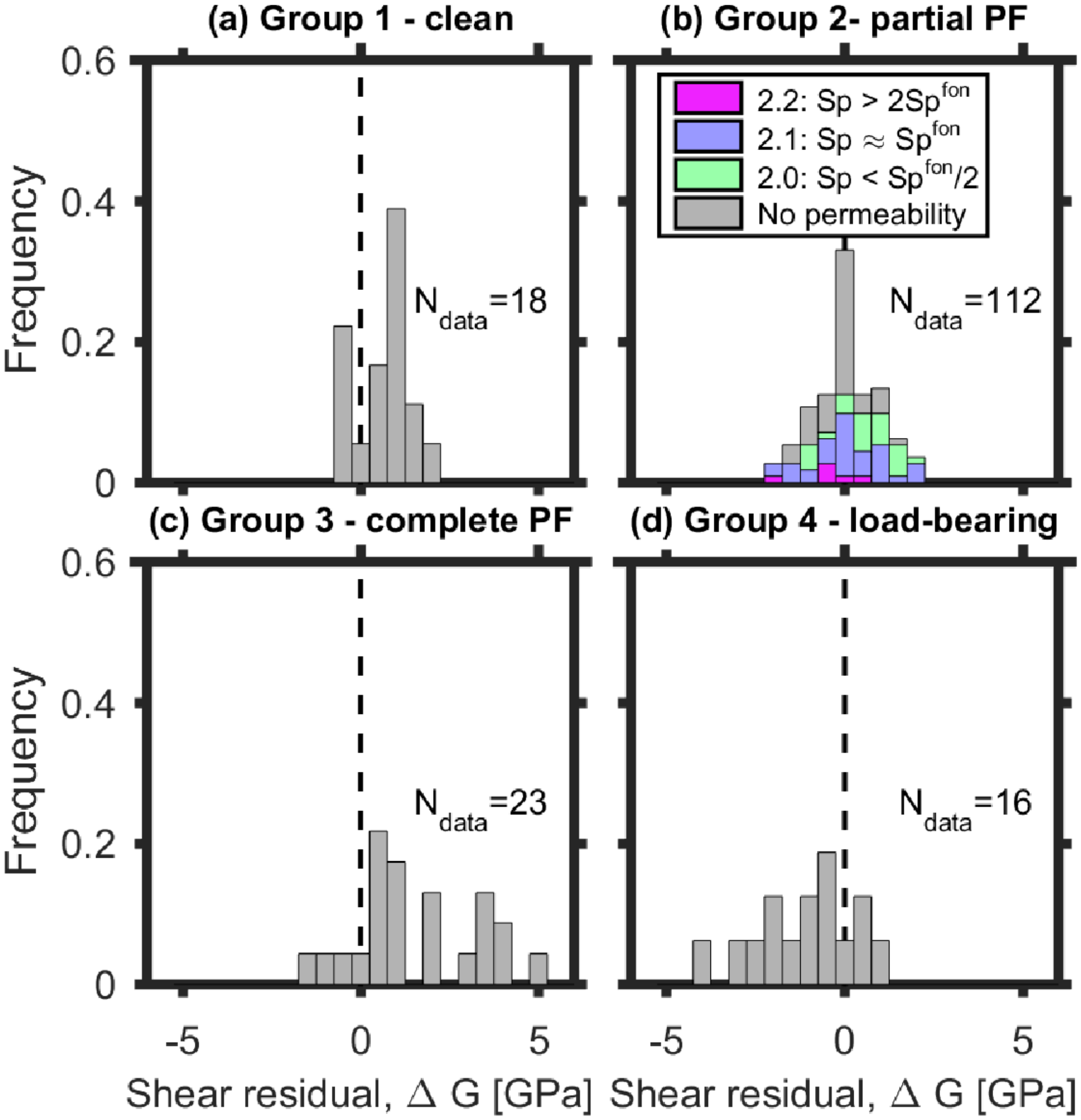

Figure 5.8: Shear modulus residual distributions for the four groups achieved by comparing saturated and dry shear moduli. Distinctly different behaviors are seen in the four groups. Group 2 (b) is color-coded to the subgroups identified by the specific surface per pore-volume in Figure 5.7b.

5.6 Distribution of bulk residuals

We calculate the bulk modulus residuals and the results are shown in Figure Figure 5.9.

- **Group 1 - Clean sandstones:** Most bulk modulus residuals are within ±2 GPa with a few extreme outliers. A prominent peak is seen at about 1.5 GPa and the distribution is slightly negatively skewed with some samples having negative bulk modulus residuals.
- **Group 2 - Partial pore-filling shale:** The bulk modulus residuals for Group 2 have a wide distribution of both positive and negative residuals. The distribution has a peak at slightly positive values and is positively skewed. Subgroup 2.1 is has predominantly positive residuals, but with a significant peak at 0. Subgroup 2.2 (transition to Group 3) has a peak at about 1 GPa, and some members in the negative end of the overall distribution. The transition Subgroup 2.0 to Group 4 has predominantly positive residuals.
- **Group 3 - Homogenous pore-fill:** Group 3 has only positive bulk modulus residuals between 0 GPa and 10 GPa, without any apparent peaks.
- **Group 4 - Load-bearing shale:** This group has consistently large positive bulk modulus residuals distributed around 7 GPa and a single outlier at about 2 GPa.

5.7 Mechanisms: Gassmann limitation or physical reality

Figure 5.8 and Figure 5.9 show the moduli residuals to have markedly different distributions in the four groups. A base-line for the residuals can be determined from the clean sandstones in Group 1 which has moduli residuals below 2 GPa. We argue that this dispersion is likely to be caused by transient pressure gradients from compliant porosity. We then compare the distribution from Group 1 to the more shaly groups to evaluate the likelihood of the same mechanisms being dominant in these rocks. For each group, we must also evaluate how uncertainty in the input parameters for the fluid substitution affects the results.

Group 1

Both shear and bulk residuals are predominantly positive in Group 1 and the spread of the distributions is the smallest of the four groups. Only small negative dispersion is seen relative to the positive dispersion and this is within the expected uncertainty. The input parameters of the fluid substitution in this group are unambiguous. Some samples contain feldspar and calcite, whereby the appropriate mineral modulus could be higher. Fluid substituting with a mineral modulus that is too low would relegate more

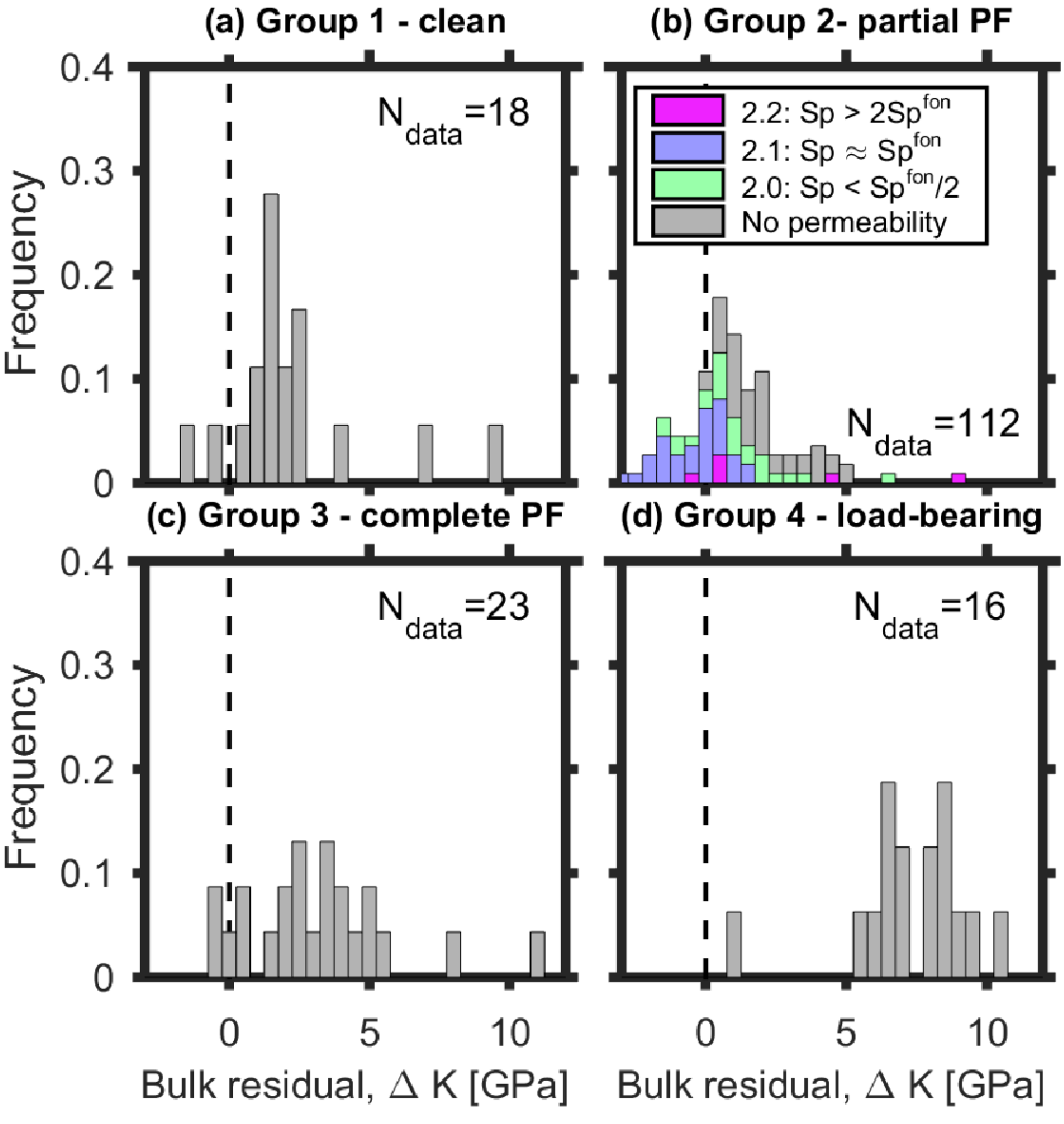

Figure 5.9: Bulk residual distributions for the four groups achieved by comparing the saturated and the Gassmann fluid substituted bulk moduli. Group 2 (b) is color-coded to the subgroups identified by the specific surface per pore-volume in Figure 5.7b.

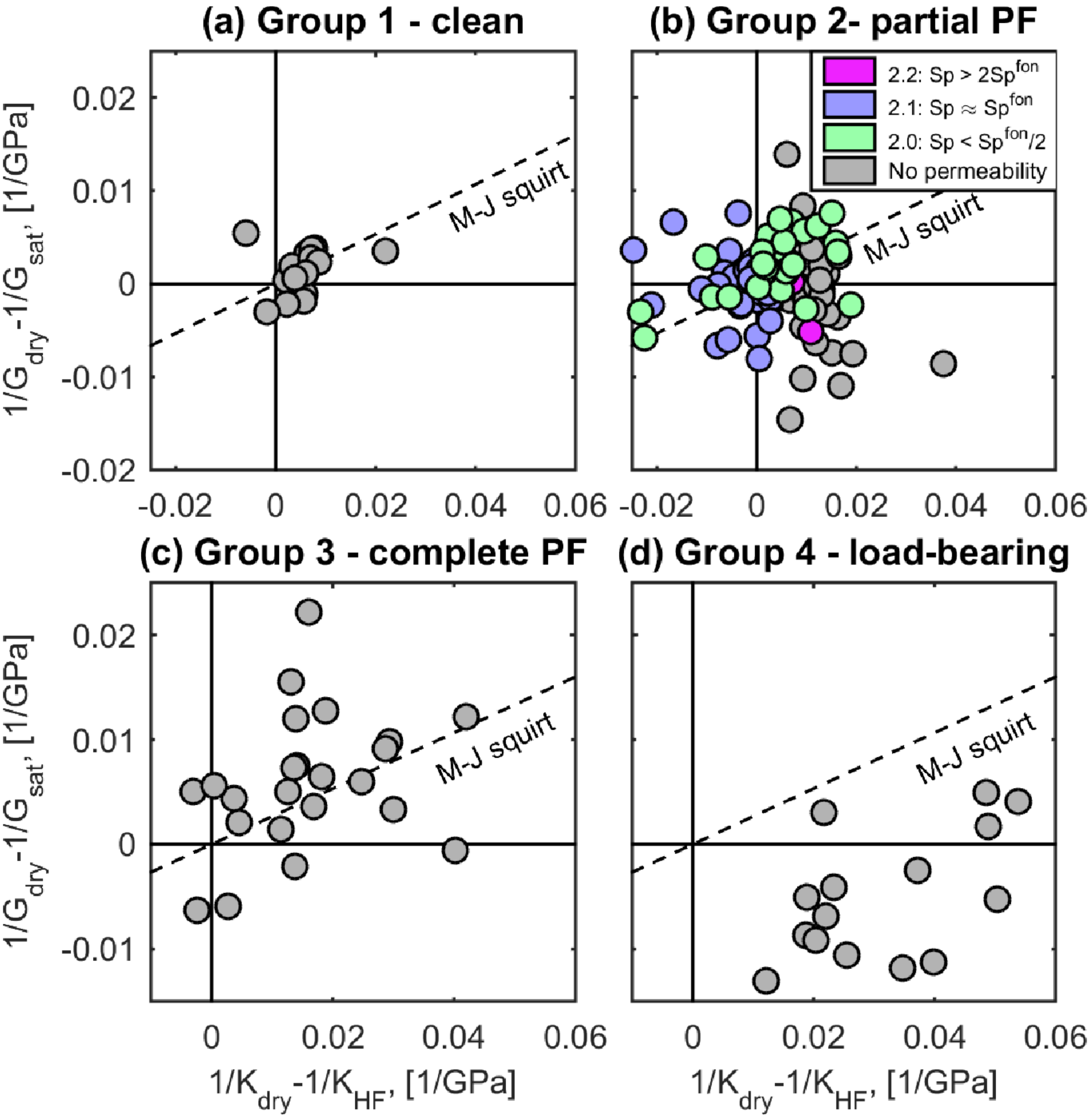

Figure 5.10: Correlation between high frequency change in frame pliability and frame compressibility for the four groups. The dashed lines show the linear correlation indicating local flow dispersion from compliant porosity in the frame found by Mavko and Jizba (1991). Points on the line are compatible with local flow dispersion from randomly distributed frame weaknesses. The color-coding for group 2 (b) corresponds to the subgroups identified by the specific surface per pore-volume in Figure 5.7, gray points are data with no permeability.

compression to the mineral phase than actually present, leading to an underestimated fluid effect (Mavko and Mukerji, 1995). The moduli of the different minerals do not differ substantially and therefore this effect is not large enough to account for the observed residuals. The magnitude of the moduli residuals are compatible with observed effects from local flow dispersion (Paula and Pervukhina, 2012). For dispersion caused by compliant porosity in the load-bearing frame, the shear and the bulk behavior are tied together since stiffening of the frame affects both. The difference between the unrelaxed frame compliance and the relaxed frame compliance, $1/K_{dry} - 1/K_{HF}$, where K_{HF} is the unrelaxed frame bulk modulus, and the difference between the unrelaxed pliability and the relaxed pliability, $1/G_{dry} - 1/G_{HF}$, where G_{HF} is the unrelaxed frame shear modulus, is linearly correlated by a factor of 4/15 (Mavko and Jizba, 1991; Gurevich et al., 2009). The unrelaxed frame shear modulus equals the saturated shear modulus while the unrelaxed frame bulk modulus can be obtained by a fluid substitution from the saturated state:

$$K_{sat} \xrightarrow[K_f=0]{Gassmann} K_{HF} \tag{5.10}$$

This analysis was suggested by Mavko and Jizba (1994) with the underlying assumption that the compliant porosity fraction is negligible. Little error is therefore introduced by substituting to the full porosity. Figure 5.10 shows the relation in the four groups. Figure 5.10 shows the dispersion in the clean sandstones to be compatible with local flow dispersion from compliant parts of the grain frame. However, the remaining groups do not comply with this prediction.

Group 2

The distribution of the shear and bulk residuals in Group 2 and both wider than Group 1. The shear residual distribution is symmetric around 0 whereas the bulk residual distribution is positively skewed with a peak at slightly positive residuals. This difference between the distributions of the residuals may suggest that the input parameters for the fluid substitution does not properly account for the shale fraction creating a systematic divergence. We used a shale mineral modulus of 12 GPa corresponding to a kaolinite mineralogy (Vanorio et al., 2003). The distribution of bulk modulus residuals in Figure 5.9 is positively skewed. This suggests that the suspension modulus that was used is too low and a larger shale mineral modulus should be used in the fluid substitution. It is also possible that the frame mineral modulus that was used is incorrect. We estimate the input parameters by varying the shale mineral modulus from 5 GPa to 30 GPa and the frame mineral modulus from 30 GPa to 60 GPa. As quantifier for prediction improvement, we use the root-mean-square (RMS) of the bulk modulus residuals as depicted in Figure 5.11a with the best distribution shown in Figure Figure 5.11b. The best prediction is found for mineral moduli between 42 GPa and 44 GPa, about 15 % larger than the bulk modulus of quartz. The best choice of mineral modulus depends on the choice of clay mineral bulk modulus with 42 GPa corresponding to a clay mineral modulus of 30 GPa and 44 GPa corresponding to a clay mineral modulus of 5 GPa. The fluid-shale suspension modulus is determined by a Reuss average (Equation 5.9) and the influence of increasing the shale mineral modulus diminishes after about 10 GPa (see inset Figure 5.11a). Above 10 GPa the shale is effectively incompressible relative to the fluid. Figure 5.11b show that changing the moduli shifts the distribution towards lower moduli residuals smoothing the distribution, but retaining the general appearance. By this analysis it is conceivable that the moduli residuals observed are a consequence of some physical mechanism beyond the assumptions of Gassmann. Figure 5.10 shows that the correlation between shear dispersion and bulk dispersion does not agree with local flow from frame weaknesses as in Group 1. Best and McCann (1995) suggested that local flow could take place from compliant porosity in the dispersed shale, a mechanism coined as clay-squirt. Clay-squirt from non-loadbearing porosity is not subject to a stringent relation between shear and bulk modulus, because stress is projected to the shale via the pore-pressure. Transient pressure gradients from dispersed shale could therefore be responsible for the bulk modulus residuals and be compatible with well predicted shear modulus. Attempts to model local flow dispersion on bulk moduli (Soerensen and Fabricius, 2013) and attenuation (Soerensen and Fabricius, 2013; Best et al., 2013) have shown that assuming a soft shale micro-porosity may indeed explain much of the dispersion.

It is possible that several mechanisms are at work in the partially filled Group 2. The subgroups defined by the specific surface in Figure 5.7b indicate that characteristics of the behavior seen in the shale dominated groups (Group 3 and Group 4) can be seen in Group 2. Subgroup 2.2 with some pores completely filled with shale has mostly positive shear and bulk residuals similar to the distribution in Group 3, albeit with smaller magnitudes. Similarly, Subgroup 2.0, which may have some load-bearing shale, has the negative shear residuals and positive bulk residuals similar to Group 4. As the distribution of shale is heterogeneous in these subgroups, the moduli residuals may be ascribed to a combination of mechanisms.

Group 3

Figure 5.8c shows the shear residuals in Group 3 to be too large relative to the bulk residuals for them to be described by local flow in the formalism of Mavko and Jizba (1991). A larger number of the data in Group 3 are measured using fluids with viscosity much higher than water. Figure 12 shows the bulk modulus residual for Group 3 plotted against the shear modulus residual shaded by viscosity. The anomalous shear residuals in Group 3 are clearly dependent on fluid viscosity. Inclusion of data from Group 2 for samples saturated with the same highly viscous fluids illustrate that the viscosity dependent shear residuals are inherent to Group 3. Although the samples from Group 2 are saturated with the same fluid they do not exhibit the large shear residuals. The difference between Group 2 and Group 3 lies in structure of the shale in the pore-space. Group 3 is close to the critical shale fraction and the pore-space overall is dominated by shale, whereas Group 2 has open porosity. The concentration of shale in the pore-space of Group 3 is between 0.5 and 0.75 (Figure 4). These values are close to the critical

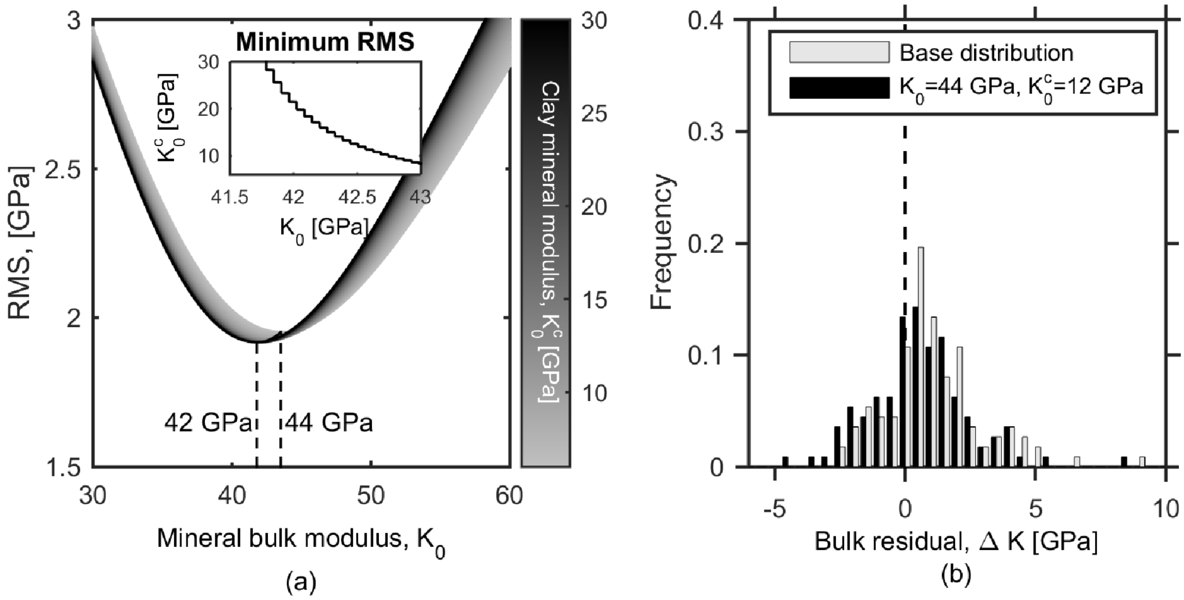

Figure 5.11: Adaptation of the input moduli to the fluid substitution in Group 2. Best choice of input moduli is found by minimizing the RMS in the group as a whole (a). The distribution achieved by using the fitted moduli is compared to the bulk residual distribution of Figure 5.9b.

porosity of a clay suspension as extracted from Atterberg liquid limits (Spagnoli and Sridharan, 2012; Moyano et al., 2012). The suspension of shale and fluid in the pores are therefore close to the fluid-solid transition. Ocean sediments are found to support shear wave propagation at a porosity of up to 0.8 in the sonic frequency range (Hamilton, 1971). The shale suspension in the pore-space in Group 3 can therefore have a finite rigidity, stiffening the rock. The bulk modulus is increased when the suspension attains rigidity, but the relative effect on the shear modulus is much higher as there was no shear modulus prior to this. Ciz and Shapiro (2009) suggested that the shear modulus of a pore-fill, G_{pf}, can be determined from the bulk shear modulus analogous to the bulk modulus fluid substitution:

$$\frac{G_{pf}}{\phi\left(G_0 - G_{pf}\right)} = \frac{G_{sat}}{G_0 - G_{sat}} - \frac{G_{dry}}{G_0 - G_{dry}} \tag{5.11}$$

The shear modulus of the frame is used to quantify the shear modulus of the pore-space assuming a homogeneous frame. Figure 5.13 shows, G_{pf}, versus pore-fluid viscosity for three lithologies in Group 3 saturated with 6 different fluids (Best, 1992). Obviously a modulus cannot be negative as seen in Figure 5.13 for the water saturated samples. This value implies a softening of the water saturated state relative to the dry state, as discussed in Section 4.3. All three lithologies show weakening when saturated with water, slight stiffening with hexane, and increasing stiffening with viscosity of the water/glycol mixtures. The pore-fill is modeled as a standard linear solid where we assume that

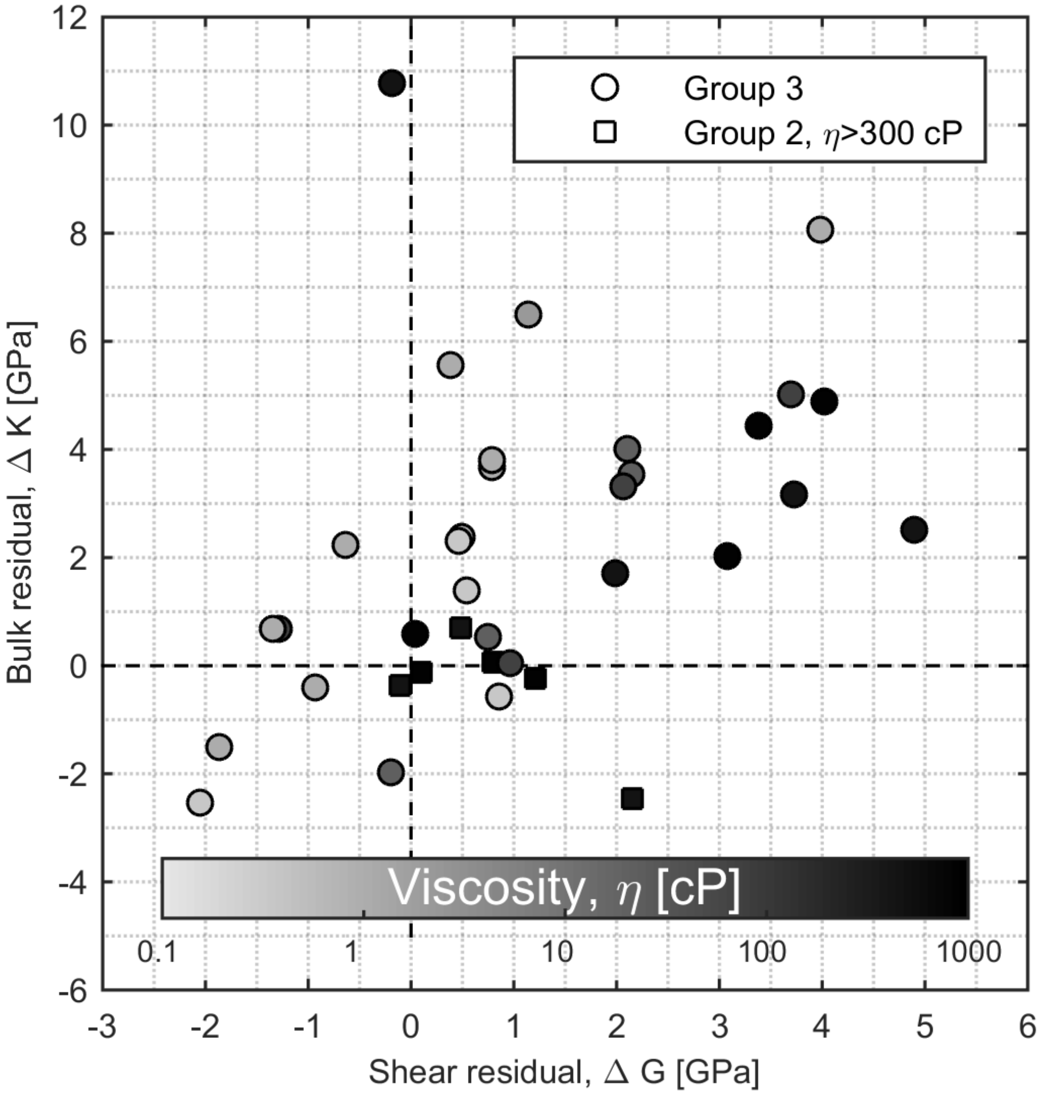

Figure 5.12: Bulk residuals plotted versus shear residuals for Group 3 color-coded to viscosity of the saturating fluid. The high viscosity increases the shear modulus more than the bulk modulus. Samples from Group 2 saturated with the same high viscosity fluid does not exhibit the same shear stiffening.

the hexane saturated pore-fill correspond to the relaxed state and the high viscosity water/glycol saturated pore-fill correspond to the unrelaxed state. As the frequency is held constant the transition can be formulated in terms of a critical viscosity, η_c. The real part of the pore-fill shear modulus is determined by, $x = \eta/\eta_c$, as (Nowick and Berry, 1972),

$$G_{pf} + G_0 \left(G_\infty - G_0\right) \frac{x^2}{1 + x^2} \tag{5.12}$$

Figure 5.13 shows that η_c differs by an order of magnitude between the samples with low shale porosity ($\eta_c = 20$) and the sample with the highest shale porosity ($\eta_c = 200$). If it is assumed that the modulus of the pore-fill depends on the degree to which shear stress is propagated between grains in the pore-fill, the difference in grain separation between the high porosity pore-fill and the low porosity pore-fill scales with viscosity as the viscous boundary layer. The viscous boundary layer scales with the square root of the viscosity (Batchelor, 2000). This means that when the ratio of critical viscosity is 10, the ratio of grain separation in the two instances is $\sqrt{10} \approx 3$. In this view, grain separation should be 3 times larger in the sample with high shale porosity than in the low-shale porosity samples. The specific surface is inversely proportional to the averaged pore-size which, for a suspension, can give an approximate indication of the grain separation. By observing Figure 5.7b we see that a ratio between the specific surface of the high porosity shale and the low porosity shale is in the range of $3 - 6$. The interpretation of a viscoelastic suspension therefore appears consistent with the permeability data.

Group 4

Group 4 is the only group where the residuals of the two moduli have opposite sign; negative shear residuals and positive bulk residuals. The shear residuals extend from 0 GPa to -5 GPa while the bulk modulus is strictly positive between 5 GPa and 10 GPa. Group 4 is heavily influenced by the shale content as Group 3, but contrary to Group 3, the shale in Group 4 is under stress. This causes the structure of the shale to change and prevents re-organization of the shale fabric at different saturations. Also the moduli of the shale are determined by the loading at the contacts in the shale part more than the cohesion of the particles. It is well known that the strength of shales depends on the saturation state (Jizba, 1991; Horsrud et al., 1998; Josh et al., 2012). This is often also found for the elastic moduli (Mondol et al., 2007; Ewy and Stankovic, 2013). Specifically, the dry state is found to have higher shear modulus than the saturated state. In the saturated state, the shear modulus especially depends on fluid, salinity, and composition. A fluid induced softening of the shale inclusion is consistent with the observation of negative shear residuals in Group 4. Modeling of the elastic moduli of saturated compacted clay using pore compliances shows shear moduli to be affected by higher aspect ratio pores than bulk moduli (Moyano et al., 2012). This indicates that, relative to the supposed clay mineral matrix, the shear modulus is reduced more than the bulk modulus, consistent with the observations for Group 4. The modulus residuals seen in Group 4 are therefore similar to those seen in shales and compacted clay.

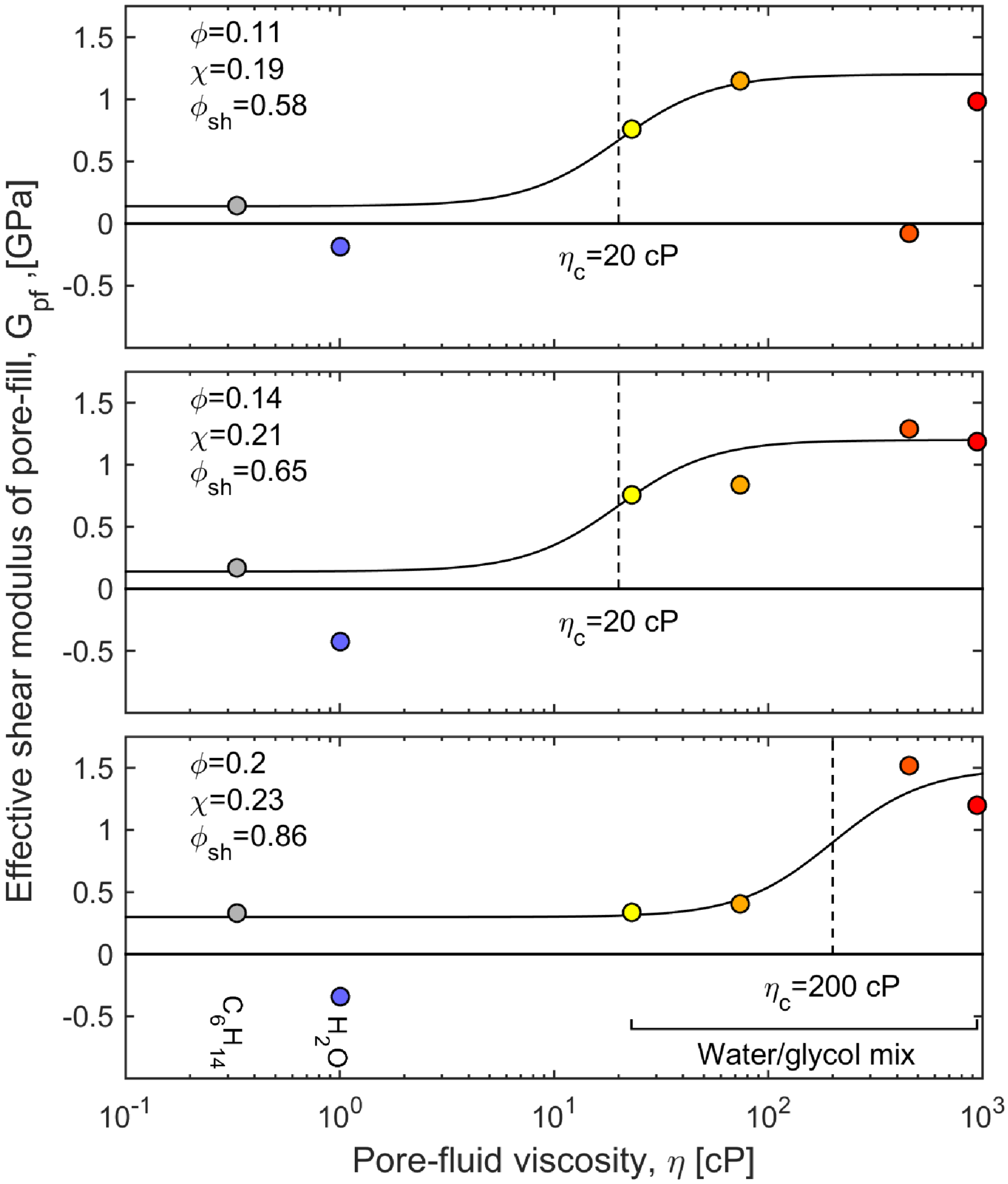

Figure 5.13: : Pore-filling shear modulus as a function of pore-fluid viscosity for three members of Group 3. The pore-filling shear modulus is stiffened by hexane, softened by water and stiffened by water/glycol mixtures as a unction of viscosity. The pore-fill is modeled as a standard linear solid with a relaxation proportional to the fluid viscosity with a transition viscosity as indicated in the figure. The highest shale porosity sample has a transition viscosity one order of magnitude larger than the lower shale porosity samples.

5.8 Summary and conclusions

Based on porosity, clay fraction, and elastic modulus, we formulated a textural classification for sandstones depending on their ”shaliness” The classification is able to identify load-bearing shales even in the instance of sand with glauconitic framework grains (greensand) which have petrophysical properties (porosity, permeability) close to arenitic lithologies. Mesoscopic homogeneity of the shale distributions was evaluated using the bulk sample permeability. The shear modulus and bulk modulus residuals in the groups normalized by Gassmann fluid substitution are both quantitatively and qualitatively dependent on the ”shaliness” Elastic moduli residuals in clean sandstones (Group 1) are found to be compatible with velocity dispersion involving transient pressure gradients in compliant frame porosity. This mechanism did not appear to be the dominant mechanism in the groups with significant shale fractions.

Lithologies with partially pore-filling shale (Group 2) have varied moduli residual distributions. Group 2 was the only group showing a symmetric distribution of the shear residual around 0 with a considerable peak in the bin ranging from ±0.25 GPa. The distribution of the bulk modulus residuals in Group 2 shows an inclination to positive residuals consistent with transient pressure gradients isolated from the frame, as in clay-squirt dispersion. Evaluation of the homogeneity of the shale distribution in Group 2 via permeability analysis identifies subgroups resembling Group 3 and Group 4. That is, subgroups where some pores are completely filled by shale and where some shale may be load-bearing. These subgroups show moduli residuals resembling those seen in Group 3 and Group 4 respectively, albeit with lesser magnitudes.

Lithologies with a pore-space dominated by shale, but where the shale still remains non-load bearing (Group 3), have large moduli residuals which depend on fluid chemistry and viscosity. A transition to high shear residuals is seen for highly viscous saturating fluids. This transition is interpreted as the shale suspension in the pores attaining a finite rigidity at sufficiently high viscosity. This transition affects the shear modulus more than the bulk modulus as the shear modulus in the relaxed state was vanishingly small compared to the low relaxed suspension bulk modulus. Comparing the critical viscosity of different lithologies gives values consistent with the specific surface of the pore-fill extracted from the permeability. In lithologies with load-bearing shale (Group 4), the loading stress dominates the shale moduli and the moduli residuals become qualitatively different from Group 3. Group 4 has negative shear residuals and positive bulk residuals. This observation is consistent with observations of compacted clay and general observations of fluid sensitivity in clay rich shales.

The classification presented here illustrates the need to consider both the shale inclusions and the grain frame in modeling the elastic parameters of sandstones. Different poro-visco-elastic mechanisms influence moduli in the different groups. The mechanisms also appear to be intimately linked to the interaction between clay and fluid and the distribution of shale in the sandstone. These findings suggest that fluid effects in shaly sandstones may not readily be modeled by simple extension of models for clean sandstones, in which the shale fraction is treated as inert pore-fill. No direct dependence on the specific mineralogy of the shale is evident. Shale mineralogy is found to be related to the shale distribution and, through this, the elastic moduli. The moduli residuals do not appear to be related to the elastic moduli of the specific clay minerals.

Out of the four groups identified only Group 1 and Group 2 contain lithologies which may be classified as good reservoirs. The permeability is low in Group 3 and Group 4 making these poor reservoirs and therefore less relevant in the discussion of sonic log correction. The shear modulus reduction and bulk modulus increase seen for Group 4 is interesting and may be important in laminated cases where permeable sand layers cause load-bearing shale to be exposed to a changing fluid saturation, which could cause a change in the moduli of the sand and shale composite. Hereby the effect on load-bearing clay will be treated in Chapter 10. Otherwise the analysis will focus on Group 2 as this group compose most of the reservoirs exploited and exhibit a behavior not complying to fluid substitution even with the extensions for pore-filling clay.

Chapter 6

Modeling clay dispersion of bulk moduli in sandstone with a homogeneous clay distribution

Group 2 in Chapter 5 show the bulk modulus to be increased by pore-filling clay in the saturated state while the shear modulus is not altered much relative to the dry state. Contrary to weaknesses of the grain frame with negligible spatial extend (Budiansky and O'Connell, 1976; Sayers and Kachanov, 1991) the geometry of clay assemblages is more complicated. A clay assemblage constitutes a porous frame imbedded in the sandstone frame complicating an explicit formulation of the geometry. The dispersion caused by relaxation of local pressure gradients is determined by the time needed for relaxation and thus the texture (Sarout, 2012). In this chapter a model is developed which evaluate the possible magnitude of clay-squirt from homogeneously distributed clay in two simple textures. These textures are; shale present as laminae and shale present solely as pore-fill. These textures constitute the extremes of how shale may influence sandstones; for the former a maximum stress is projected to the shale and it strongly changes the moduli of the sandstone while for the latter a minimum stress is projected to the shale minimizing the effect on the sandstone bulk modulus. The primary aim of the model is to evaluate the possible magnitude of clay-squirt on the bulk modulus in the low- and high-frequency limit. The difference between these two limits corresponds to the possible magnitude of dispersion caused by clay-squirt. The model presented will not address changes on the shear modulus as shear waves are polarized and therefore require assumptions regarding the explicit distribution of shale in the sandstone. Squirt-flow models generally employ relations between the bulk modulus dispersion and the shear modulus dispersion (Gurevich et al., 2010; Mavko and Jizba, 1991). This approach is not valid in the case treated here as shale have non-negligible spatial extend and may not be load-bearing. The model relies on a phenomenological approach using Gassmann fluid substitution to determine induced pressures. In the model, shale bearing sandstone is seen as a composite of two frames; a quartz frame and a shale frame composed of a clay mineral aggregate. For both frames the moduli are parameterized using the iso-frame model (Fabricius et al., 2010) allowing the frame moduli to be expressed in terms of iso-frame value, porosity, and mineral moduli. The induced pressures are determined in the individual frames using Gassmanns equations. The initial state composes the high-frequency limit where the bulk modulus of the sandstone is determined by the isolated properties of the two frames. The low-frequency limit is achieved by determining an average pressure from volumetric considerations. Input variables are estimated from laboratory data found in the literature. First we present the parameterization of the frame moduli using the iso-frame model. We then present and justify the choice of input variables needed. The formulation of the Gassmann fluid substitution is then presented. Finally the model implementations for shale laminae and dispersed shale are presented. To evaluate the model we compare the predictions to a data set of ultrasonic elastic moduli collected from the literature. Only data for dispersed shale is found, but a qualitative discussion based on observations are conducted to evaluate the case of shale laminae.

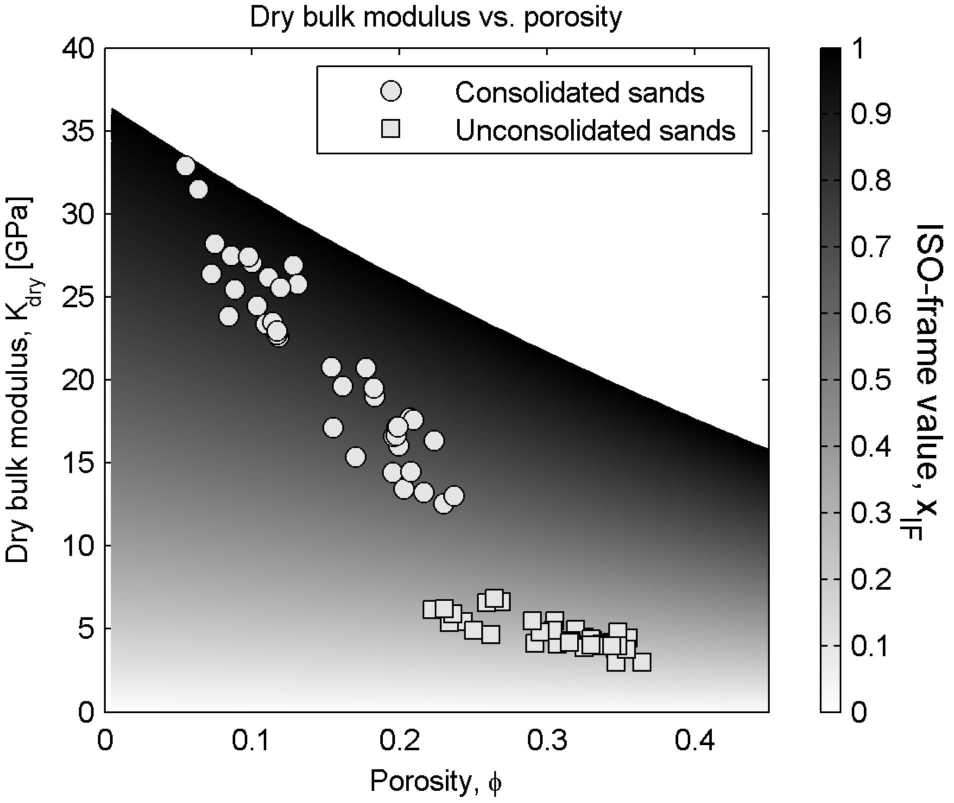

Figure 6.1: Bulk modulus for unsaturated clean sandstones compared to iso-frame value to estimate relevant, (ϕ, x_{IF}), combinations for clean quartz frame. Consolidated sandstones have iso-frame values between $0.7 - 1$ and unconsolidated sands have iso-frame values in the range $0.2 - 0.35$

6.1 Choice of mineral and frame parameters

The parameterization of the frame bulk modulus requires input of porosity, iso-frame value, and mineral moduli. The iso-frame model requires input of both mineral bulk modulus, and mineral shear modulus. Mineral moduli for quartz are well documented and the values used are found in Table 6.1. Typical iso-frame values for sandstone can be determined by observing clean sands and sandstones. Figure 6.1 shows a collection of frame bulk modulus for clean consolidated sandstones measured as dry samples (Best et al., 1994; Han, 1986; King, 1966) and unconsolidated sands (Jizba, 1991). It is assumed that the dry bulk modulus estimates the frame bulk modulus of the sandstone. Clean samples are defined as samples with a volumetric shale fraction,χ, less than 5% of the total volume. The data are all from ultrasonic measurements on dry rocks recorded at isotropic stress between 40 MPa and 60 MPa. Consolidated sandstones have iso-frame values ranging from $0.7 - 1$ and unconsolidated sands fall between $0.2 - 0.35$. Figure 6.1 also shows that the porosity of clean consolidated sandstone ranges from 0.05 to 0.25 and clean unconsolidated sands at high stress from 0.2 to 0.35.

Mineral	K_0, [GPa]	G_0, [GPa]	Method	Source
Quartz	36.6	45	Crystal vibration	(Koga et al., 1958)
Kaolinite	11	6	Ultrasonic extrap.	(Vanorio et al., 2003)
Kaolinite (dry)	7.9	10.2	Ultrasonic extrap.	(Mondol et al., 2008)
Kaolinite (sat)	17.8	4.7	Ultrasonic extrap.	(Mondol et al., 2008)
Kaolinite	47.9	19.7	Epoxy cast	(Wang et al., 2001)
Smectite	5.75	4.02	Ultrasonic extrap.	(Vanorio et al., 2003)
Smectite	9.3	6.9	Epoxy cast	(Wang et al., 2001)
Smectite (dry)	12.3	15.6	Ultrasonic extrap.	(Mondol et al., 2008)
Smectite (sat)	29	7.9	Ultrasonic extrap.	(Mondol et al., 2008)
Illite	60.1	25.3	Epoxy cast	(Wang et al., 2001)
Chlorite	164.3	51.4	Epoxy cast	(Wang et al., 2001)

Table 6.1: Mineral moduli of clay minerals and quartz published in the literature.

Clays comprise several mineral groups; the properties of a selection of these are listed in Table 6.1. It is evident that there is large uncertainty involved in determining the clay mineral moduli. We therefore apply a range of mineral moduli. The proper range of frame moduli for a shale frame at a given porosity is also difficult to assess. For shale laminae the frame properties can be evaluated by observing the relation between ultrasonic velocity and stress for aggregates of clay powders.

Figure 6.2 shows the dry bulk modulus of a kaolinite powder as a function of stress (Yin, 1992). With increasing stress the porosity decreases and the iso-frame value increases, ranging from 0.08 at low differential stress to 0.65 at high differential stress. As clay minerals do not readily form cement, compaction is a good measure of the modulus development. We therefore use the compaction trend from Figure 6.2 as guidance for the choice of iso-frame values in the case of shale laminae. Burial of 2 km to 4 km corresponds approximately to an effective stress of 20 MPa to 40 MPa assuming hydrostatic pore-pressure. From Figure 6.2 this is equivalent to iso-frame values between 0.38 and 0.65 which is used for shale laminae. The elastic properties of dispersed shale are more complicated to estimate as authigenic clay form as individual particles smaller than the pores and not as connected frames (Wilson and Pittman, 1977). Dispersed shale is not subjected to an effective stress and therefore no compaction occurs. Although compaction does not occur the clay frame will still have a non-zero frame modulus when the particles are in contact. The frame modulus is related to how the clay is formed in the pores, but no data exist to directly determine the relation. Based on the assumption that compaction is the dominant factor in consolidation of shales, the iso-frame value of dispersed clay assemblages is low. We adopt an iso-frame value span for dispersed shales of 0.05 to 0.4. The porosity of shale is also related to compaction (Mondol et al., 2007). Figure 6.2 shows the porosity of the kaolinite aggregates to vary from 0.6 at low stress to 0.2 at high stress. Hurst and Nadeau (1995) and Liu et al. (1994) showed a wide

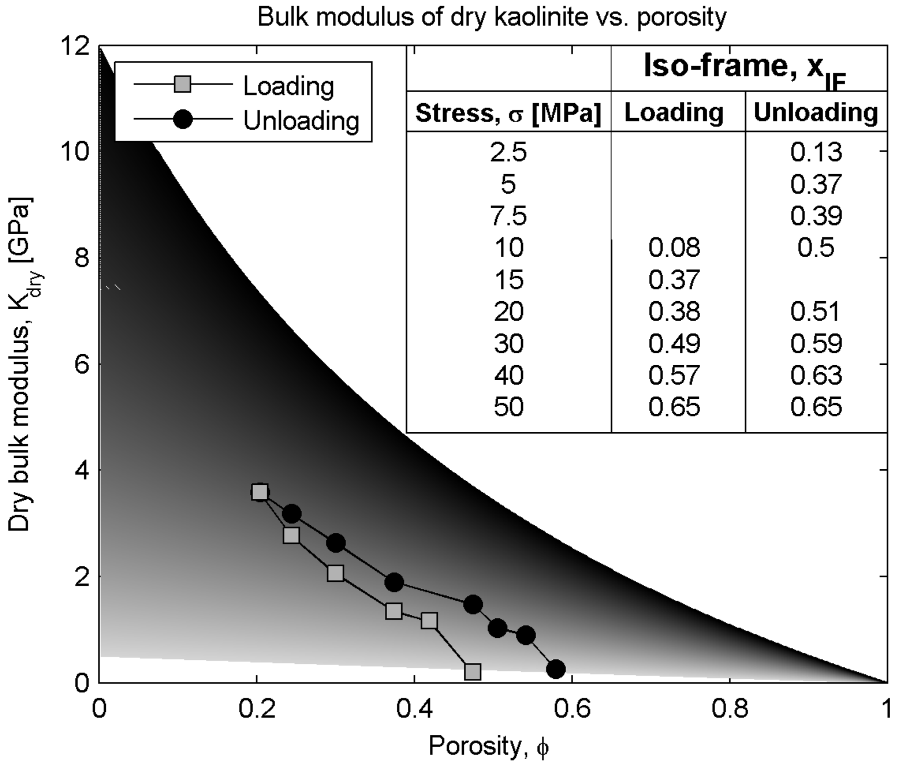

	Iso-frame, x_{IF}	
Stress, σ [MPa]	Loading	Unloading
2.5		0.13
5		0.37
7.5		0.39
10	0.08	0.5
15	0.37	
20	0.38	0.51
30	0.49	0.59
40	0.57	0.63
50	0.65	0.65

Figure 6.2: Dry bulk modulus of kaolinite aggregate versus porosity and compared to iso-frame assuming, $K_0^c = 12$ GPa, and $G_0^c = 6$ GPa (Vanorio et al., 2003). Iso-frame values increase and porosity decrease with increasing stress. An appropriate, (ϕ, x_{IF}), combination for kaolinite compacted at $20-40$ MPa is porosity between 0.2 and 0.4 and iso-frame values between 0.38 and 0.65.

range of shale porosity in sandstones depending on whether the shales are load-bearing, and compacted, or not. From Figure 6.2 we affix a porosity range of 0.2 to 0.4 for load-bearing shales. Based on the data of Hurst and Nadeau (1995) we assign a porosity range from 0.4 to 0.8 for dispersed shale.

6.2 Gassmann and induced pore-pressure

Compressing a porous frame in an undrained state ($dm_{fluid} = 0$) induces a pore-pressure, P. This induced pressure is inherent to the specific frame, and is the reason the saturated bulk modulus, K_{sat}, is higher than the frame bulk modulus, K_{frame}. The induced pressure is proportional to the applied external stress, σ, for linear deformations (Dvorkin

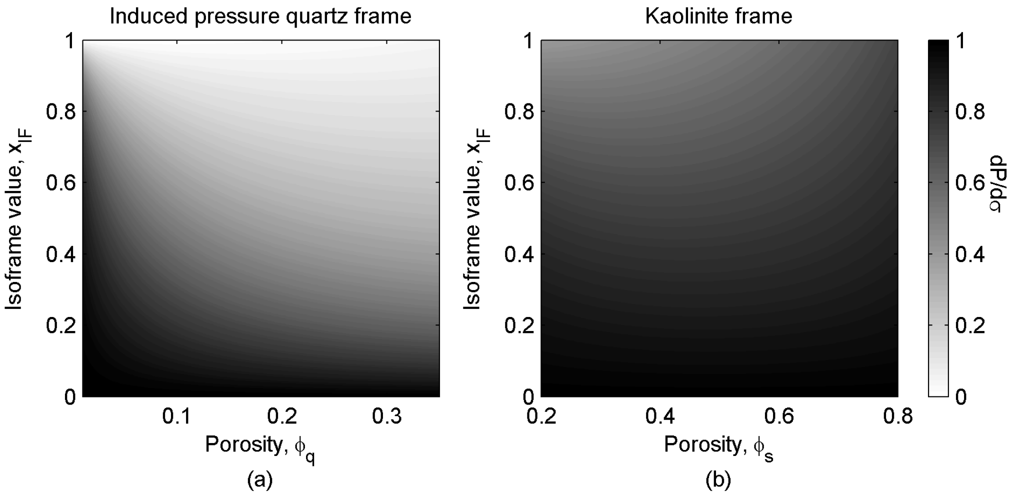

Figure 6.3: Induced pressures in a quartz (a) frame and a kaolinite (b) frame depending on porosity and iso-frame value. The kaolinite frame (b) clearly has a higher induced pressure than do the quartz frame (a).

et al., 1995),

$$\frac{dP}{d\sigma} = -\frac{1}{\alpha\left(1+\frac{K_{frame}\phi}{\alpha^2 F}\right)} \tag{6.1a}$$

$$\frac{1}{F} = \frac{1}{K_f} + \frac{1}{\phi Q} \tag{6.1b}$$

$$Q = \frac{K_0}{\alpha - \phi} \tag{6.1c}$$

where $\alpha = 1 - K_{frame}/K_0$, is Biot's coefficient. External compressional stress and induced pressure is directed oppositely, whereby the expression is negative. The ratio in Equation 6.1a is equivalent to Skempton's B coefficient (Skempton, 1954). Several formulations of this parameter is introduced in the literature (Zimmerman, 2000; Rice and Cleary, 1976; Biot, 1962). Simplification of Equation 6.1a can be achieved by introducing aggregate moduli as the pore-modulus (Mavko and Mukerji, 1995), we have chosen this form however as it involves only bulk moduli of the mineral and fluid and Biot's coefficient to quantify the frame properties.

Figure 6.3a shows the normalized induced pressure for a quartz frame and Figure 6.3b for a shale frame using the parameterization introduced by the iso-frame value and porosity. The induced pressure increases with decreasing frame modulus. Induced pressure makes

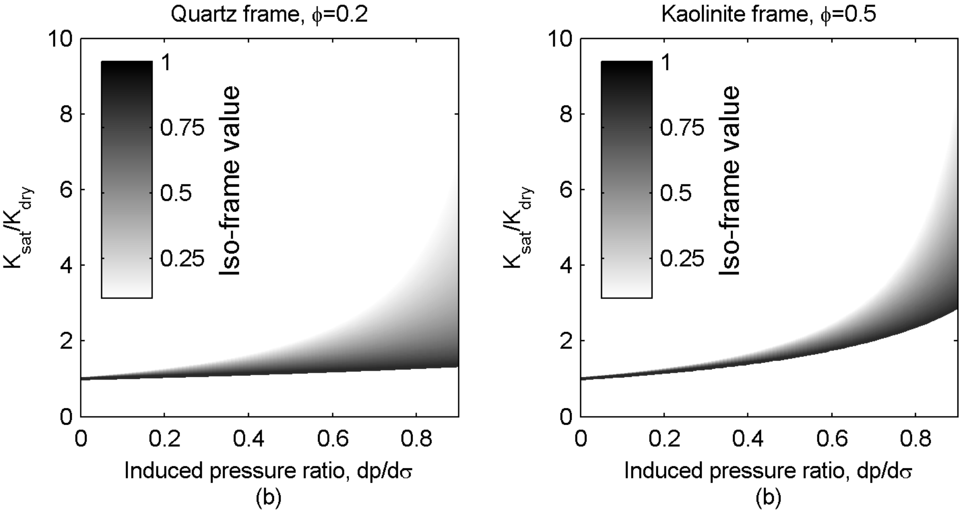

Figure 6.4: Effect of an induced pressure on the saturated bulk modulus for a quartz frame (a) and a kaolinite frame (b). The kaolinite frame has a higher sensitivity to pressure changes.

the saturated frame bulk modulus, K_{sat}, larger than the frame modulus, K_{frame},

$$K_{sat} = \frac{K_{frame}}{1 - \alpha \frac{dP}{d\sigma}} \tag{6.2}$$

Equation 6.2 holds true if $dP/d\sigma$ is maintained at the value inherent to the frame. If the induced pressure is changed from the frame inherent induced pressure the saturated bulk modulus changes, the change is quantified by Equation 6.2. Figure 6.4 shows the effect of induced pressure ratios on the bulk modulus for a clean quartz frame and a kaolinite frame. It is important to note that Figure 6.4 illustrates the situation where $dP/d\sigma$ is changed by an external interaction.

6.3 Frequency range

The model presented quantifies the bulk modulus dispersion as the difference between a high frequency bulk modulus and a low frequency bulk modulus. In order to formulate these two states we need to address what is meant by high and low frequency. Firstly, all frequencies are low enough for the composite of sand and shale to be in the long-wavelength limit. This means that wave-length, λ, is always longer than the composite of sand and shale. For the laminated texture this restriction means that the $\lambda >> L$ where L is the thickness of a laminae. For the dispersed shale texture the long-wavelength restriction requires the wavelength to be much longer than the pore-size of the sand

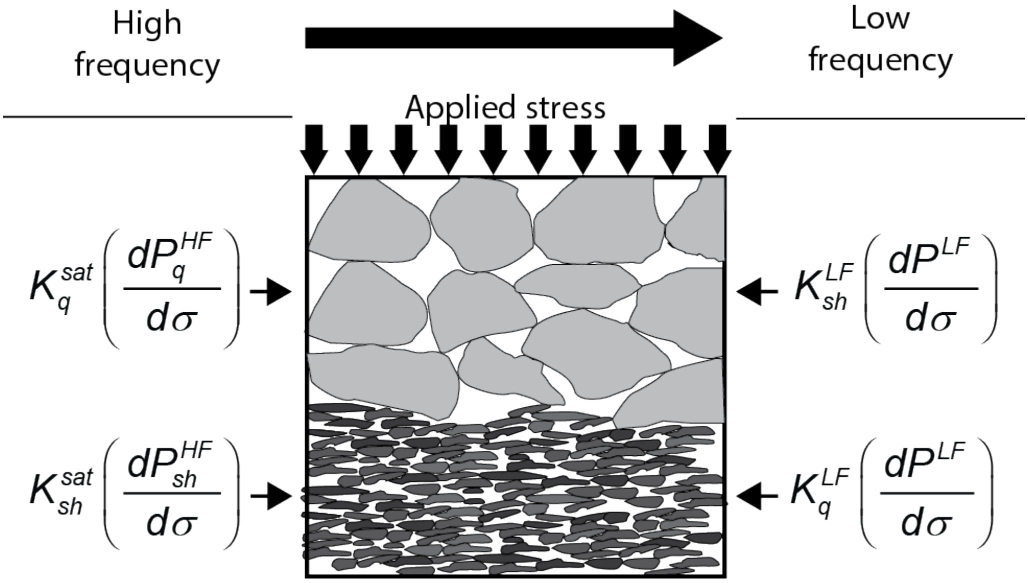
High frequency
Low frequency
Applied stress
$K_q^{sat}\left(\frac{dP_q^{HF}}{d\sigma}\right)$
$K_{sh}^{sat}\left(\frac{dP_{sh}^{HF}}{d\sigma}\right)$
$K_{sh}^{LF}\left(\frac{dP^{LF}}{d\sigma}\right)$
$K_q^{LF}\left(\frac{dP^{LF}}{d\sigma}\right)$

Figure 6.5: Illustration of the laminated model. At high-frequency the pressure induced in the quartz and shale frame are unchanged, and there is a different pressure in the two frames which can be calculated by Equation 6.1a. For the low-frequency case fluid flows from the shale frame to the quartz frame and the bulk modulus is changed.

frame. The high frequency limit is therefore defined as the frequency where pressure diffusion from shale porosity is negligible, but the system is still in the long wavelength limit. For the low-freqeuncy case there is no lower restriction. The frequency in the low-frequency limit must only be significantly below the characteristic frequency for pressure diffusion from the shale porosity.

6.4 Model formulation: Shale laminae

The laminated model is illustrate in Figure 6.5, where initially the pressures induced in the layers are determined by Equation 6.1a, after sufficient time (low-frequency) fluid will have moved from the shale frame to the quartz frame, resulting in a uniform pressure. With the shale distributed as laminae between layers of clean sand both the shale frame and the sand frame will be subjected to the same stress, σ, with the frequency constrained to the long wavelength approach. The bulk modulus of the laminated rock can be determined by a Reuss average of the individual frames. In the high frequency limit the quartz and the shale frames are undrained individually,

$$\frac{dm_q^{HF}}{d\sigma} = \frac{dm_{sh}^{HF}}{d\sigma} = 0. \tag{6.3}$$

Where, dm_q^{HF}, refers to the change in water in the quartz frame pore-volume and, dm_{sh}^{HF}, the corresponding quantity for the shale frame. With the individual frames being undrained the induced pressure in the frames can be determined by Equation 6.1a for each frame. The saturated bulk moduli of the layers are given by inserting the induced pressure into Equation 6.2. The saturated bulk moduli of the individual frames, $\left(K_q^{sat}, K_{sh}^{sat}\right)$, can be combined to the high-frequency saturated bulk modulus of the rock, K_{HF}, by the Reuss average of the saturated frame bulk moduli,

$$\frac{1}{K_{HF}} = \frac{1-\chi}{K_q^{sat}} + \frac{\chi}{K_{sh}^{sat}} \tag{6.4}$$

A higher pressure is induced in the shale frame than the quartz frame due to the difference in frame bulk moduli as illustrated in Figure 6.3. If the frequency is reduced allowing pressure communication between the two frames, fluid flows from the shale frame to the quartz frame. This equilibrates the pressure to a uniform pressure in the entire pore-space, $dP^{LF}/d\sigma$. This is a reduction of the shale pressure with a consequent compression of the shale frame and an increase in the pressure of the quartz frame and expansion of this frame. The individual frames are no longer undrained, but the compsite of the two frame is undrained, whereby the mass of fluid moved from the shale frame must equal the fluid mass added to the quartz frame,

$$\frac{dm_q^{HF}}{d\sigma} - \frac{dm_q^{LF}}{d\sigma} = -\left(\frac{dm_{sh}^{HF}}{d\sigma} - \frac{dm_{sh}^{LF}}{d\sigma}\right). \tag{6.5}$$

Where dm_q^{LF} is the change in fluid mass in the quartz frame, and dm_{sh}^{LF} the corresponding value for the shale frame. A change in pore-volume associated with a change in pore-pressure at constant external stress was formulated by Zimmerman et al. (1986),

$$C_{pp} = \frac{1}{K_{pp}} = \frac{1}{V_p}\left.\frac{\partial V_p}{\partial P}\right|_{\sigma} = \left(\frac{1}{K_{frame}} - \frac{1+\phi}{\phi}\frac{1}{K_0}\right). \tag{6.6}$$

Using this, a change in fluid mass can be written as a function of the induced pressure,

$$\frac{dm}{d\sigma} = \frac{dV_p}{d\sigma} + \frac{V_p}{K_f}\frac{dP}{d\sigma} = V_p\left(C_{pp} + \frac{1}{K_f}\right)\frac{dP}{d\sigma}. \tag{6.7}$$

By substituting this in Equation 6.5 and normalizing all terms to the total pore-volume, $V_p = V_p^q + V_p^{sh}$, using the factors,

$$f_q = \frac{V_p^q}{V_p} = \frac{(1-\chi)\,\phi_q}{\phi},$$
$$f_{sh} = \frac{V_p^{sh}}{V_p} = \frac{\chi\phi_{sh}}{\phi}.$$

we get:

$$\frac{dP^{LF}}{d\sigma} = \frac{1}{A}\left(f_q \frac{dP_q^{HF}}{d\sigma}\left(C_{pp}^q + 1/K_f\right) + f_{sh}\frac{dP_{sh}^{HF}}{d\sigma}\left(C_{pp}^{sh} + 1/K_f\right)\right). \tag{6.9}$$

Where,

$$A = 1/K_f + f_q C_{pp}^q + f_{sh} C_{pp}^{sh}.$$

The induced pressure in the low-frequency state from Equation 6.9 can be substituted into Equation 6.2 to determine the bulk moduli of the quartz and shale frames at the relaxed pressure, $\left(K_q^{LF}, K_{sh}^{LF}\right)$. The low frequency composite bulk modulus can then be determined by a Reuss average,

$$\frac{1}{K_{LF}} = \frac{1-\chi}{K_q^{LF}} + \frac{\chi}{K_{sh}^{LF}} \tag{6.10}$$

The dispersion on the bulk moduli caused by clay-squirt is given by the difference between the high frequency composite bulk modulus, K_{HF}, and the low frequency composite bulk modulus, K_{LF}.

6.5 Model formulation: Dispersed shale

For dispersed shale the shale fraction is assumed non-load bearing contrary to the laminated case. Therefore the stress projected to the shale frame is only the pore-pressure induced in the quartz frame, since the shale is dispersed in the pores of the quartzite frame. The induced pressure in the quartz frame depends on the shale frame bulk modulus, as this stiffens the pore-fill. In the high frequency limit porosity inside the shale frame will be shielded from the pressure induced in the quartz frame. This means that at high frequency the shale fraction contributes to the pore-filling moduli by the saturated shale frame bulk modulus. The resulting bulk modulus of the shale pore-fluid suspension, K_{sus}^{HF}, can be determined by a Reuss average,

$$\frac{1}{K_{sus}^{HF}} = \frac{1-S_{sh}}{K_f} + \frac{S_{sh}}{K_{sh}^{sat}} \tag{6.11}$$

The weight, $S_{sh} = \chi/\phi$, is the fraction of the pore-space filled by shale. The high frequency bulk modulus of the shale bearing quartz frame can then be determined by substituting the suspension modulus from Equation 6.11 into Equation 6.1a and Equation 6.2. When the frequency is reduced, the pressure is equilibrated in the entire pore-space, including the shale porosity, whereby only the solid clay minerals contribute to the suspension modulus. The suspension modulus of the fluid and the clay minerals is then,

$$\frac{1}{K_{sus}^{LF}} = \frac{1-S_c}{K_f} + \frac{S_c}{K_c^0} \tag{6.12}$$

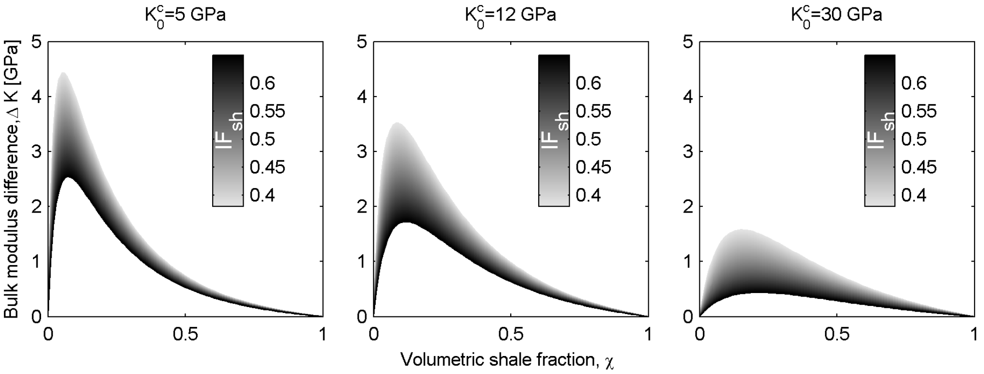

Figure 6.6: Clay-squirt dispersion on saturated bulk modulus of sandstone with shale laminae assuming different clay mineral modulus. The clay-squirt effect increases with decreasing clay mineral modulus. The effect is drastically higher at a shale fractions about $\chi \approx 0.2$

Where $S_c = \chi\left(1-\phi_{sh}\right)/\phi$, is the fraction of quartz pore-space filled by solid clay minerals. The low frequency bulk modulus of the shale bearing quartz frame can be determined by Equation 6.1a and Equation 6.2. The shale fraction has to be less than the quartz frame porosity to be accommodated in the pores. The model breaks down before this limit, however, as the pore-volume outside the shale frame must be sufficient to equilibrate the pressure inside the shale porosity.

6.6 Results – Shale laminae

The model relies on 7 parameters, $\left(\chi, \phi_q, x_{IF}^q, \phi_{sh}, x_{IF}^{sh}, K_0^c, G_c^0\right)$, complicating a full analysis. Figure 6.6 shows the results of the model in the case of shale laminae in a consolidated quartz frame with a porosity of 0.2. Three sets of different clay moduli are chosen; smectite from ultrasonic extrapolation, kaolinite from ultrasonic extrapolation and kaolinite from epoxy cast (Table 6.1). The porosity of the shale frame is set to 0.4 corresponding to compacted shale (Figure 6.2). The difference between low- and high-frequency bulk moduli increases as the contrast between quartz mineral moduli and clay mineral moduli increases. As we have fixed a range to the iso-frame value of 0.38 to 0.65 the mineral modulus and the frame modulus effect becomes coupled. So the dependence on mineral modulus also reflects the relation between clay mineral bulk modulus and shale frame modulus.

Figure 6.7 shows the magnitude of the clay-squirt effect as a function of shale frame bulk modulus and shale porosity for a kaolinite mineralogy, $K_c^0 = 12$ GPa. As the quartz frame bulk modulus is kept constant in Figure 6.7 this explicitly shows that the effect increases with increasing difference between the shale frame bulk modulus and the quartz frame bulk modulus as reflected in a lower, x_{IF}^{sh}. This is caused by the relation

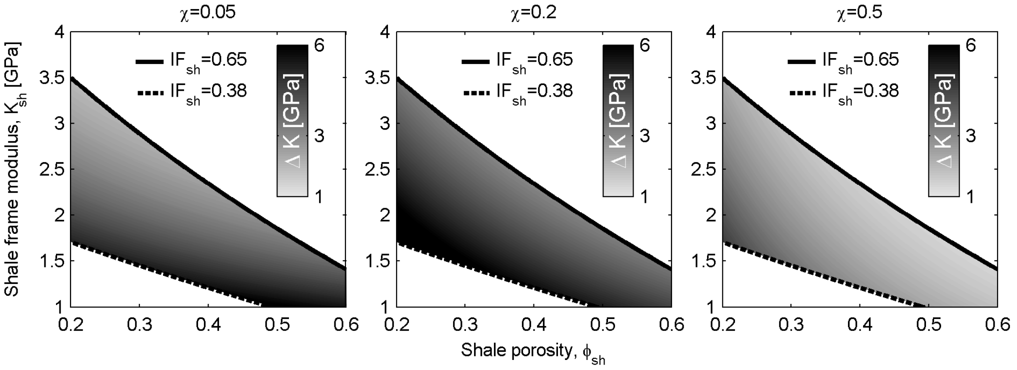

Figure 6.7: Clay-squirt dispersion on saturated bulk modulus of sandstone with shale laminae depending on shale porosity and iso-frame value. The three plots show snap-shots at different shale fractions. The clay-squirt effect reduces as the frame bulk modulus of the shale increases.

between induced pressure and bulk modulus as illustrated in Figure 6.4. As the shale frame bulk modulus decreases the effect of changing the pressure increases and increased dispersion is observed on the composite bulk modulus.

6.7 Results – Dispersed shale

Figure 6.8 shows the difference between the low- and high-frequency saturated bulk modulus for the same three clay moduli as in Figure 6.6. The sandstone frame used for Figure 6.8 has a porosity of 0.3 whereby the maximum shale fraction is 0.3. The effect increases monotonically with shale content. In practice the dispersion will be 0 when the entire porosity is filled with shale since only one type of porosity exists in this case. The model is however not valid when $\chi \approx \phi_q$ why the effect does not disappear in Figure 6.8. The dispersion increases with increasing clay mineral bulk modulus contrary to the laminated case, because the pressure difference between the shale porosity and the open porosity increases with shale frame bulk modulus. At a fixed iso-frame value, the shale frame bulk modulus increases with clay mineral modulus and thereby the dispersion increases. The dispersion is seen to be significantly smaller than in the laminated case for clay mineral moduli generally used in the literature. For a clay mineral bulk modulus of 12 GPa the maximum dispersion is only about 1 GPa. If the mineral bulk modulus is higher a significant effect can be observed.

6.8 Comparison with data

We wish to compare the predictions of Figure 6.6 and Figure 6.8 with ultrasonic data reported in the literature. The cross-over frequency between the low- and the high-frequency regime is determined by the fluid properties, distribution, and size of the clay

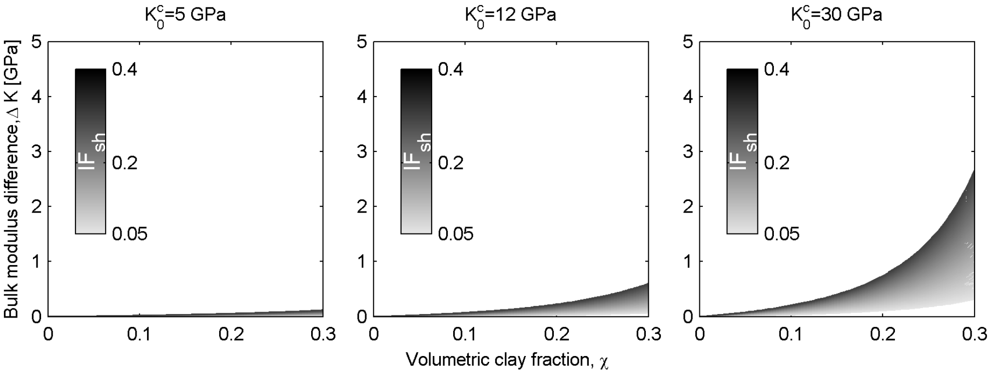

Figure 6.8: Clay-squirt dispersion on the saturated bulk modulus of sandstone with dispersed clay with three different clay mineral moduli. Clay-squirt dispersion increases as the clay mineral modulus increases due to a higher shielding of the micro-porosity within the shale frame.

assemblages. This information is not available for the reported data and therefore we do not attempt a forward modeling of the saturated moduli, but merely perform an estimated inversion to assess whether the observed bulk modulus dispersion could be associated with clay-squirt. We found no data in the literature reported to represent evidently laminated sands, so we base the comparison on an assumption of dispersed shale. Figure 6.9 shows the data set collected from the literature on sandstones (King, 1966; Han, 1986; Best, 1992). The data are obtained from a wide range of locations as seen from Figure 6.9. Also the fluids involved have a significant viscosity span as seen from Figure 6.9.

Since we do not know whether a specific sample is relaxed or unrelaxed, we calculate the suspension modulus,K_{sus}^{gass} , which would be consistent with Gassmann fluid substitution,

$$\begin{aligned} A = \frac{K_{sus}^{gass}}{\phi_{frame}\left(K_0 - K_{sus}^{gass}\right)} &= \frac{K_{sat}}{K_0 - K_{sat}} - \frac{K_{dry}}{K_0 - K_{dry}} \\ K_{sus}^{gass} &= \frac{AK_0\phi_{frame}}{1 + A\phi_{frame}} \end{aligned} \tag{6.13}$$

Where, ϕ_{frame}, is the porosity of the grain frame which is determined as the measured porosity plus the pore-space occupied by clay minerals (Gal et al., 1999),

$$\phi_{frame} = \phi + (1 - \phi_{sh})\,\chi \tag{6.14}$$

Based on the mineral bulk moduli in Table 6.1 it is reasonable to assume that the clay mineral bulk modulus is higher than the fluid modulus. This implies that the shale frame bulk modulus is also higher than the fluid bulk modulus. For dispersed shale the

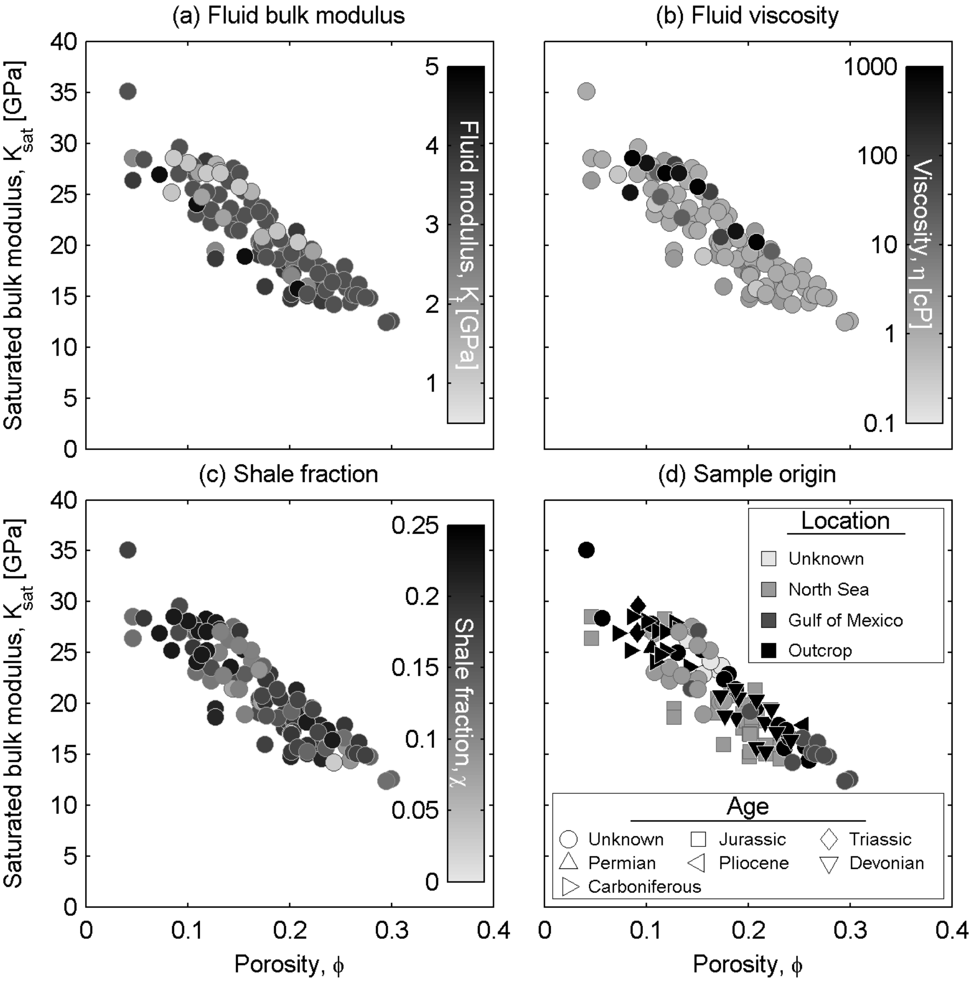

Figure 6.9: Overview of the sandstone data. The saturated bulk moduli are plotted against porosity and shaded to fluid bulk modulus (a), fluid viscosity (b), shale fraction (c), and geological location and age (d).

modulus of shale suspended in the fluid is calculated using Equations 6.11 or Equation 6.12 depending on the frequency.

The limit where,

$$\frac{S_{sh}}{K_{sh}} \to 0 \tag{6.15}$$

gives the maximum suspension modulus corresponding to an incompressible shale fraction. Since the limit involves the shale fraction and $S_{sh} < 1$ the shale modulus need not be much higher than the fluid modulus. The suspension modulus in this upper limit is given by,

$$K_{unr}^{max} = \frac{K_f}{1 - S_{sh}} \tag{6.16}$$

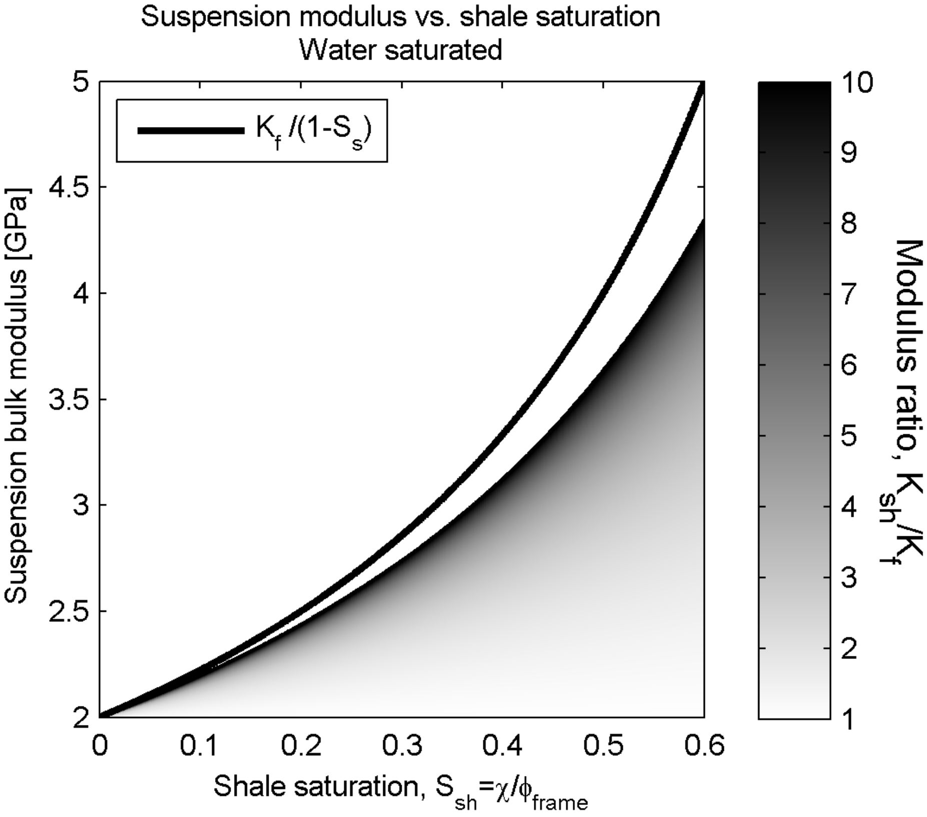

Figure 6.10: Limiting behavior of the suspension modulus versus shale saturation. The suspension modulus at low shale saturation quickly approaches the upper limit. A similar relation is valid for the clay mineral saturation replacing the shale parameters with the clay mineral parameters.

The same analysis apply for Equation 6.12, replacing, K_{sh} with K_0^c, and S_{sh} with S_c.

This applicability of Equation 6.16 is illustrated in Figure 6.10 where the suspension modulus is plotted versus shale saturation for different ratios of fluid bulk modulus to shale bulk modulus. A lower limit can be established by observing that if $K_{sh} = K_f$ then the suspension modulus is equal to the fluid modulus. These limits can be used as bounds for the fluid modulus consistent with Gassmann fluid substitution from Equation 6.13,

$$K_f < K_{sus}^{gass} < \frac{K_f}{1 - S_{sh}} \tag{6.17}$$

Figure 6.11 shows the Gassmann consistent suspension bulk modulus plotted against the upper limit suspension modulus limit based on shale content and fluid bulk modulus. Samples which have dispersion exceeding the clay-squirt prediction are marked with ‘x’ in Figure 6.11. These points maybe associated with heterogeneous distribution of shale or load-bearing shales. The model presented here implicitly assumes a homogeneous shale distribution. A “patchy” shale distribution may lead to larger dispersion, but

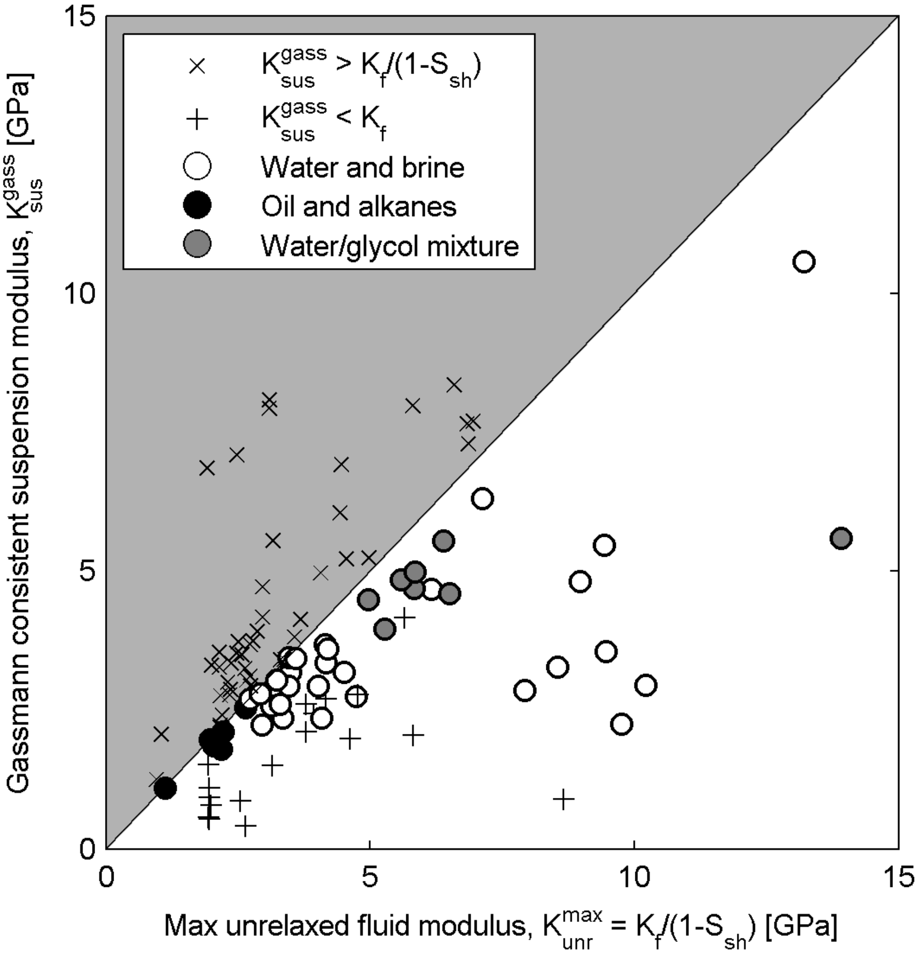

Figure 6.11: Gassmann consistent suspension modulus for the data compared to the maximum suspension modulus achieved from the shale fraction and fluid modulus according to Equation 6.16. Data in circles may be consistent with clay-squirt dispersion.

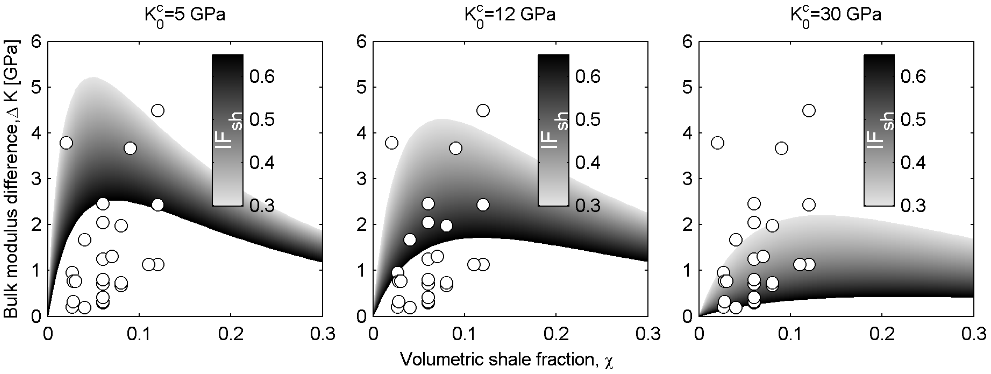

Figure 6.12: Data from Figure 6.11 with $K_{sus}^{gass} > K_{sus}^{max}$ compared qualitatively with the predictions from the laminated model at three different clay mineral moduli. The dispersion for these data are can be accounted for by load-bearing shale.

incorporation of heterogeneous shale requires assumptions regarding the distribution and geometry of the dispersed shales beyond the scope of this study. The larger dispersion can also be caused by load-bearing clay either complete or partial. Figure 6.12 shows the data points with $K_{sus}^{gass} > K_{unr}^{max}$ compared to the prediction for laminated sands in Figure 6.6. Constraint on the laminated model similar to Equation 6.17 depends heavily on the mineral composition and compaction of the shale layers. Therefore Figure 6.12 only qualitatively illustrate that the excess dispersion can be described within the clay-squirt model assuming load-bearing shale. Some samples have Gassmann consistent suspension moduli lower than the fluid modulus. This cannot be explained by clay-squirt as K_F is the lower bound of the saturated shale modulus. Samples which have Gassmann consistent suspension moduli lower than the fluid modulus are generally high permeable samples ($k > 200mD$) with a significant shale fraction. The permeability may then be governed by the inter-grain porosity (Rosenbrand, 2014). This may act to bypass the micro-porosity causing the shale part to be only partially saturated. The lower bound for the shale fraction is therefore closer to the dry shale modulus, drastically reducing the suspension modulus. We limit the data set to the samples that may be compatible with the clay-squirt model.

We do not know a priori if the samples are in the relaxed or unrelaxed state. By fitting the Gassmann consistent fluid modulus to Equation 6.11 and Equation 6.12 using a bisection algorithm we find that no samples are compatible with both a relaxed and an unrelaxed model. The distribution of fitted shale frame moduli for unrelaxed samples are shown in Figure 6.13a and the fitted clay mineral bulk moduli for relaxed samples are shown in Figure 6.13b, both are plotted against the shale porosity. Figure 6.13a clearly shows a decreasing trend in the shale frame modulus with increasing shale porosity, which is to be expected. Two trends are observable one which tends to a mineral modulus of $\approx$ 25 GPa and one pointing to a mineral bulk modulus of 45 GPa. The latter trend

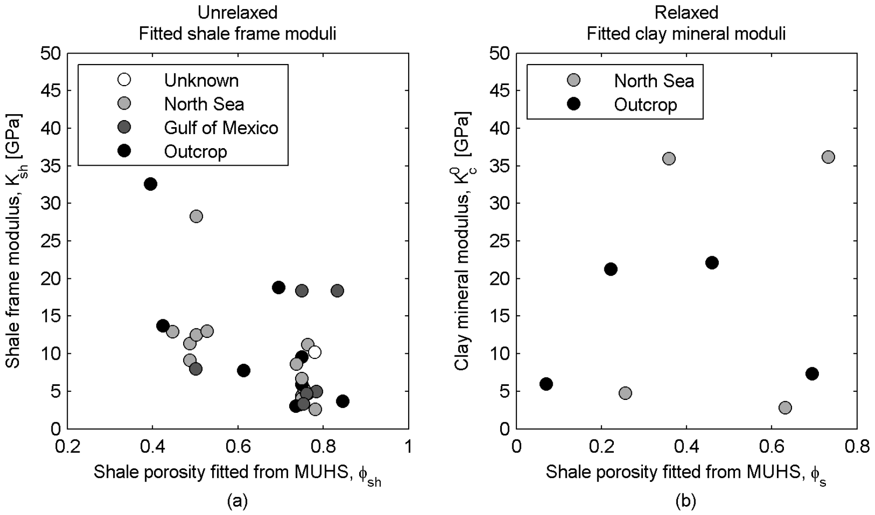

(a)

(b)

Figure 6.13: Fitted saturated shale moduli from lithologies with unrelaxed dispersed shale versus shale porosity (a). Two trends are seen correlating the saturated shale moduli to the shale porosity: one trend with a grain modulus at zero porosity of about 40 GPa and one at about 25 GPa. Fitted clay mineral moduli for relaxed samples plotted shale porosity (b) show no correlation. Three distinct mineral moduli are however identified where the two are compatible with the shale moduli in Figure 13a.

contains few definite data points while the former is better resolved. The shales in sandstones are a mixture of different mineralogies. This complicates the interpretation, but the lower trend in Figure 6.13a is consistent with kaolinite mineralogy. The data in Figure 6.13a and Figure 6.13b are colorcoded to the information provided for the location of the samples. Figure 6.13a shows good consistency with North Sea samples having dominant kaolinite mineralogy. The fitted clay mineral moduli for the relaxed samples are independent of shale porosity again as expected. Three different moduli can be determined at 7 GPa, 22 GPa, and 37 GPa. The two larger mineral moduli correspond well with the extrapolated mineral moduli in Figure 6.13a. They are also plausible when compared to the data in Table 1. As we have no direct measure of the relaxation state of the different samples it is no certainty that the obtained moduli correspond to completely relaxed or unrelaxed moduli. The actual state of the samples may therefore be intermediate between the relaxed and unrelaxed states. The main result of Figure 6.13 is however the correlation with shale porosity for the unrelaxed samples and the lack of correlation with shale porosity for the relaxed samples. This suggests that clay-squirt may indeed be the cause of the observed dispersion.

Distinction between the samples which are relaxed and those which are unrelaxed can be seen from Figure 6.14. The relaxed samples generally have high permeabilities. The transition between unrelaxed and relaxed states is governed by the characteristic length of the shale inclusions, implicitly the shale distribution. As this also strongly affects

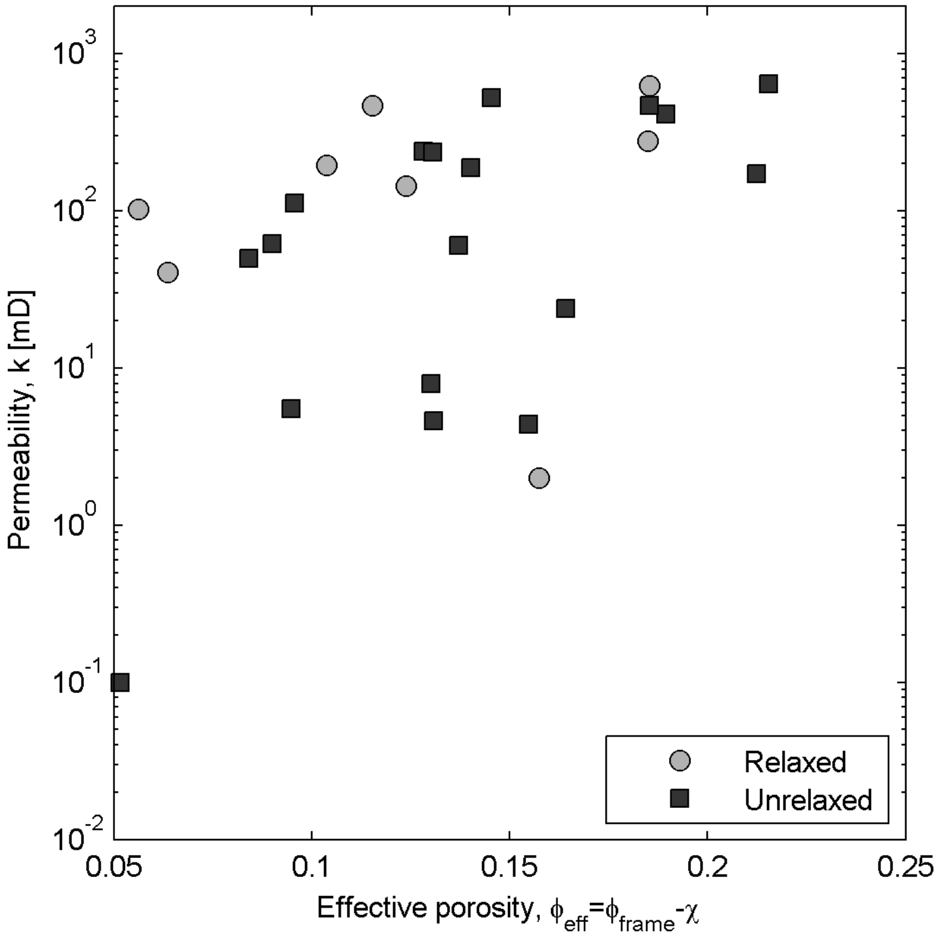

Figure 6.14: Cross-plot of effective porosity and permeability for the samples fitted to the clay-squirt model. Generally the relaxed samples are seen to have a higher permeability than the unrelaxed samples as expected. When the permeability increases pressure diffuses over longer distances

the permeability there will be a connection between low permeability and unrelaxed behavior although not stringent as it also depends on the inherent permeability of the clay assemblages.

6.9 Conclusions

We have presented a model capable of quantifying dispersion associated with local flow from compliant clay mineral assemblages. The approach is split into two idealized limiting geometries; shale laminae and completely dispersed shale. Depending on clay mineral bulk modulus and shale bulk modulus significant dispersion can be caused by clay-squirt. The relation to clay mineral moduli is opposite in the two geometries with the laminated clay-squirt increasing with decreasing clay mineral moduli and the dispersed clay squirt increasing with increasing clay mineral moduli. Clay-squirt dispersion from shale laminae reaches a maximum at intermediate shale fraction of about 0.2 while clay-squirt from dispersed shale increases monotonically with increasing shale fractions. A comparison was conducted with literature data for sandstones identified as having predominantly dispersed shale. Not all dispersion could be attributed to dispersed clay-squirt. A number of samples had excess dispersion. Excess dispersion compared to the dispersed model, was qualitatively shown to be compatible with clay-squirt from load-bearing shales. Some samples showed too little dispersion to be caused by clay-squirt. This discrepancy was possibly associated with difficulties in accessing the micro-porosity with the fluid during saturation preparation. For the samples compatible with clay-squirt we achieved a group of unrelaxed samples and a group of relaxed samples. The fitted shale frame moduli for the unrelaxed samples showed a correlation with the shale porosity albeit the moduli were higher than expected. Fitted clay mineral moduli for relaxed samples were not dependent on shale porosity. The magnitudes of the fitted moduli were consistent between the relaxed and unrelaxed states and literature values for clay minerals. Based on these observations it is feasible that a significant amount of dispersion in shale bearing sandstone may be associated with clay-squirt from the compliant porosity in the clay assemblages.

Chapter 7

Experimental procedures for sandstones with partial pore-filling clay

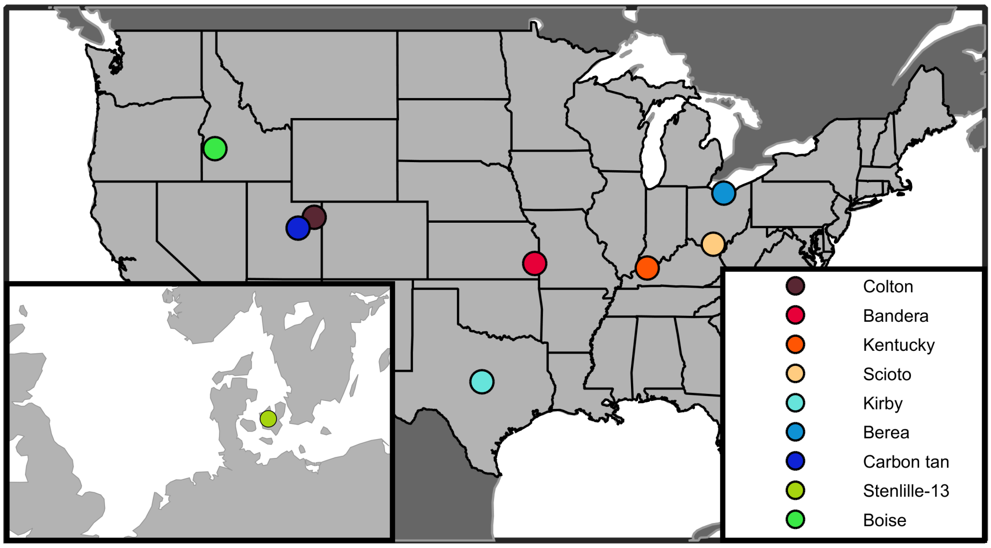

Figure 7.1: Outcrop and well site locations.

7.1 The samples

A suite of samples from 9 different locations is used in the study eight are from formations with outcrops in the continental USA and one is a jurassic sandstone core from the gas storage at Stenlille, Denmark. The location of the outcrops and the well is shown in Figure 7.1. The lithologies are chosen so as to be generally well consolidated and cover the permeability range commonly seen for sandstone reservoirs (Ehrenberg and Nadeau, 2005). Polished thin sections are prepared and backscatter scanning electron microscopy (BSEM) images are obtained, as seen in Figure 7.2 and Figure 7.3. These images illustrate the different characteristics of the lithologies which are classified according to the classification of Pettijohn et al. (1972) and are described as:

- **Colton sandstone** is a well consolidated medium- to fine-grained sub-arkosic arenite, with some carbonate cementation, and significant pore-filling clay. The BSEM in Figure 7.2(a) show the carbonate cementation, and abundant pore-filling clay.
- **Bandera** is a well consolidated fine-grained sub-arkosic arenite. The BSEM image seen in 7.2(b) shows dolomite cementation and some pore-filling clay.
- **Kentucky sandstone** is a well consolidated very fine-grained sub-arkosic arenite. The BSEM image seen in 7.2(c) shows the very fine-grains, feldspar, and pore-filling clay.
- **Scioto** is a well consolidated very fine-grained sub-arkosic arenite. The BSEM image seen in 7.2(d) shows the very fine-grains, feldspar, some mica, and little pore-filling clay.

- **Kirby** is a poorly sorted well consolidated fine-grained sub-arkosic arenite. The BSEM image in Figure 7.3(a) show weak carbonate cementation and little pore-filling clay mostly in form of kaolinite.
- **Berea** is a well consolidated medium- to fine-grained sub-arkosic arenite. The BSEM image in Figure 7.3(b) show mostly quartz grains with pore-filling kaolinite and small amounts of feldspar.
- **Carbon tan** is a well consolidated fine-grained quartz arenite with substantial carbonate cementation. The BSEM in Figure 7.3(c) shows carbonate cementation and pore-filling clay.
- **Stenlille-13** is medium grained poorly consolidated quartz arenite of Jurassic age. The BSEM in Figure 7.3(d) shows a clean quartz frame with little feldspar and no apparent clay.
- **Boise** is a medium to coarse grained arkosic arenite with quartz cementation. The BSEM in Figure 7.3(e) shows degraded feldspar grains and quartz grains.

7.2 Cleaning and routine core analysis

All plugs used are cleaned by soxhlet extraction first in methanol to remove salt and then in toluene to remove any hydrocarbon contamination. Side trimmings intended for characterization follow the same preparation procedure as the plug samples. When cleaned, the samples are oven dried for 48 h at 60 °C. The samples are then cooled down to ambient temperature (22 °C) in a dessicator for at least 24 h. Gas permeability is measured at 3 upstream pressures with a constant differential pressure at a confining pressure of 2.76 MPa (400 psi). From the gas permeabilities the Klinkenberg corrected permeability is determined. Any further reference to permeability in this analysis is the Klinkenberg corrected permeability. Grain volume is measured by helium expansion, and bulk volume measured by mercury immersion to yield the porosity and grain density.

7.3 Mercury intrusion capillary pressure, MICP

MICP is measured on trimmings of ≈ 3 g weight. The trimmings are dried at 60 °C for 48 h before measurement and allowed to cool. An intrusion curve is measured using a Quantachrome *Poremaster GT 33*, with a maximum injection pressure of 217 MPa (31500 psia). Giving a minimum pore-throat size measurable of ≈ 3 nm estimated by the Washburn equation (Washburn, 1921),

$$r_c = \frac{\gamma \cos(\theta)}{P_c}. \tag{7.1}$$

Where γ denotes the surface tension of mercury set to a value of 485 mN/m and θ is the contact angle of mercury set to 140° (Adamson and Gast, 1997).

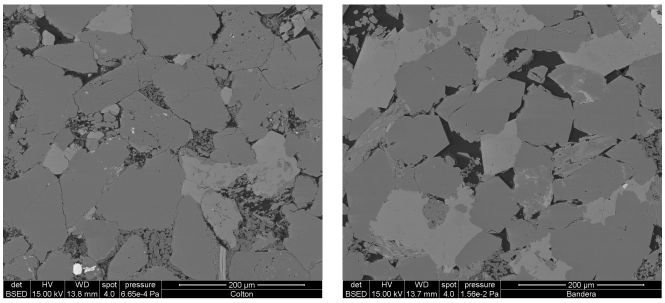
det HV WD spot pressure
BSED 15.00 kV 13.8 mm 4.0 6.65e-4 Pa
200 µm
Colton
det HV WD spot pressure
BSED 15.00 kV 13.7 mm 4.0 1.56e-2 Pa
200 µm
Bandera

(a) Colton sandstone: Quartz grains, with some carbonate cementation, feldspar, and abundant pore-filling clay

(b) Bandera sandstone: Quartz grains, dolomite cement, partially degraded feldspar, and pore-filling clay

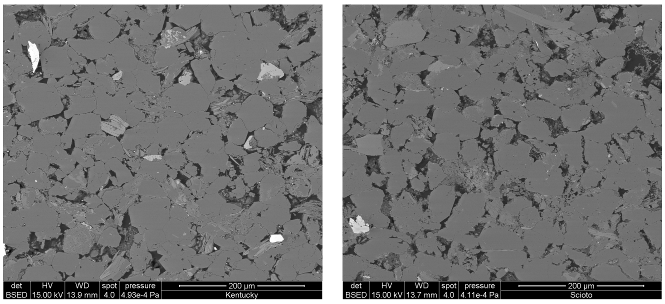
det HV WD spot pressure
BSED 15.00 kV 13.9 mm 4.0 4.93e-4 Pa
200 µm
Kentucky
det HV WD spot pressure
BSED 15.00 kV 13.7 mm 4.0 4.11e-4 Pa
200 µm
Scioto

(c) Kentucky sandstone: Quartz grains, with some feldspar and pore-filling clay

(d) Scioto sandstone: Quartz grains, mica, some feldspar, and pore-filling clay

Figure 7.2: Back-scatter SEM images of Colton, Bandera, Kentucky, and Scioto sandstones.

The capillary pressures measured from the MICP tests are converted from the mercury-air system to a air water system using the Leverett J-function,

$$J\left(S\right)=\frac{P\left(S\right)\sqrt{k/\phi}}{\gamma\cos\left(\theta\right)}. \tag{7.2}$$

This frunction $J\left(S\right)$ is constant for a given sample and allow determination of capillary pressures for different fluid systems characterized by their interfacial tension and contact angle. The parameters used for the mercury-air, and air-water system are: mercury-air $\gamma_{m-a}=485$ mN/m, $\theta_{m-a}=140$ °, $\gamma_{a-w}=72$ mN/m, $\theta_{a-w}=0$ °.

7.4 X-ray diffraction, XRD

A powder sample is prepared for each lithology and XRD diffraction is performed. First a scan is conducted from 2 ° – 65 ° measuring 2 s at 2θ angle intervals of 0.1 °. From

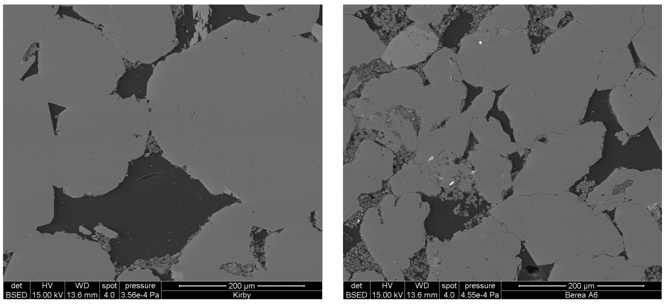
det
HV
WD
spot
pressure
BSED
15.00 kV
13.6 mm
4.0
3.56e-4 Pa
200 µm
Kirby
det
HV
WD
spot
pressure
BSED
15.00 kV
13.6 mm
4.0
4.55e-4 Pa
200 µm
Berea A6

(a) Kirby sandstone: Quartz grains, weak carbonate cementation, and little pore-filling kaolinite

(b) Berea sandstone: Quartz grains, little feldspar, some pore-filling clay

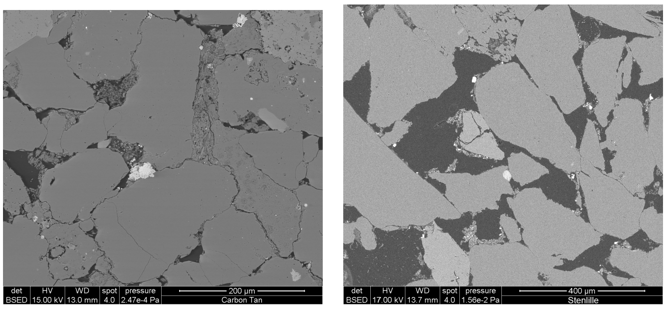
det
HV
WD
spot
pressure
BSED
15.00 kV
13.0 mm
4.0
2.47e-4 Pa
200 µm
Carbon Tan
det
HV
WD
spot
pressure
BSED
17.00 kV
13.7 mm
4.0
1.56e-2 Pa
400 µm
Stenlille

(c) Carbon tan: Quartz grains, some mica, and pore-filling clay

(d) Stenlille-13: Quartz grains predominantly, no apparent clay.

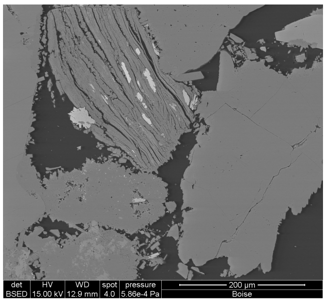
det
HV
WD
spot
pressure
BSED
15.00 kV
12.9 mm
4.0
5.86e-4 Pa
200 µm
Boise

(e) Boise: Quartz cemented, with abundant partially degraded feldspar

Figure 7.3: Back-scatter SEM images of Kirby, Berea, Carbon tan, Stenlille, and Boise sandstones.

this scan the constituents are identified and the relative quantity of these constituents are subsequently estimated by measuring the integrated amplitude recorded for selected peaks in the spectrum of the minerals and these are weighted by a correction factor. The peaks and their corrections factors are: Quartz (100), 0.25; K-feldspar (220), 0.1; Plagioclase (002) 0.1; Calcite (104) 0.076; Dolomite (104) 0.076; Clay minerals (020) 1.

7.5 Low-field NMR T_2 relaxation

Low field NMR measurements were carried out on all saturated samples to determine the transverse relaxation time, T_2, spectra. The instrument used was an Oxford GeoSpec2 NMR Core Analyser, operating at 2.0 MHz. The polarizing magnetic field, (B_0), was provided by a 49 mT permanent magnet oriented in the z-direction. The Carr–Purcell–Meiboom–Gill (CPMG) pulse sequence was used with an echo spacing of 50 µs and 32768 echoes. We recorded 32 scans with 0.75 s delay between scans. T_2 spectra were obtained by inverting the decays into 256 logarithmically spaced bins between 10 µs and 10^7 µs.

T_2 relaxation times are the combination of bulk relaxation, surface relaxation, and diffusion working in parallel. Theoretical and experimental studies show that T_2 relaxation times in sandstones are dominated by relaxation at the surface of the pores (Kenyon, 1997). Diffusion rearrange the pore-fluid such that hydrogen atoms are transported to the surface of the pores at which they decay. In sandstones the diffusion is commonly sufficiently fast relative to the surface relaxation time to keep a constant magnetization across the pore known as the fast diffusion limit. In the fast diffusion limit the T_2 relaxation rate is directly proportional to the ratio of pore surface to volume S/V, with the correlation parameter, ρ, termed the surface relaxivity,

$$\frac{1}{T_2} = \frac{\rho S}{V}. \tag{7.3}$$

7.6 Saturation preparation

Full saturation

De-aired distilled water and de-aired 3.5 wt% NaCl brine are used for saturation. Full saturation is achieved by vacuum and pressure saturation. Samples are dried at 60 °C for 24 h then placed in a vacuum dessicator, and a vacuum is applied for 24 h. The saturating fluid is then added to the container while under vacuum. When the samples are completely immersed a low vacuum is maintained for 24 h. The samples are then removed from the dessicator, placed in a pressure vessel filled with the saturating fluid and pressurized to 10 MPa for 48 h.

Controlled evaporative drying

Partial saturation is prepared by drying as this method may be used to prepare partial saturation below the irreducible water saturation seen for capillary invasion techniques such as centrifuging. In the saturation range $S_{w,irr} < S_w < 0.95$ evaporative drying of a porous medium is dominated by capillary transport to the surface and subsequent evaporation (Scherer, 1990). Since the redistribution of fluids are done by capillary transport the fluid distribution resembles that of drainage invasion (Le Bray and Prat, 1999). The partial saturations prepared by drying therefore resemble the saturation state found under drainage invasion of gas. Drying have previously been used to prepare partial saturations in sandstone (Knight and Nolen-Hoeksema, 1990; Goertz and Knight, 1998; Murphy, 1982). These authors have prepared partial saturation by drying keeping the relative humidity and temperature constant. The equilibrium state of drying under these conditions is the adsorption isotherm for the given sandstone at the specified temperature and humidity. Adsorption isotherms of sandstone depends on sandstone texture, but generally correspond to saturations less than $S_w = 0.1$ (Clark et al., 1980). Higher saturations can be achieved by stopping the process, but this saturation state will not be in equilibrium. Also simulations have shown that drying causes areas of the pore-space to be completely dry (Prat, 2007). Meaning that these regions are devoid of the water-film present in water-wet sandstones. In this study we therefore employ a drying scheme where partial saturation are achieved as equilibrium states at 100 % relative humidity. This is achieved by sealing the sample in a confined container of fixed volume. Water evaporates from the sample increasing the humidity until 100 % relative humidity. Condensation on the inner surface of the container will delay saturation of the air in the container, removing additional water from the sample. With the temperature, container volume, and container material kept constant, the loss of moisture, ΔV_f, is the sum of the volume of water condensed on the container surface, V_{surf} and the volume of water suspended as vapor in the container, V_{air}. This technique thus allow preparation of partial saturation by an iso-thermal evaporation terminating at 100 % relative humidity and with a controlled loss of fluid between each saturation step. The time allowed for equilibration is no less than 24 h. Saturation is determined by sample weight. Ultrasonic velocities are measured at every saturation step, and drying is continued until the bulk modulus of the partially saturated sandstone is reduced to the dry bulk modulus or the saturation becomes smaller than $S_w = 0.10$.

7.7 Sample loading and ultrasonic measurement techniques

Sample loading

Plugs of 37.5 mm in length and 37.5 mm in diameter are prepared with plane parallel ends. The plugs are loaded into the triaxial setup illustrated in Figure 7.4. Axial stress is applied to the top piston by a servo controlled 50 kN force actuator manufactured by GDS instruments. Radial stress is applied by a pump likewise manufactured by GDS instruments capable of applying 64 MPa through a Hoek-cell, as shown in Figure 7.4. The maximum axial stress applied to the samples is 40 MPa, chosen to be above the closure stress of frame weaknesses caused by unloading and coring. Samples are loaded

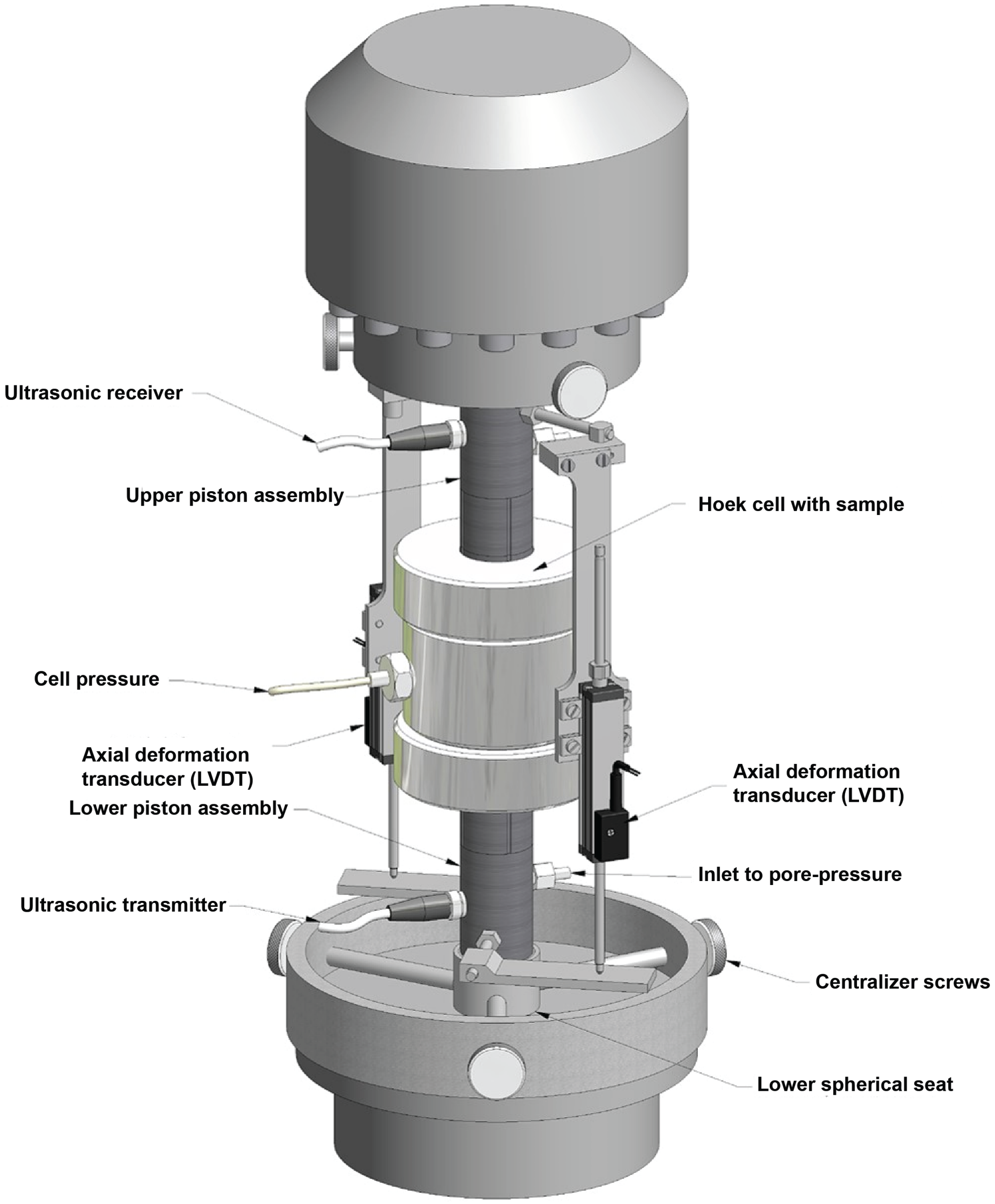
Ultrasonic receiver
Upper piston assembly
Hoek cell with sample
Cell pressure
Axial deformation transducer (LVDT)
Lower piston assembly
Axial deformation transducer (LVDT)
Inlet to pore-pressure
Ultrasonic transmitter
Centralizer screws
Lower spherical seat

Figure 7.4: The experimental assembly. The ultrasonic piezo transducers are housed in the end pistons. Axial stress is supplied by a servo controlled force actuator and radial stress by a hydraulic pump connected to a Hoek cell.

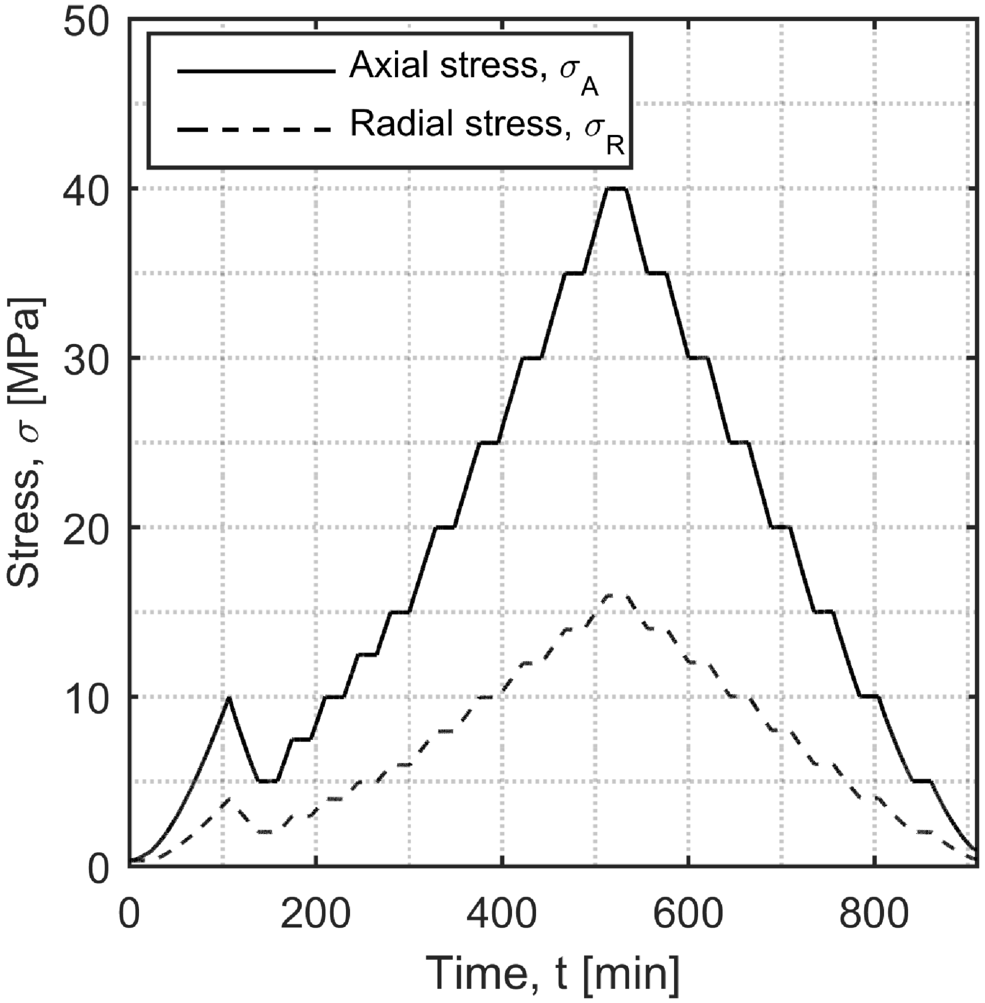

Figure 7.5: Example of the loading program followed for the samples. A constant rate of strain of 1 %/h is used and the ratio of axial to radial stress, $K0$ is determined by the dry Poisson's ratio.

at a constant rate of strain (CRS) of 1 % per hour, corresponding to 0.375 mm/h, the loading scheme is illustrated in Figure 7.5. A low stress settlement loop to 10 MPa is done before the actual loading. The ratio between axial and radial stress, $K0 = \sigma_R/\sigma_A$ is chosen in order to simulate compaction with no lateral deformation (i.e. constant cross-sectional area). The $K0$ ratio is estimated via the Poisson's ratio determined from dry ultrasonic velocity measurements, ν_{dry},

$$\nu_{dry} = \frac{V_p^2 - 2V_s^2}{2\left(V_p^2 - V_s^2\right)}. \tag{7.4}$$

From the Poisson's ratio $K0$ can be determined (Teeuw, 1971),

$$K0 = \frac{\sigma_R}{\sigma_A} = \frac{\nu_{dry}}{1 - \nu_{dry}}. \tag{7.5}$$

The $K0$ values used are in the narrow range $0.25 < K0 < 0.35$. At predetermined axial stresses loading is paused for 20 min to measure ultrasonic P- and S-wave velocity, only the measurements at 40 MPa will be used in this analysis.

Ultrasonic velocity measurements

Velocities are measured using an ultrasonic pulse-transmission method Birch (1960). Piezo-electric transducers housed in the pistons in Figure 7.4 compose the transmitter receiver pairs for P-wave and S-wave excitation. The transmitter is placed in the bottom piston and the receiver in the top piston. The central frequency of the P-wave signal is 200 kHz and for the S-wave the central frequency is 500 kHz, as obtained from fast Fourier transformation (FFT) of the received wave forms. A low loading rate is chosen to avoid any uncertainty introduced by sample relaxation under stress. A velocity measurement consists of two individual waveforms recorded with opposite polarity of the pulse sent to the transmitter. Each recorded wave-form consists of 1024 stacked and averaged wave forms. The final waveform is the average of the measurements at different polarity. Velocities are determined by first-break picking. A minimum of 4 independent measurement and first-break picks are conducted over a waiting time of at least 20 min at 40 MPa. The reported values in the analysis are the averaged values of the 4 measurements. The difference between individual measurements at each stress level was found to be unsystematic and within the uncertainty. The uncertainty associated with the picking procedure is 0.1 µs for P-waves and 0.5 µs for S-waves. Length is measured within an uncertainty of 0.25 mm. By the variance formula the uncertainty of V_p and V_s is 1 % and 1.5 % respectively. The repeated measurements have been used to reduce the uncertainty on the arrival time.

Gassmann fluid substitution

Gassmann fluid substitution are a set of phenomenological relations linking the moduli where the fluid are allowed to escape under compression, (K_{frame}, G_{frame}) with the moduli where no fluid is allowed to escape, (K_{sat}, G_{sat}) (Gassmann, 1951). In the undrained case a finite pore-pressure is induced. Fluid substitution requires input of the mineral bulk modulus, K_0, the fluid modulus, K_f, and the porosity, ϕ, Bourbié and Coussy (1987)

$$K_{sat} = K_{frame} + \alpha^2 F, \tag{7.6a}$$

$$G_{sat} = G_{frame}, \tag{7.6b}$$

where

$$\alpha = 1 - \frac{K_{frame}}{K_0}, \qquad 1/F = \frac{\alpha - \phi}{K_0} + \frac{\phi}{K_f}$$

. Gassmanns equations are exact if the mineral frame is homogeneous (mono-mineralic), the frame modulus is unaltered by saturation, and a uniform pore pressure is induced in the undrained state. Generally sandstones do not comply to these assumptions, but the violations can be remedied with effective extensions. Sandstones are rarely mono-mineralic as in addition to quartz significant fractions of feldspar, carbonate, and clay are common. In such poly-mineralic frames fluid substitution can be done using an effective mineral modulus formulated as an average of the constituent mineral moduli as long as these are of same order of magnitude (Mavko and Mukerji, 2013; Knackstedt et al., 2005). Generally a Voight-Reuss-Hill (VRH) average is applied. In this study we will apply the slightly narrower bounds defined by the Hashin-Shtrikman bounds (Hashin and Shtrikman, 1963).

For mixed saturation a set of upper and lower bounds can be formulated as a function of saturation. The upper bound is defined as where there is different induced pressure in isolated regions saturated with the different fluids. Assuming that the shear modulus does not depend on saturation the bulk modulus at the upper bound, K^+, is determined via an harmonic average of the compressional modulus of the patches, (Hill, 1963)

$$K^+ = \left\langle \frac{S_i}{K_i + 4/3G} \right\rangle^{-1} - 4/3G. \tag{7.7}$$

The subscript i denotes a specific fluid phase and the angles signifies an average weighted by the saturation of the fluid phase, S_i. The bulk moduli of the specific patches can be achieved by Equation 7.6a.

The lower bound is determined as the fluid substitution to a saturation of an effective fluid, S_i, with modulus given by the harmonic Reuss (iso-stress) average of the fluid moduli $K_{f,i}$ (Mavko and Mukerji, 1998),

$$\frac{1}{K_f^{eff}} = \left\langle \frac{S_i}{K_{f,i}} \right\rangle. \tag{7.8}$$

Chapter 8

Characterization results: the influence of clay on the pore-space

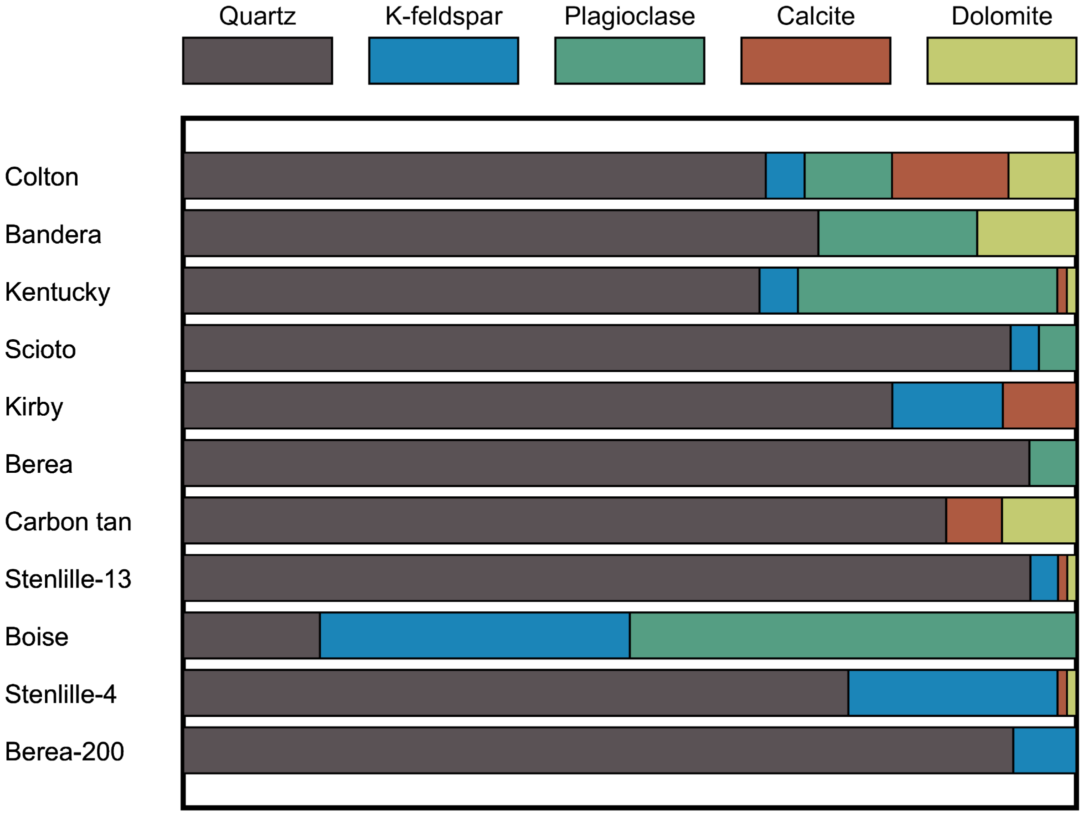

Figure 8.1: Graphical depiction of the fractional composition of the solid mineral frame as determined from semi-quantitative XRD. The result obtained for the whole of the solid material (including clay) is tabulated in Appendix A.

8.1 X-ray diffraction and mineral moduli

The mineral composition obtained from semi-quantitative XRD analysis are given in Appendix A and depicted in Figure 8.1. Most lithologies contain significant amounts of feldspar and carbonate. We use the mineral moduli listed in Table 8.1 to determine the effective mineral moduli, as described in Section 4.3. The moduli in Table 8.1 are approximated as the mean of the Hashin-Shtrikman bounds based on the full stiffness tensor measured for a single crystal (Brown, 2014).

The amount of solid clay estimated to be present in each lithology, per bulk volume of rock is shown in Figure 8.2. It is the explicit assumption that for the lithologies investigated have only pore-filling clay.

Significant fractions of clay ($x_{clay} > 5\ \%$) are found in Colton, Bandera, Kentucky, and Scioto. Berea and Carbon Tan have some clay as well while Stenlille, Kirby, and Boise have little clay. The mineralogical composition determined from XRD are given in

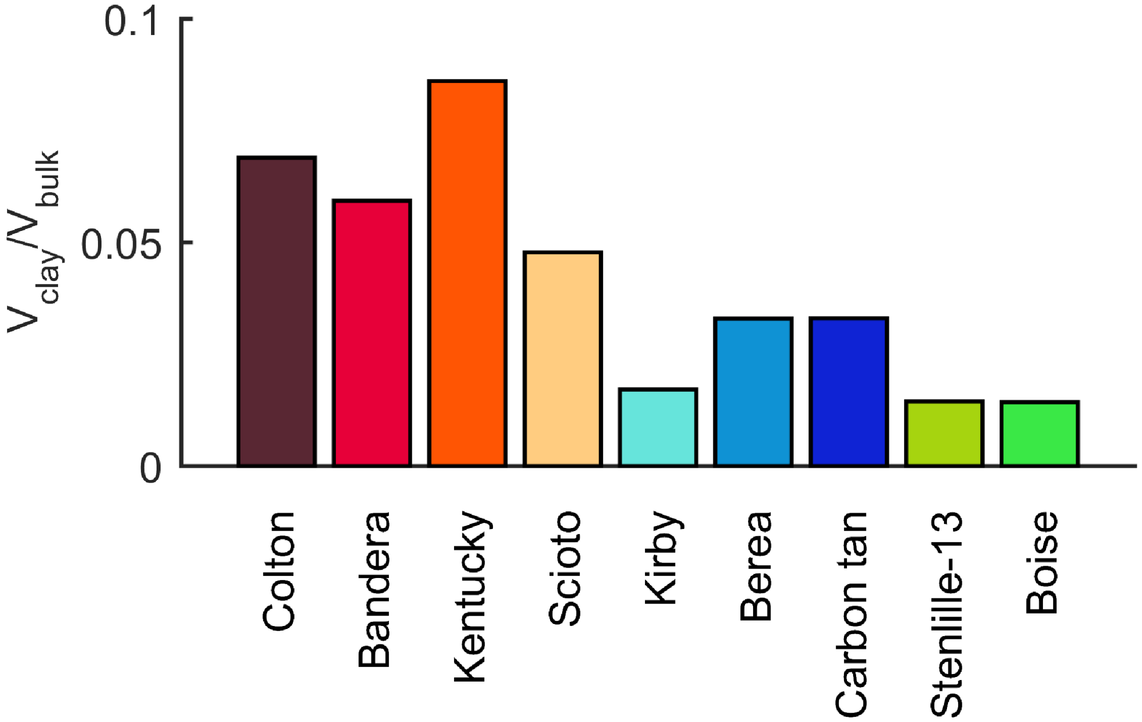

Figure 8.2: Fraction of clay found in the nine lithologies relative to the bulk volume of the rock. Colton, Bandera, Kentucky and Scioto are seen to have appreciable clay contents.

fractions of the total solid material. As clay is assumed not to be incorporated in the frame the measured fraction is corrected. The solid frame consists of the solid material minus the solid fraction of clay, x_{clay}. The fraction of the frame composed by mineral i, given by x_i is determined as,

$$x_{i,load} = \frac{x_i}{\sum_i x_i - x_{clay}} \tag{8.1}$$

We compute Hashin-Shtrikman bounds for the mineral moduli using the constituent moduli in Table 8.1 and the fractions normalized to the load-bearing frame (Berryman, 1995). The effective mineral moduli are plotted in Figure 8.3 relative to the mineral moduli of quartz. The difference in the upper and lower Hashin-Shtrikman bounds is very small, but the change in absolute mineral modulus from that of quartz is significant. The average of the Hashin-Shtrikman bounds is tabulated in Table 8.2 and will be used as effective mineral moduli for the respective lithologies henceforth. The effective superscript is dropped and references to the mineral moduli means the effective mineral moduli from Table 8.2.

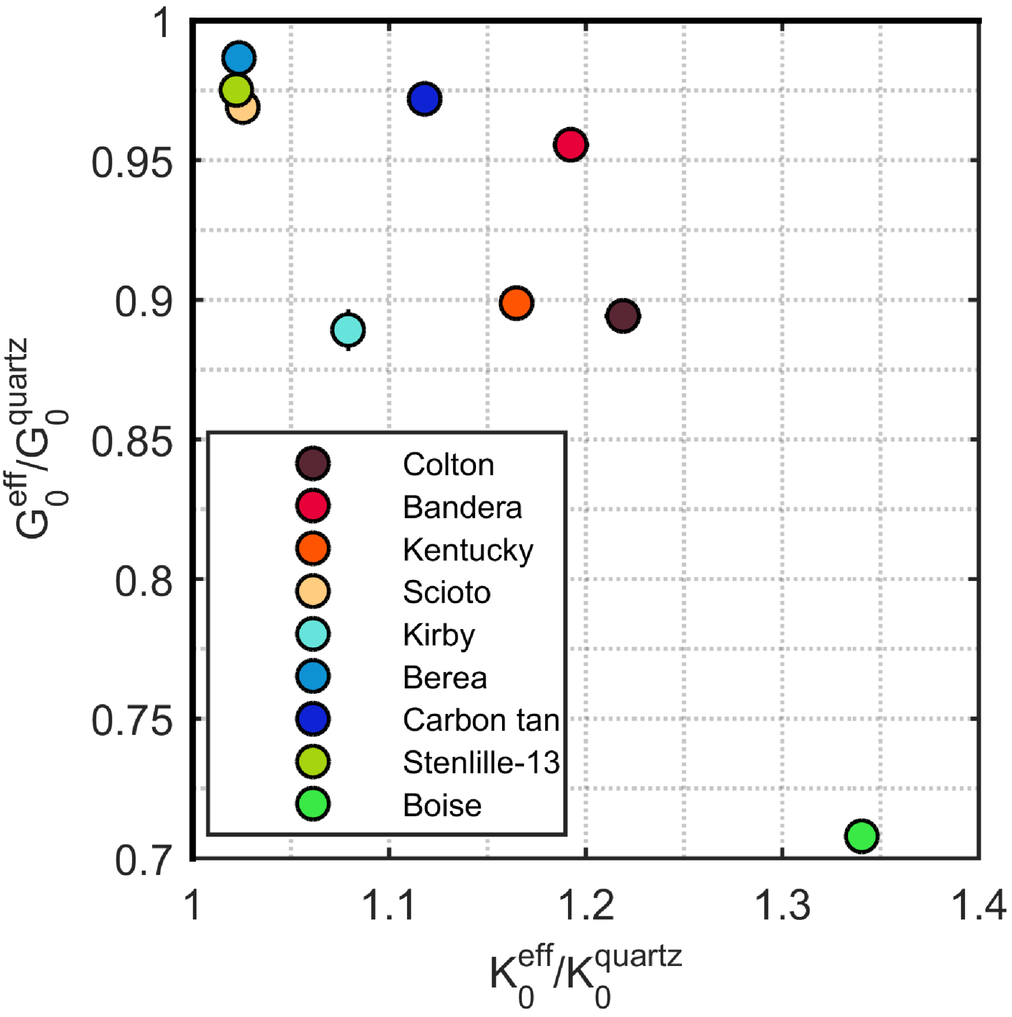

Figure 8.3: Effective mineral modulus determined as Hashin-Shtrikman bounds of the constituent moduli identified by semi-quantitative XRD analysis relative to the mineral moduli of pure quartz. Markers indicate the bound average and lines indicate the magnitude of the bounds, for most lithologies the marker-size covers the bounds. The effective mineral bulk modulus is universally higher than quartz while the effective mineral shear modulus is lower.

Mineral	Bulk modulus K_0, [GPa]	Shear modulus G_0, [GPa]	Source
Quartz	38	45	(Koga et al., 1958)
K-feldspar (Perthite)	47	24	(Carmichael, 1989)
Plagioclase (Albite)	59	35	(Brown et al., 2006)
Calcite	70	29	(Peselnick and Robie, 1963)
Dolomite	95	45	(Humbert and Plicque, 1972)

Table 8.1: Mineral moduli used for determining the effective mineral modulus based on the semi-quantitative XRD analysis.

Lithology	K_0^{eff}, [GPa]	G_0^{eff}, [GPa]	M_0^{eff}, [GPa]
Colton	46	40	100
Bandera	45	43	103
Kentucky	44	40	98
Scioto	39	44	97
Kirby	41	40	94
Berea	39	44	98
Carbon tan	42	44	101
Stenlille	39	44	97
Boise	45	37	94

Table 8.2: Effective mineral moduli determined as the average of the Hashin-Shtrikman bound based on the relative fractions determined by XRD analysis

8.2 Porosity and permeability

Figure 8.4 shows a cross-plot of the measured porosity and permeability. Curves based on the Kozeny-Carman relation for a specific characteristic pore-size is added to Figure 8.4 (Carman, 1937). Points connected by these lines have similar effective pore-size, and the change in permeability is caused by changing porosity. All lithologies have a close clustering of porosity and permeability. Out of the nine lithologies two (Stenlille, Boise) have high porosity, $\phi > 0.15$, and the remaining seven have intermediate porosity $(0.12 < \phi < 0.18)$. The permeability of the samples range from 0.3 mD to 1.5 D. Three groups are apparent from Figure 8.4; 1. Colton, Bandera, Kentucky, and Scioto have intermediate porosity and low permeability ($k < 10$ mD), 2. Kirby, Berea, and Carbon tan have intermediate porosity and permeability (10 mD $< k <$ 100 mD), 3. Stenlille, and Boise have high porosity and permeability ($k >$ 100 mD). Comparing these groups with the mineral composition in Figure 8.1 indicates that the lithologies with low permeability are those with a high clay fraction identified by XRD analysis. Pore-filling clay is often found to have detrimental effect on the permeability.

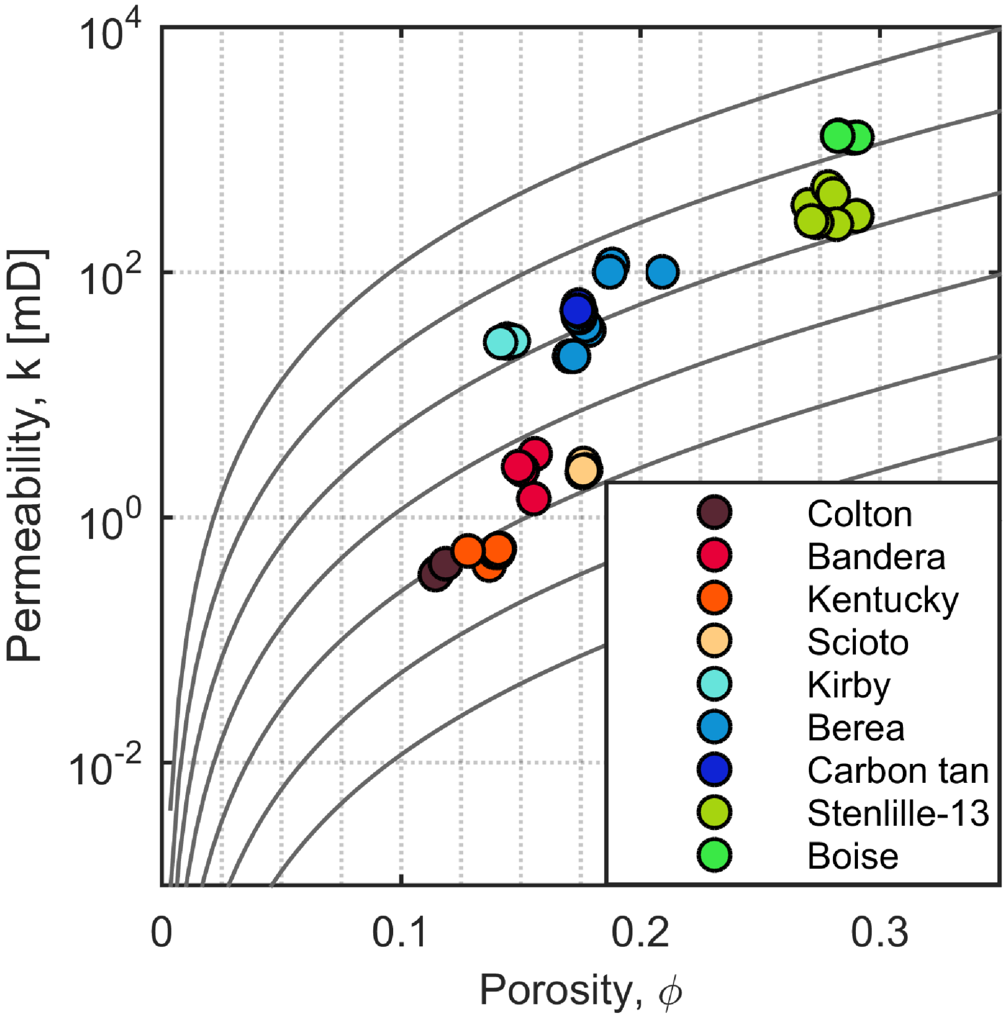

Figure 8.4: Cross-plot of porosity and permeability for all samples used in the study. Curves of equal pore-size are added based on the Kozeny-Carman relation.

8.3 Mercury injection capillary pressure

Figure 8.5 and Figure 8.6 show MICP curves translated to air-water capillary curves. The pore-volume of the samples used for the MICP measurement are calculated from the measured porosity from routine core analysis and the bulk volume of the sample. The maximum injected volume of mercury is compared to the total pore-volume quantifying the volume of pore-space not invaded by the mercury. This volume is not accessible due to either narrow pore-throats or areas isolated by the percolation of the mercury.

The volume not invaded by mercury is closely related to the irreducible water saturation, $S_{w,ir}$ and we estimate the irreducible water saturation based on the difference between the maximum volume of mercury injection and the pore-volume present in the sample,

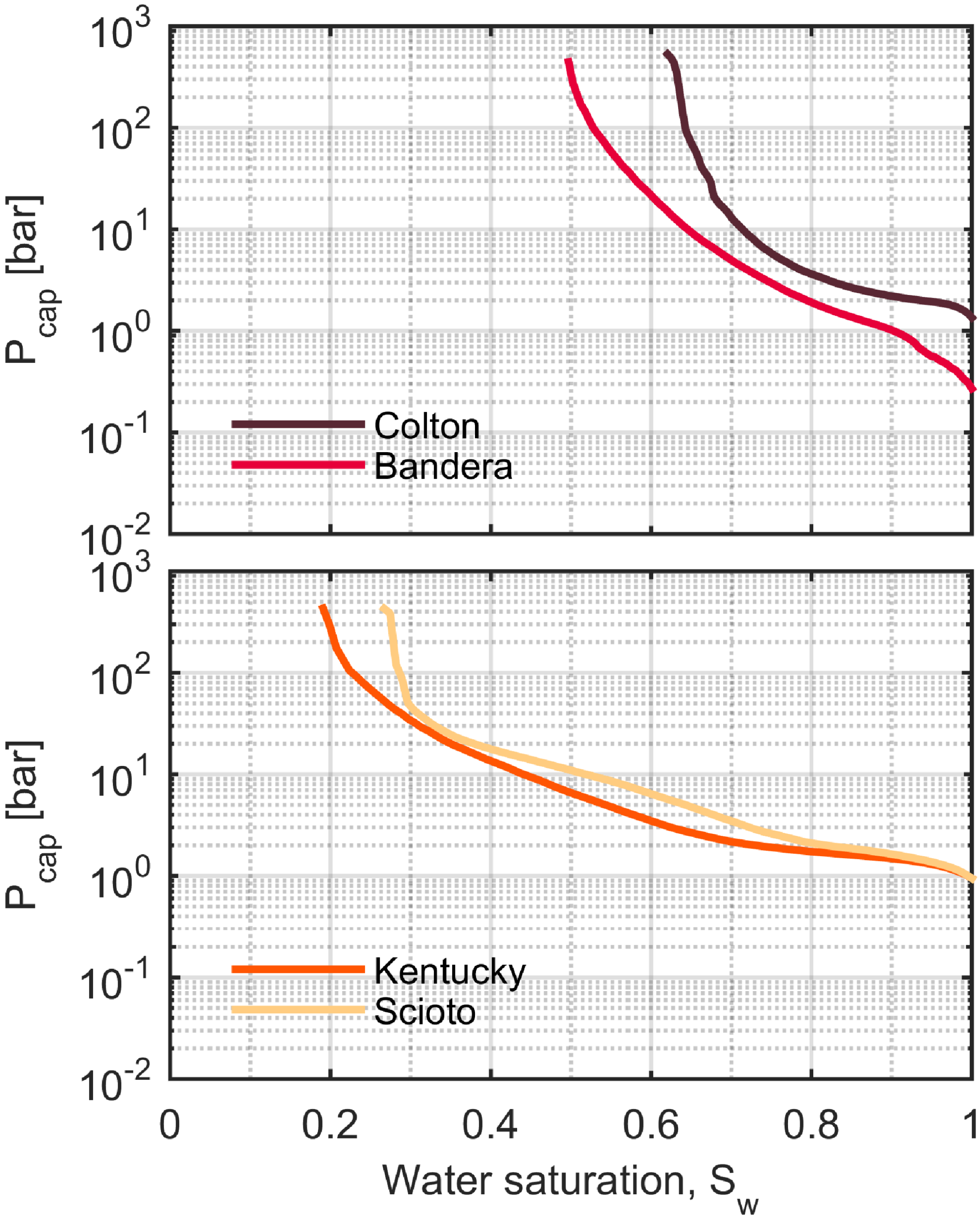

Figure 8.5: Capillary curves recorded by MICP for Colton, Bandera, Kentucky, and Scioto. Lithologies are grouped from top to bottom in order of increasing permeability as may be seen by comparison with Figure 8.4.

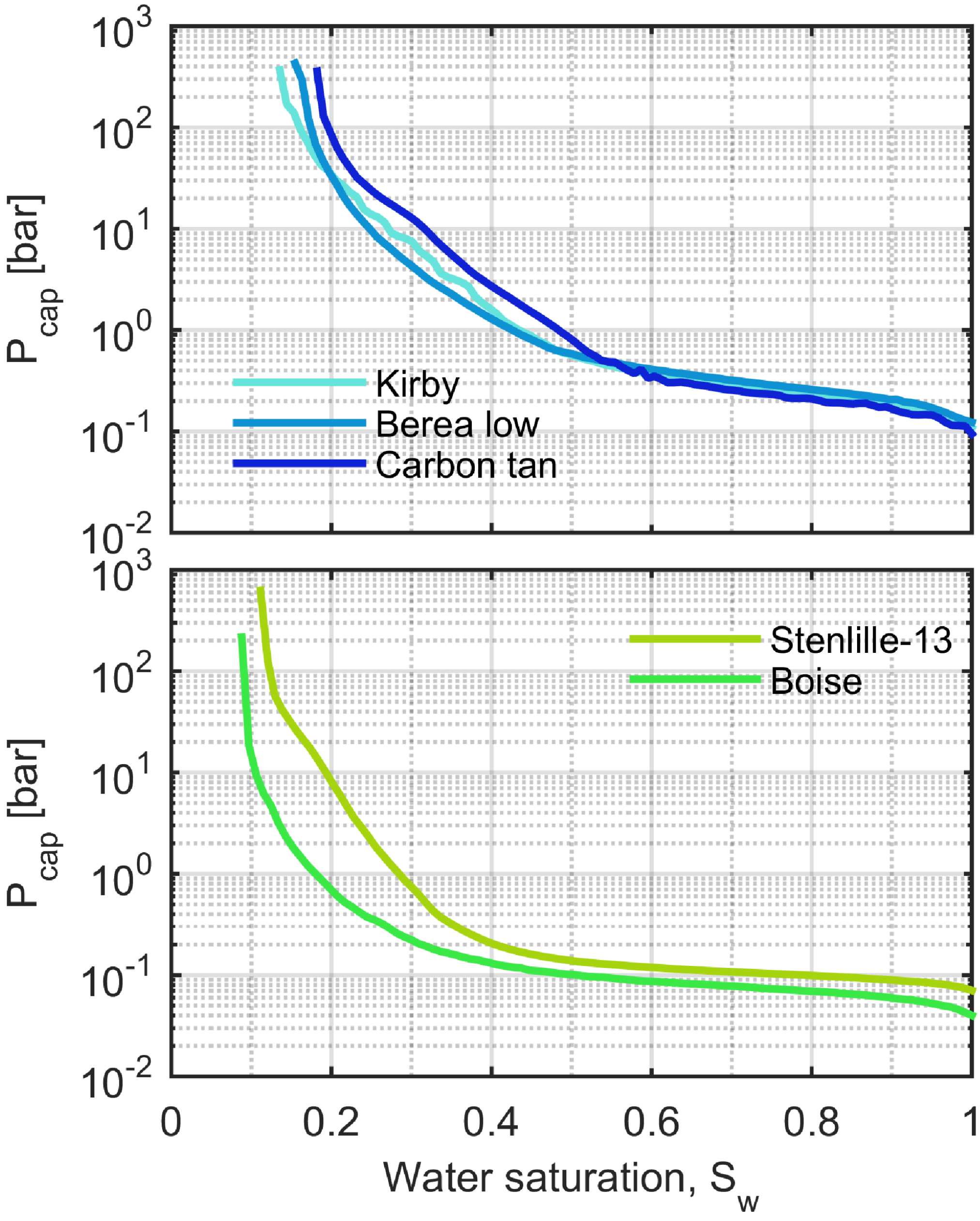

Figure 8.6: Capillary curves recorded by MICP for Kirby, Berea, Carbon tan, Stenlille, and Boise. Lithologies are grouped from top to bottom in order of increasing permeability as may be seen by comparison with Figure 8.4.

Lithology	S_w^5	S_w^{10}	S_w^{20}	$S_{w,ir}$
Colton	0.76	0.71	0.68	0.62
Bandera	0.70	0.65	0.60	0.51
Kentucky	0.54	0.44	0.35	0.19
Scioto	0.64	0.52	0.38	0.27
Kirby	0.32	0.27	0.24	0.14
Berea	0.29	0.25	0.22	0.15
Carbon tan	0.36	0.32	0.26	0.18
Stenlille	0.22	0.19	0.17	0.11
Boise	0.12	0.11	0.10	0.03

Table 8.3: $S_{w,ir}$ estimated from comparison of injected mercury volume and total pore-volume.

$$S_{w,ir} = \frac{V_{mercury}^{max}}{V_p}. \tag{8.2}$$

This definition of irreducible water saturation in effect assumes an infinite capillary pressure. $S_{w,ir}$ for the nine lithologies are listed in Table 8.3. The values attained for the irreducible water saturation may be less than those attained by other methods, as centrifuging. We therefore also determine the water saturation at 5 bar, 10 bar, and 20 bar listed in Table 8.3. The slope of the capillary curves is evident from the saturations in Table 8.3, Kentucky, and Scioto have large pore volumes invaded at air-water capillary pressure of ≈ 10 bar. Whether or not a set of pores remain unrelaxed during the oscillation of a wave depends on the fluid mobility and hence the indirectly the capillary pressure. Pores with a capillary entry pressure of ≈ 10 bar have a equivalent tube diameter of about 1 µm. These pores may or may not be unrelaxed depending on their geometrical extent. Scioto, and Kentucky are the only lithologies that have a significant porosity in this intermediate region, the other lithologies either have smaller or large pores.

8.4 Low-field NMR spectra for fully saturated samples

Low field T_2 relaxation spectra recorded for a fully saturated sample of each lithology, are shown in Figure 8.7. The fraction corresponding to the irreducible water saturation estimated from MICP, $S_{w,ir}$, is colored in black and the effective porosity in blue. The T_2 spectra in Figure 8.7 are related to the the pore-size distributions of the lithologies. T_2 relaxation times above ≈ 35 ms are associated with large inter-granular porosity, T_2 times between 5 ms and 35 ms are associated with small pores as between clay sized particles, and T_2 times below 5 ms are associated with surface bound water in clays (Chitale et al., 1999; Matteson et al., 2000). These regions are shaded by gray in

Figure 8.7. Irreducible water saturation is identified from T_2 spectra using a threshold T_2. Standard thresholds with the 35 ms cut-off for small inter-clay pores are commonly used, but lithology specific calibrations from cores desaturated by centrifuging yields a range with extremes from 10 ms to 700 ms (Coates et al., 1998). Figure 8.7 shows the 35 ms threshold is inconsistent with $S_{w,ir}$ from MICP. The irreducible saturations all fall in T_2 region signifying capillary bound water or surface bound water. Bi-modal spectra are seen for Colton, Kentucky, Carbon tan, and Stenlille, whereas Bandera have a tri-modal distribution. The remainder of the lithologies have a single mode with a long tail to low T_2 values. Colton, Bandera, Kentucky, and Carbon Tan have the highest fraction of solid clay (Figure 8.2). The mode at low T_2 is likely associated with pores dominated by clay. Clays have a have a large specific surface and therefore provide an efficient way for relaxation of the spin alignment. Diffusion may have time to occur from effective porosity to clay dominated pores, shifting signal into the lower T_2 bins by allowing the protons from larger pores to be relaxed at the clay surface (Anand et al., 2008).

Figure 8.8 shows T_2 distributions measured during drying. The same shading corresponding to the generic classification of pore morphology in Figure 8.7 is applied to Figure 8.8. The development of the T_2 spectrum during de-saturation depends on the texture of the pore-space. Residual saturation during de-saturation can be found in capillary blocked pores or it may be adhering to the mineral surfaces, as illustrated in Figure 8.9. A simple T_2 cut-off definition of $S_{w,ir}$ assumes only the bi-modal de-saturation model. Data published in the literature indicate a combination of the two (Kleinberg and Boyd, 1997; Chen et al., 1998; Kenyon, 1997). The development of the T_2 spectra as a function of de-saturation indicates the distribution of the fluids. Scioto have nearly no shift in T_2 during de-saturation, while Colton shifts the main mode to significantly lower T_2. The development of Scioto is indicative of de-saturation following the film model i.e. where the wetting and the gas phase occupy the same pores, the behavior of Colton is indicative of the bi-modal model. In the film model the reduction of water volume reduces T_2 according to Equation 7.3, but the new T_2 is not associated with a pore-size merely the same pores with less water (Talabi and Blunt, 2010). De-saturation according to the film model introduces signal in T_2 bins which are not present in the original spectrum. This is seen most clearly for Boise, which develops an increase in the amplitude of T_2 bins lower than the main mode in the fully saturated state. Contrary to de-saturation by the film model de-saturation in the bi-modal model will shift the main mode to a T_2 mode already observed in the fully saturated spectrum. The change in relative magnitude of the two modes will appear as a reduction in T_2. Based on this rationale we interpret the T_2 spectra under de-saturation to indicate that Colton, Bandera, Kentucky, and Carbon tan have distinct porosity entities which remain saturated during de-saturation. At sufficiently low saturation the secondary mode is completely established and the reduction of the dominant T_2 modes ceases. After this point the de-saturation proceeds to empty the secondary mode following the film model.

The primary mode T_2 value for Kirby, and Berea is reduced under de-saturation, but the primary mode T_2 shifts along the tail of the T_2 spectrum and not to any distinct secondary mode.

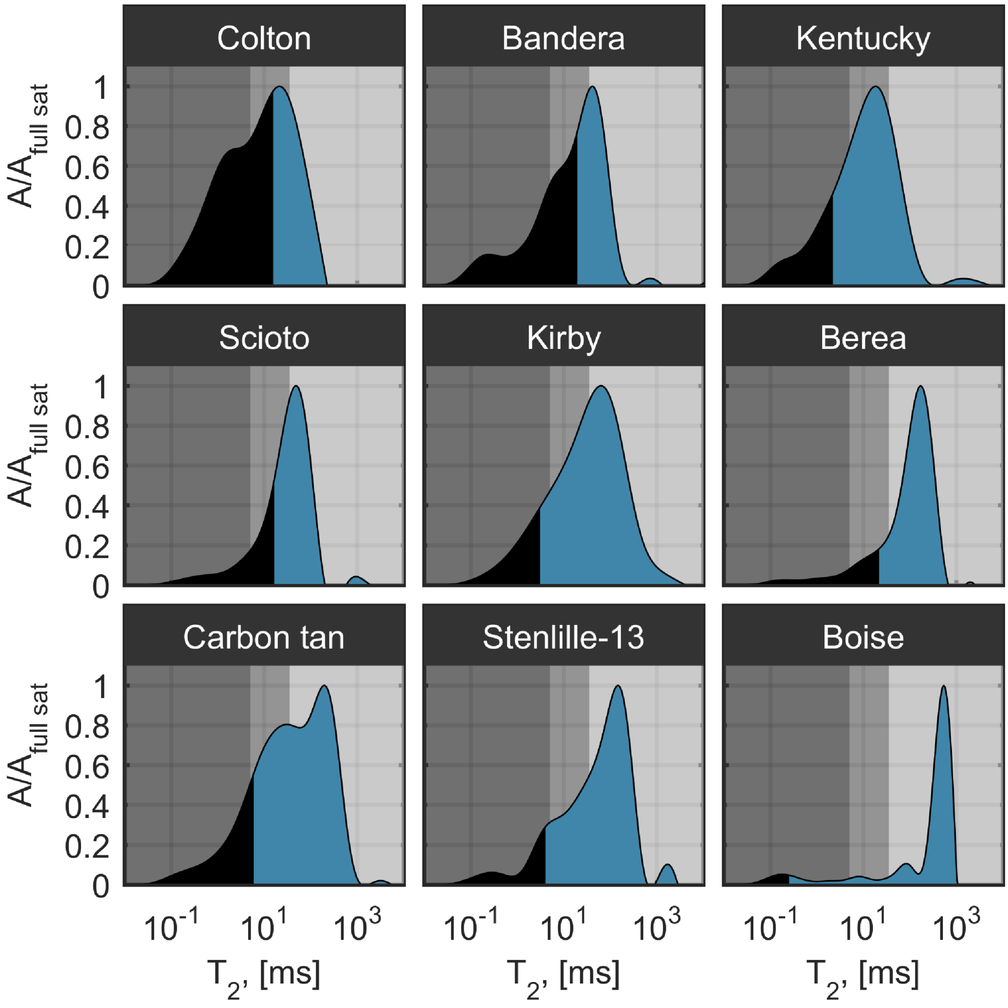

Figure 8.7: Low-field NMR T_2 spectra obtained for fully saturated samples of the nine lithologies. A generic T_2 region for clay bound water is shaded by dark gray, a T_2 region associated with clay inter-particle porosity is medium gray, and inter-granular porosity is light gray. The irreducible water saturation from MICP is marked by black shading.

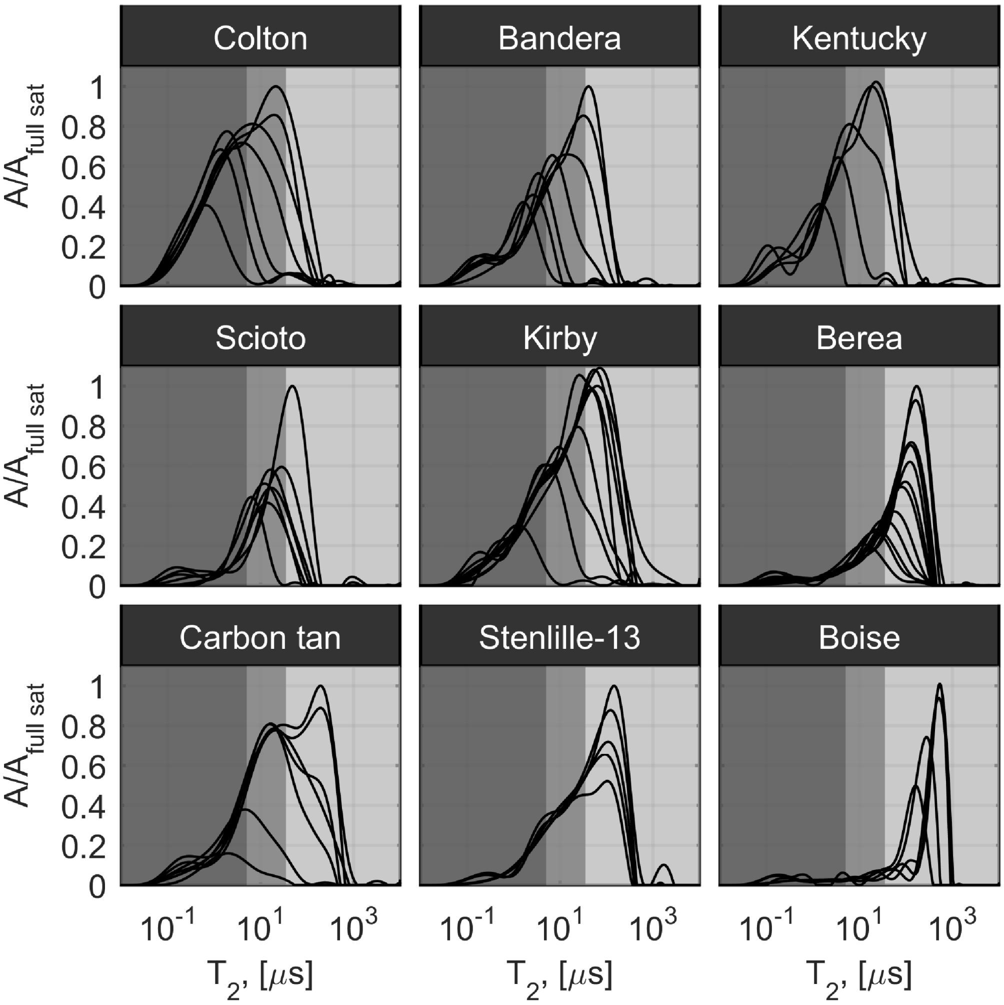

Figure 8.8: The development of low-field NMR T_2 distributions for the nine lithologies under drying. A generic T_2 region for clay bound water is shaded by dark gray, a T_2 region associated with clay inter-particle porosity is medium gray, and inter-granular porosity is light gray.

Scioto, Stenlille, and Boise have only limited shift of their primary T_2 mode during de-saturation, indicative of a film model de-saturation. The primary T_2 mode of Boise have the largest shift seen for film model de-staturation during the first saturation step. There is no reason to assume that the thickness of the water film present will depend on the size of the pore. Therefore the largest pores will experience the largest relative reduction in water volume when air enters the pore. Boise has very large pores as evident from the capillary pressure, therefore Boise is likely to experience the largest reduction in T_2 when air enters the pores.

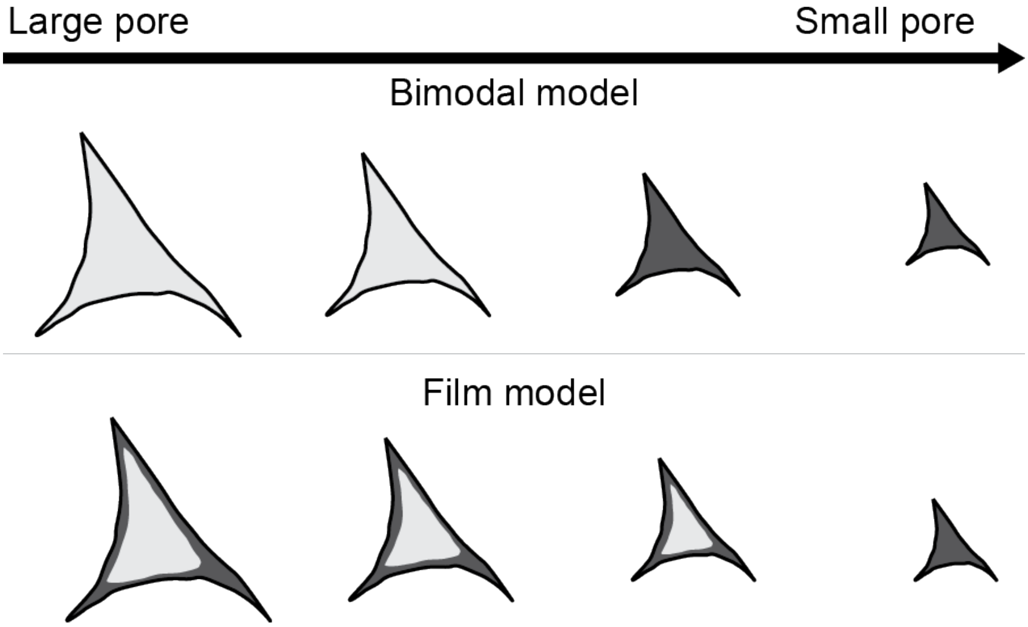
Large pore
Small pore
Bimodal model
Film model

Figure 8.9: Illustration of the two distributions of partial saturation. In the bimodal model an invading non-wetting phase effective displace water from the larger pores. In the film model water remains present in significant quantities in the larger pores as a fluid film on the surface of the minerals.

Chapter 9

Clay distribution effect on ultrasonic velocities and moduli

9.1 Dry and fully saturated velocities

Figure 9.1 shows the ultrasonic velocities measured at 40 MPa with no fluid saturation. The dry P-wave velocities exhibit a tight pattern for the individual lithologies except for Kirby which have a larger spread of P-wave velocities. Kirby also have significantly higher velocities than the other lithologies at the same porosity, indicative of a higher degree of cementation. The samples identified by XRD and BSEM to be more affected by clay (Colton, Bandera, Kentucky) have P-wave velocities significantly below the MUHS bound. The Kirby sandstone is cemented to a higher degree than the other lithologies in this porosity section. The high-porosity lithologies (Boise and Stenlille) have P-wave velocities consistent with the MUHS bound. S-wave velocities are clustered for the individual lithologies. Figure 9.2 shows a cross-plot of the saturated shear wave velocities versus compressional wave velocities. The position of the data in Figure 9.2 reflects the V_p/V_s ratios. The data are all to the left of the correlation by Han et al. (1986). The V_p/V_s ratios are thus higher than expected from the data of Han et al. (1986). The lithologies with low shale contents are actually better described by the mud-rock line, given by the punctuated line, and the more shaly lithologies have even higher V_p/V_s. The data of Han et al. (1986) are measured at hydrostatic stress, whereas the measurements in this study are done at zero lateral deformation. The influence of the different stress states is investigated by measuring dry velocities in a Berea sample as a function of $K0$ at 40 MPa axial stress. Figure 9.3 shows the dry P-wave velocity versus S-wave velocity for different values of $K0$. The S-wave velocity is increase significantly with the applied radial stress while the P-wave velocity only changes slightly. S-waves are polarized in parallel to the radial stress direction and perpendicular to the axial stress, increasing $K0$ means increasing the radial stress and increasing the stress on grain contacts in direction of S-wave polarization, causing significant increase of the S-wave velocity. The difference in V_p/V_s as a function of stress-path questions the assumption of isotropy. Sandstones in an unstressed state are often reported to be weakly anisotropic (Wang, 2002). Yin (1992) and Sayers et al. (1990) found Berea sandstone to be transversely isotropic at low stress, but to develop isotropy at an axial to radial stress ratio of $K0 \approx 0.4$. Further loading perpendicular to the bedding at constant radial stress (i.e. decreasing $K0$) caused cracks to open parallel to the applied stress. The $k0$ applied in this study is aimed to mimic the in-situ stress thought to remain as an imprint in the sandstone framework expressed by the poisson's ratio. The $K0$ obtained from the dry Poisson's ratio is close to the 0.4 found by Yin (1992) and Sayers et al. (1990) to produce isotropy. Although the aim of these studies were not to determine the stress state closest to the in-situ state, we take the coincidence of the $K0$ achieving isotropy and the $K0$ corresponding to zero lateral deformation, to mean that this stress state is closer to the stress state under which the rock formed. Hereby the isotropy is likely to be smaller at the stress state applied in this study than the commonly applied hydrostatic stress. The anisotropy observed at $K0 < 0.4$ may be due to coring and stress release (Holt et al., 2000).

Anisotropy of sandstones may be the imprint of an in-situ stress. Applying the appropriate $K0$ could reduce any observed anisotropy. We assume the anisotropy of the lithologies to be at most comparable to those reported for sandstones (commonly about 2 %) (Wang, 2002). As such we deem the influence of anisotropy to be insignificant and proceed with the analysis as though the samples are isotropic.

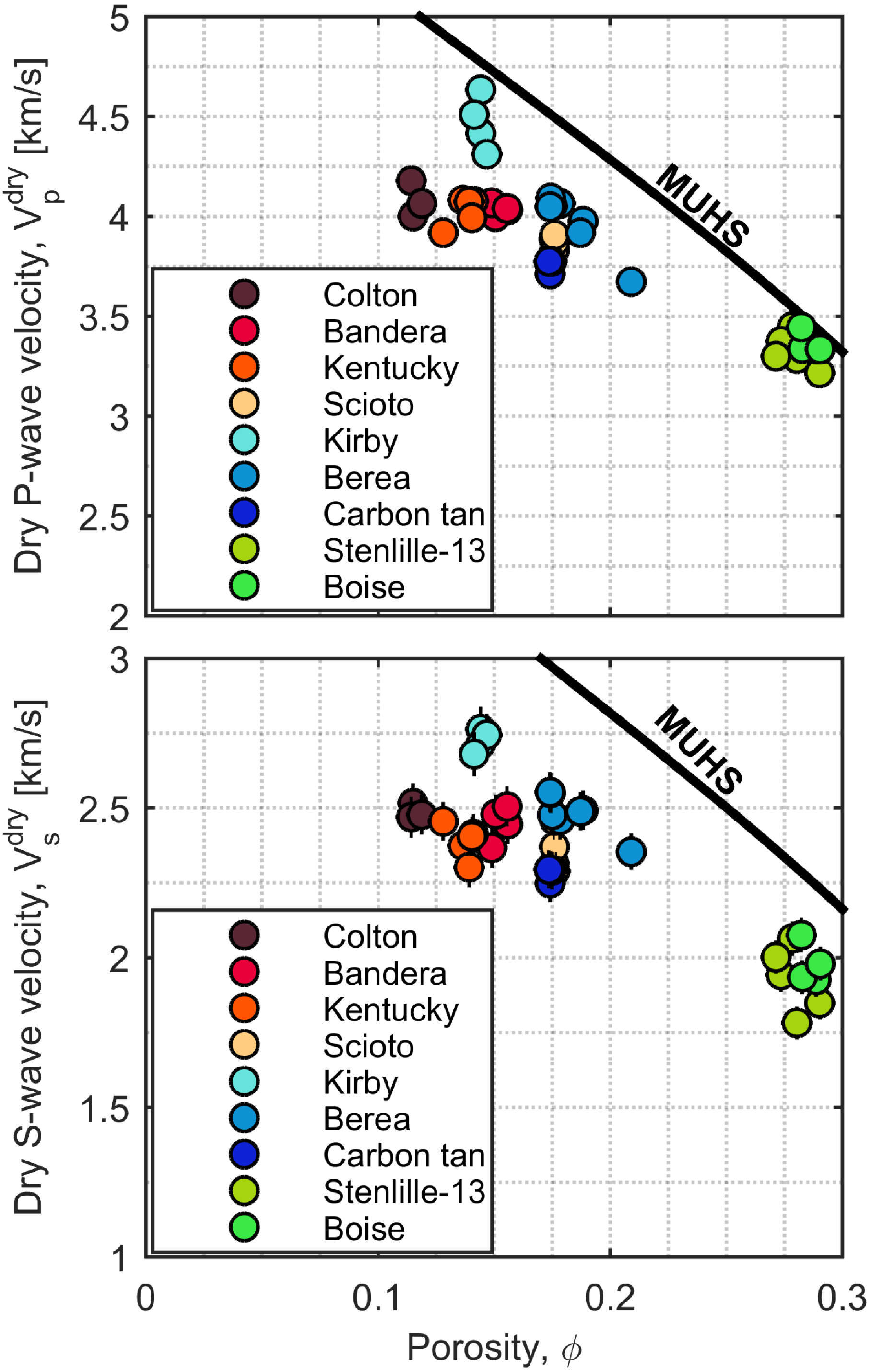

Figure 9.1: P-wave velocity and S-wave velocity for the dry samples as a function of porosity, plotted along with the MUHS bound.

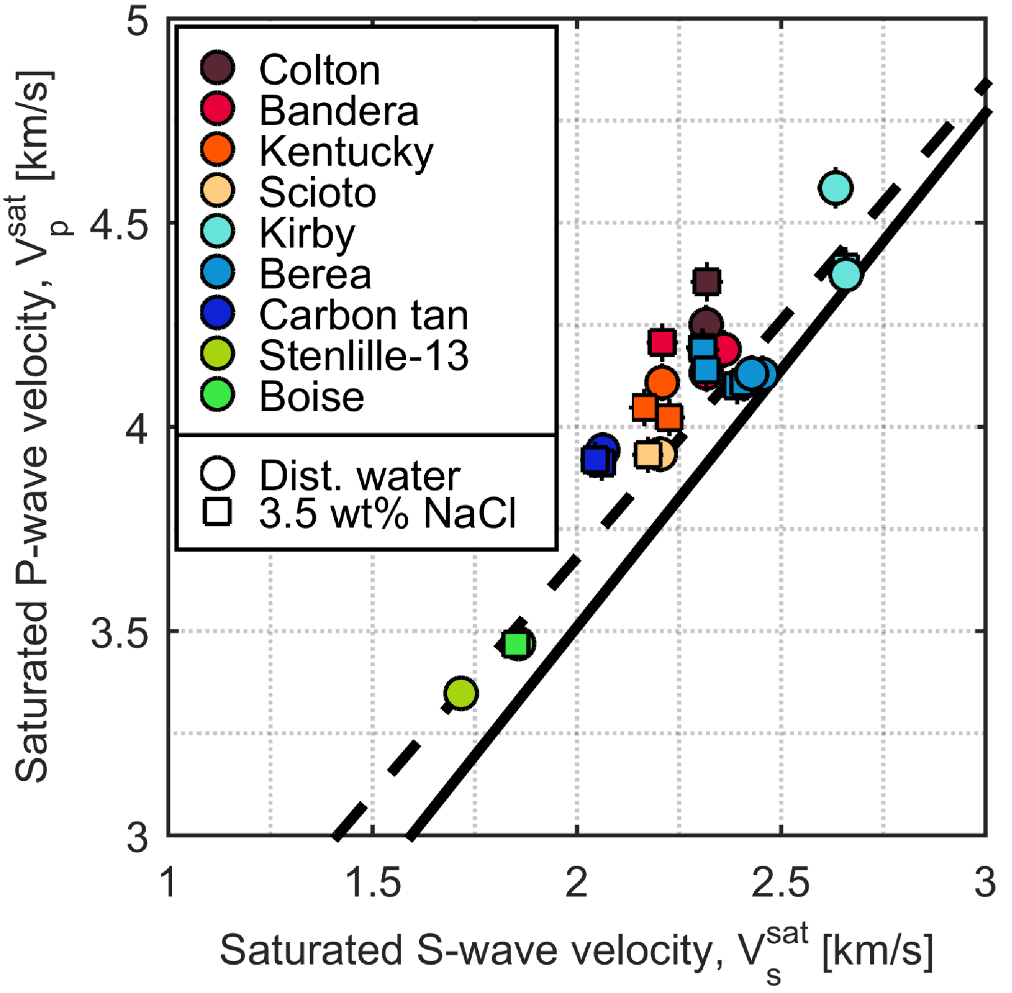

Figure 9.2: Saturated P-wave velocities versus saturated S-wave velocities. The measured data are compared to empirical correlations suggested by Han et al. (1986) (solid line) for clean sandstones $\chi < 0.25$ and the mud-rock line by Castagna et al. (1985) (punctuated line).

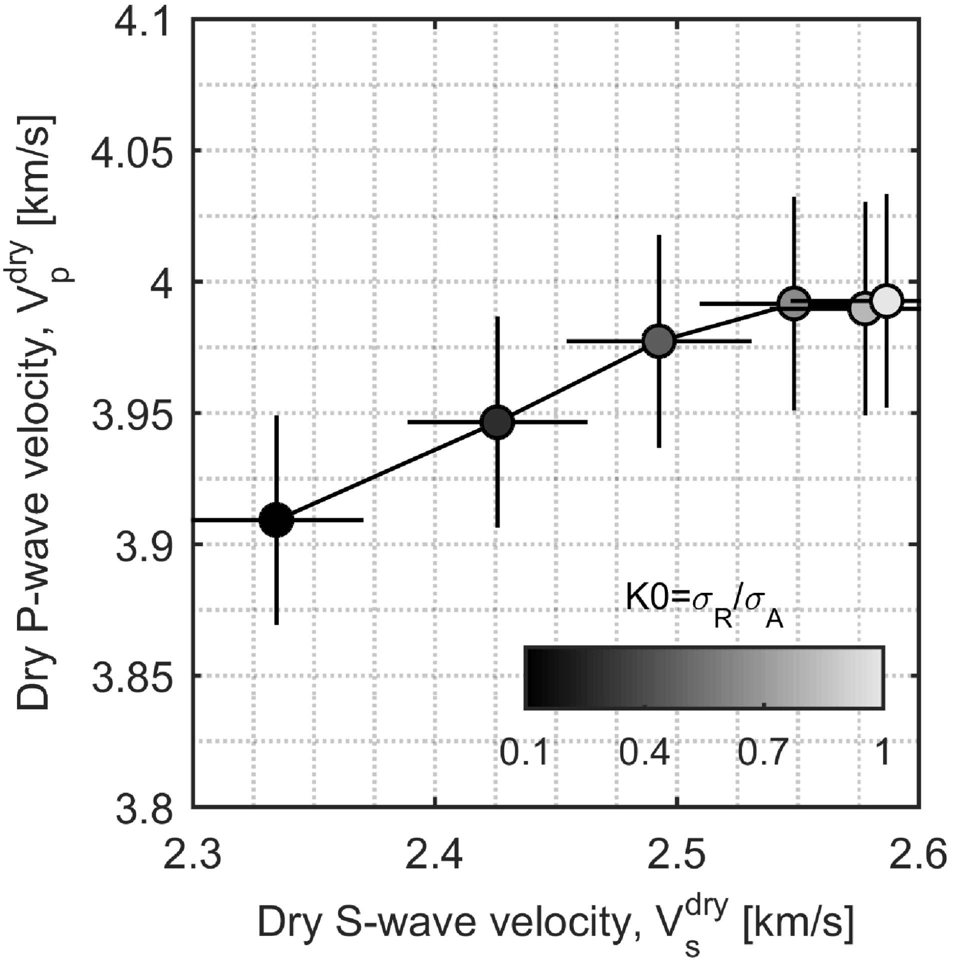

Figure 9.3: Dry V_p versus V_s for a Berea sandstone colored to $K0 = \sigma_R/\sigma_A$. The P-wave velocity changes only slightly with increasing $K0$ while the S-wave velocity increases significantly with increasing radial stress (increasing $K0$). This effect leads to a reduced V_p/V_s.

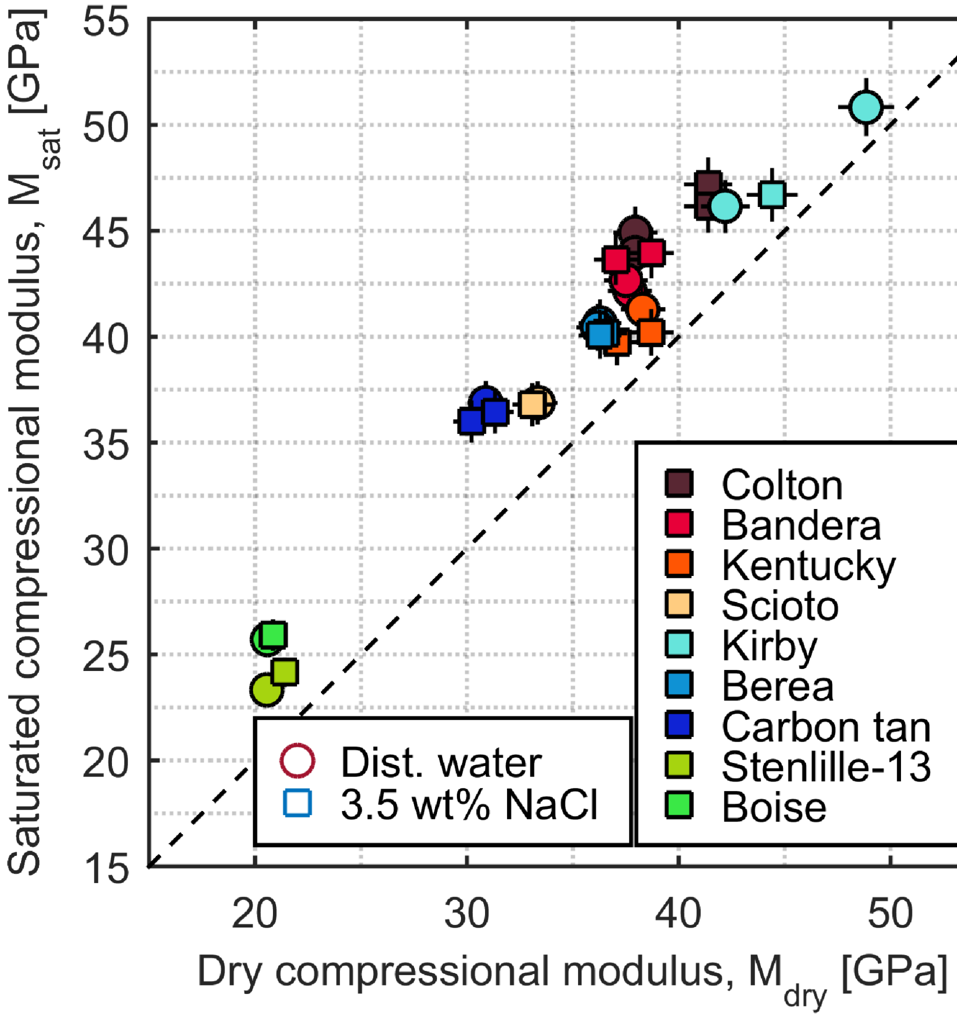

Figure 9.4: Crossplot of the dry compressional moduli and saturated compressional modulus as calculated from the measured ultrasonic velocity.

9.2 Moduli

Figure 9.4 shows the saturated compressional moduli, M_{sat} versus dry compressional moduli, M_{dry}. Saturated compressional moduli are higher than the dry compressional moduli due to induced pressure in the pore-fluid under compression. The Kentucky sandstone have unusually low compressional moduli in the saturated state relative to the dry state. This is caused by a large decrease in shear modulus upon saturation as seen in Figure 9.5 which shows the saturated shear modulus, G_{sat}, versus the dry shear modulus, G_{dry}. Contrary to the compressional modulus and bulk modulus the shear modulus involves no compression and therefore the shear modulus should be unaffected by water saturation, if the frame of the rock remains unaltered Gassmann (1951).

Figure 9.5 shows this to be the case for some of the lithologies while others have lower

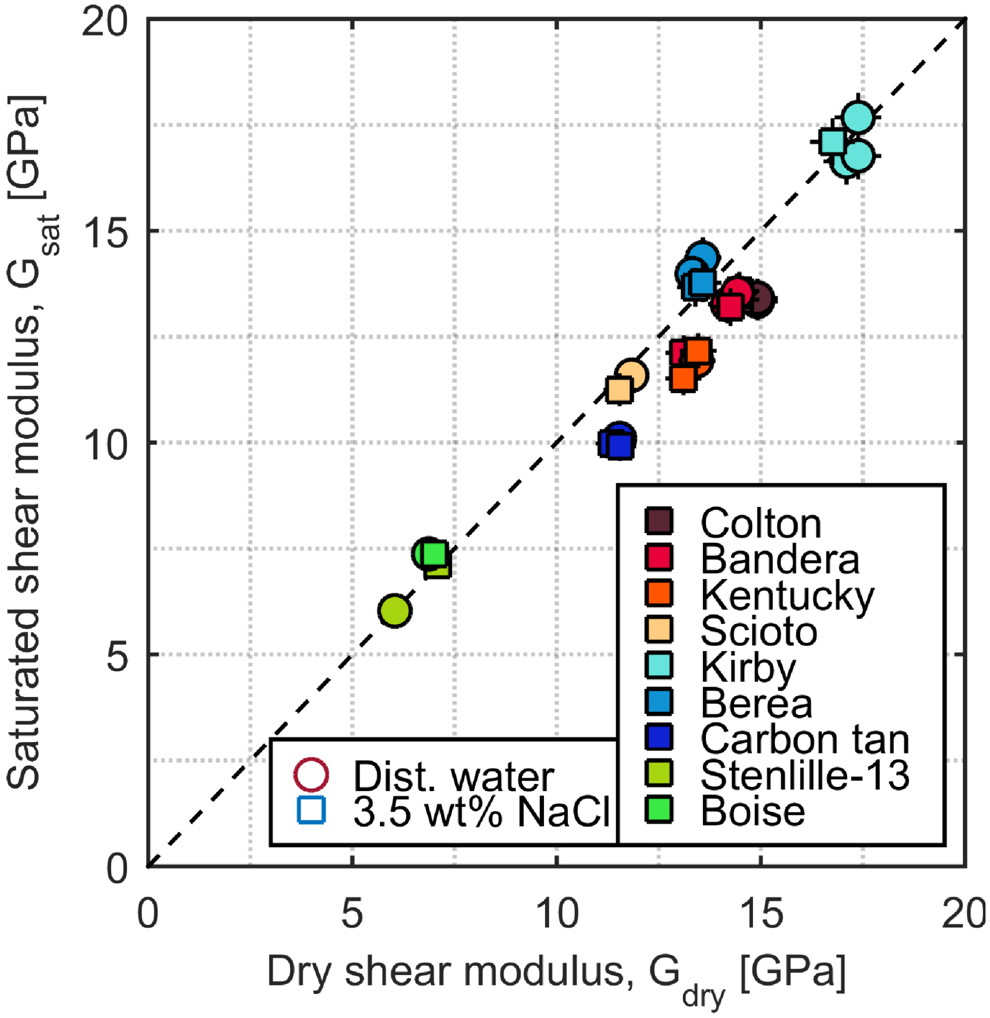

Figure 9.5: Crossplot of dry shear modulus and saturated shear modulus. Some lithologies show softening of the shear modulus by fluid saturation.

Fluid	Modulus, K_f[GPa]
Distilled water	2.2
3.5 wt% NaCl	2.41

Table 9.1: Fluid bulk modulus used for fluid substitution

shear moduli when saturated. Kentucky, Colton, Bandera, and Carbon tan have significantly lower shear moduli when saturated. We wish to evaluate to what degree the saturated moduli in Figure 9.4 and Figure 9.5 agree with fluid substitution in the form of Equation 7.6a. We calculate the Gassmann predicted saturated bulk modulus from the dry bulk modulus using the porosity measured, and the fluid bulk moduli given in Table 9.1. The fluid moduli are based on the correlations by Batzle and Wang (1992).

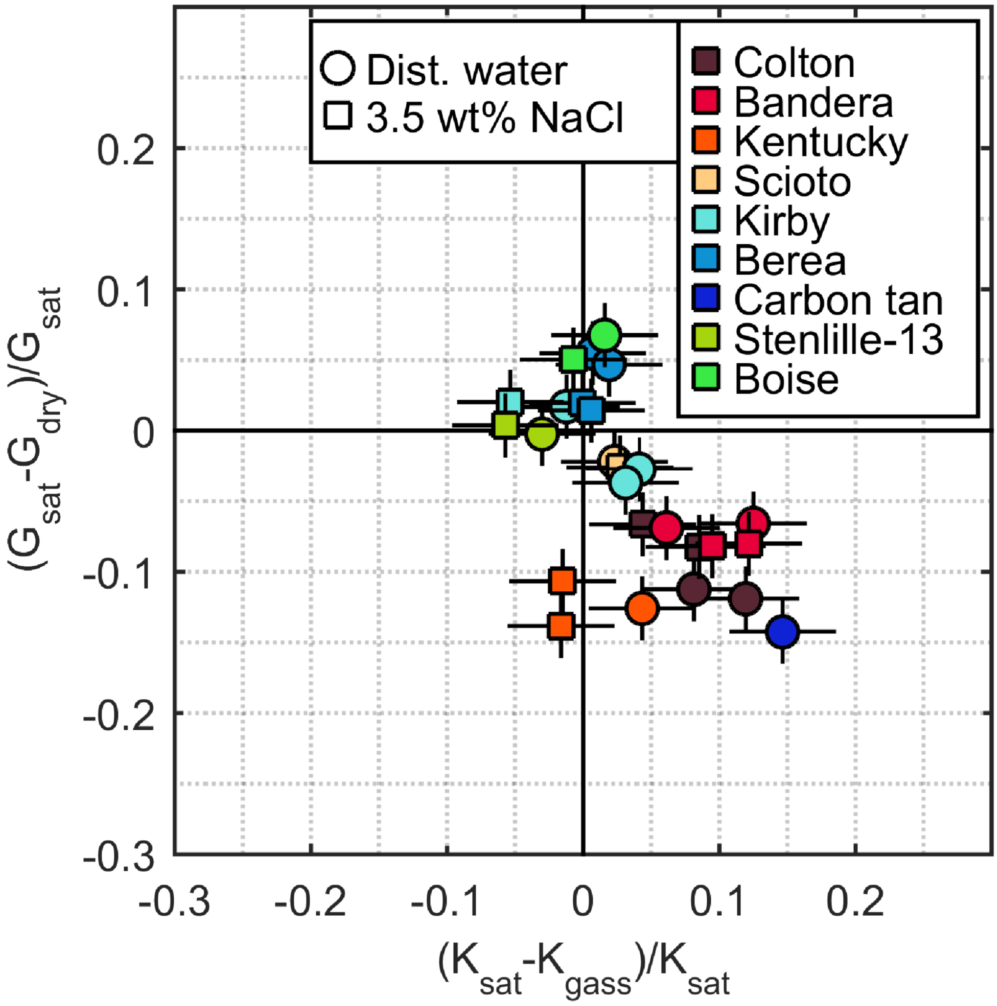

Figure 9.6: The error of fluid substitution on the bulk and shear modulus relative to the measured saturated moduli. Disagreements below 5 % are observed for most lithologies, except Colton, Bandera, Kentucky, and Carbon tan.

Figure 9.6 shows the relative disagreement between the fluid substituted and the fluid substituted bulk modulus, and shear modulus. For the majority of the lithologies the disagreement between measured bulk moduli and fluid predicted bulk moduli are within measurement uncertainty, both when saturated with distilled water and NaCl brine. The lithologies which were seen in Figure 9.5 to have a reduced shear modulus with saturation are seen to also have a significant disagreement with the fluid substituted bulk modulus. These lithologies are Colton, Bandera, Kentucky, and Carbon tan. Fluid substitution underpredicts the saturated bulk moduli for Colton, Bandera, and Carbon tan with about 10 % and overpredicts the bulk moduli for Kentucky by about 7 %.

9.3 Moduli under evaporative drying

The compressional modulus, shear modulus, and bulk modulus are presented in Figure 9.7, 9.8, and 9.9 respectively. All moduli are presented as the difference between the saturated modulus of the sample and the dry modulus to emphasize the contribution of the fluid. The irreducible water saturation estimated from MICP are illustrated in Figure 9.7 by the gray shaded area. The absolute modulus values of the fully saturated samples are found in Figure 9.4 and Figure 9.5. Compressional modulus are reduced for all lithologies as the saturation decreases. Replacing water with gas decreases the modulus of the pore-fill and consequently the induced pressure. Decreasing saturation invariably reduce the bulk modulus and the compressional modulus, the question being the rate of decrease.

Berea and Kirby have a linear decrease in compressional modulus connecting the fully saturated and dry states. Colton, Bandera, Kentucky, and Carbon tan have one slope at high saturation and another slope at low saturation. For Colton, Bandera, and Kentucky the change of slope is remarkably close to the irreducible water saturation from MICP. Scioto, Stenlille, and Boise have steep slopes bringing the compressional modulus down to the dry compressional modulus at high saturation ($S_w > 0.5$). Water saturation affects both stiffness and rigidity of the grain frames as seen in Figure 9.6. The relation between compressional modulus and saturation comprises the combination of the saturation effect on the bulk modulus and the shear modulus. The development of shear modulus as a function of water saturation during drying is shown in Figure 9.8 and Figure 9.9 shows the same for the bulk modulus. The irreducible water saturation is shaded gray on both figures, with the shading referring to the pressure needed. Shear moduli are significantly decreased for Colton, Bandera, Kentucky, Kirby, and Carbon tan and are slightly increased for Berea, and Boise. The largest differences between dry and saturated shear modulus occur in low-permeability high clay content lithologies (Colton, Kentucky, Bandera), these lithologies have reduced shear modulus in the range of 2 GPa relative to the dry state. The carbonate cemented lithologies with low clay content (Kirby, Carbon tan) also have appreciable reduction in shear modulus when saturated, with reductions of about 1 GPa. The reduction for the litholgies that are neither clay rich or carbonate cemented are all below 1 GPa. Bandera, and Kentucky have shear moduli increasing with decreasing saturation towards the dry shear modulus, all other lithologies have shear modulus that are close to constant over the saturation range measured. This is consistent with observations of shear modulus changes in sandstone occurring over the first few percent of saturation (Goertz and Knight, 1998; Vo-Thanh, 1995). Measurements in this study are not continued to very low saturation whereby the expected restoration of the shear modulus to the dry shear modulus is not observed.

Figure 9.9 shows the bulk modulus of the nine lithologies as a function of water saturation under drying. Bulk moduli for all lithologies decrease with saturation as the gas fraction increases reducing the induced pressure due to the high compliance of the gas phase. The change in slope observed for the compressional modulus of Colton, Bandera, Kentucky, and Carbon tan is evident in the bulk modulus. The observation of the effect for the

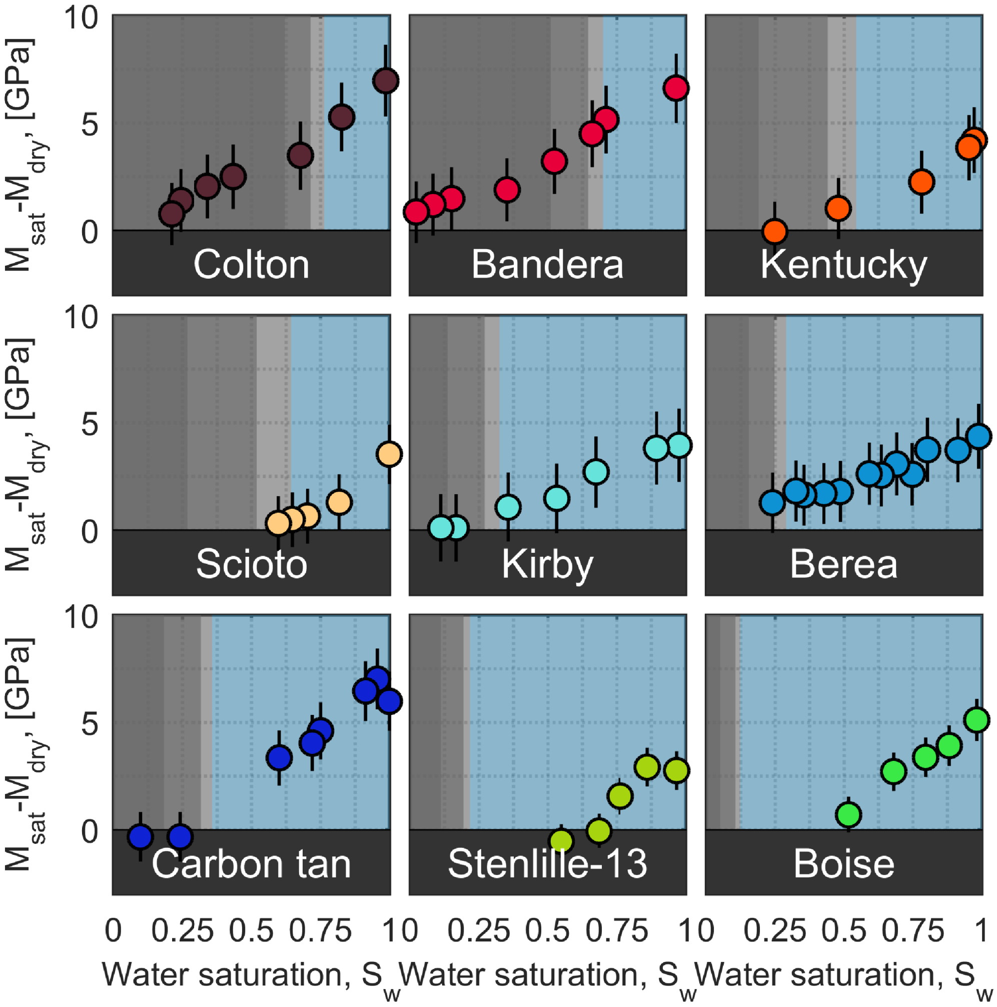

Figure 9.7: Fluid effect on the compressional modulus, $\Delta M = M_{sat} - M_{dry}$, as a function of water saturation for the nine litholgies under evaporative drying. The gray shaded area signifies the irreducible water saturation from MICP. The darkest shading is $S^{\infty}_{w,ir}$, the medium shading is $S^{20}_{w,ir}$, and the lightest shading is $S^{10}_{w,ir}$. The blue shading illustrates the effective porosity available at 10 bar.

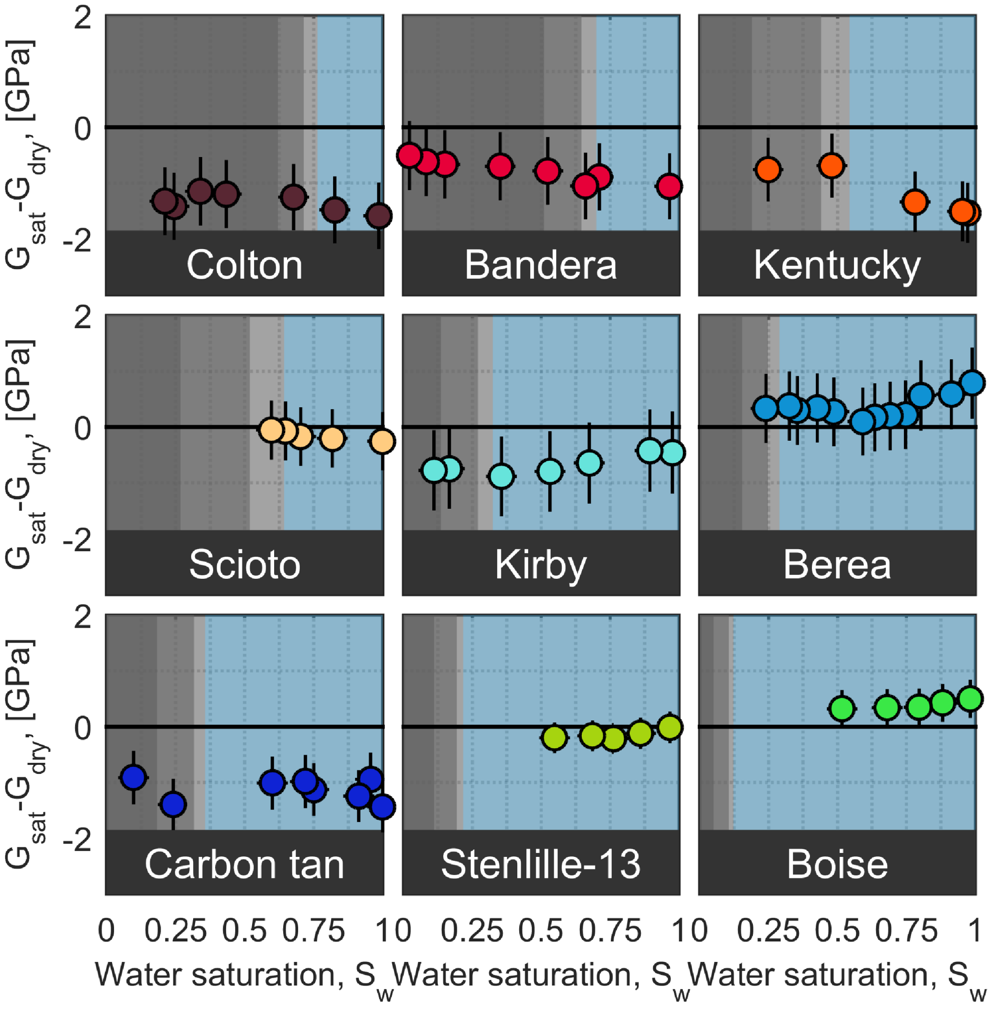

Figure 9.8: Fluid effect on the shear modulus, $\Delta G = G_{sat} - G_{dry}$, as a function of water saturation for the nine litholgies under evaporative drying. The gray shaded area signifies the irreducible water saturation from MICP. The darkest shading is $S_{w,ir}^{\infty}$, the medium shading is $S_{w,ir}^{20}$, and the lightest shading is $S_{w,ir}^{10}$. The blue shading illustrates the effective porosity available at 10 bar

bulk modulus and not significantly for the shear modulus indicates that the cause of the observation is associated with the magnitude of the induced pressure. The upper bound, formulated in Equation 7.7, and the lower bound, formulated in Equation 7.8, are plotted in Figure 9.9. All substitutions used for evaluating the bound are done from the fully saturated state. For partial saturation the lower bound quickly decreases to the dry frame modulus consistent with the measured bulk modulus. The contrast between the bulk modulus of air ($K_a \approx 1.4 \cdot 10^{-4}$ GPa), and that of water ($K_w = 2.2$ GPa) is so large that the bulk modulus of air quickly dominates the mixture. If the lithologies are consistent with fluid substitution the dry bulk modulus coincide with the lower bound. Meaning the lower bound should for a saturation lower than 0.98 coincide with the x-axis in Figure 9.9. For lithologies that are not consistent with Gassmann fluid substitution the difference between 0 and the lower bound gives the divergence from fluid substitution. Kirby and Berea is well predicted by the upper bound from Equation 7.7, albeit Kirby has an effective frame modulus slightly higher than the dry bulk modulus. This divergence for Kirby occur at low saturations and may be associated with induced pressure gradients from grain frame weaknesses (squirt flow) Mavko and Jizba (1991). Scioto, Stenlille, and Boise follow the upper bound at high saturation and then decrease rapidly to the lower bound which coincides with the dry bulk modulus. Colton, Bandera, Kentucky and Carbon tan follow a common development, but the lower limit does not coincide with the dry bulk modulus. The bulk moduli of Colton, Bandera, and Kentucky decrease below the lower bound at a high saturation comparable to the irreducible water saturation from MICP, for Carbon tan the bulk modulus decreases below the lower bound at a saturation much higher than the irreducible water saturation. It is a common observation that the fluid effect is underestimated by fluid substitution in clay bearing sandstone (Han, 1986; Best et al., 1994). The determining mechanism have been proposed to be poor pressure diffusion from clay rich pores (Best et al., 1994) with high pressure induced due to increased pore-filling modulus by clay (Marion et al., 1992). Dvorkin et al. (2007) proposed restricting fluid substitution to the effective porosity to counter the effect of clay fill in the porosity, but restricted the volume of unrelaxed fluid to water bound to the surface of clay. With the low permeability of clay, bulk water in pores dominated by clay may, however, also retain unequilibrated pressure. Dvorkin et al. (2007) suggested an effective mineral modulus where the unrelaxed clay filled porosity is incorporated into the mineral frame, similar to the procedure used to account for the poly-mineralic frame. This concept is illustrated by the diagram in Figure 9.10. We attempt to adapt this mechanism to explain the departure from fluid substitution seen in the low-permeable lithologies. Since the clay is not load-bearing it will not affect the bulk modulus in the dry state. In the saturated state the bulk modulus will be higher in the clay dominated part of the frame than the effective porosity parts due to the higher pore-filling bulk modulus in the clay dominated porosity. On a the pore-scale the effective bulk modulus of a clay water suspension, K_{sus}, comply with the lower bound mixing of the water bulk modulus, K_f, and the mineral bulk modulus of

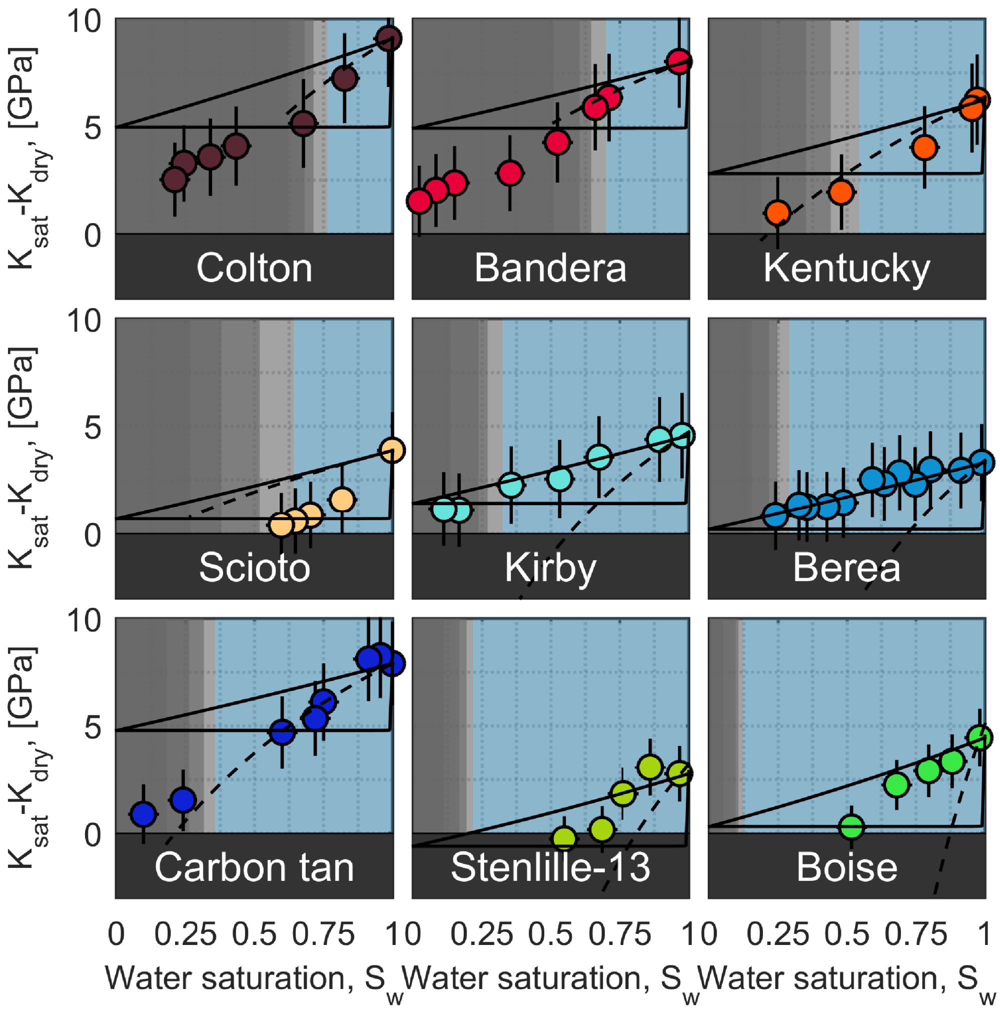

Figure 9.9: Fluid effect on the bulk modulus, $\Delta K = K_{sat} - K_{dry}$, as a function of water saturation for the nine litholgies under evaporative drying. The gray shaded area signifies the irreducible water saturation from MICP. The darkest shading is $S^{\infty}_{w,ir}$, the medium shading is $S^{20}_{w,ir}$, and the lightest shading is $S^{10}_{w,ir}$. The blue shading illustrates the effective porosity available at 10 bar. The solid lines illustrate the upper and lower bounds for fluid substitution to mixed saturation. The dashed line illustrates the effective porosity substitution.

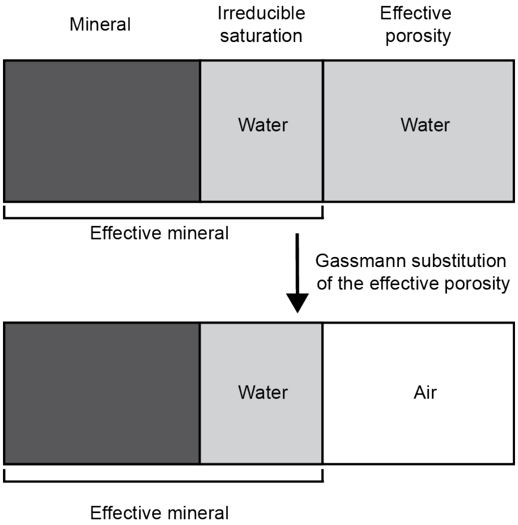
Mineral
Irreducible saturation
Effective porosity
Water
Water
Effective mineral
Gassmann substitution of the effective porosity
Water
Air
Effective mineral

Figure 9.10: Illustration of the effective porosity fluid substitution. Porosity with unrelaxed pressures is lumped into the mineral frame and fluid substitution is performed on the effective porosity using the effective mineral modulus.

the clay, K_0^c (Marion et al., 1992),

$$\frac{1}{K_{sus}} = \frac{S_c}{K_0^c} + \frac{1 - S_c}{K_0^c} \tag{9.1}$$

Where S_c is the saturation of solid clay in the pore-space. If we assume the entire irreducible water saturation is contained in clay filled pores, the pore-volume of clay per bulk volume, V_p^c must equal the pore-volume occupied by the irreducible saturation,

$$V_p^c = \phi S_{w,ir}. \tag{9.2}$$

Using the fraction of solid composed of clay determined from XRD, x_{clay} the total volume of clay, and clay porosity per bulk volume, χ, is,

$$\chi = V_p^c + x_{clay} = \phi S_{w,ir} + x_{clay}. \tag{9.3}$$

Since the clay and clay porosity is found in the pores of the frame it must occupy a frame pore-volume of the same size. Therefore, S_c is equal to the ratio of solid clay material to the total clay volume,

$$S_c = \frac{V_s^c}{V_p} = \frac{x_i}{\chi} \tag{9.4}$$

The values determined for Colton, Bandera, Kentucky, and Carbon Tan are tabulated in Table 9.2. To estimate the bulk modulus of the clay dominated pores knowledge of K_0^c is needed. This value is however very ill determined (Vanorio et al., 2003; Mondol et al., 2008; Katahara, 1996). There is, however, a consensus that the clay mineral modulus is

Lithology	S_c	K_0, [GPa]	K_0^{eff}, [GPa]
Colton	0.48	47	39
Bandera	0.52	47	38
Kentucky	0.21	47	39
Carbon tan	0.44	43	35

Table 9.2: Effective mineral moduli obtained by inversion of Equation 7.6a for the substitution illustrated in Figure 9.10

higher than the bulk modulus of water. We can then assume $K_0^c >> K_f$ and Equation 9.1 reduces to,

$$K_{sus} \approx \frac{K_f}{1 - S_c}. \tag{9.5}$$

We use this pore-filling modulus and substitute into the dry frame with Equation 7.6a. We then combine the substituted values with the mineral modulus as done for the polymineralic frame. We assume that the irreducible water saturation is also a measure of the fraction of the bulk of the frame dominated by clay. The effective mineral moduli estimated for Colton, Bandera, Kentucky, and Carbon Tan are seen in Table 9.2 along with the mineral moduli for comparison. Fluid substitution is then performed using these effective mineral moduli and the effective porosity, the results of the substitution is seen in Figure 9.9. The effective porosity substitution improves the prediction of Colton, Bandera, Kentucky, and Carbon tan, but significantly overestimates the fluid effect in the remainder of the lithologies where pressure is not retained in the clay filled pores. Identification of which lithologies are to be substituted to the effective porosity is difficult. Colton, and Bandera are easily distinguished by the high irreducible water saturation, but Carbon tan, and Kentucky are not. Distinguishing the behavior of the Kentucky lithology over the Scioto is difficult. Carbon tan is also difficult to identify as having unrelaxed pressures. If the NMR spectrum of the fully saturated sample is available the characteristic feature identifying the lithologies best modeled by an effective porosity substitution is those with a multi-modal spectrum. Applying this effective porosity substitution to the fully saturated shown in Figure 9.6 produce the prediction seen in Figure 9.11

Comparing Figure 9.6 and 9.11 shows the prediction to be markedly improved by employing the effective porosity substitution.

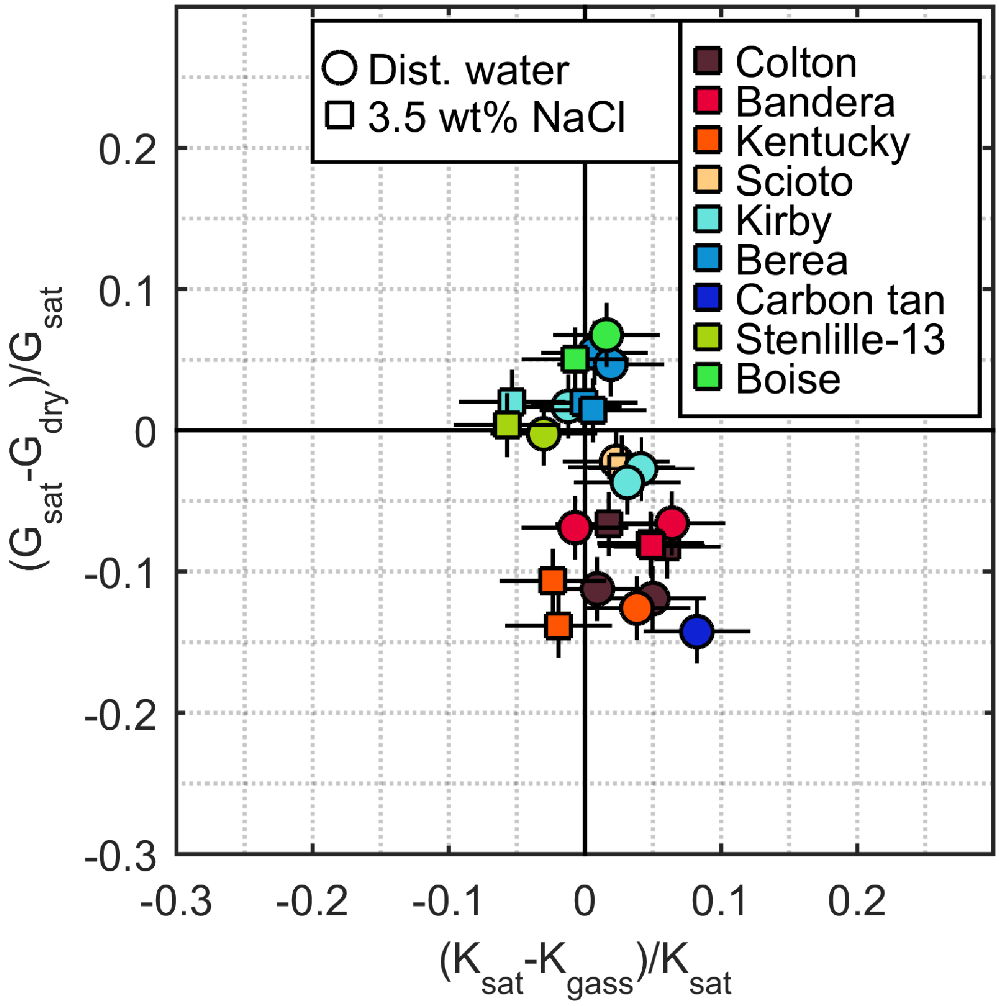

Figure 9.11: Relative divergence of the fluid predicted shear modulus and bulk modulus using the effective porosity substitution for clay rich lithologies, assuming the clay rich porosity regions have unrelaxed pressure.

Discussion and conclusion

The aim of the study was to facilitate invasion correction of sonic logs. A relation was sought bringing together the properties of the pore-space as reflected by capillary pressure curves which determines the range of saturation that can be affected during invasion. Special emphasis was placed on velocities at the irreducible water saturation as for reservoirs this will often be the saturation found in the invaded zone, and any saturation state will be relative to this saturation.

Significant reductions in shear modulus upon fluid saturation ($1 - 2$ GPa) was found for lithologies with high clay fractions and carbonate cementation. The shear modulus reduction in clay rich lithologies decreases slowly with water saturation. In the context of fluid substitution in the subsurface, where fluid can only be replaced in the effective porosity, the change of shear modulus is small as the irreducible water saturation is high in the clay rich sandstone. The lithology Carbon tan also had a significant reduction in shear modulus induced by fluid saturation, but this reduction did not depend on the saturation in the range measured. For the range of rock textures measured in this study fluid induced shear changes is deemed not to be influential for a fluid substitution from one fluid to another.

Regarding the bulk modulus three behaviors were identified depending on pore-texture identified by MICP curves, low-field T_2 NMR spectra, and the development of the T_2 spectra under desaturation. Lithologies with high clay fractions was found to have an effective double porosity system. Clay or clay dominated pores composed one porosity system and inter-granular effective porosity composed another. Lithologies with intermediate clay fractions had a pore-space uniformly or gradually affected by clay, giving rise to a long tail in the T_2 spectra, a uniform slope in the capillary pressure curve, and only a slight change in T_2 spectra under drying conforming to a long tail at low T_2 in the fully saturated T_2 spectra. The final pore-texture is comprised of a single porosity dominated by inter-granular porosity characterized by long T_2 values, a flat capillary curve from MICP, and a very low change in T_2 under drying.

Clay in the pore-space is associated with a large irreducible water saturation. The rate of change in bulk modulus with water saturation changes at a saturation comparable to the irreducible saturation. This was taken as an indication of the clay dominated porosity not being in pressure equilibrium with the remainder of the porosity under compression. Adaptation of an effective mineral modulus guided by the measured bulk modulus at the irreducible saturation and in the fully saturated state leads to a good prediction of the slope of bulk modulus versus saturation in the effective porosity region, and a good prediction of fully saturated moduli. This suggests that for clay rich samples the fluid substitution may best be done using the effective porosity fluid substitution.

Lithologies without a distinct separation between clay dominated porosity and open porosity exhibit T_2 spectra with a dominant mode at high T_2 and a long tail stretching to low T_2. This texture had a linear decrease in bulk modulus from fully saturated state to the dry state. No significant divergence from Gassmann fluid substitution was seen for this texture. According to the data obtained in this study the elastic velocities in this group would be well predicted by the upper bound formulated for mixed saturation.

Lithologies with an open pore texture dominated by inter-granular porosity was identified by a flat capillary curve from MICP, a strongly dominating primary T_2 mode, and a low change in the dominant T_2 mode during drying. This pore texture resulted in a steeply decreasing relation between bulk modulus and water saturation. A good prediction was afforded by fluid substitution using the effective fluid modulus predicted employing an effective fluid modulus formulated as the Reuss bound of the fluid phases. The two latter pore-textures are both well predicted by the total porosity fluid substitution. At partial and possibly mixed saturation they converge to different bounds. For a mixed saturation of two fluids with low modulus contrast, this distinction is irrelevant, but for mixtures of gas and fluid the difference may be significant.

This study have provided measurements of the elastic velocities in a range of sandstones with a rather complex texture. The results coincide with findings of previous studies on the partially saturated sandstones. By characterizing the texture of the pore-space in the sandstones we have connected these developments of velocity directly to the rock properties. The relevance of the findings in the context of correcting sonic logs for invasion was evaluated by observing the development relative to the irreducible water saturation. We found that clay rich lithologies are best substituted using the effective porosity. More permeable sandstones generally agree with the total porosity substitution.

Chapter 10

Effect of saturation on load-bearing clay

Elastic properties of shales and mudstones are dominated by the load-bearing clay matrix in which silt and sand grains are suspended. Rock physics modeling of mudstones and shales typically formulates a background matrix medium and then introduce a pore-structure (Sarout and Guéguen, 2008; Pervukhina et al., 2008). The assumption is that the background medium is defined by the mineral moduli of the clay composing the framework. Relative to the mineral dependent background medium the pore-structure is what defines the moduli of the framework. The inability to directly measure mineral moduli of clay due to the small size of clay particles introduces ambiguity in formulation of the background medium. Attempts to attain mineral moduli via extrapolation of moduli measured on clay particle aggregates does not produce consistent results (Vanorio et al., 2003). Further, extrapolated mineral moduli are found to be lower than mineral moduli attained from simulation (Katahara, 1996; Militzer and Wenk, 2011), or from a correlation with mineral density (Chen and Evans, 2006). Mondol et al. (2008) extrapolated ultrasonic moduli measured on dry and brine saturated compacted kaolinite and smectite powders to nil porosity to determine the mineral moduli. This study found the mineral moduli of the two clay minerals to differ between the dry and the brine saturated state. In addition the bulk modulus and the shear modulus were changed in opposite directions by saturation. Bulk moduli of the two clay minerals increased by saturation, whereas the mineral shear modulus was reduced. Brine has a higher bulk modulus than air so replacing air with brine in any pore-structure cannot decrease the moduli. Clays are, however, known to be very reactive with water and an interaction between the clay and water can alter the framework. Dehydration pressures of clay minerals are very high in the range of 100 MPa (van Olphen, 1962; Colten, 1986) making it viable that water present at grain contacts may remain under compaction and may therefore account for the observed discrepancies. Simulation of water between clay platelets finds that water such confined diverge from bulk water, attaining a finite shear modulus and an increased bulk modulus (Kolstøand Holt, 2012). The implication of water between contacts would be that a background medium cannot be specified based on mineralogy alone, but have to directly incorporate the fluid composition. We investigate the effect of water coating and estimate the relative importance of the water coating on the elastic moduli of clay by normalizing the data recorded by Mondol et al. (2007). We identify clay mixtures that are comparable in the dry and the saturated state, assume that they have the same averaged contact area and from this resolve the relative change in average moduli in the dry and saturated state.

10.1 The data

The data consists of ultrasonic velocities, porosity, and density recorded as a function of oedometric stress in dry and brine saturated mixtures of smectite and kaolinite (Mondol et al., 2007). The mixtures are characterized by the weight fraction of smectite from 100 $wt\%$ smectite to 0 $wt\%$ smectite in steps of 20 $wt\%$. The dataset thereby involve 6 sets of dry and saturated compacted clay frames. The loading is done in an oedometer and the maximum axial stress is $\sigma = 50$ MPa.

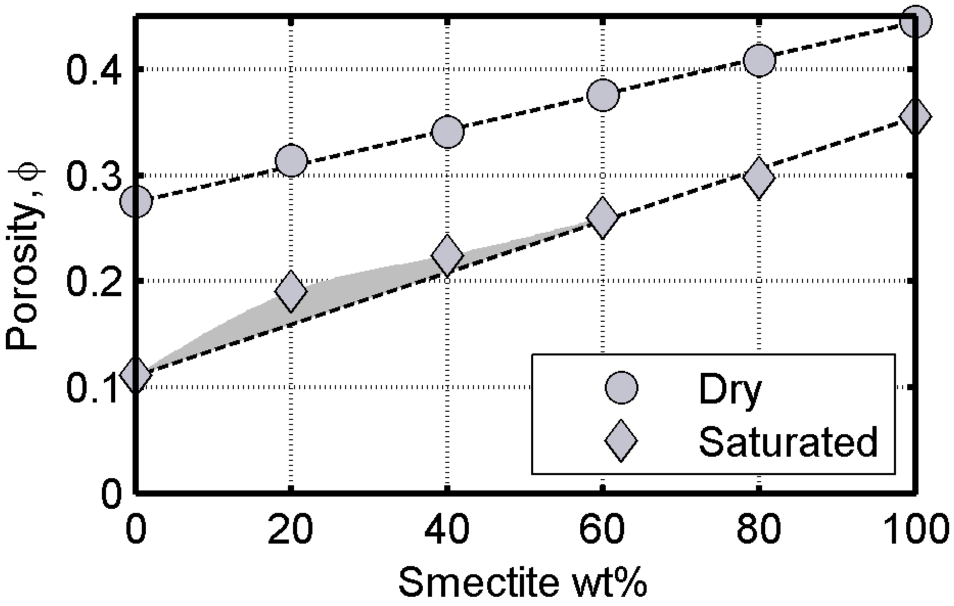

Figure 10.1: Porosity as a function of smectite weight fraction at $\sigma = 50$ MPa, in the dry ($\circ$) and saturated ($\diamond$) state. Linear relations are seen for mixtures with high smectite content.

10.2 Dry and saturated frameworks

Clay particles are far from spherical, and the properties of the compacted clay frame depends on the orientation of the clay particles (Hornby et al., 1994). Orientation of the clay platelets depends on the attraction and repulsion of the platelets, which are sensitive to the pore fluid composition (Wang and Siu, 2006). Comparison between frames deposited in a dry and in a saturated state requires evaluation of the uniformity of the mixture. Figure 10.1 shows the porosity of the clay mixtures in the dry and the brine saturated state at $\sigma = 50$ MPa.

In the dry state all mixtures comply with a linear mixing between the two end points. For the saturated state, however, there is an excess of porosity at high kaolinite contents, indicated by the shading in Figure 10.1. As the mixtures are characterized by their weight fraction, a linear relation with porosity suggests that the pore-space at 50 MPa is determined by porosity inherent to the specific mineralogies. When this is the case in both the dry and the saturated state a comparison of the frames is viable.
Figure 10.2 shows Poisson's ratio of the mixtures as a function of axial stress in the dry and in the saturated state. We see that mixtures high in kaolinite have an abnormal behavior in the dry state with negative Poisson's ratio. Materials with negative Poisson's ratio are known as auxetic materials. For granular media auxetic behavior can not be associated with a change in contacts stiffnesses, but is caused by the structure of the contacts (Koenders, 2009). The observation of auxetic behavior for the kaolinite

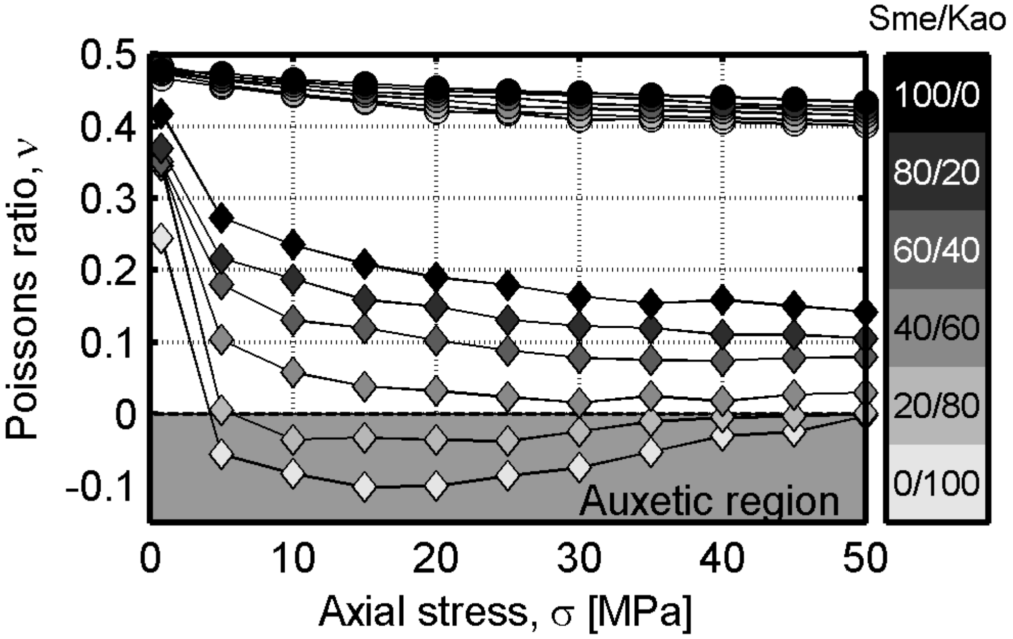

Figure 10.2: Poisson's ratio for clay mixtures in the dry (○) and saturated (◇) state as a function of axial stress. Poisson's ratio is negative for kaolinite rich mixtures with an inflection point at 15 MPa

dominated mixtures may be associated with a predominance of face-to-edge contacts in kaolinite (Wang and Siu, 2006). For further analysis in this paper, we neglect the mixtures dominated by kaolinite from the analysis as the apparent special structure does not prompt an isotropic comparison between the dry and saturated state. The smectite dominated mixtures does however appear to have comparable textures in the dry and saturated state.

10.3 Contact area: The iso-frame model

The cross-section of a porous medium is composed of porosity, ϕ, and solid, $1-\phi$. In granular media stress in the frame is projected through a fraction of the solid cross-section involved in grain contacts. The iso-frame model formulated by Fabricius (2003) address the fact that not the entire solid area participates in the load-bearing frame. The fraction of solid cross-sectional area that participates in the load-bearing frame is given by the iso-frame value, x_{IF}. The model assumes that the load-bearing frame is characterized by a set of moduli, (M_c, G_c), and that the load-bearing frame complies with the upper Hashin-Shtrikman bound (Hashin and Shtrikman, 1962) determined for these moduli. The solid cross-sectional area, $1-\phi$, is adjusted by the iso-frame value, $(1-\phi)\, X_{IF}$ to make the observed modulus comply with the upper Hashin-Shtrikman bound for (M_c, G_c). Uncemented lithologies (i.e. soils and unconsolidated sands) have low contact areas and thus low iso-frame values, while highly cemented sandstones have large iso-frame values originating from the large contact area arising from cementation. The contact moduli are averaged over the contact area and are difficult to obtain in clay frames compared to quartz frame. Quartz cementation of sandstones progressively transforms the originally granular sand-pack into a continuum frame of quartz. In this structure the contact moduli are obviously close to those of the quartz minerals. Clay minerals are not cemented in the same manner and retain the granular nature. Combined with the large surface reactivity of clays the contact moduli comes to depend on mineralogy, texture, and saturation state. These influences may be associated with the difficulty in defining mineral moduli at zero porosity, the extrapolated moduli are simply governed by the contact moduli not the mineral moduli.

Based on these considerations we do not propose any absolute values for the contact moduli, we only assume that the contact area (i.e. the iso-frame value) involved in compressional and shearing deformation must be the same. We perform a least-squares fit of the contact moduli to achieve the same iso-frame value for the dry compressional modulus, M_{dry}, and dry shear modulus, G_{dry}, as a function of axial stress. Guided by reported values for the contact moduli we choose an arbitrary starting value of 20 GPa for the contact bulk modulus, K_c, in the dry state. The iso-frame values are plotted in Figure 10.3 and the adapted contact moduli are listed in Table 10.1. The bulk modulus is determined from the compressional modulus in order to isolate the effect of compression.

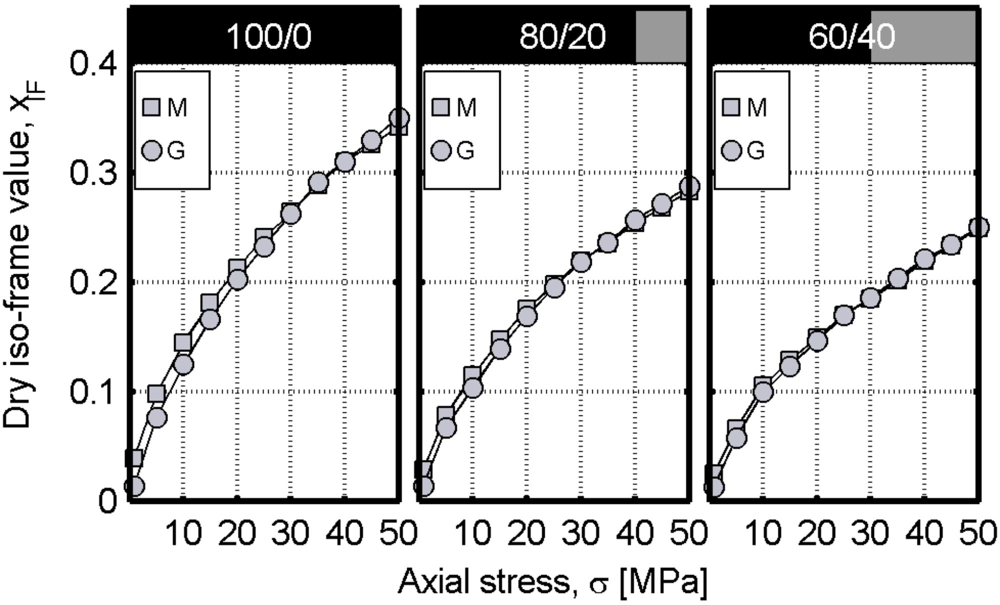

Figure 10.3: The iso-frame values, x_{IF}, for the dry compressional and dry shear moduli are assumed to be the same and fitted to the experimental data. The iso-frame values found for each mixture as a function of stress is a measure of the contact area per area of solid cross-section.

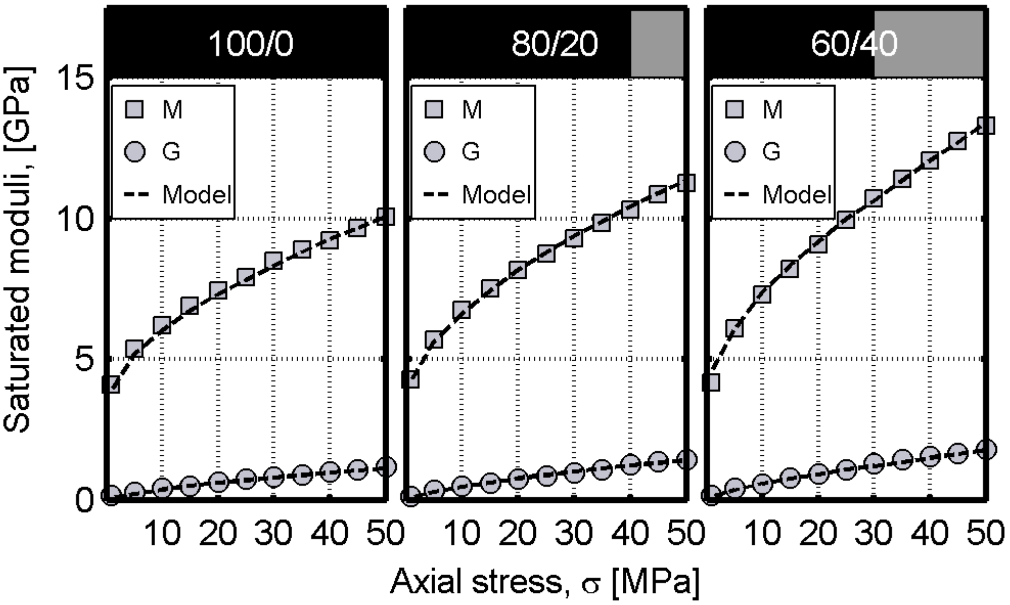

Figure 10.4: The iso-frame values found for the dry mixtures is assumed to be applicable to the saturated frame. From the iso-frame values and the measured saturated compressional and the saturated shear modulus, the contact moduli, (M_c, G_c) in the saturated state can be determined relative to the contact moduli in the dry state.

Table 10.1: Contact moduli used in the model and their ratios.

Sme/kao *wt*%	K_c^{dry} [GPa]	G_c^{dry} [GPa]	K_c^{sat} [GPa]	G_c^{sat} [GPa]	$\frac{K_c^{sat}}{K_c^{dry}}$	$\frac{G_c^{sat}}{G_c^{dry}}$
100/0	20	21	32	8	1.6	0.4
80/20	20	27	31	12	1.6	0.45
60/40	20	33	40	17	2	0.5

The basic assumption of the approach is that, for a given stress, the same fraction of solid cross-section (i.e. the iso-frame value is unchanged) is involved in contacts of the dry and saturated state. Using the iso-frame values attained in the dry state we can adjust the contact moduli to the moduli measured in the saturated state. The result of this is given in Figure 10.4 and the saturated contact modulus tabulated in Table 10.1. The iso-frame model accounts for fluid in the porosity in a way consistent with Gassmann fluid substitution, meaning that for a given frame modulus the influence of induced fluid pressure is incorporated in the analysis.

10.4 Discussion

Only the ratio K_c/G_c is uniquely determined by fitting the contact moduli to achieve the same iso-frame values for the compressional and shear waves. Increasing the two moduli retaining the ratio, will decrease the iso-frame value and decreasing the moduli will increase the iso-frame value, but keeping the same iso-frame value for the shear and compressional modulus. Accurate determination of the moduli of the clay aggregates could affix these values. At present however the model provides only relative values between the dry and saturated state. The ratio between the contact moduli in the dry and saturated state is given in Table 10.1. Contacts are stiffened in compression and softened in shear by addition of a brine saturation. This split in behavior is consistent with previous modeling of the same data using a differential effective medium approach by Moyano et al. (2012). In this study the authors modeled the same data by small aspect ratio pores in a background matrix and found the bulk and shear moduli were affected by two different pore populations. Pores dominating the bulk modulus were found to be stiffer than those dominating the shear modulus. That two excitations of the same framework should be governed independently of two pore populations seem contradictory as populations should be affected by both excitations. We arrive at the same qualitative result using a phenomenological and granular approach. The observed split of the bulk and shear moduli upon saturation is likely caused by the strong interaction between clay and saturating fluid. Relaxation of fluids in the contact region is too slow to occur at the ultrasonic frequency applied leading to an increase in the bulk modulus of the saturated frame. In shear deformation the action of fluid is opposite, because the fluid in the contact acts as a lubricating film decreasing the tangential stiffness of the contact reducing the shear modulus of the frame. The softening of the contact shear modulus is averaged over the contact area and is as such a direct measure of the effective friction at the contacts at low strain. Comparison with measurements of the dry and the water saturated friction coefficients in large strain shear for smectite show good agreement with the 60 % reduction in shear modulus (Morrow et al., 2000). The findings also shed some light on the discussion into the properties of water films in clay, as the shear modulus reduction is consistent with the adsorbed fluid retaining fluid properties. Fluid close to a clay surface are suggested to have a rigid structure with a finite shear modulus, this is, however, inconsistent with the lubricating effect observed in this study (Martin, 1960).

The changes in contact moduli listed in Table 10.1 must be observed as extremes because the contrast in interaction between air and brine is larger than what would be observed between different brines. It is therefore the hope that further analysis along this route could predict the magnitude of the observed slippage as a function of fluid composition.

10.5 Conclusion

We have proposed a granular model explicitly incorporating the texture of compacted clay. By this model we have quantified the relative effect of fluid saturation on the apparent contact moduli of compacted smectite clay and smectite/kaolinite mixtures.

We argue that these contact moduli may coincide with the moduli of the clay end members used in many rock-physics models. We see that the contact bulk modulus is stiffened substantially upon water saturation while the shear modulus is softened. We interpret the split as though fluid is still present at contacts even at high stress and that the fluid retain fluid like properties.

Chapter 11

Conclusion and future work

The elastic moduli of sandstones depend on the saturation through the induced pressure in the pore-space (Biot, 1962). This causes mud-filtrate to affect the readings of a sonic log in the invaded zone. Sonic logs commonly run and processed with industry standard arrival detection are sensitive to less than half a meter of the formation (Xu et al., 2012; Zeroug et al., 2006; Baker and Winbow, 1988; Baker, 1984). The depth of invasion is comparable to or deeper than this depth making sonic logs sensitive to mud-filtrate invasion (Allen et al., 1991; Phelps, 1995; Salazar and Torres-Verdín, 2008).

Prior investigations of the fluid effects on elastic moduli of sandstone (Eberhart-Phillips et al., 1989; Han et al., 1986; Jones, 1986; Gist, 1994; Klimentos, 1991; Best and McCann, 1995; Best et al., 1994), fluid substitution (Han, 1986; Han and Batzle, 2004; Grochau and Gurevich, 2009), and the specific application of fluid substitution to sonic log correction (Xu et al., 2012; Chi et al., 2006) sought correlations using dry moduli as the frame of reference. These studies have considered a coupling between specific pore entities and the induced pressure in the form of grain-frame weaknesses (Jones, 1986; Mavko and Jizba, 1991). For clean sands this approach provides good predictions in the fully saturated state (Paula and Pervukhina, 2012) and for partial saturation clean sandstones are consistent with the bounds formulated by Mavko and Mukerji (1998). Compliant porosity may contribute to the elastic moduli through local flow (Mavko and Jizba, 1991), but there is no relative effect when fluid substitution is performed between two states where the wetting saturation is at or higher than the irreducible water saturation. These bounds formulated by Mavko and Mukerji (1998) neglect any coupling between the fluid saturation and minerals in the pore-space, and any affinity regions of the pore-space might have to a specific fluid.

A radial step profile saturation does not capture the likely fluid distribution caused by invasion (Phelps, 1995; Briceo and Peeters, 2005; Head et al., 1992; Allen et al., 1991). The saturation is likely to be higher than the irreducible wetting saturation in the annulus probed by a sonic log. The step profile is a good base case as the irreducible wetting saturation reflects the saturation which is always unaffected by invasion and which may contribute differently to the elastic moduli by induced pressure than the effective porosity. The irreducible wetting saturation couples directly to the fluid distribution from invasion and the departure from the assumptions of fluid substitution. Recognition of this coupling shifts the problem from accurately determining the properties of the invaded zone to determining the irreducible wetting saturation and the pore-space causing this saturation.

Comparing the drained compressional modulus to a reference trend defined for clean sandstones gives a measure of the amount of clay filling the pores (Gal et al., 1999). Comparison of this clay fraction to the amount of clay determined by image analysis, defines a quantitative classification of the clay distribution. If the clay fraction determined in the two way agree the clay is pore-filling, if not it is load-bearing. Distribution of clay in the bulk volume directly affects the applicability of fluid substitution. The classification scheme formulated in this analysis identifies the effect and significance of the clay distribution on the elastic moduli of a saturated sandstone [Manuscript C]. Clay in the pore-space increase the saturated elastic bulk moduli above the values expected from fluid substitution. This is consistent with the results of Paula and Pervukhina (2012) who attempted to describe the dispersion observed for clay-rich members of the Han (1986) data set, which is also included in the analysis in this thesis.

In Chapter 6 [Manuscript C] the possible effect of clay-squirt from homogeneously distributed clay was evaluated by formulation of a model explicitly incorporating fluid pressure equilibration between intra-clay porosity and the effective porosity in a sandstone. The model predictions for pore-filling clay under-predicts the saturated elastic moduli of the data set treated in Chapter 5. Combining this result with an analysis of the permeability of the sandstones observed in Chapter 5 as guided by Revil and Cathles (1999) conspire to indicate that the discrepancy with fluid substitution in the data may be caused by a heterogeneous distribution of pore-filling clay. Such a distribution is commonly observed for clay minerals as kaolinite which is abundant in sandstones and form in pore-bodies (Shelton, 1964; Wilson and Pittman, 1977; Neasham, 1977).

A suite of sandstone with partial pore-filling clay was selected for measurement. The pore-space was thoroughly characterized as described in Chapter 7. Measurements of the elastic moduli as a function of water saturation during drying showed a distinct dependence on the characteristic of the pore-space, most notably the distribution of clay. A homogeneous pore-space affected by clay leads to the sandstone moduli conforming to the bounds suggested by Mavko and Mukerji (1998). An open uniform pore-space, essentially without clay, leads to a quick reduction from the fully saturated moduli to a moduli consistent with the moduli measured in the drained state [Manuscript C]. In sandstone with an open pore-space the entire porosity have a similar saturation. Hereby this type of pore-space have no areas with a specific affinity to a fluid. In a sandstone with well distributed clay-filled pores throughout the framework, the clay saturation in each pore is low, and the saturated moduli are consistent with the upper bound defined by Mavko and Mukerji (1998). Finally sandstone with a distinct bi-modal pore-space caused by clay filling some pores, whereas others are clean, have saturated elastic bulk moduli significantly higher than predicted by fluid substitution. The relation between the elastic moduli and fluid saturation changes as the saturation approaches the irreducible wetting saturation [Manuscript C].

The change in elastic moduli with saturation can be accounted for by an effective porosity fluid substitution similar to that proposed by Dvorkin et al. (2007). The application in this study differs from that applied by Dvorkin et al. (2007) as the amount of saturation expected to to be unrelaxed is extended to include capillary bound water in clay dominated pores. The irreducible water saturation from MICP is used as a measure of the unrelaxed saturation. This formulation is convenient as the irreducible water saturation is related to the fluid distribution by invasion. Dvorkin et al. (2007) incorporated clay as a part of the load-bearing by specifying a mineral modulus of the clay. In this study we acknowledge the characterization of the pore-space indicating that the clay is pore-filling. We then assume that the clay mineral moduli is significantly higher than the fluid modulus. Hereby the pore-filling modulus of the clay-filled porosity can be determined as an upper limit the clay and fluid suspension modulus, determined by the Reuss average. The clay mineral phase is assumed incompressible relative to the fluid modulus. This approach eliminates the need to specify a clay mineral modulus and requires only the clay saturation in the clay-filled pores. This effective porosity substitution provides good predictions of the bulk modulus from the fully saturated state to the partially saturated state. Fluid substitution can correct sonic logs at mixed saturation by identification of three different regimes defined by the distribution of clay in the pore-space.

Saturation cause a reduction of the shear modulus in sandstone with load-bearing clay, as observed in in Chapter 5. When normalized to a common reference defined by the iso-frame model ultrasonic moduli for, dry and saturated, compacted clay powders have a similar behavior as sandstone with load-bearing clay Chapter 10 [Manuscript C]. The reduction of the shear modulus is approximately 50 % while the bulk modulus is increased with about the same fraction. The origin of effect is suggested to be fluid present at the contacts between clay platelets. This fluid retains some fluid characteristics whereby it facilitates sliding, reducing the shear modulus, but a pressure is induced under compression increasing the bulk modulus.

11.1 Recommendations for future work

This investigation addressed the effect of pore-filling clay and the pore-space on the saturated moduli of sandstone with a mixed saturation. In the analysis, only ultrasonic data is considered, both from the literature and measurements conducted in this study. Unrelaxed pressures associated with a wave of a finite frequency will have a frequency at which they relax. It is an open question how the transition frequency of the effect proposed in this thesis relates to the properties of the sandstones.

The classification in Chapter 5 illustrated a clear relation between the elastic moduli of saturated sandstone and the clay distribution. The classification involves data not commonly available for exploration or other applications. It is feasible that the characteristics of the clay distribution is related to the clay mineralogy (Shelton, 1964; Wilson and Pittman, 1977; Neasham, 1977). Establishing a link between the geological knowledge of a sandstone formation and the irreducible water saturation could make the approach more applicable. Establishing such a link will require further analysis of the clay mineralogy and relation to the irreducible wetting saturation

The data presented in this study suggests a set of fluid saturated moduli characterized by a frame incorporating the irreducible wetting saturation. Evaluation of the fluid effect is however achieved by using both the fully saturated moduli and the at the irreducible water saturation. In practical applications only one moduli is readily available. The similarity between the relations in the effective porosity and the clean sandstones, along with the almost linear decrease of the elastic bulk modulus with saturation suggests that correction could be attained by characterizing the effective frame modulus by assessing the irreducible water saturation from deep probing resistivity logs. Decomposition of the measured moduli is possible using the limiting formulation of the pore-filling suspension modulus, under the assumption of an incompressible clay mineral phase. Possible correlation between the effective frame bulk modulus, the measured bulk modulus by the log, and the fully saturated bulk modulus could then be achieved. More data concerning the connection between the three moduli as a function of the sandstone framework moduli is needed. Emphasis in this study was placed on well-consolidated sandstones. Application to in-situ data requires inclusion of consolidation and the dependence on frequency. Reliable application to sonic logs would be facilitated by measurements of the dispersion arising from the pore-filling clay as a function of frequency and framework properties.

One major problem in the approach proposed is distinguishing the pore-space causing dispersion from those that does not. NMR appears promising as a distinguishing parameter. The modality of the T_2 distribution appear to reflect the properties of the pore-space texture causing dispersion. The data presented in this analysis is however for fully saturated and partially saturated systems. Saturations by two fluids will have a distinctly different signal with water and oil phases clearly separated in the NMR spectrum. In this case, identification of the response from heterogeneously distributed clay is not trivial. Further measurements of the T_2 spectra in clay bearing sandstones saturated with two-fluid phases are needed.

The interaction of water with clay platelets observed in Chapter 10 is speculated to be the extremes of an effect determined by the interaction between the clay minerals and the saturating fluid. The shear softening and bulk stiffening may depend on the fluid chemistry and the interaction with the clay minerals. Salinity variations can then be found somewhere in between these two extremes explaining the water sensitivity of clay rich shales. The influence of different saturating fluids will establish a possible correlation with fluid chemistry that applicable for an estimation of the water sensitive strength of clay rich shales.

Bibliography

Abrams, A., 1977, Mud design to minimize rock impairment due to particle invasion: Journal of petroleum technology.

Adamson, A. W., and A. P. Gast, 1997, Physical Chemistry of Surfaces: John Wiley & Sons, Inc.

Adelinet, M., J. Fortin, and Y. Guéguen, 2011, Dispersion of elastic moduli in a porous-cracked rock: Theoretical predictions for squirt-flow: Tectonophysics, **503**, 173–181.

Allen, D., F. Auzerais, and E. Dussan, 1991, Invasion revisited: Oilfield Review. July.

Anand, V., G. Hirasaki, and M. Fleury, 2008, NMR Diffusional Coupling: Effects of Temperature and Clay Distribution: Petrophysics.

Anstey, N. A., 1991, Velocity in thin section: First Break, **9**, 449–457.

Bailey, L., E. Boek, S. Jacques, T. Boassen, O. Selle, J. Argillier, and D. Longeron, 2000, Particulate Invasion From Drilling Fluids: SPE Journal, **5**, 412–419.

Baker, L. J., 1984, The effects of the invaded zone on full wavetrain acoustic logging: Geophysics, **49**, 796–809.

Baker, L. J., and G. Winbow, 1988, Multipole P-wave logging in formations altered by drilling: Geophysics, **53**, 1207–1218.

Batchelor, G. K., 2000, An Introduction to Fluid Dynamics: Cambridge University Press.

Batzle, M. L., and Z. Wang, 1992, Seismic properties of pore fluids: Geophysics, **57**, 1396–1408.

Beard, D. C., and P. K. Weyl, 1973, Influence of Texture on Porosity and Permeability of Unconsolidated Sand: AAPG Bulletin, **57**, 349–369.

Berryman, J. G., 1980, Confirmation of Biot's theory: Applied Physics Letters, **37**, 382–384.

———, 1995, Mixture theories for rock properties, *in* Rock Physics & Phase Relations: A Handbook of Physical Constants: American Geophysical Union, volume **3** *of* AGU Reference Shelf, 205–228.

Berryman, J. G., S. R. Pride, and H. F. Wang, 2002, A differential scheme for elastic properties of rocks with dry or saturated cracks: Geophysical Journal International, **151**, 597–611.

Best, A. I., 1992, The prediction of the reservoir properties of sedimentary rocks from seismic measurements: PhD thesis, University of Reading.

Best, A. I., T. Han, and J. Sothcott, 2013, Elastic wave attenuation and electrical formation factor of shaly sandstones: Presented at the Second International Workshop on Rock Physics.

Best, A. I., and C. McCann, 1995, Seismic attenuation and pore-fluid viscosity in clay-rich reservoir sandstones: Geophysics, **60**, 1386–1397.

Best, A. I., C. McCann, and J. Sothcott, 1994, The relationships between the velocities, attenuations and petrophysical properties of reservoir sedimentary-rocks: Geophysical Prospecting, **42**, 151–178.

Biot, M. A., 1941, General theory of three-dimensional consolidation: Journal of applied physics, **12**, 110–113.

———, 1956a, Theory of propagation of elastic waves in a fluid-saturated porous solid. I. Low-frequency range: The Journal of the Acoustical Society of America, **28**, 168–178.

———, 1956b, Theory of propagation of elastic waves in a fluid-saturated porous solid. II. Higher frequency range: The Journal of the Acoustical Society of America, **168**, 179–191.

———, 1962, Mechanics of deformation and acoustic propagation in porous media: Journal of applied physics, **33**, 1482–1498.

Birch, F., 1960, The velocity of compressional waves in rocks to 10 kilobars: 1.: Journal of Geophysical Research, **65**, 1083–1102.

Black, A., H. Dearing, and B. DiBona, 1985, Effects of Pore Pressure and Mud Filtration on Drilling Rates in a Permeable Sandstone: Journal of Petroleum Technology, **37**, 1671–1681.

Blatt, H., G. V. Middleton, and R. C. Murray, 1980, Origin of sedimentary rocks.

Bloch, S., 1991, Empirical Prediction of Porosity and Permeability in Sandstones (1): AAPG Bulletin, **75**, 1145–1160.

Bourbié, T., and O. Coussy, 1987, Acoustics of Porous Media.

Bourbié, T., and B. Zinszner, 1985, Hydraulic and Acoustic Properties as a Function of Porosity in Fontainebleau Sandstone: Journal of geopysical research, **90(B13)**, 11524–11532.

Briceo, M. G., and M. Peeters, 2005, Sloping Invasion Profiles Derived from Shallow Wireline Logs.

Brown, J. M., 2014, Determination of Hashin-Shtrikman Bounds on the Effective Elastic Moduli of Polycrystals of any Symmetry: Submitted.

Brown, J. M., E. H. Abramson, and R. J. Angel, 2006, Triclinic elastic constants for low albite: Physics and Chemistry of Minerals, **33**, 256–265.

Brown, R. J. S., and J. Korringa, 1975, On the dependence of the elastic properties of a porous rock on the compressibility of the pore fluid: Geophysics, **40**, 608–616.

Budiansky, B., and R. J. O'Connell, 1976, Elastic moduli of a cracked solid: International journal of solids and structures, **12**, 81–97.

Burley, S. D., and R. H. Worden, eds., 2003, Sandstone Diagenesis: Blackwell Publishing Ltd.

Cadoret, T., 1993, Effet de la saturation eau/gaz sur les proprietes acoustiques des roches: Etude aux frequences sonores et ultrasonores: PhD thesis, Paris diderot.

Carman, P. C., 1937, Fluid flow through granular beds: Transactions-Institution of Chemical Engineeres, **15**, 150–166.

Carmichael, R., 1989, Practical handbook of physical properties of rocks and minerals, 1 ed.: CRC Press.

Castagna, J. P., M. L. Batzle, and R. L. Eastwood, 1985, Relationships between compressional-wave and shear-wave velocities in clastic silicate rocks: Geophysics, **50**, 571–581.

Chapman, M., S. V. Zatsepin, and S. Crampin, 2002, Derivation of a microstructural poroelastic model: Geophysical Journal International, **151**, 427–451.

Chen, B., and J. R. G. Evans, 2006, Elastic moduli of clay platelets: Scripta Materialia, **54**, 1581–1585.

Chen, S., R. Arro, C. Minetto, D. Georgi, and C. Liu, 1998, Methods For Computing Swi And Bvi From Nmr Logs.

Chenevert, M. E., and J. Dewan, 2001, A model for filtration of water-base mud during drilling: determination of mudcake parameters: Petrophysics.

Cheng, C. H., and M. N. Toksöz, 1979, Inversion of seismic velocities for the pore aspect ratio spectrum of a rock: Journal of geopysical research, **84**, 7533–7543.

Chi, S., C. Torres-Verdín, J. J. Wu, and F. O. Alpak, 2006, Assessment of Mud-Filtrate-Invasion Effects on Borehole Acoustic Logs and Radial Profiling of Formation Elastic Properties: SPE Reservoir Evaluation & Engineering, **9**, 553–564.

Chitale, D. V., P. Day, and G. Coates, 1999, Petrophysical implications of laboratory NMR and petrographical investigation on a shaly sand core: SPE annual technical conference, 1–9.

Ciz, R., and S. A. Shapiro, 2009, Stress-dependent anisotropy in transversely isotropic rocks: Comparison between theory and laboratory experiment on shale: GEOPHYSICS, **74**, D7–D12.

Ciz, R., A. F. Siggins, B. Gurevich, and J. Dvorkin, 2008, Influence of microheterogeneity on effective stress law for elastic properties of rocks: Geophysics, **73**.

Clark, V. A., B. R. Tittmann, and T. W. Spencer, 1980, Effect of volatiles on attenuation (Q^{- 1}) and velocity in sedimentary rocks: Journal of Geophysical Research, **85**, 5190–5198.

Close, D., D. Cho, F. Horn, and H. Edmundson, 2009, The Sound of Sonic: A Historical Perspective and Introduction to Acoustic Logging: CSEG Recorder.

Coates, G., J. Galford, D. Mardon, and D. Marschall, 1998, A New Characterization Of Bulk-volume Irreducible Using Magnetic Resonance.

Colten, V., 1986, Hydration states of smectite in NaCl brines at elevated pressures and temperatures: Clays and Clay Minerals.

Davies, J. P., and D. K. Davies, 2001, Stress-dependent permeability: characterization and modeling: SPE Journal.

Dewan, J. T., and M. E. Chenevert, 1993, Mud cake build-up and invasion in low permeability formations: application to permeability determination by measurement while drilling: Presented at the Canadian Well Logging Society Symposium, Society of Petrophysicists and Well-Log Analysts.

Diallo, M., M. Prasad, and E. Appel, 2003, Comparison between experimental results and theoretical predictions for P-wave velocity and attenuation at ultrasonic frequency: Wave Motion, **37**, 1–16.

Dvorkin, J., G. Mavko, and B. Gurevich, 2007, Fluid substitution in shaley sediment using effective porosity: Geophysics, **72**, O1–O8.

Dvorkin, J., G. Mavko, and A. Nur, 1995, Squirt flow in fully saturated rocks: Geophysics, **60**, 97–107.

Eberhart-Phillips, D., D.-H. Han, and M. D. Zoback, 1989, Empirical relationships among seismic velocity, effective pressure, porosity and clay content in sandstone: Geophysics, **54**, 82–89.

Ehrenberg, S., and P. Nadeau, 2005, Sandstone vs. carbonate petroleum reservoirs: A global perspective on porosity-depth and porosity-permeability relationships: AAPG bulletin.

Ewy, R. T., and R. Stankovic, 2013, Shale Swelling, Osmosis, and Acoustic Changes Measured Under Simulated Downhole Conditions: SPE Drilling & Completion, **25**, 177–186.

Fabricius, I. L., 2003, How burial diagenesis of chalk sediments controls sonic velocity and porosity: AAPG bulletin, **87**, 1755–1778.

Fabricius, I. L., G. T. Bächle, and G. P. Eberli, 2010, Elastic moduli of dry and water-saturated carbonates - Effect of depositional texture, porosity, and permeability: Geophysics, **75**, N65–N78.

Fabricius, I. L., C. Hø ier, P. Japsen, and U. Korsbech, 2007, Modelling elastic properties of impure chalk from South Arne Field, North Sea: Geophysical Prospecting, **55**, 487–506.

Ferguson, C., and J. Klotz, 1954, Filtration From Mud During Drilling: Journal of Petroleum Technology, **6**, 30–43.

Gal, D., J. Dvorkin, and A. Nur, 1998, A physical model for porosity reduction in sandstones: Geophyiscs, **63**, 454–459.

———, 1999, Elastic-wave velocities in sandstones with non-load-bearing clay: Geophysical Research Letters, **26**, 939–942.

Gassmann, F., 1951, Uber die Elastizitaet poroeser Medien: Vierteljahresschrift der Naturforschenden Gesellschaft, Zuerich, **96**, 1–23.

Gist, G. A., 1994, Fluid effects on velocity and attenuation in sandstones: Journal of the Acoustical Society of America of America, **96**, 1158–1173.

Goertz, D., and R. J. Knight, 1998, Elastic wave velocities during evaporative drying: Geophysics, **63**, 171–183.

Gray, D., and I. Fatt, 1963, The effect of stress on permeability of sandstone cores: Society of Petroleum Engineers Journal, 95–100.

Green, D. H., and H. F. Wang, 1986, Fluid pressure response to undrained compression in saturated sedimentary rock: Geophysics, **51**, 948–956.

Gregory, A. R., 1976, Fluid saturation effects on dynamic elastic properties of sedimentary rocks: Geophysics, **41**, 895–921.

Grochau, M., and B. Gurevich, 2009, Testing Gassmann fluid substitution: sonic logs versus ultrasonic core measurements: Geophysical Prospecting, **57**, 75–79.

Gurevich, B., D. Makarynska, O. B. de Paula, and M. Pervukhina, 2010, A simple model for squirt-flow dispersion and attenuation in fluid-saturated granular rocks: Geophysics, **75**, N109–N120.

Gurevich, B., D. Makarynska, and M. Pervukhina, 2009, Ultrasonic moduli for fluid-saturated rocks: Mavko-Jizba relations rederived and generalized: Geophysics, **74**, N25–N30.

Haldorsen, J. B. U., D. Johnson, T. J. Plona, B. K. Sinha, H.-P. Valero, and K. W. Winkler, 2006, Borehole acoustic waves: Oilfield Rev.

Hamilton, E. L., 1971, Elastic properties of marine sediments: Journal of Geophysical Research, **76**, 579–604.

Han, D.-H., 1986, Effects of porosity and clay content on acoustic properties of sandstones and unconsolidated sediments: PhD thesis, Stanford University.

Han, D.-H., and M. L. Batzle, 2004, Gassmann's equation and fluid-saturation effects on seismic velocities: Geophysics, **69**, 398–405.

Han, D.-H., A. Nur, and D. Morgan, 1986, Effects of porosity and clay content on wave velocities in sandstones: Geophysics, **51**, 2093–2107.

Han, T., A. I. Best, J. Sothcott, and L. M. MacGregor, 2011, Joint elastic-electrical properties of reservoir sandstones and their relationships with petrophysical parameters: Geophysical Prospecting, **59**, 518–535.

Hashin, Z., and S. Shtrikman, 1962, A variational approach to the theory of the elastic behaviour of polycrystals: Journal of the Mechanics and Physics of Solids, **10**, 343–352.

———, 1963, A variational approach to the theory of the elastic behaviour of multiphase materials: Journal of the Mechanics and Physics of Solids, **11**, 127–140.

Head, E., D. E. Cannon, D. Allen, and L. Colson, 1992, Quantitative Invasion Description.

Hill, R., 1963, Elastic properties of reinforced solids: Some theoretical principles: Journal of the Mechanics and Physics of Solids, **11**, 357–372.

Holt, R. M., M. Brignoli, and C. J. Kenter, 2000, Core quality: quantification of coring-induced rock alteration: International Journal of Rock Mechanics and Mining Sciences, **37**, 889–907.

Hornby, B., L. M. Schwartz, and J. Hudson, 1994, Anisotropic effective-medium modeling of the elastic properties of shales: Geophysics.

Horsrud, P., E. Sø nstebø, and R. Bø e, 1998, Mechanical and petrophysical properties of North Sea shales: International Journal of Rock Mechanics and Mining Sciences, **35**, 1009–1020.

Humbert, P., and F. Plicque, 1972, Proprietes elastiques de carbonate rhomboedriques monocristallins: calcite, magnesite, dolomie: Comptes Rendus de l'Academie des Sciences, **275**, 391–394.

Hurst, A., and P. Nadeau, 1995, Clay microporosity in reservoir sandstones: an application of quantitative electron microscopy in petrophysical evaluation: AAPG bulletin, **79**, 563–573.

Jizba, D. L., 1991, Mechanical and acoustical properties of sandstones and shales: PhD thesis, Stanford University.

Johnson, D., 2001, Theory of frequency dependent acoustics in patchy-saturated porous media: Journal of the acoustical society of America, **110**, 682–694.

Jones, T. D., 1986, Pore fluids and frequency-dependent wave propagation in rocks: Geophysics, **51**, 1939–1953.

Josh, M., L. Esteban, C. Delle Piane, J. Sarout, D. N. Dewhurst, and M. Clennell, 2012, Laboratory characterisation of shale properties: Journal of Petroleum Science and Engineering, **88-89**, 107–124.

Katahara, K., 1996, Clay mineral elastic properties: 1996 SEG Annual Meeting, 1–4.

Kendall, R. F., B. A. B. Aker, F. S. Manning, E. Donaldson, and B. A. Baker, 1975, Surface-Area Measurement of Geologic Materials: SPE journal, **15**, 111–116.

Kenyon, W. E., 1997, Petrophysical principles of applications of NMR logging: Log Analyst.

Khaksar, A., C. M. Griffiths, and C. McCann, 1999, Compresional- and shear-wave velocitites as a function of confining stress in dry sandstones: Geophysical prospecting, **47**, 487–508.

Khazanehdari, J., and C. McCann, 2005, Acoustic and petrophysical relationships in low-shale sandstone reservoir rocks: Geophysical prospecting, **53**, 447–461.

Khazanehdari, J., and J. Sothcott, 2003, Variation in dynamic elastic shear modulus of sandstone upon fluid saturation and substitution: Geophysics, **68**, 472–481.

King, M. S., 1966, Wave velocities in rocks as a function of changes in overburden pressure and pore-fluid saturants: Geophysics, **31**, 50–73.

King, M. S., J. R. Marsden, and J. W. Dennis, 2000, Biot dispersion for P- and S-wave velocities in partially and fully saturated sandstones: Geophysical Prospecting, **48**, 1075–1089.

Kleinberg, R. L., and A. Boyd, 1997, Tapered cutoffs for magnetic resonance bound water volume: Presented at the SPE Annual Technical Conference and Exhibition, Society of Petroleum Engineers.

Klimentos, T., 1991, The effects of porosity-permeability-clay content on the velocity of compressional waves: Geophysics, **56**, 1930–1939.

Knackstedt, M. A., C. H. Arns, and W. Val Pinczewski, 2005, Velocity-porosity relationships: Predictive velocity model for cemented sands composed of multiple mineral phases: Geophysical Prospecting, **53**, 349–372.

Knight, R. J., and R. C. Nolen-Hoeksema, 1990, A laboratory study of the dependence of elastic wave velocities on pore scale fluid distribution: Geophysical Research Letters, **17**, 1529–1532.

Koenders, M., 2009, Wave propagation through elastic granular and granular auxetic materials: Physica Status Solidi (b), **246**, 2083–2088.

Koga, I., M. Aruga, and Y. Yoshinaka, 1958, Theory of plane elastic waves in a piezoelectric crystalline medium and determination of elastic and piezoelectric constants of quartz: Physical Review, **109**, 1467–1473.

Kolstø, M. I., and R. M. Holt, 2012, Water in Clay and Shale - Molecular Scale and Rock Physics Modelling vs. Experiments: Presented at the 74th EAGE Conference & Exhibition.

Kozeny, J., 1927, Über kapillare Leitung des Wassers im Boden: Sitzungsberichte der WIener Akademie der Wissenschaften, **136**, 271–306.

Krueger, R., 1988, An overview of formation damage and well productivity in oilfield operations: An update: paper SPE.

Lane, H. S., 1993, Numerical Simulation Of Mud Filtrate Invasion And Dissipation.

Le Bray, Y., and M. Prat, 1999, Three-dimensional pore network simulation of drying in capillary porous media: International Journal of Heat and Mass Transfer, **42**, 4207–4224.

Lebedev, M., J. Toms-Stewart, B. Clennell, M. Pervukhina, V. Shulakova, L. Paterson, T. M. Müller, B. Gurevich, and F. Wenzlau, 2009, Direct laboratory observation of patchy saturation and its effects on ultrasonic velocities: The Leading Edge, **28**, 24–27.

Lenormand, R., 1990, Liquids in porous media: Journal of physics: Condensed matter, **2**, SA79–SA88.

Liu, X., L. Vernik, and A. Nur, 1994, Effects of saturating fluids on seismic velocities in shale: SEG Technical Program Expanded Abstracts 1994, 1121–1124.

MacBeth, C., 2004, A classification for the pressure-sensitivity properties of a sandstone rock frame: GEOPHYSICS, **69**, 497–510.

Makarynska, D., B. Gurevich, and R. Ciz, 2007, Finite Element Modelling of Gassmann Fluid Substitution of Heterogeneous Rocks: Presented at the 69th EAGE Conference and Exhibition incorporating SPE EUROPEC 2007.

Mann, R. L., and I. Fatt, 1960, Effect of pore fluids on the elastic properties of sandstone: Geophysics, **25**, 433–444.

Marion, D., 1990, Acoustical, mechanical, and transport properties of sediments and granular materials: PhD thesis, Stanford University, Dept. of Geophysics.

Marion, D., A. Nur, and H. Yin, 1992, Compressional velocity and porosity in sand-clay mixtures: Geophysics, **57**, 554–563.

Marketos, G., and A. I. Best, 2010, Application of the BISQ model to clay squirt flow in reservoir sandstones: Journal of geopysical research, **B06209**.

Martin, R., 1960, Adsorbed water on clay: a review: Presented at the Clays and clay minerals. Proceedings of the Ninth National Conference on Clays and Clay Minerals.

Matteson, A., J. Tomanic, M. Herron, D. Allen, and W. Kenyon, 2000, NMR Relaxation of Clay/Brine Mixtures.

Mavko, G., and D. L. Jizba, 1991, Estimating grain-scale fluid effects on velocity dispersion in rocks: Geophysics, **56**, 1940–1949.

———, 1994, The relation between seismic P- and S-wave velocity dispersion in saturated rocks: Geophysics, **59**, 87–92.

Mavko, G., and T. Mukerji, 1995, Seismic pore space compressibility and Gassmann's relation: Geophysics, **60**, 1743–1749.

———, 1998, Bounds on low-frequency seismic velocities in partially saturated rocks: Geophyscs, **63**, 918–924.

———, 2013, Estimating Brown-Korringa constants for fluid substitution in multimineralic rocks: Geophysics, **78**, L27–L35.

Mavko, G., T. Mukerji, and J. Dvorkin, 2003, The Rock Physics Handbook: Cambridge University Press.

Militzer, B., and H. Wenk, 2011, First-principles calculation of the elastic moduli of sheet silicates and their application to shale anisotropy: American ….

Minear, J., 1982, Clay Models and Acoustic Velocities: Presented at the Proceedings of SPE Annual Technical Conference and Exhibition, Society of Petroleum Engineers.

Mondol, N. H., K. Bjø rlykke, J. Jahren, and K. Hø eg, 2007, Experimental mechanical compaction of clay mineral aggregates - Changes in physical properties of mudstones during burial: Marine and Petroleum Geology, **24**, 289–311.

Mondol, N. H., J. Jahren, K. Bjø rlykke, and I. Brevik, 2008, Elastic properties of clay minerals: Leading edge, **27**, 758–770.

Morrow, C. A., D. E. Moore, and D. A. Lockner, 2000, The effect of mineral bond strength and adsorbed water on fault gouge frictional strength: Geophysical Research Letters, **27**, 815–818.

Mortensen, J., F. Engstrø m, and I. Lind, 1998, The relation among porosity permeability and specific surface of chalk from the Gorm Field, Danish North Sea: SPE reservoir evaluation and engineering, **1**, 245–251.

Moyano, B., K. T. Spikes, T. A. Johansen, and N. H. Mondol, 2012, Modeling compaction effects on the elastic properties of clay-water composites: Geophysics, **77**, D171–D183.

Murphy, W. F., 1982, Effects of partial water saturation on attenuation in Massilon sandstone and Vycor porous glass: The Journal of the Acoustical Society of America, **71**, 1458.

———, 1984, Acoustic measures of partial gas saturation in tight sandstones: Journal of Geophysical Research, **89**, 11549.

Murphy, W. F., K. W. Winkler, and R. L. Kleinberg, 1984, Frame modulus reduction in sedimentary rocks: The effect of adsorption on grain contacts: Geophysical research letters, **11**, 805–808.

Neasham, J. W., 1977, The Morphology Of Dispersed Clay In Sandstone Reservoirs And Its Effect On Sandstone Shaliness Pore Space And Fluid Flow Properties: Presented at the Annual Fall Technical Conference and Exhibition, Society of Petroleum Engineers.

Nelson, P. H., 1994, Permeability-porosity Relationships In Sedimentary Rocks.

Nowick, A., and B. Berry, 1972, Anelastic relaxation in crystalline solids: Academic, New York.

O'Connell, R. J., and B. Budiansky, 1974, Seismic velocities in dry and saturated cracked solids: Journal of Geophysical Research, **79**, 5412–5426.

Owen, N. A., O. R. Inderwildi, and D. A. King, 2010, The status of conventional world oil reserves—Hype or cause for concern?: Energy Policy, **38**, 4743–4749.

Paula, O. D., and M. Pervukhina, 2012, Modeling squirt dispersion and attenuation in fluid-saturated rocks using pressure dependency of dry ultrasonic velocities: Geophysics, **77**, WA157–WA168.

Pervukhina, M., D. N. Dewhurst, B. Gurevich, U. Kuila, A. F. Siggins, M. D. Raven, and H. M. N. r. Bolå s, 2008, Stress-dependent elastic properties of shales: Measurement and modeling: The Leading Edge, **27**, 772–779.

Peselnick, L., and R. a. Robie, 1963, Elastic Constants of Calcite: Journal of Applied Physics, **34**, 2494.

Pettijohn, F. J., P. E. Potter, and R. Siever, 1972, Sand and sandstones: Springer - Verlag.

Phelps, G. D., 1995, Computation of Mud Filtrate Invasion Profiles: Journal of Canadian Petroleum Technology, **34**.

Pimienta, L., J. Fortin, and Y. Gueguen, 2014, Investigation of elastic weakening in limestone and sandstone samples from moisture adsorption: Geophysical Journal International, **199**, 335–347.

Prat, M., 2007, On the influence of pore shape, contact angle and film flows on drying of capillary porous media: International Journal of Heat and Mass Transfer, **50**, 1455–1468.

Rasolofosaon, P. N. J., B. Zinszner, and H. Ling, 2009, Poroelastic equations closely examined by ultrasonic experiments in rocks: ...IV, Proceedings of the ....

Ravalec, M. L., and Y. Gueguen, 1996, High-and low-frequency elastic moduli for a saturated porous/cracked rock-Differential self-consistent and poroelastic theories: Geophysics, **61**, 1080–1094.

Revil, A., and L. M. Cathles, 1999, Permeability of shaly sands: Water Resources Research, **35**, 651–662.

Rice, J., and M. Cleary, 1976, Some basic stress diffusion solutions for fluid-saturated elastic porous media with compressible constituents: Reviews of Geophysics, **14**, 227–241.

Rosenbrand, E., 2014, Effect of temperature on sandstone permeability: Mineral fluid interaction: PhD thesis, Technical University of Denmark.

Salazar, J. M., and C. Torres-Verdín, 2008, Quantitative comparison of processes of oil- and water-based mud-filtrate invasion and corresponding effects on borehole resistivity measurements: Geophysics.

Sams, M. S., and M. Andrea, 2001, The effect of clay distribution on the elastic properties of sandstones: Geophysical Prospecting, **49**, 128–150.

Sarout, J., 2012, Impact of pore space topology on permeability, cut-off frequencies and validity of wave propagation theories: Geophysical Journal International, **189**, 481–492.

Sarout, J., and Y. Guéguen, 2008, Anisotropy of elastic wave velocities in deformed shales: Part 2 — Modeling results: Geophysics, **73**, D91–D103.

Sayers, C. M., and D.-H. Han, 2002, The effect of pore fluid on the stress-dependent elastic wave velocities in sandstones: 2002 SEG Annual Meeting.

Sayers, C. M., and M. Kachanov, 1991, A simple technique for finding effective elastic constants of cracked solids for arbitrary crack orientation statistics: International Journal of Solids and Structures, **27**, 671–680.

Sayers, C. M., J. G. V. Munster, and M. S. King, 1990, Stress-induced ultrasonic anisotrophy in Berea sandstone: International Journal of Rock Mechanics and Mining Sciences & Geomechanics Abstracts, **27**, 429–436.

Scherer, G. W., 1990, Theory of Drying: Journal of the American Ceramic Society, **73**, 3–14.

Scherer, M., 1987, Parameters Influencing Porosity in Sandstones: A Model for Sandstone Porosity Prediction: AAPG Bulletin, **71**, 485–491.

Shatilo, A. P., C. H. Sondergeld, and C. S. Rai, 1998, Ultrasonic attenuation in Glenn Pool rocks, northeastern Oklahoma: Geophysics, **63**, 465–478.

Shelton, J. W., 1964, Authigenic Kaolinite in Sandstone: Journal of Sedimentary Research, **34**.

Skempton, A., 1954, The pore-pressure coefficients A and B: Geotechnique.

Soerensen, M. K., and I. L. Fabricius, 2013, Quantifying the Effect of Squirt Flow Dispersion from Compliant Clay Porosity in Clay-Bearing Sandstones: Poromechanics V: Proceedings of the Fifth Biot Conference on Poromechanics, 249–258.

Spagnoli, G., and A. Sridharan, 2012, Liquid limit of mixtures of smectite, kaolinite and quartz powder with water and NaCl solution: International Journal of Geotechnical Engineering, **6**, 117–123.

Spencer, J. W., 1981, Stress relaxation at low frequencies in fluid-saturated rocks: Attenuation and modulus Dispersion: Journal of geopysical research, **86**, 1803–1812.

Talabi, O., and M. J. Blunt, 2010, Pore-scale network simulation of NMR response in two-phase flow: Journal of Petroleum Science and Engineering, **72**, 1–9.

Tao, G., M. S. King, and M. Nabi-Bidhendi, 2006, Ultrasonic wave propagation in dry and brine-saturated sandstones as a function of effective stress: laboratory measurements and modelling: Geophysical prospecting, **43**, 299–327.

Teeuw, D., 1971, Prediction of formation compaction from laboratory compressibility data: Transactions of the Society of Petroleum Engineers, **251**, 263–271.

Tittmann, B. R., V. A. Clark, J. M. Richardson, and T. W. Spencer, 1980, Possible mechanism for seismic attenuation in rocks containing small amounts of volatiles: Journal of Geophysical Research, **85**, 5199–5208.

Tosaya, C., 1982, Acoustical properties of clay-dearing rocks: PhD thesis, Stanford University.

Tserkovnyak, Y., and D. Johnson, 2002, Capillary forces in the acoustics of patchy-saturated porous media: Journal of the acoustical society of America, **114**, 27.

van Olphen, H., 1962, Compaction of Clay Sediments in the Range of Molecular Particle Distances: Clays and Clay Minerals, **11**, 178–187.

Vanorio, T., M. Prasad, and A. Nur, 2003, Elastic properties of dry clay mineral aggregates, suspensions and sandstones: Geophysical Journal International, **155**, 319–326.

Vernik, L., 1994, Predicting lithology and transport properties from acoustic velocities based on petrophysical classification of siliciclastics: Geophysics, **59**, 420–427.

Vo-Thanh, D., 1995, Influence of fluid chemistry on shear-wave attenuation and velocity in sedimentary rocks: Geophysical Journal International, **121**, 737–749.

Walsh, J. B., 1965, The effect of cracks on the compressibility of rock.

Wang, Y. H., and W. K. Siu, 2006, Structure characteristics and mechanical properties of kaolinite soils. I. Surface charges and structural characterizations: Canadian Geotechnical Journal, **43**, 587–600.

Wang, Z., 2002, Seismic anisotropy in sedimentary rocks, part 2: Laboratory data: GEOPHYSICS, **67**, 1423–1440.

Wang, Z., H. F. Wang, and M. Cates, 2001, Effective elastic properties of solid clays: Geophysics, **66**, 428–440.

Washburn, E. W., 1921, The Dynamics of Capillary Flow: Physical Review, **17**, 273–283.

Wilson, M., and E. Pittman, 1977, Authigenic clays in sandstones: recognition and influence on reservoir properties and paleoenvironmental analysis: Journal of Sedimentary petrology, **47**, 3–31.

Winkler, K. W., 1985, Dispersion analysis of velocity and attenuation in Berea sandstone: Journal of Geophysical Research, **90**, 6793.

Winkler, K. W., R. L. Kleinberg, and W. F. Murphy, 1986, Acoustic relaxation in sedimentary rocks: Dependence on grain contacts and fluid saturation: Geophysics, **51**, 757–766.

Winkler, K. W., and T. J. Plona, 1982, Technique for Measuring Ultrasonic Velocity and Attenuation Spectra: Journal of Geophysical Research, **87**, 10–776.

Worden, R. H., and S. Morad, 1999, Controls on Formation, Distribution and Evolution, in Clay Mineral Cements in Sandstones, *in* In Clay Minerals in Sandstones: Blackwell Publishing Ltd.

Wu, J., C. Torres-Verdín, K. Sepehrnoori, and M. Proett, 2005, The influence of water-base mud properties and petrophysical parameters on mudcake growth, filtrate invasion, and formation pressure.

Xie, J., 2001, Models for filtration during drilling, completion and stimulation operations.

Xu, C., C. Torres-Verdín, J. Ma, and W. Li, 2012, Fluid substitution analysis to correct borehole geophysical measurements acquired in gas-bearing formations invaded by oil-base mud: 2012 SEG Annual Meeting.

Yin, H., 1992, Acoustic velocity and attenuation of rocks: Isotropy, intrinsic anisotropy, and stress induced anisotropy: Ph.d, Stanford University.

Zeroug, S., H.-P. Valero, S. Bose, and H. Yamamoto, 2006, Monopole radial profiling of compressional slowness: SEG Technical Program Expanded Abstracts, 354–358.

Zimmerman, R. W., 2000, Coupling in poroelasticity and thermoelasticity: International Journal of Rock Mechanics and Mining Sciences, **37**, 79–87.

Zimmerman, R. W., W. H. Somerton, and M. S. King, 1986, Compressibility of porous rocks: Journal of Geophysical Research, **91**, 12712–12765.

Appendix A

X-ray diffraction data

Lithology	Quartz	K-feldspar	Plagioclase	Calcite	Dolomite	Clay
Colton	60	4	9	12	7	8
Kentucky	74	16	-	-	-	10
Bandera	64	-	16	-	11	9
Scioto	88	3	4	-	< 1	6
Kirby	77	12	-	8	< 1	2
Berea	90	-	5	-	< 1	4
Berea-200	92	7	0	-	< 1	< 1
Carbon tan	82	-	-	6	8	4
Stenlille-4	71	22	-	1	1	4
Stenlille-13	92	3	-	1	1	2
Boise	25	33	38	< 1	< 1	2

Table A.1: Fractional composition of the solid frame by semi-quantitative XRD.

Table A.2: Fractional composition of the solid frame by semi-quantitative XRD.

Lithology	Kaolinite	Illite	Chlorite	Smectite
Colton	-	-	-	-
Bandera	18	39	37	6
Kentucky	42	53	6	-
Scioto	51	31	15	3
Kirby	85	15	-	-
Berea	47	35	19	-
Berea-200	60	27	13	-
Carbon tan	85	15	-	-
Stenlille-4	77	15	8	-
Stenlille-13	80	9	11	< 1
Boise	53	42	5	< 1

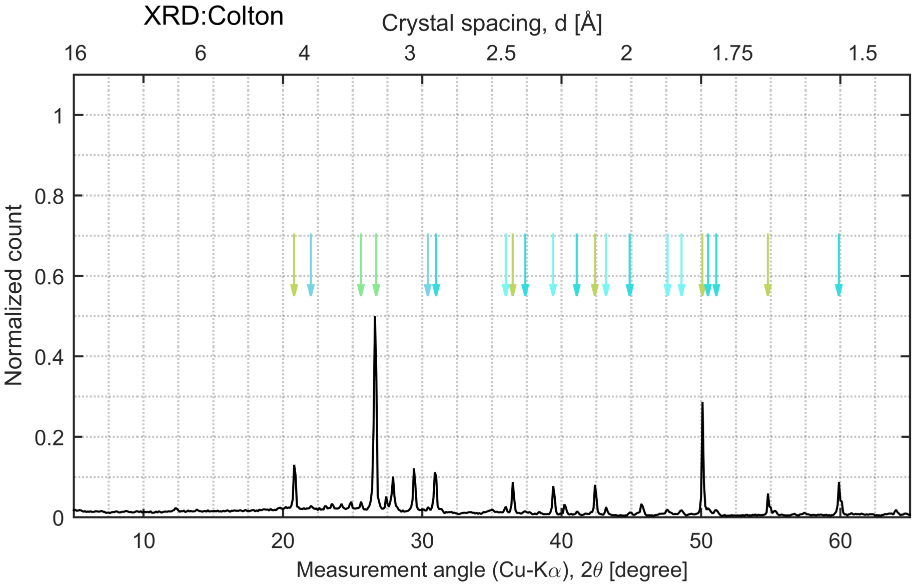

Figure A.1: XRD spectrum for Colton

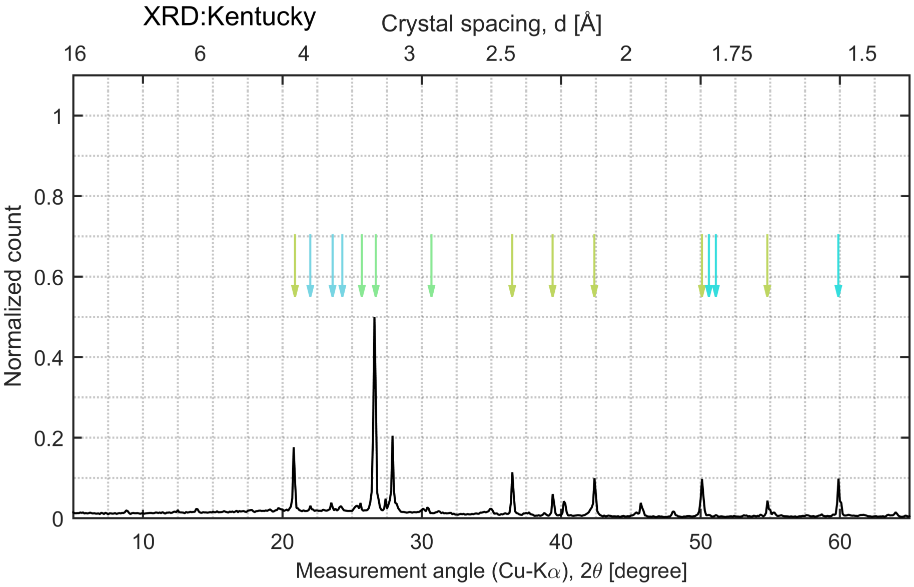

Figure A.2: XRD spectrum for Kentucky

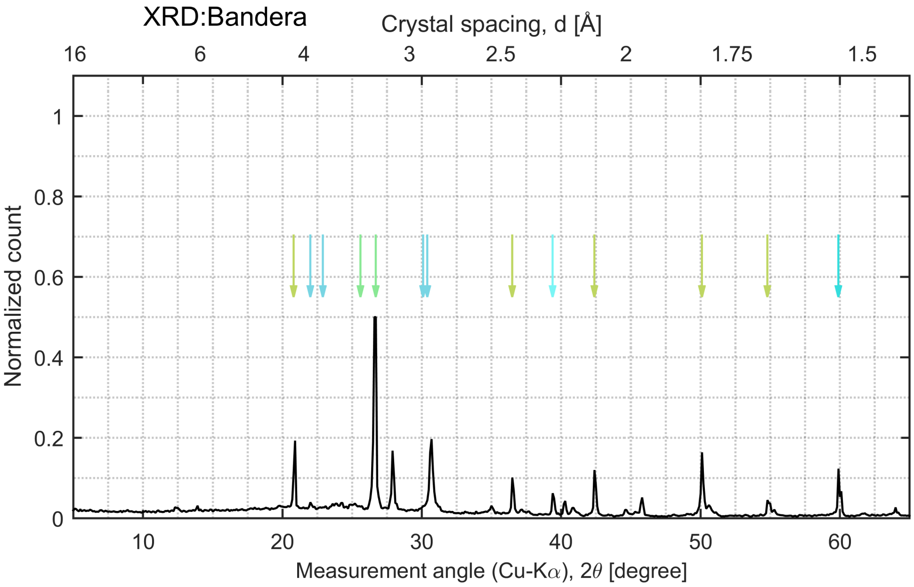

Figure A.3: XRD spectrum for Bandera

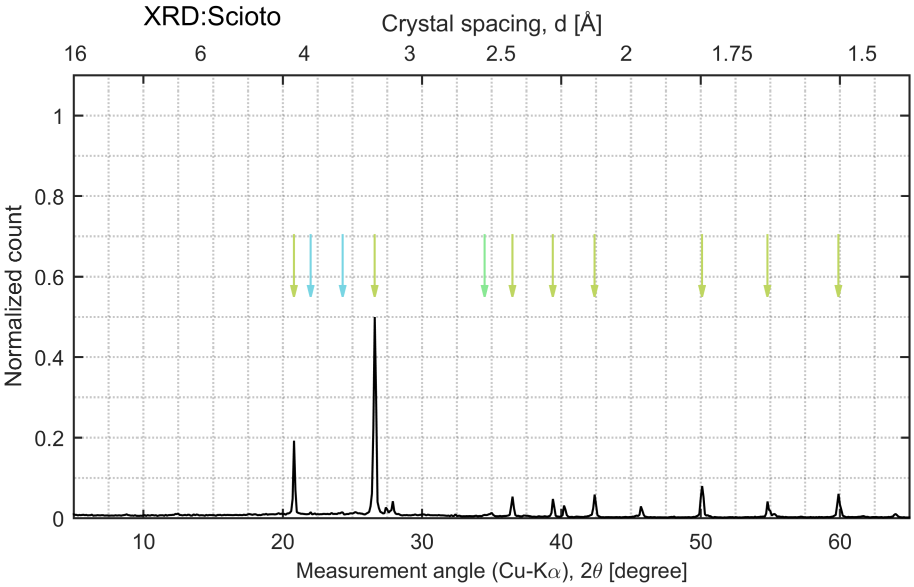

Figure A.4: XRD spectrum for Scioto

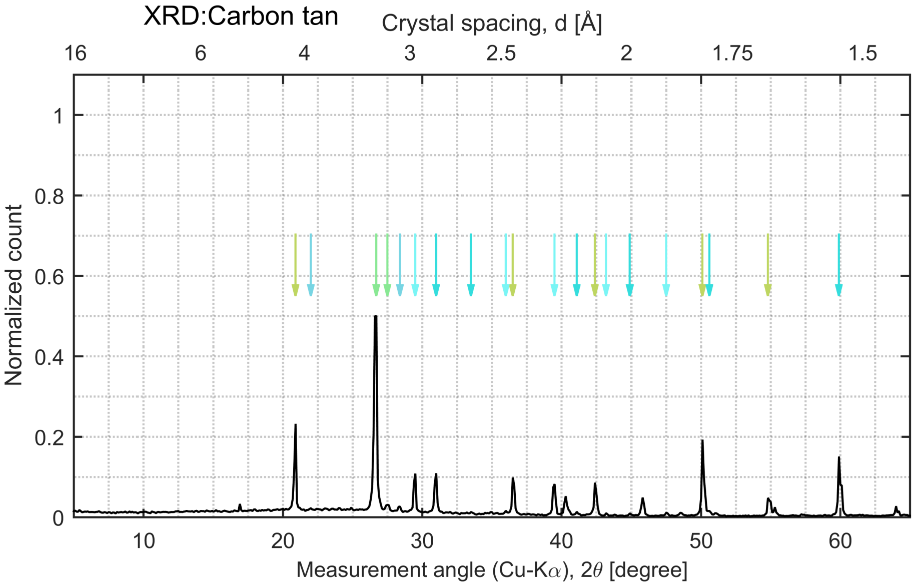

Figure A.5: XRD spectrum for Carbon tan

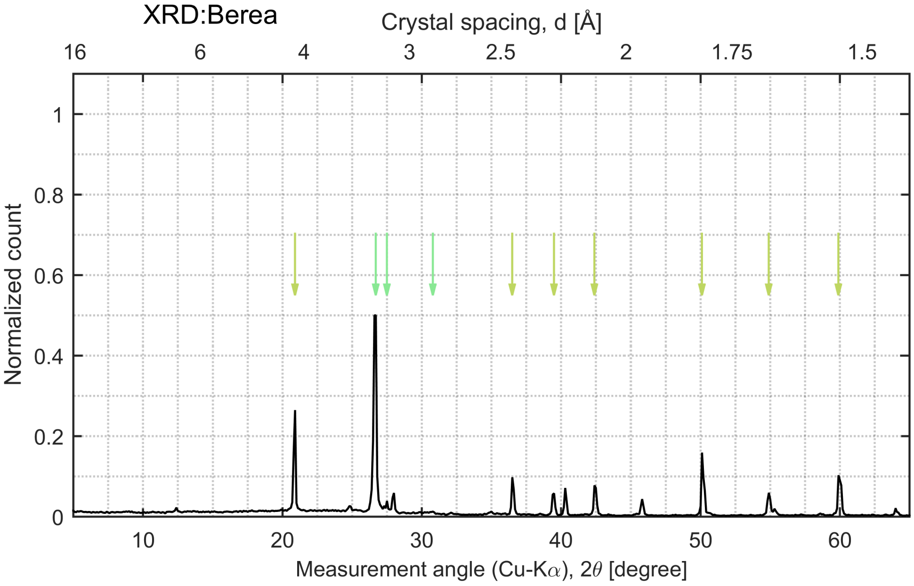

Figure A.6: XRD spectrum for Berea

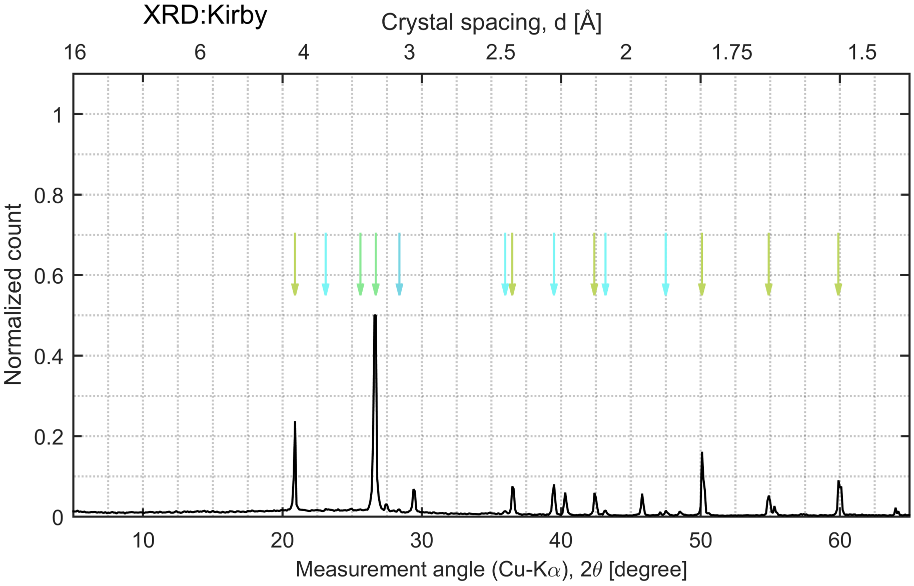

Figure A.7: XRD spectrum for Kirby

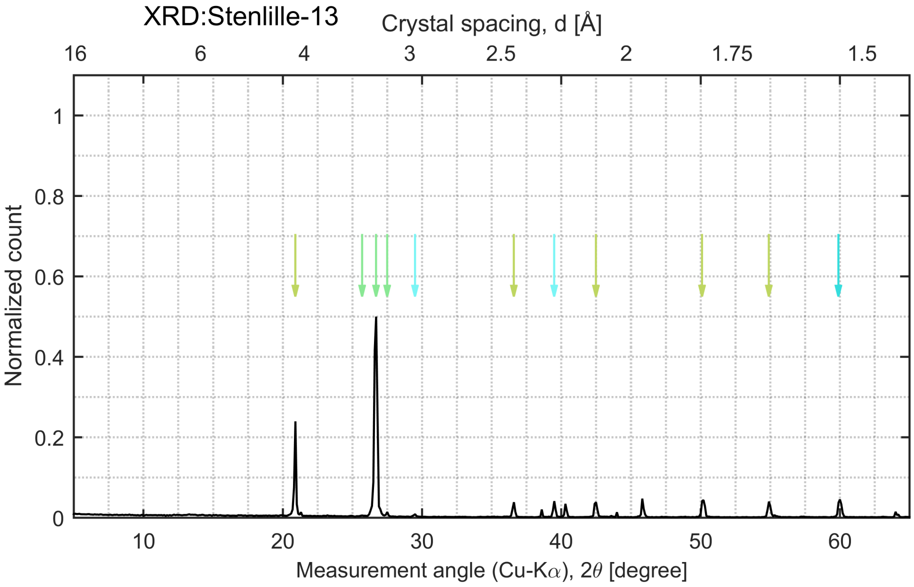

Figure A.8: XRD spectrum for Stenlille

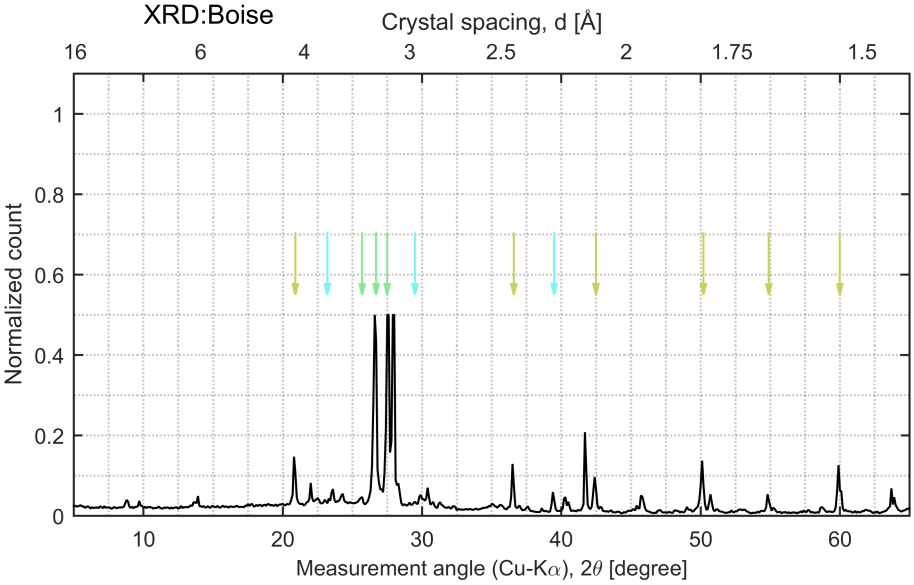

Figure A.9: XRD spectrum for Boise

Appendix B

Velocity data

Fully saturated samples

Lithology	Sample	Porosity [V/V]	Perm. [mD]	V_p^{dry} [km/s]	V_s^{dry} [km/s]	V_p^{dist} [km/s]	V_s^{dist} [km/s]	V_p^{brine} [km/s]	V_s^{brine} [km/s]
Colton	Col1	0.1150	0.36	4.00	2.52	4.25	2.32		
-	Col2	0.1142	0.34	4.18	2.47			4.36	2.32
-	Col3	0.1187	0.42	4.06	2.48				
-	Col4	0.1162	0.37						
Bandera	Ban1	0.1558	3.30	4.03	2.45				
-	Ban2	0.1507	2.43	4.00	2.48				
-	Ban3	0.1490	02.61	4.07	2.37			4.21	2.21
-	Ban4	0.1555	1.43	4.04	2.51	4.19	2.36		
Kentucky	Ken1	0.1410	0.56	4.08	2.41	4.11	2.21		
-	Ken2	0.1366	0.41	4.08	2.37				
-	Ken3	0.1392	0.52	4.07	2.30				
-	Ken4	0.1405	0.55	4.00	2.41			4.02	2.23
Scioto	Sci1	0.1758	2.34	3.89	2.32	3.93	2.20		
-	Sci2	0.1759	2.58	3.83	2.37				
-	Sci3	0.1763	2.74	3.87	2.29			3.93	2.17
-	Sci4	0.1770	2.43	3.23	1.97				
Kirby	Kir1	0.1441	26.7	4.63	2.76				
-	Kir2	0.1442	28.7	4.41	2.71			4.39	2.66
-	Kir3	0.1468	27.4	4.31	2.74	4.37	2.66		
-	Kir4	0.1414	27.0	4.51	2.68				
Berea	BerA1	0.1784	33.9	4.07	2.46			4.10	2.39
-	BerA8	0.1720	20.8	4.04	2.60			4.19	
-	BerB3	0.1883	116	3.98	2.49				
-	BerB5	0.1872	101	3.92	2.49				
-	BerC6	0.1751	41.0	4.05	2.48	4.13	2.45		
-	BerD6	0.1743	42.7	4.09	2.55			4.14	2.32
-	BerD8	0.1740	43.7	4.05	2.55	4.13	2.43		

Lithology	Sample	Porosity [V/V]	Perm. [mD]	V_p^{dry} [km/s]	V_s^{dry} [km/s]	V_p^{dist} [km/s]	V_s^{dist} [km/s]	V_p^{brine} [km/s]	V_s^{brine} [km/s]
Carbon tan	Carb1	0.1742	50.5	3.75	2.29	3.94	2.06		
-	Carb2	0.1741	53.8	3.71	2.25				
-	Carb3	0.1749	47.5	3.78	2.29			3.92	2.04
-	Carb4	0.1735	48.9	3.77	2.30				
Stenlille-13	21A	0.2804	433	3.45	2.10	3.35	1.72		
-	14	0.2700	354	3.41	2.08				
-	111	0.2902	289	3.21	1.83				
-	14B	0.2735	255	3.38	1.95			3.33	1.81
Boise	Boi1	0.2887	1250	3.34	1.93	3.47	1.86		
-	Boi2	0.2827	1306	3.34	1.93			3.47	1.85
-	Boi3	0.2905	1262	3.34	1.98				
-	Boi4	0.2823	1290	3.45	2.08				

Partially saturated samples

Lithology	Sample	Saturation [V/V]	Density [kg/m^3]	V_p [km/s]	V_p [km/s]
Colton	Col1	0.83	2467	4.19	2.33
	Col1	0.67	2448	4.18	2.37
	Col1	0.43	2422	4.09	2.38
	Col1	0.34	2411	4.07	2.39
	Col1	0.24	2400	4.05	2.37
	Col1	0.21	2396	4.02	2.38
Bandera	Ban4	0.71	2430	4.19	2.36
	Ban4	0.66	2422	4.16	2.35
	Ban4	0.52	2400	4.12	2.38
	Ban4	0.35	2374	4.07	2.41
	Ban4	0.15	2342	4.08	2.42
	Ban4	0.08	2332	4.07	2.43
Kentucky	Ken1	0.95	2443	4.09	2.21
	Ken1	0.78	2418	4.03	2.24
	Ken1	0.48	2376	4.01	2.32
	Ken1	0.25	2343	3.98	2.33
Scioto	Sci1	0.82	2351	3.84	2.22
	Sci1	0.70	2331	3.82	2.24
	Sci1	0.65	2321	3.82	2.25
	Sci1	0.60	2312	3.82	2.26
	Sci1	0.42	2283	3.83	2.25
Kirby	Kir3	0.98	2413	4.59	2.63
	Kir1	0.89	2401	4.59	2.70
	Kir3	0.67	2368	4.63	2.76
	Kir3	0.53	2348	4.51	2.64
	Kir3	0.36	2322	4.53	2.66
	Kir3	0.17	2294	4.47	2.63
	Kir1	0.11	2286	4.46	2.77

Lithology	Sample	Saturation [V/V]	Density [kg/m^3]	V_p [km/s]	V_p [km/s]
Berea	BerC6	0.99	2385	4.13	2.45
	BerC6	0.91	2371	4.11	2.44
	BerC6	0.80	2352	4.12	2.45
	BerC6	0.75	2342	4.07	2.43
	BerC6	0.69	2333	4.11	2.43
	BerC6	0.64	2323	4.09	2.43
	BerC6	0.59	2315	4.10	2.43
	BerC6	0.49	2297	4.07	2.46
	BerC6	0.43	2286	4.08	2.47
	BerC6	0.35	2274	4.08	2.47
	BerC6	0.33	2269	4.10	2.48
	BerC6	0.24	2254	4.08	2.48
Carbon tan	Carb1	1	2373	3.94	2.06
	Carb1	0.96	2364	4.00	2.12
	Carb1	0.75	2328	3.90	2.11
	Carb1	0.72	2323	3.88	2.13
	Carb1	0.60	2302	3.86	2.14
	Carb1	0.24	2239	3.68	2.13
	Carb1	0.10	2214	3.72	2.19
Stenlille-13	21A	0.97	2177	3.35	1.72
	21A	0.86	2147	3.37	1.74
	21A	0.76	2119	3.31	1.68
	21A	0.69	2098	3.31	1.71
	21A	0.55	2059	3.29	1.74
Boise	Boi1	0.98	2136	3.47	1.86
	Boi1	0.88	2107	3.41	1.86
	Boi1	0.80	2082	3.39	1.86
	Boi1	0.68	2049	3.37	1.88
	Boi1	0.52	2001	3.26	1.89

Appendix C

Journal manuscripts

How sandstone-shale mixtures are reflected in dispersion of elastic moduli

Authors	Morten Kanne Soerensen, Angus Ian Best, and Ida Lykke Fabricius
Submitted to	Geophysical prospecting
Covered in chapters:	5

Clay-squirt: Local flow dispersion on bulk modulus from the shale porosity in shale bearing sandstones.

Authors	Morten Kanne Soerensen, and Ida Lykke Fabricius
Submitted to	Geophysics
Covered in chapters:	6

Sonic log correction in sandstones by fluid substitution of the effective porosity

Authors	Morten Kanne Soerensen, and Ida Lykke Fabricius
Submitted to	Petrophysics
Covered in chapters:	7, 8, and 9

Effect of adsorbed water on contact moduli in compacted clay

Authors	Morten Kanne Soerensen, and Ida Lykke Fabricius
Submitted to	Geophysics
Covered in chapters	10

Appendix D

Conference contributions

83rd SEG Annual meeting, Houston, 2013

Unexpectedly large effects of partial oil-brine saturation on the elastic wave velocities of Berea sandstone

Morten. K. Soerensen and Ida L. Fabricius, Technical University of Denmark*

Summary

Velocities of elastic waves measured in the subsurface generally involve saturations of multiple phases. This is commonly modeled by fluid substitution using an effective fluid modulus determined. In order to address the applicability of this approach we measure the ultrasonic velocities of a Berea sandstone core partially saturated with brine and crude oil through drainage. The measurements show decreases in compressional velocity and consequently bulk modulus far exceeding the values expected from general fluid substitution. We propose the variations to be caused by the presence of kaolinite in the pores of the sandstone.

Introduction

Velocities of elastic waves are readily accessible characteristics of the subsurface. Improvements in seismic processing and rock physics modeling allow extraction of many formation parameters from seismic surveys. Well ties are employed to constrain seismic inversions. To achieve accurate well ties, good quality sonic logs are required. The penetration depth of sonic logs is however shallow, making the tool susceptible to invasion effects. Invasion leads to a partial saturation state in the area probed by the sonic log differing from the virgin formation. Correction of the measured velocities to the virgin properties is necessary for proper well ties. Corrections are currently based on extensions of Gassmann fluid substitution. Domenico (1976) suggested that fluid substitution may be applied if the fluid modulus is replaced by an effective modulus given by the iso-stress average of the constituent phases. This concept was expanded by Mavko and Mukerji (1998) who separated the behavior into two extreme bounds. The bounds are defined from the pressure distribution between the phases of the saturant. Which bound is realized depends on the frequency of the elastic wave and the flow properties of the formation. A fluid phase with a low modulus will have a low pressure induced and a fluid phase with a high modulus will have a high pressure induced. If the frequency is low enough a single average pressure will be established in the pore-space. This corresponds to the case proposed by Domenico (1976) and constitutes the lower bound of Mavko and Mukerji (1998). If on the other hand the initial pressures remain due to low mobility or high frequency the upper bound of Mavko and Mukerji (1998) is realized.

Many studies have been devoted to the study of partial saturations in the literature. Generally studies are involved with partial saturations of gas and brine, motivated by the very large influence of gas on the elastic wave velocities. Common to all studies is that the acoustic response is dependent on the saturation mechanism. Knight and Nolen-Hoeksema (1990) observed hysteresis on the ultrasonic velocities in sandstones saturated with gas and brine depending on whether the saturation was prepared through drainage or imbibitions. Cadoret et. al (1995) using CT imaging established that the distribution of fluid phases depend on the saturation process with drainage leading to pores saturated with either phase while imbibition caused pores to be saturated by both phases. Saturations achieved through drainage is best described by the upper bound and saturations prepared through imbibitions are best described by the lower bound.

Data involving measurements of elastic wave velocities in a system of two fluid systems is scarce due to the tightness of the bounds predicted by Mavko and Mukerji (1998). Hereby no significant effect is expected. Some data show, however, that the distribution of the fluid phases in the pore-space is not only dependent on whether the saturation is prepared by drainage of imbibitions, but also on the dynamics of the saturation. Specifically Lebedev et al. (2009) found that a shift between the upper and lower bound was dependent on the flow velocity involved in preparation of the saturation. This may suggest that different behavior is achieved depending on whether saturations are prepared from pressure driven invasion or by evaporation as is the common method of preparing partial saturations of gas and brine.

Since invasion is a pressure driven phenomenon and usually a drainage process we wish to study the effect of a pressure driven drainage of an oil invading a water bearing sandstone and the consequences on the acoustic velocities.

Theory

If the phases of the saturant are homogeneously dispersed the effective modulus of the fluid is given as the harmonic mean of the constituents:

$$\frac{1}{K_{\mathrm{f}}^{\mathrm{eff}}} = \left\langle \frac{1}{K_f} \right\rangle$$

Where K_f refer to the moduli of the individual fluid phases. The effective modulus of the saturated rock can then be calculated using Gassmann fluid substitution.

Unexpected effect of partial oil-brine saturation on elastic wave velocity

The upper bound is calculated as if the different parts of the rock are completely saturated by one phase. If the shear modulus is unaffected by the fluid saturation the effective modulus of the rock may then be exactly determined as the harmonic average of the compressional moduli of the patches (Hill, 1963):

$$\frac{1}{K_{sat} + 4G/3} = \left\langle \frac{1}{K_{sat}^{f} + 4G/3} \right\rangle$$

Where G denotes the shear modulus of the rock and K^f_{sat} denotes the rock saturated with the individual fluid phases. Figure 1 show these bounds for the Berea sandstone studied here saturated with 35.000 ppm brine and gas and 35.000 ppm brine and oil. The upper and lower bound for the oil/brine system can almost not be distinguished due to the low contrast between the moduli of the brine at 2.36 GPa and that of the oil at 1.6 GPa. Both fluid moduli are calculated using the relations of Batzle and Wang (1992).

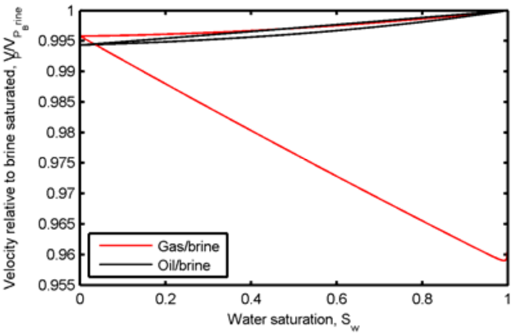

Figure 1 shows the bounds predicted by fluid substitution for the Berea sandstone studied here in the case of gas/brine and oil/brine saturations.

Method

We experimentally prepare partial saturations of crude oil and brine in a Berea sandstone core. The characteristic of the sample is given in Table 1.

Table 1 gives the data for the Berea sample studied.

Sample	Porosity	Permeability	Grain density
	[%]	[mD]	[g/cm^3]
BER1	17.20	20.8	2.668

The fluids used are a 35.000 ppm NaCl brine and a light crude oil taken from the South Arne field in the North Sea. The properties of the fluids applied are given in Table 2.

Table 2 give the basic properties of the fluids involved in the preparation of the saturations.

Fluid	Density	Bulk modulus
	[g/cm^3]	[GPa]
Brine	1.023	2.36
Crude oil	0.843	1.6

Ultrasonic measurements are performed using a pulse transmission technique, measuring both compressional, and shear velocities. The central frequency of both transducers is approximately 200 kHz. Initial measurements are conducted on a twin plug in order to determine the stress necessary to reach steady velocities as well as determine Poissons ratio in order to determine the ratio of axial to radial stress in order to simulate uniaxial compaction. Ultrasonic velocities are recorded between 5 MPa and 40 MPa axial stress under uniaxial strain loading conditions.

Saturations are prepared using a porous plate. The sample is completely saturated with brine. Saturation by brine is done by first drawing a vacuum over the sample and then introducing the brine. The sample is then left at vacuum for 24 hours. Following this the sample is immersed in brine and pressurized to 100 bar for 48 hours. The saturation is determined by Archimedes test to be above 99%.

After the initial saturation ultrasonic velocities are measured and the sample is inserted in the core holder with a 15 bar porous plate. Mercury intrusion data is used as a guide to estimate the expected saturations from a given capillary pressure. The 4 pressure steps chosen are given in Table 3

Table 3 shows the capillary pressure steps employed and the resulting saturations, determined from weight and production of water.

	Step 1	Step 3	Step 3	Step 4
Pressure	0.08 bar	0.3 bar	1 bar	4 bar
S_{oil}	40 %	50%	60%	80%

Results

Both shear and compressional velocities are recorded for each saturation step as well as for the dry and brine saturated cases. The velocities are seen in Figure 2.

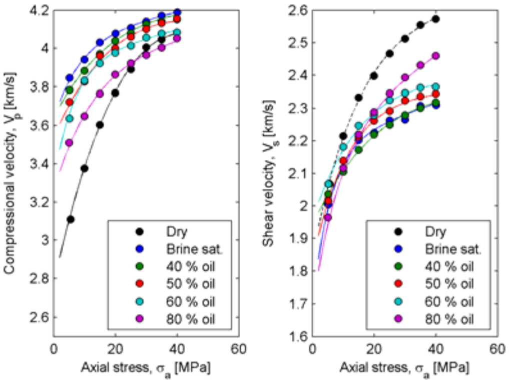

Figure 2 show the compressional and shear velocity as a function of axial stress.

Fits are made to the velocities based on the functional relation suggested by Khaksar et al. (1999). These fits guide the eye and illustrate the different development between the dry and the saturated cases. The velocity increase is much less steep for the saturated cases than for the dry. For the last pressure step the behavior approach the dry measurements. For the shear velocity the dry sample and the sample with the highest oil saturation show similar behavior while the remainder group close together.

At each saturation step the weight of the sample is recorded and based on this the densities are determined and from these the moduli can be determined. These are shown in Figure 3.

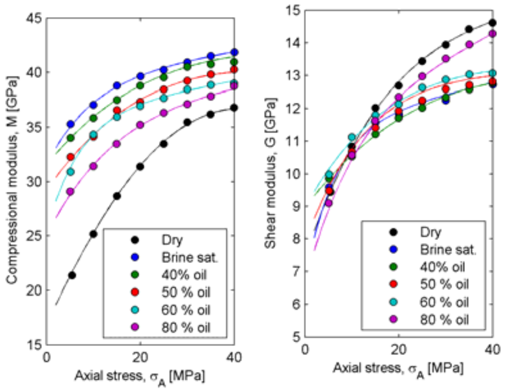

Figure 3 shows the compressional and shear moduli at each saturation step and at dry and brine saturated conditions.

The moduli behave much like the velocities the only difference in ordering is the dry compressional modulus which falls below the high oil saturation point, contrary to the velocities. This shift is due to the high density contrast between the dry and the oil saturated case.

As seen in Figure 3 the influence of oil saturation is largest on the compressional modulus. In order to separate the effects due to compression and shear we extract the bulk modulus. The bulk moduli for the measurements at the highest axial stress are shown in Figure 4. The values are taken at the highest stress to minimize effects caused by micro-cracks.

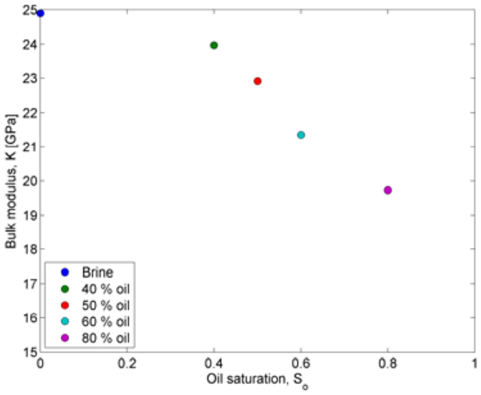

Figure 4 shows the bulk moduli at the different saturations at 40 MPa axial stress.

Mercury intrusion data have been converted to a pore-throat distribution as seen in Figure 5.

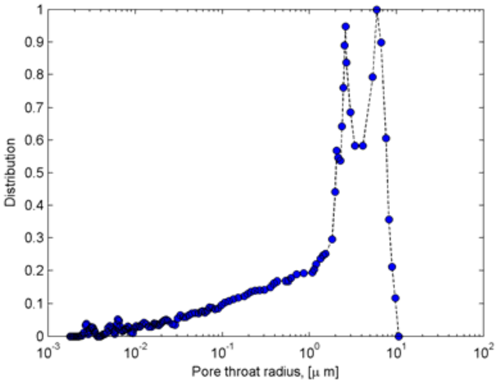

Figure 5 showing the pore-throat distribution attained from mercury intrusion. A clear bimodal distribution and a long tail with small pores are seen.

On Figure 5 we see a clear bimodal distribution with a long tail at low pore-sizes. SEM backscattering images was also taken as seen in Figure 6.

Unexpected effect of partial oil-brine saturation on elastic wave velocity

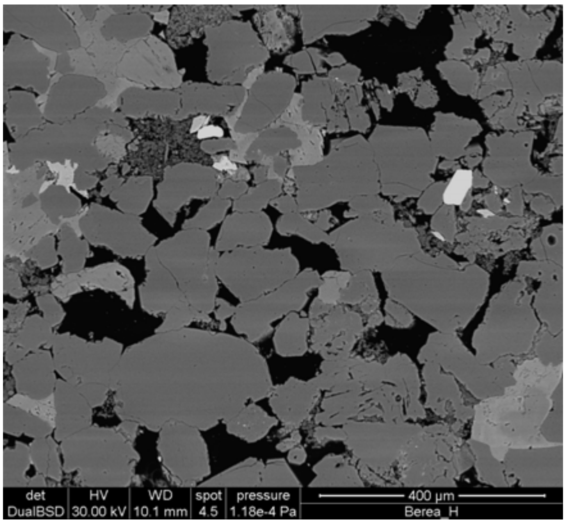

Figure 6 shows an SEM image of a thin section of the Berea sandstone. We see that some of the pores are completely filled with clay, identified as kaolinite.

In Figure 6 we see many pores filled with clays which are identified as kaolinite. This observed bimodal pore-size distribution is ascribed to the large open pores and the smaller pores in the pore-filling clay as seen in Figure 6.

Discussion

It is evident by comparing Figure 1 to Figure 4 that the observed change in bulk moduli far exceeds the predictions by the bounds. If we observe the bimodal pore-size distribution along with the SEM evidence of pore-filling kaolinite we suggest that this presence of kaolinite cause the large effect. Because some of the pores are filled with kaolinite the porosity differ from the measured values. The actual porosity may be determined as:

$$\phi_{\text{true}} = \phi_{measured} + \chi\left(1-\phi_{\text{clay}}\right)$$

We use this value for the porosity in the fluid substitution. The results of the substitution are shown in Figure 7 relative to the measured values.

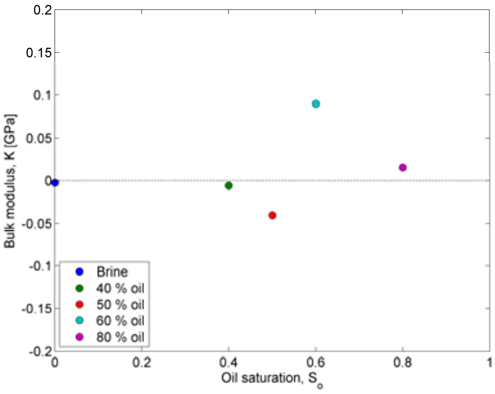

Figure 7 shows the comparison of the modeled bulk moduli and measured moduli.

In the fully brine saturated case the effective fluid modulus is determined as the harmonic average between the water saturated kaolinite and the brine in the larger pores.

For the next two saturation steps the oil pressure is such that the oil will only enter the large pores and the effective fluid modulus can be determined as the harmonic average between the water saturated kaolinite and the mixture of oil and water in the large pores.

For the third step the capillary pressure is assumed to be sufficient for oil to enter the pores filled with kaolinite. The presence of oil in the kaolinite reduces the modulus of this phase and the dehydration of the kaolinite causes the structure of the kaolinite to diminish whereby the modulus is decreased further. The effective modulus of the pore-filling material is given by the harmonic average of the weakened kaolinite with partial oil saturation and the mixture of oil and water in the quartz porosity.

For the fourth step the invasion of the invasion of the Kaolinite continues. The effective fluid modulus can be determined as the harmonic average of the reduced kaolinite modulus and the mixed oil and brine modulus.

Conclusion

We have carried out measurements of ultrasonic velocities for partial oil-brine saturations of Berea sandstone. We found that the decrease in compressional velocity and bulk modulus is significantly larger than expected, based on the bounds normally employed in modeling of partial saturation. The decrease in bulk modulus was modeled by explicitly incorporating the effects of kaolinite in the pore space and the effect of oil saturation on this.

2nd International workshop on rock physics, Southampton, 2013

Second International Workshop on Rock Physics
Southampton
4-9 August 2013

Modulus changes caused by pore-filling clays in partially saturated sandstones

Morten Kanne Soerensen [a] and Ida Lykke Fabricius[a].

[a]*Center for Energy Resources Engineering, Department of Civil Engineering, Technical University of Denmark;*

Summary

We carried out measurements of elastic wave velocities in Berea sandstones saturated with oil and brine. We found moduli changes exceeding the values predicted by Gassmann fluid substitution. Using mercury intrusion data we link these changes in moduli to the presence of pore-filling clays. The findings suggest that at high confining pressure, communication of pressure between clay dominated pores and surrounding high mobility porosity is a substantial cause of dispersion.

Introduction

Elastic wave velocities are some of the most readily accessible data from the subsurface e.g. through seismic surveys or sonic logs. For the vast majority of cases relevant to exploration measurement of elastic velocities will be done in formations containing more than one fluid. Knowledge of the interaction between the rock and the saturating fluid mixture resulting in the observed elastic wave velocity is therefore crucial to rock physics modelling of elastic wave velocities. Modelling of the fluid effects on elastic moduli of rocks are commonly done using Gassmann fluid substitution incorporating multiple saturant phases through effective fluid moduli (Mavko and Mukerji, 1998). Studies involving partial saturation of gas and water in Berea sandstone have indicated an intimate link between pore structure and the elastic response to saturation with multiple phases (Goertz and Knight, 1997). We wish to address such relations with emphasis on the relation between the dynamics of the saturation preparation and the effects on elastic wave velocities. Therefore we employ a pressure driven porous plate technique where brine is displaced by crude oil. This saturation process is inherently a two phase flow system, thus resembling the fluid dynamics of the subsurface more closely. Furthermore we couple the results to the pore structure of the rock by obtaining mercury intrusion data allowing us to evaluate the properties of the pores saturated at a given pressure step.

Methods

Two Berea sandstone samples are used with the properties given in Table 1. The properties of the brine and crude oil used for saturations are given in Table 2.

Ultrasonic compressional and shear wave velocities are measured at 40 MPa axial stress at each saturation step using a pulse transmission method with a central frequency of 200 kHz for both shear and compressional waves.

Table 1 giving the properties of the samples studied.

Sample	Porosity, [%]	Grain density, [g/cm^3]	Permeability, [mD]
BER1	17	2.669	19
BER2	21	2.663	280

Table 2 showing the properties of the fluids used for the saturations

Fluid	Density, [g/cm^3]	Bulk modulus, [GPa]
Brine, NaCl 3.5% wt	1.023	2.36
Light crude oil	0.843	1.6

Results

Figure 1 shows the distribution of pore throat radii for the two samples obtained from mercury intrusion. Assuming a drainage displacement of brine i.e. a water wet system we can evaluate which parts of the pore-space are saturated with oil at the given pressure steps. This saturation distribution is illustrated by the colouring. SEM images of BER1 shows kaolinite present in pores, consistent with earlier studies conducted on Berea sandstone (Churcher et al., 1991). For both samples we assign 1 µm as the threshold between clay dominated pores and open pores. We see that for both samples the first two saturation steps only affect the open pores while pressure step 3 allows oil to enter the clay dominated pores.

Figure 2 shows the moduli obtained from the ultrasonic velocities at 40 MPa axial stress. Initially we see a decreasing compressional modulus for BER1 (Fig. 2a) as the oil saturation increases and an increasing shear modulus from the third saturation step. Similar behaviour is evident for BER2 (Fig. 2b). For BER1 the compressional modulus decreases between the fully brine saturated state and the first partial saturation at 40 % oil. Following this initial decrease the modulus decreases only slightly. Then between 50 % oil saturation and 70% oil saturation the moduli decreases significantly again. For both BER1 and BER2 the shear modulus remain unchanged until the third saturation step where a significant increase is observed and the maximum modulus is achieved at the highest oil saturation achieved.

Combining these observations with the estimates of oil distribution in the pore network obtained from Figure 1 we can identify the mechanism of the different regions as denoted in Figure 2. At full brine saturation the pores dominated kaolinite are isolated from the open pores at the time scales imposed by the frequency. The clay dominated pores are therefore unrelaxed and the porosity involved in the fluid substitution is reduced to the open porosity.

Based on Figure 1 the effective porosity of BER1 is about 60 % of the porosity and for BER2 about 80% of the porosity present. Fluid substitution may then be carried out on the open porosity incorporating the clay dominated pores into the mineral modulus as suggested by Dvorkin et al. (2007).

At the first saturation step oil have invaded the open porosity and reduced the effective modulus of the fluid in these pores. Given the size of the pores and the consequent high mobility of the fluid in these we may model the effective modulus of the fluid mixture by the relaxed lower bound proposed by Mavko and Mukerji (1998). Substituting the brine with this effective fluid in the open porosity results in the decrease of compressional modulus observed in the first saturation step.

Since the high mobility in the open pores allows for relaxation of the fluids the effective modulus of the fluid in the open pores is dominated by the oil modulus both at the first and second saturation step. Therefore the addition of more oil into the open porosity between saturation step 1 and 2 only reduce the compressional modulus slightly.

Between the second and third saturation step oil enters the clay dominated porosity reducing the effective modulus of the clay. This causes a decrease in the effective mineral modulus and consequently the compressional modulus decreases. For BER1 the fourth saturation step introduce more oil into the clay dominated porosity further reducing the compressional modulus.

The increase in shear modulus as the oil is allowed to enter the clay-dominated porosity is not encompassed by the effective porosity model. The stiffening is however not evident in the compressional moduli suggesting that the shear stiffening is a dynamic effect associated with the shear excitation of the rock and not with the mechanical structure of the mineral frame.

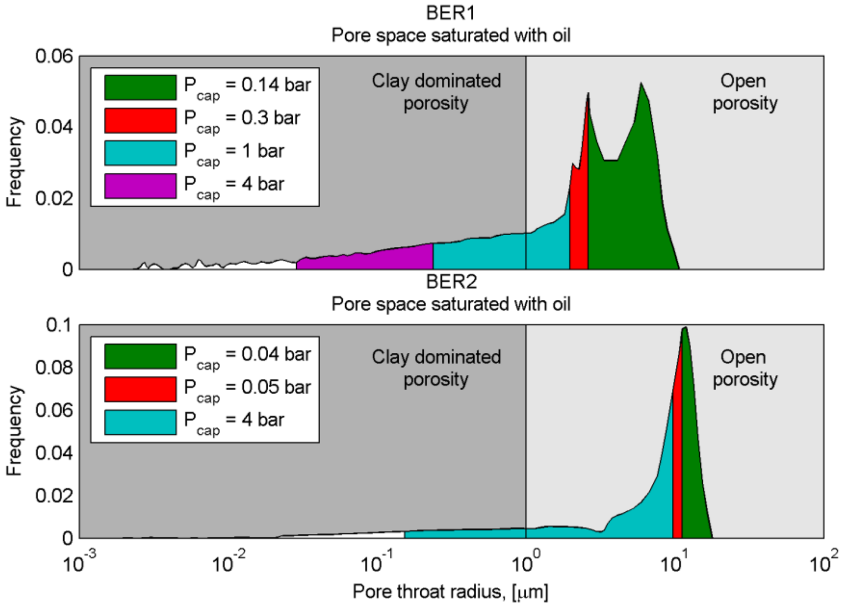

Figure 1.Distribution of pore throat radii for the two Berea samples obtained by mercury intrusion. The pore size theoretically accessible at each saturation step is indicated by the colouring.

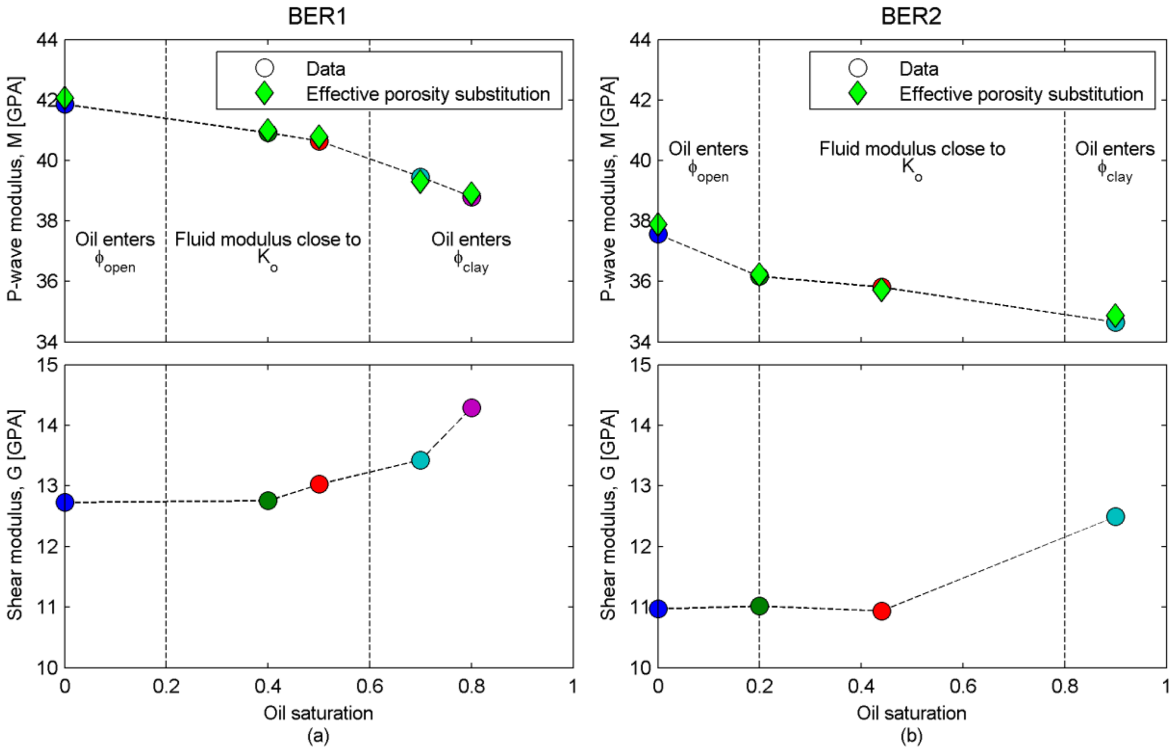

(a)

(b)

Figure 2.Shows the compressional moduli and shear wave moduli for BER1 (a) and BER2 (b). Fluid substitution predictions are obtained using an effective porosity approach assuming no pressure communication between clay dominated pores and surrounding porosity.

Conclusions

We measured the elastic wave velocities of Berea sandstone with partial oil-brine saturations prepared using multiphase flows. By comparing the resultant elastic moduli with the possible saturation of the pore network measured by mercury intrusion we found evidence that fluid related compressional wave dispersion in Berea sandstone was caused by unrelaxed pressure gradients between pores dominated by clay and open pores.

References

Churcher, P., French, P., Shaw, J. and Schramm, L., 1991, Rock properties of Berea sandstone, Baker dolomite, and Indiana limestone, *SPE International Symposium on Oilfield Chemistry*.

Dvorkin, J., Mavko, G., and Gurevich, B., 2007, Fluid substitution in shaley sediment using effective porosity, *Geophysics,* **72,** O1-O8.

Goertz, D., and Knight, R. 1997, Elastic wave velocities during evaporative drying, *Geophysics,* **63**, 171-183.

Mavko, G., and Mukerji, T., 1998, Bounds on low-frequency seismic velocities in partially saturated rocks, *Geophysics* **63**, 918-924.

5th Biot conference on poromechanics, Vienna, 2013

Quantifying the effect of squirt flow dispersion from compliant clay porosity in clay bearing sandstones

M. K. Soerensen[1] and I. L. Fabricius[1]

[1]Center for Energy Resource Engineering, Department of Civil Engineering, Technical University of Denmark, Brovej 118, 2800 Kgs. Lyngby; PH (+45) 30292813; email: moks@byg.dtu.dk

ABSTRACT

Compliant porosity in the form of cracks is known to cause significant attenuation and velocity dispersion through pore pressure gradients and consequent relaxation, dubbed squirt flow. Squirt flow from cracks vanish at high confining stress due to crack closing. Studies on clay bearing sandstones, however, show high attenuation and velocity dispersion remaining at high confining stress. Such dispersion is proposed to be caused by pressure gradients induced by compliant porosity within clay inclusions. By modeling the response of two extreme systems we quantify the possible effects of such clay-squirt flow on the bulk modulus of a clay bearing sandstone. The predicted magnitude of the clay-squirt effect on the bulk modulus is compared with experimental data. The clay-squirt effect is found to possibly account for a significant portion of the deviances from Gassmann fluid substitution in clay-bearing sandstones.

INTRODUCTION

Fluids affect the elastic properties of porous rocks through pore pressure induced by mineral frame compression. Gassmann (1951) quantified the effects of fluid on the bulk modulus and introduced the concept of a frame modulus. Gassmann fluid substitution quantifies the fluid effect on elastic properties under the assumption of isotropy and homogeneity of both frame and fluid properties. These assumptions preclude dynamic effects associated with the time scale involved in compression by acoustic waves. Experimental data show elastic moduli exceeding those predicted by fluid substitution from measurements of frame moduli on dry samples. Such modulus increase has been explained by gradients in the pore pressure induced in compliant areas of the pore network with high specific surfaces allowing the retention of the induced pressure. The archetype of such porosity has through the development of the squirt theory been that of cracks (Mavko and Jizba, 1991). Such cracks are either present as unloading strain cracks caused by coring or inherent at grain contacts. One unique feature of such cracks exploited by Mavko and Jizba (1991) is their inherent stress dependent compressibilities. At high stresses cracks will have reduced sufficiently in size so that their compressibilities no longer makes them weaker than the average of the mineral frame. This makes squirt effects associated with cracks stress dependent by nature and they therefore should vanish at high stress. Experimental data conducted on clay-rich samples have, however shown that moduli in excess of those predicted by fluid substitution remain at high stress (Han, 1986; Best and McCann, 1995). Best et al. (1994) suggested these modulus changes to be caused by squirt flow from compliant clay inclusions within the mineral frame. The moduli of clay inclusions will have a limited stress dependency and will therefore not be evident in the relation between applied stress and elastic properties. Pore pressure gradients are however likely to be present between the inclusions and the surrounding porosity. Therefore squirt stiffening may be present at high stresses due to these inclusions.

In this study we model the possible magnitude of the clay-squirt effect from compliant clay porosity. The treatment is limited to an investigation of the possible maximum magnitude of the effect not including any considerations of the dynamics of the system linking it to frequency. The model is based on the bound averaging method (BAM) and two extreme cases are considered, in between which the possible values of a system lie.

THE MODEL

We observe a clay bearing sandstone as a composite composed of a quartz frame and a clay frame. Squirt flow dispersion is caused by pore pressure gradients requiring a way of expressing the pressure distribution between the two individual frames. We deal with two extreme cases illustrated in Figure 1 for which the stress distribution can be accessed.

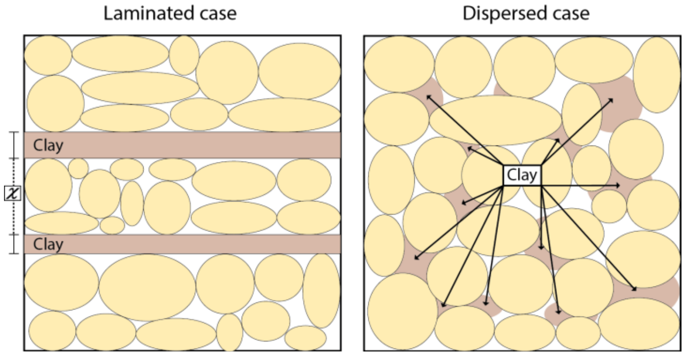

Figure 1 shows the two extremes of clay distribution observed. The laminated case corresponds to the lower HS bound and the dispersed to the upper HS bound

In the first case, clay is deposited as laminae in the quartz frame and in the second case clays are present as pore-filling material. In the laminated case clay is load bearing and a uniform stress is applied to all parts of the composite. For the dispersed case the stress is applied to the quartz frame and only propagated to the clay frame through the induced pore pressure.

Initially a pressure is induced in the pores of the different mineral frames; high pressure in the compliant frame, low pressure in the stiff frame. If sufficient time is available pressure will diffuse from the high pressure frame to low pressure frame resulting in a uniform pore pressure in the end stage. The result is a softening of the compliant frame and a stiffening of the stiff frame. Modulus dispersion is caused by the different response of the mineral frames to a change in pore pressure.

We observe the bulk modulus of the quartz/clay composite to be dependent on the moduli of the individual frames and the volumetric fraction of the clay frame $K_B\left(K_q,K_c,\chi\right)$. Where K_B,K_q,K_c denote the composite, quartz frame and clay frame bulk modulus respectively. The volumetric clay fraction is given by χ. Clay-squirt stiffening is the difference between the composite bulk moduli in the case with equilibrated pore pressures and that with unequilibrated pore pressures :

$$\Delta K = K_B^{uneq} - K_B^{eq} = K_B\left(K_q^{P_q},K_c^{P_c},\chi\right) - K_B\left(K_q^{P_{avg}},K_c^{P_{avg}},\chi\right)$$

An explicit functional relation between the bulk moduli of the mineral frames and the composite bulk modulus is needed to combine the effects on the individual mineral frames into the composite bulk modulus. Marion and Nur (1991) suggested that a weighted average between the upper and lower Hashin-Shtrikman (HS) bounds is uniquely determined by the geometry of the frame whereby the bulk modulus of a composite frame can be quantified by the relative fractions of the constituents and the weighted average given as:

$$x = \frac{K\left(K_q,K_c,\chi\right) - K_{\min}^{HS}\left(K_q,K_c,\chi\right)}{K_{\max}^{HS}\left(K_q,K_c,\chi\right) - K_{\min}^{HS}\left(K_q,K_c,\chi\right)}$$

The HS bounds are determined using the formulation of Berrymann (1995). The effect of an induced pore pressure normalized by the applied stress may be expressed as (Dvorkin and Nur, 1995):

$$K_{sat} = \frac{K_{dry}}{1+\alpha\dfrac{dP}{d\sigma}} \tag{1}$$

Where K_{sat} and K_{dry} denote the saturated and dry bulk modulus. P gives the pore pressure, σ is the stress applied to the frame. Stress and pore pressure acts opposite to each other such that $\frac{dP}{d\sigma}$ is negative as seen later. Therefore it is always true that $K_{sat} > K_{dry}$. Biot's coefficient, α, is given by (Biot, 1941):

$$\alpha = 1 - \frac{K_{dry}}{K_0}$$

Where K_0 is the mineral modulus. The ratio of induced pore pressure to applied stress is dependent on the frame modulus, K_{dry}, fluid modulus, K_f porosity ϕ and Biot's coefficient. The expressions involved are (Dvorkin and Nur, 1995):

$$\begin{aligned} \frac{dP}{d\sigma} &= -\frac{1}{\alpha\left(1+\frac{K_{dry}\phi}{\alpha^2 F}\right)} \\ \frac{1}{F} &= \frac{1}{K_f} + \frac{1}{\phi Q} \\ Q &= \frac{K_0}{\alpha - \phi} \end{aligned} \tag{2}$$

Using Equation 1 and Equation 2 we can determine the unequillibrated bulk modulus of the mineral frames and combine them to give the composite modulus. The equilibrated composite bulk modulus can be calculated by working out the induced pressures in the mineral frames and then determine the average pressure after equilibration. The mineral frame bulk moduli can then be determined by Equation 1and the composite bulk modulus by the BAM. In order to carry out the calculation knowledge of the stress distribution needs to be assumed.

Laminated case

In the laminated case both the quartz and the clay frame are subjected to the same stress. Since the stress works equally on both the mineral frames and the composite frame we can determine the averaged induced pore pressure after equilibration as the average between the induced pore pressures weighted by the ratio of mineral frame pore volume relative to total pore volume:

$$\frac{dP_{eq}}{d\sigma} = \frac{V_p^q \frac{dP_q}{d\sigma} + V_p^c \frac{dP_c}{d\sigma}}{V_p^q + V_c^c} = \frac{(1-\chi)\phi_q \frac{dP_q}{d\sigma} + \chi\phi_c \frac{dP_c}{d\sigma}}{V_p}$$

Where V_p^q and V_c^q denote the pore volumes of the quartz and clay frames respectively. Porosities of the two frames are given by ϕ_q and ϕ_c and the total pore volume by V_P. This averaged induced pressure can now be substituted into Equation 1 to get the equilibrated moduli for the two mineral frames. These are combined to yield the composite modulus. To do this we must note that the laminated case with equal stress distribution corresponds to the lower HS bound and a BAM value of 0.

In the unequilibrated case no pressure diffusion is allowed to occur so the originally induced pore pressure in the mineral frames remain and the composite bulk modulus can be determined by applying the BAM to the mineral frame moduli determined through Equation 1 and Equation2.

Dispersed case

When the clay frame is distributed in the pores of the quartz frame the two frames do not experience the same stress. The clay frame is only affected by the pressure induced in the pores of the quartz frame. In the unequilibrated case the pressure inside the clay frame will thus be shielded by the clay frame leading to an induced pressure given by:

$$\frac{dP_c}{d\sigma} = \frac{dP_c}{dP_q}\frac{dP_q}{d\sigma}$$

From this the modulus of the clay frame can be determined from Equation 1. The induced pressure in the quartz frame is, however, affected by the presence of the clay in the pores. The quartz frame porosity will be filled partly by fluid and partly by clay. The presence of the clay frame causes the pore-filling fluid to have a larger effective modulus given by (Marion et al., 1992):

$$\frac{1}{K_f^{eff}} = \frac{1-S_{clay}}{K_f} + \frac{S_{clay}}{K_{clay}}$$

Where S_{clay} denotes the fraction of pore space occupied by clay. Using this value for the fluid modulus the induced pore pressure in the quartz frame may be determined. Equilibration thus acts to stiffen the clay frame by removing the shielding effect of the clay frame to the pore pressure induced by the quartz frame compression. The effect on the quartz frame is a pressure drop and consequent softening. These effects effectively occur within the quartz frame therefore we treat the dispersed case as a three phase system. In the unrelaxed case the system is composed of the mineral quartz, the free fluid and the clay phase containing the fluid shielded from the pore pressure by the clay frame. In the relaxed case we have the mineral quartz, the free fluid, and the clay frame with pore pressure equal to the quartz frame pressure.

Model input

In order to quantify the moduli of the mineral frames we require a parameterization of these. This is achieved by applying BAM to the mineral frames. Through this we can specify the bulk moduli of the mineral frames by their BAM value and porosity. Figure 2 shows bulk moduli for a range of sandstones versus porosity. Data are collected from Han (1986) and Best and McCann (1995).

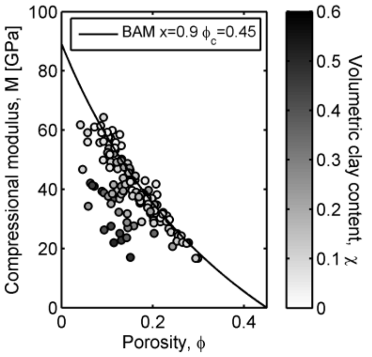

Figure 2 shows the compressional modulus for a range of sandstones. Clean sandstone moduli are well described by a BAM value of 0.9 and a critical porosity of 0.45.

We employ a critical porosity of 45% in the evaluation of the HS bounds for quartz. As seen from Figure 2 clean quartz sandstone tend to have high BAM values whereby we assign a BAM value of 0.9 to the quartz frame in the model consistent with the data. We allow the porosity of the quartz frame to vary between 1% and 40%.

For the clay frame, direct data on the bulk modulus is less accessible. Therefore we allow the BAM value of the clay frame to be a free parameter in the model. The porosity of the clay frame is dependent on mineralogy, deposition and diagenesis. Hurst and Nadeau (1995) arrived at a range of porosities for different mineralogies given in Table 1.

Table 1 showing the possible porosity ranges of three different clay mineralogies.

	Kaolinite	**Illite**	**Chlorite**
	[%]	[%]	[%]
Porosity	15-61	47-76	44-58

For the mineral moduli the value for quartz given in Table 2 is well established and does not vary significantly. For the clay phase the moduli is substantially lower than that for quartz and depend on the mineralogy. To simplify the treatment we restrict ourselves to considering only kaolinite. The important parameters are the clay frame porosity and the clay frame modulus. Since the mineral moduli of the different mineralogies in Table 2 are comparable the HS bounds for the different minerals will cover similar areas. Restriction to kaolinite therefore does not limit the results considerably, but reduces the number of variables.

Table 2 giving the mineral moduli for quartz and three different clay mineralogies.

Mineralogy	Bulk modulus	Shear modulus	Source
	[GPa]	[GPa]	
Quartz	36.6	45	Koga et al. (1958)
Kaolinite	11	6	Vanorio et al. (2003)
Smectite	5.75	4.02	Vanorio et al. (2003)
Na-Montmorillonite	11	5.5	Vanorio et al. (2003)

RESULTS

Laminated case

Pressure exchange between the mineral frames leads to a decrease in pressure and softening of the clay frame and an increase of pressure and stiffening of the quartz frame. The net effect is a balance between these two competing effects. Figure 3 shows the effect on the bulk modulus from changing the pressure in the quartz and clay frames.

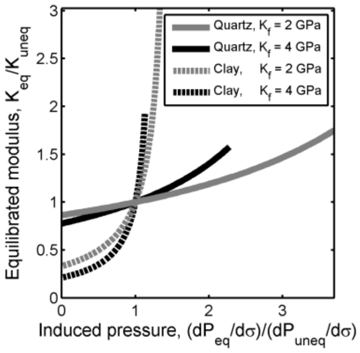

Figure 3 shows the change in saturated bulk modulus of the quartz and clay frame with increasing induced pore pressure. The pressure cannot exceed the applied stress whereby $\frac{dP_{eq}}{d\sigma} < 1$.

The softening of the clay frame is seen to be larger than the stiffening of the quartz frame. Figure 4 shows the effect of equilibration on the bulk modulus for a quartz frame with a porosity of 15% and a clay frame with a porosity of 40 %.

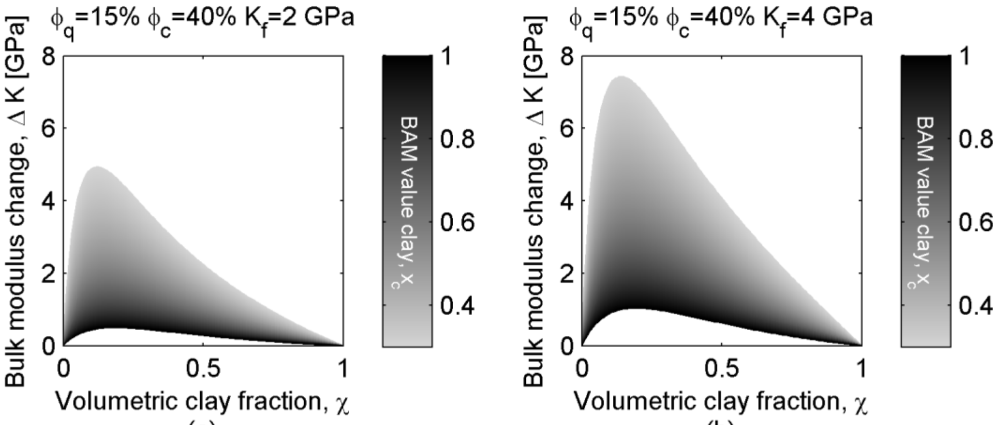

(a) (b)

Figure 4 shows the effect of clay-squirt stiffening on the bulk modulus of for a sandstone of 15 % porosity saturated with fluids having a bulk modulus of (a) 2 GPa and (b) 4 GPa.

The clay-squirt effect have the largest effect at a clay fraction of ≈ 0.15. After the maximum the stiffening drops off steeply. This behavior can be understood by observing the averaged induced pressures relative to the applied stress as seen in Figure 5.

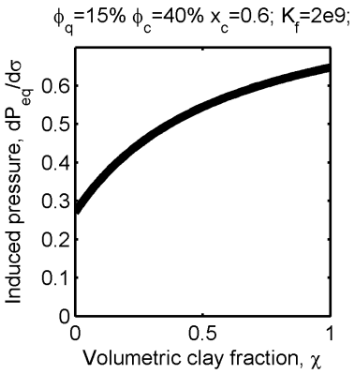

Figure 5 showing the averaged relative pore pressure versus clay fraction. The change is seen to be steepest at low clay fractions and when the slope starts to decrease the effect of clay-squirt starts to decline.

The averaged induced pore-pressure rises most quickly at low clay fractions until the clay induced pore pressure dominates and the effect diminishes.

Dispersed case

For the dispersed case the effect of clay-squirt is a softening as seen in Figure 6.

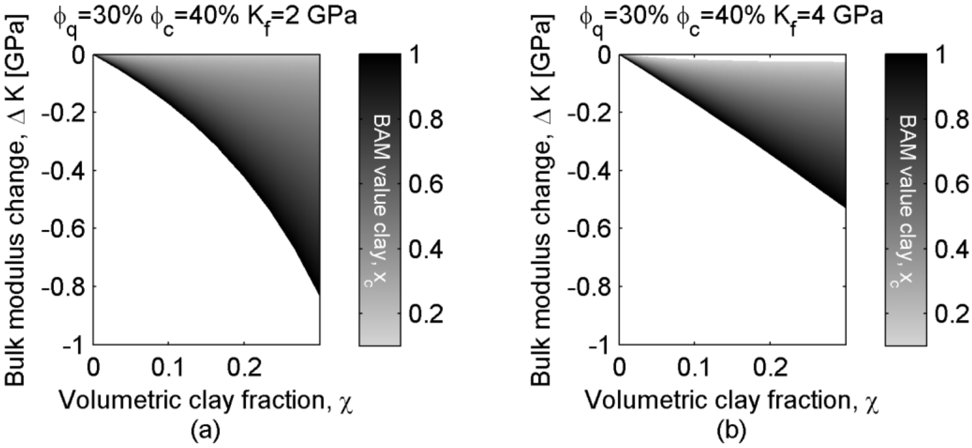

Figure 6 showing the effect of pore-pressure equilibration on the bulk modulus of the quartz-clay composite in the case where the clay is dispersed in the pores.

The clay filling in the pores acts to shield some of the fluid from the pore pressure induced in the surrounding quartz frame. Equilibration release some of the pore pressure induced in the quartz frame leading to a softer frame. The effect is significantly smaller than for the laminated case.

COMPARISON WITH EXPERIMENTAL DATA

Direct comparison with experimental data is hampered by the inaccessibility of many of the parameters involved. We can ascertain the likelihood of whether experimentally observed modulus changes between fluid substituted bulk moduli, and experimentally observed values may be explained by the clay-squirt effect. Figure 7 shows comparison between experimental data and the prediction of the clay-squirt model presented using a BAM value of 0.6 for the clay frame in the laminated case. The laminated case is observed since we wish to estimate if the clay-squirt effect is sufficient to describe the differences between fluid substituted values and the experimental data. The BAM values applied for plotting in Figure 7 and Figure 8 are based on HS bounds involving saturating fluid and quartz. These BAM values may therefore only serve as estimates of the true BAM values when clay is included. Load bearing clays shifts the BAM values calculated in the quartz/fluid system downwards making this quantity a measure of load bearing clays.

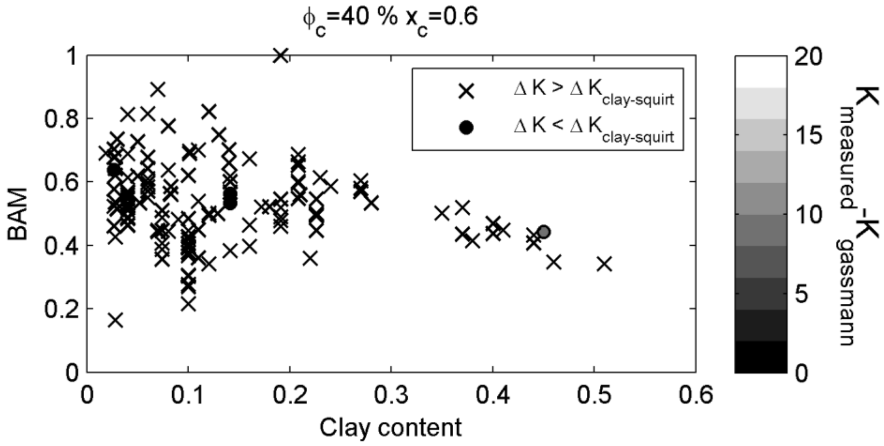

Figure 7 compares the observed difference between theoretical and experimental data to the possible values obtained by modeling the clay-squirt effect. Crosses designate data for which the experimental deviance exceeds the possible clay-squirt effect.

Very few data are explained with the parameters employed in Figure 7. Figure 8 shows the same comparison with the clay BAM value reduced to 0.1.

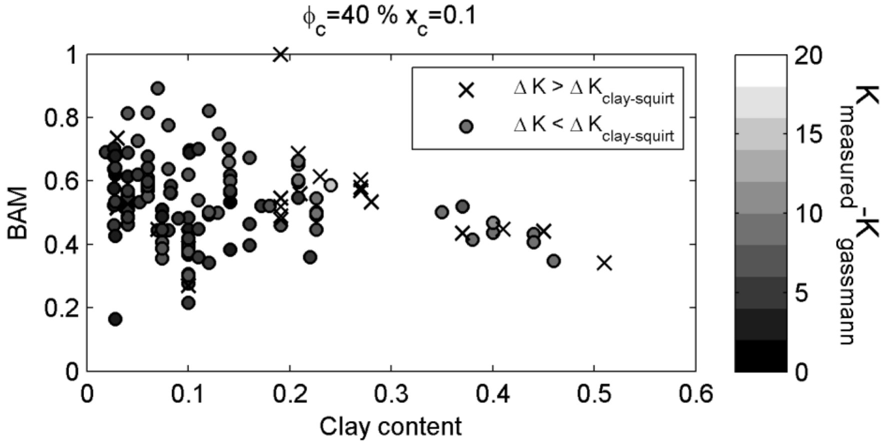

Figure 8 compares the observed difference between theoretical and experimental data to the possible values obtained by modeling the clay-squirt effect. Crosses designate data for which the experimental deviance exceeds the possible clay-squirt effect.

Thus reducing the BAM value for the clay frame makes it possible that the clay-squirt effect may be the cause of most of the stiffening seen experimentally.

CONCLUSION

We modeled the effect of squirt flow from compliant clay porosity by extending the framework of fluid substitution and employing the BAM. We found that significant stiffening may be induced by the clay-squirt mechanism. Under the right circumstances the clay squirt effect is a possible explanation to the experimentally observed stiffening of bulk moduli. The parameters needed to achieve sufficient stiffening is in the fringe of the likely values for a clay bearing sandstone. The conclusion is therefore that the clay-squirt mechanism is capable of accounting for the observed stiffening, but it is likely that other effects are involved.

REFERENCES

Berryman, J. (1995). “Mixture theories for rock properties”, *A Handbook of Physical Constants*, American Geophysical Union, 205-228.

Best, A., McCann, C. And Sothcott, J. (1994). “The relationships between the velocities, attenuations, and petrophysical properties of reservoir sedimentary rocks”, *Geophysical Prospecting*,42, 151-178.

Best, A. and McCann, C. (1995). “Seismic attenuation and pore-fluid viscosity in clay-rich reservoir sandstones”, *Geophysics*, 60(5), 1386-1397.

Biot, M. A. (1941). “General theory of three-dimensional consolidation”, *J. Appl. Phys.*,12 , 155-164.

Dvorkin, J., Mavko, G. and Nur, A. (1995). “Squirt flow in fully saturated rocks”, *Geophysics*, SEG, 60(1), 97-107.

Gassman, F. (1951). “Über die elastizitaet poroeser medien”, *Vierteljahresschrift der Naturforschenden Gesellschaft*, Zurich, *96*,1-23.

Han, D.-H (1986), “Effects of porosity and clay content on acoustic properties of sandstones and unconsolidated sediments”, *Stanford University*

Hurst, A. and Nadeau, P. (1995). “Clay microporosity in reservoir sandstones; an application of quantitative electron microscopy in petrophysical evaluation”, *AAPG Bulletin*, 79, 563-573.

Koga, I.,Aruga, M., and Yoshinaka, Y. (1958). “Theory of Plane Elastic Waves in a Piezoelectric Crystalline Medium and Determination of Elastic and Piezoelectric Constants of Quartz”, *Phys. Rev.*, 109(5), 1467-1473.

Marion, D. and Nur, A. (1991). “Pore-filling material and its effect on velocity in rocks”, *Geophysics*, SEG, 56(2), 225-230.

Marion, D., Nur, A. and Han, D. (1992). “Compressional velocity and porosity in sand-clay mixtures”, *Geophysics*, 57(4), 554-563.

Mavko. G, and Jizba, D. (1991). “Estimating grain-scale fluid effects on velocity dispersion in rocks”, *Geophysics*, 56(12), 1940-1949.

Nur, A., Mavko, G., Dvorkin, J. and Galmudi, D. (1998). “Critical porosity: A key to relating physical properties to porosity in rocks”, *The Leading Edge*, 17, 357-362.

Vanorio, T., Prasad, M., and Dvorkin, J. (2003). “Elastic properties of dry clay mineral aggregates, suspensions and sandstones”, *Geophysical Journal International*, 155, 319-326.

74th EAGE annual conference, Copenhagen, 2012

Introduction

Fluid identification using sonic velocities is becoming increasingly important due to the application of time-lapse seismics for reservoir monitoring. Accuracy of surveys may be increased by tying the interpretation to sonic logs or laboratory data taken on cored material. Fluid identification in the seismic band and extrapolation from higher frequencies to the seismic band require accurate knowledge of the fluid and frequency effects on the saturated rock moduli. Gassmann (1951) formulated a fundamental theory accounting for fluid effects on saturated moduli of a porous rock. Gassmanns approach divides the moduli into frame moduli which is stiffened by a fluid saturant due to an induced pore-pressure in undrained conditions. This approach has shown good correspondence with experiments for lithologies with homogeneous mineralogies (Berrymann, 1980; Murphy, 1985). For clay bearing lithologies stiffening in excess of the Gassmann predicted values are reported at low fluid mobility (Klimentos and McCann 1990; Best and McCann 1995). This stiffening is proposed by Best and McCann (1995) to be the result of a clay squirt effect. The clay-squirt effect is related to the squirt effect associated with cracks formulated by Mavko and Jizba (1991). Fluid trapped in the micro-pores of the softer clay will experience a higher induced pore-pressure than the fluid in pores of the stiffer quartz phase. Gassmann modelling incorporates induced pore-pressures through an average bulk modulus over both the quartz and clay phase. Therefore stiffening occurs relative to Gassmann modelling when the fluid mobility is too low or the frequency too high for induced pressures to be equilibrated.

In this paper a simple model is applied to estimate the magnitude of the clay-squirt effect. The emphasis is placed on determining whether an undrained clay phase embedded in a pure quartz matrix can account for the stiffening observed by Best and McCann (1995).

Theory

It is assumed that the clay is embedded in a pure quartz matrix with the clay inclusions large enough for a bulk modulus to be defined. If it is assumed that the fluid mobility is so low that no pressure equilibration takes place between the clay phase and the quartz phase the effect of the fluids on the different phase can be ascertained by Gassmann modelling of the individual phases. Following this, bounds for the composite bulk modulus can be determined using the bounds formulated by Hashin and Shtrikman (1963) cast in the formulation of Berryman, 1995:

$$\begin{aligned} K_{HS}^{+} &= \left\langle \frac{1}{K_i + \frac{4}{3}G_{max}} \right\rangle^{-1} - \frac{4}{3}G_{max} \\ K_{HS}^{-} &= \left\langle \frac{1}{K_i + \frac{4}{3}G_{\mathbf{min}}} \right\rangle^{-1} - \frac{4}{3}G_{\mathbf{min}} \end{aligned} \tag{1}$$

Where K_{HS}^{+} defines the stiffest combination of the constituents and K_{HS}^{-} defines the softest combination of the constituents. The bulk moduli of the phases are given as $K_i = K_c$ for the clay phase and $K_i = K_q$ for the quartz phase. The shear modulus is incorporated as G_{min} and G_{max} where G_{min} in this case is equal to the clay phase shear modulus G_c and G_{max} equals the quartz phase shear modulus, G_q. The angled brackets signify an average weighted by the clay phase fraction, χ_c and the quartz phase fraction, $1 - \chi_c$.

Bounds for the clay-squirt effect can then be estimated by observing the differences between the HS bounds for the clay-quartz aggregate when the clay phase is undrained relative to the drained case.

Method

Besides the bulk and shear moduli of the clay and quartz phases the problem depends on the fluid bulk modulus, K_f, quartz phase porosity, φ_q, clay phase porosity, φ_c, and clay fraction. Gassmann modelling is a monotonic relation between drained and undrained bulk moduli bounded by the mineral bulk modulus and fluid bulk modulus. Any quartz phase frame bulk modulus and porosity will have saturated bulk modulus in this span. Therefore the full variation is still retained by observing only the saturate quartz phase moduli allowing it to vary between the fluid bulk modulus and the mineral bulk modulus. Hereby we eliminate the quartz phase porosity from the model. The bulk modulus applied for quartz is 39 GPa.

Analysis of the influence of shear moduli shows little influence on the results when varied shear between $\frac{1}{2}K \leq G \leq K$ for both the quartz and clay phase. Therefore this variable is fixed at $G = \frac{1}{2}\mathrm{K}$ for both the quartz and clay phases.

The bulk modulus of the clay phase and the porosity of the clay phase are correlated as illustrated by the HS bounds for the dry clay bulk modulus in Figure 1. Therefore these two values are incorporated in the bounds as a set of parameters. To do this the average of the upper HS bound and the lower HS bound for the dry clay phase is applied. The mineral bulk modulus and shear modulus of clay phase is set to 11 GPa and 5.5GPa respectively from Vanorio et al. (2003). These values assume a Kaolinite mineralogy which has the highest reported mineral moduli for the clay minerals. Analysis shows that using these values leads to the most extreme bounds since the absolute difference between the drained and undrained bulk moduli increase with increasing mineral moduli. This means that low mineral moduli of the clay phase softens both the drained and undrained moduli of the aggregate resulting in a lower aggregate moduli but not a larger clay squirt effect. As seen from Figure 1 the relative effect between the undrained clay phase bulk modulus, $K_{c,und}$, and the drained clay phase bulk modulus, $K_{c,dr}$ increase at increasing clay phase porosity. To give conservative bounds the clay phase bulk modulus corresponding to a clay phase porosity of $\varphi_c = 0.7$ is applied.

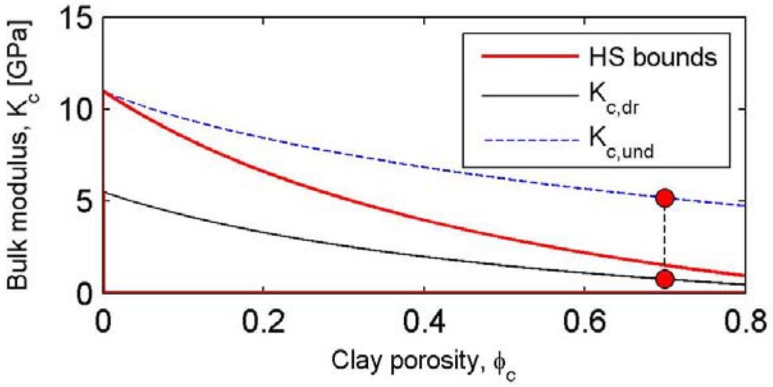

Figure 1 *modelling of the drained clay phase bulk modulus* $K_{c,dr}$ *from the HS bounds of Kaolinite and air. An average of the upper and lower bounds is applied as the drained bulk modulus. The undrained bulk modulus,* $K_{c,und}$ *is also plotted based on a fluid bulk modulus of* 4 GPa*. The selected value is indicated at* $\varphi_c = 0.7$.

Estimation of the saturated clay phase moduli with the equilibrated pressures induced in the aggregate is difficult. Since this is only an effort to estimate the magnitude of the effect we apply the dry bulk modulus of the clay phase for the drained case leading to an overestimation of the effect. At low clay fractions the average pressure is likely to be significantly lower than the induced pressure in the clay phase whereby stiffening of the clay phase at equilibrated pressures can be assumed to be low.

We wish to compare the results to experimental data by Best and McCann (1995). To ensure an undrained clay phase only the data with the highest viscosity is used since these will have the lowest fluid mobility (Pride 2005). This also gives an upper estimate of the fluid effect since the fluid bulk modulus of the highly viscous water/glycol mixture applied by Best and McCann (1995) is $K_f = 4\ GPa$. This will serve as fluid bulk modulus for all calculations.

Given these definitions the only variable remaining is the clay fraction and the saturated bulk modulus of the quartz phase. These two variables are treated as independent variables together constituting the variability of the system.

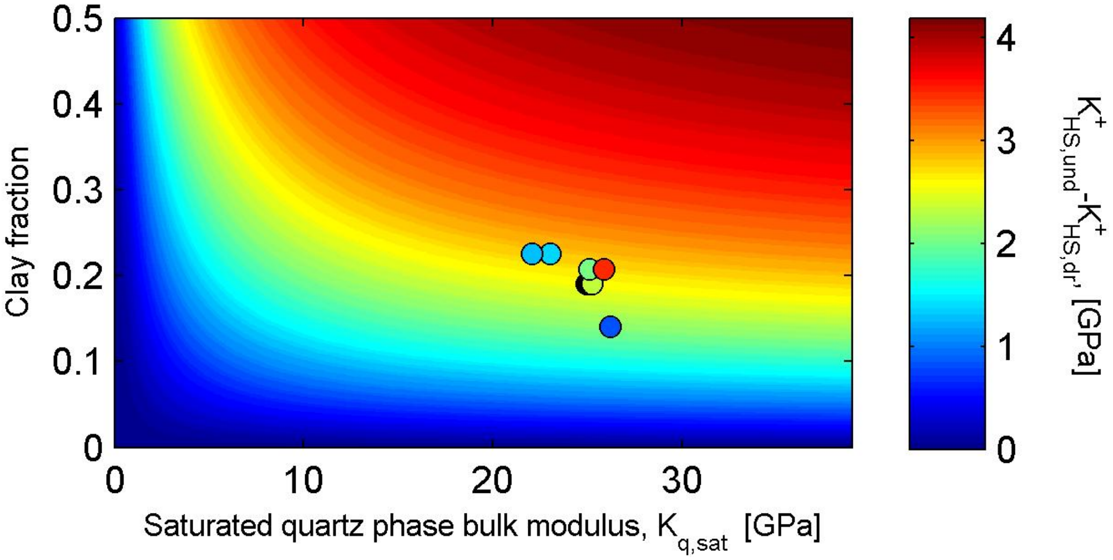

Figure 2: *Bulk moduli change between the modulus* $K_{HS,und}^{-}$ *with an undrained clay phase and* $K_{HS,dr}^{-}$ *with a drained clay phase assuming the stiffest geometrical arrangement of the phases. The points indicate the non-Gassmann stiffening of the data from Best and McCann (1995).*

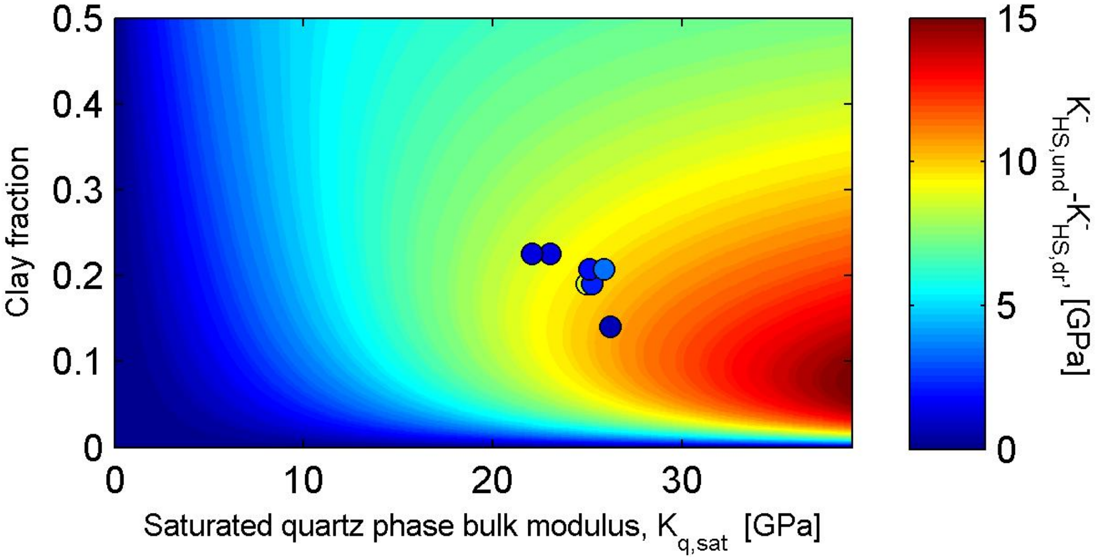

Figure 3: *Bulk moduli change between the modulus* $K_{HS,und}^{-}$ *with an undrained clay phase and* $K_{HS,dr}^{-}$ *with a drained clay phase assuming the softest geometrical arrangement of the phases. The points indicate the non-Gassmann stiffening of the data from Best and McCann (1995).*

Conclusions

The set of parameters involved in determination of the bounds were greatly reduced by the application of bounds and averaging. Most of the variability is, however, still retained due to the monotonic relation between drained and undrained moduli. The most significant reduction made to the system is the choice of dry clay phase bulk modulus. This value has a significant impact on the bounds. An extreme value is chosen to estimate the widest conceivable bounds.

Figure 2 shows the upper bound of the clay-squirt effect on the bulk modulus when the clay and quartz phases are arranged in the stiffest possible configuration as determined by the upper HS bound. Figure 3 shows the maximum effect of clay squirt on the bulk modulus when the quartz and clay phases are arranged in the softest possible configuration determined by the lower HS bound. The maximum values are seen for saturated quartz phase bulk modulus close to the mineral bulk modulus. In this high quartz phase bulk modulus the quartz phase the implicitly incorporated quartz phase porosity will be negligible. Hereby the peak value of 4 GPa for the upper HS bound and 15 GPa for the lower HS bound is a less realistic combination of parameters.

As seen by the comparison with data in Figures 2 and 3 the magnitude of the bound is sufficient to explain the non-Gassmann stiffening experimentally observed on the bulk modulus of clay bearing sandstones. Even in the stiffest arrangement showing the least effect of the clay phase all but two data points can readily be explained by the clay-squirt effect. Therefore based on the bound developed here it is credible that the bulk modulus stiffening observed on clay-bearing sandstones can be explained by a squirt mechanism from the clay phase. Future work may address predictive modelling of the effect as well as the estimation of the effect on shear modulus stiffening.

References

Best, A. I. and McCann, C., 1995. Seismic attenuation and pore-fluid viscosity in clay-rich reservoir sandstones, Geophysics 60, 1386-1397.

Berryman, J. G., 1980, Confirmation of Biot’s theory, Applied Physics Letters 37, 382-384.

Berryman, J. G. 1995. Mixture theories for rock properties , in *A Handbook of Physical Constants*, T.J. Ahrens ed., American Geophysical Union, 205-228.

Gassmann, F., 1951. Über die Elastizitaet poroeser Medien, Vierteljahresschrift der Naturforschenden Gesellschaft, Zürich 96, 1-23.

Hashin, Z. and Shtrikman, H., 1963. A variational approach to the elastic behavior of multiphase materials, Journal of the Mechanics and Physics of Solids 11, 127-140.

Klimentos, T. And McCann, C., 1990. Relationships among compressional wave attenuation, porosity, clay content, an permeability, Geophysics 55, 998-1014.

Murphy, W. F., 1985, Sonic and ultrasonic velocities: Theory versus experiment, Geophysical Research Letters 12, 85-88.

Pride, S.R., 2005. Relationships between seismic and hydrological properties, in *Hydrogeophysics*, Rubin, Y and Hubbard, S. S. ed., Springer, 235-291.

Vanorio, T., Prasad, M. and Dvorkin, J., 2003, Elastic properties of dry clay mineral aggregates, suspensions and sandstones, Geophysical Journal International 155, 319-326.

81st SEG Annual meeting, San Antonio, 2011

Downloaded 03/05/15 to 130.225.93.130. Redistribution subject to SEG license or copyright; see Terms of Use at http://library.seg.org/

Elastic moduli of sandstones saturated with a range of pore fluids correlated with kinematic viscosity and frequency ratio

Morten Kanne Sørensen and Ida Lykke Fabricius, Department of Civil Engineering, Technical University of Denmark.*

Summary

Modeling of the elastic properties of saturated porous rocks is a common need in exploration geophysics. Such modeling commonly involves formulation of a set of frame parameters which are then perturbed by the presence of a fluid in the pores. Frame parameters are extracted from laboratory measurements on dry samples meaning samples saturated only with air. The purpose of this study is to investigate if frame parameters can be extracted from air saturated measurements in sandstones, because earlier studies have shown that air may have a non-negligible effect on carbonates due to the high kinematic viscosity of air (Fabricius et al., 2010).

Introduction

Measurement of the elastic properties of porous rocks by wave propagation allows for non-destructive probing of both solid and fluid properties. This dual sensitivity is however also a major complication in the modeling of elastic properties. Fluid and solid effects are intertwined and identification of individual contributions is difficult.

A fundamental model applied for identifying fluid contributions to the elastic properties have long been Gassmann's equations. Under the assumption of pseudostatic deformation, statistical isotropy and homogeneity, decomposition of the elastic moduli into solid contributions and fluid contributions can be made (Gassmann, 1951). Hereby the possibility of predicting elastic properties at varying saturations is available if the properties are known for a specific saturation state.

This procedure does however not incorporate the effects of frequency. It is well established that acoustic propagation in porous media is inherently dispersive which is why many perturbations of Gassmann's approach have been formulated. Common for these is that they incorporate dispersion by leaving the quasi-static approach of Gassmann and incorporating dispersion by considering time dependent fluid movement within pores.

A General distinction is made between models considering relative movement of solid and fluid across the entire front of wave propagation known as global flow (Biot 1956a, 1956b) and models employing local flow known as squirt-flow models (Mavko and Jizba, 1991,1994). The latter abandon the assumption of homogeneity and allow for non-uniform pore compressibility leading to non-equal deformation of soft and hard pores resulting in a pressure gradient transverse to the wave propagation and consequent flow on small length scales.

Common for all the models is, however, that they treat the fluid contribution as a perturbation on the properties of the solid frame. Therefore they all require reliable determination of frame parameters. This information is commonly attained by recording acoustic wave propagation data on samples saturated only by air.

Due to the importance of adequate determination of frame moduli it is essential to investigate.

Theory and Method

The premise of this study is that air can influence the elastic properties of a porous rock due to the high kinematic viscosity. At 20℃ the kinematic viscosity of air is approximately 15 cSt whereas the value for water is only about 1 cSt. This relation is postulated to have an effect due to the increased viscous coupling between fluid and solid (Fabricius et al., 2010). Kinematic viscosity quantifies the ratio of viscous forces to inertial in the fluid and is given by:

$$\nu = \frac{\eta}{\rho_{fl}} \tag{1}$$

Where η denotes the dynamic viscosity of the fluid and ρ denotes the density. Viscous coupling of fluid and solid is also expected to depend on the area of the interface. In the formulation of Biot a reference frequency is defined as the frequency at which the viscous propagation of the pore-wall movement affects the whole pore-volume (Biot 1956b). Thus when the frequency approaches this critical frequency the viscous skin depth in the fluid is equal to half the effective pore diameter. The critical frequency is given by:

$$f_c = \frac{\phi\eta}{2\pi k\rho_{fl}} = \nu\frac{S_p^2}{c2\pi} \tag{2}$$

Where k is the Klinkenberg permeability, ϕ is the porosity and S_p is the interface area per volume which is related to

Downloaded 03/05/15 to 130.225.93.130. Redistribution subject to SEG license or copyright; see Terms of Use at http://library.seg.org/

porosity and permeability through Kozeny's equation (Kozeny, 1927):

$$S_p = \sqrt{\frac{c\phi}{k}} \tag{3}$$

The factor c is known as Kozeny's factor and have been found to be a function of porosity (Mortensen et al., 1998). Since viscous effects are frequency dependent it is proposed that the best measure of the influence of viscous fluid-solid coupling is the frequency normalized by the reference frequency:

$$\text{frequency ratio} = \frac{f}{f_c} \tag{4}$$

The possible effect of fluid-solid viscous coupling on the moduli recorded is addressed by applying the Gassmann model to a selection of datasets recorded from the literature. In the model, measurements on air-saturated samples will be applied as the frame values. From these frame values the effect of the fluid saturation will be incorporated by the use of Gassmann's equations given by:

$$K_{sat} = K_{frame} + \frac{\left(1 - \frac{K_{frame}}{K_{min}}\right)^2}{\frac{\phi}{K_{fl}} + \frac{1-\phi}{K_{min}} - \frac{K_{frame}}{K_{min}^2}} \tag{5}$$

$$G_{sat} = G_{frame}$$

Where K_{fl} denotes the bulk modulus of the saturating fluid and K_{min}denotes the mineral bulk modulus.

To focus on fluid contributions, in this study we apply a simple model where the solid is assumed to be composed of pure quartz with a mineral grain bulk modulus of $K_{min} = 39\ GPa$. The solid frame is also assumed to be statistically isotropic and homogeneous, assumptions fundamental for Gassmann's equations in their standard form.

Samples

The data treated in this study are collected from the literature. Only sandstone samples are considered, but with a wide range of porosity, permeability, cementation and clay content. Data are selected due to the wide viscosity range of the saturating fluids. The kinematic viscosity of saturating fluids range from 0.5 cSt to 600 cSt and involve both polar and non-polar fluids. Figure 1 shows a porosity-permeability cross-plot for all samples included in this study. It can be seen that the spectrum of samples cover a wide range of permeabilities from 10^{-2} mD to 10^{3} mD. As indicated from equation 3 this is equivalent to a large spread in the solid-fluid interface area. It is also noted, however that the low permeable samples generally contain more clay.

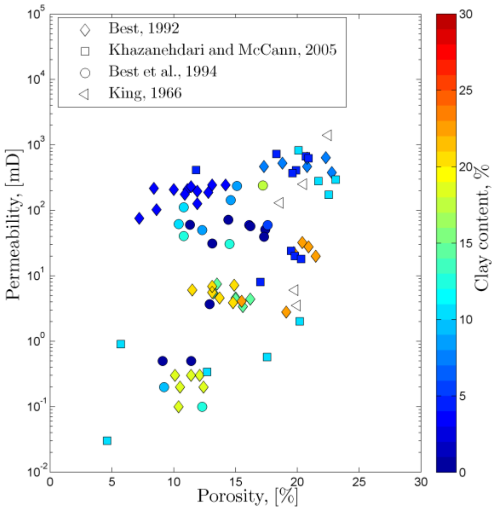

Figur 1: Permeability plotted versus porosity for the samples observed. The colors indicate the clay content. Samples without clay content data are depicted as open symbols

All measurements are done at effective stresses above 40 MPa. Measurements of dry sample properties are available for all datasets, although dry measurements in the dataset from Best, 1992 are done on reference samples with characteristics similar to the saturated samples.

Results

Using the dry measurements as frame values we use Gassmann's equations to predict the saturated moduli. As prediction is the aim of the model the Gassmann predicted compressional modulus is determined using dry shear modulus along with the Gassmann modeled bulk modulus.

The plot showing the deviation of the Gassmann predicted values compared to the measured saturated values are shown in Figurs 3-5. As explained, the discrepancies are plotted against the frequency ratio in order to address effects of fluid-solid interaction at the solid-fluid interface. The data points have been colored depending on the type of saturant.

© 2011 SEG

Downloaded 03/05/15 to 130.225.93.130. Redistribution subject to SEG license or copyright; see Terms of Use at http://library.seg.org/

Fluid coloration is arranged relative to the kinematic viscosities.

Discussion

Figure 2 depicts the compressional moduli extracted from the compressional wave velocities compared with the ones extracted from the dry samples. Here a clear difference is observed between the behavior of the low viscosity saturated samples and the high viscosity saturated samples. Generally both groups are seen to correlate well with the frequency ratio lending some credibility to the assumption of importance of viscous propagation into the pore-space and the consequent relation to the ratio between pore-size and interface area. The difference in moduli for high viscosity saturated samples are seen to increase as the frequency ratio decreases while the low viscosity saturated samples exhibit a slight negative trend with decreasing frequency ratio. The convergence of moduli difference at higher frequencies indicates that the dispersion observed is not of the global flow Biot type since this will result in opposite dispersion trends as already noted by Khazanehdrari and Sothcott (2003).

In Figurs 3-5 the data is modeled using Gassmann's equations. All three moduli show deviations from the predicted values. For the compressional modulus and shear modulus the maximum deviation is of the order of 20% while for the bulk modulus it is only about 10%. The deviation of the compressional moduli follows the trends suggested by figure 2 with a underprediction of the high viscosity saturated samples and a somewhat smaller overprediction of the low viscosity saturated samples.

This trend is also generally observable for the shear modulus in Figure 4. However there seems to be a split for the low viscosity saturated samples. It appears that the water based fluids leads to the expected underprediction while the the low viscosity hydrocarbons (hexane, kerosene and dead oil) leads to an overprediction. It is noteworthy though that the underprediction of the low viscosity hydrocarbon saturated samples seems to be independent of frequency ratio. It is therefore possible that these fluids somehow affect the solid frame. The samples saturated with low viscosity water based fluids do show a slight correlation with frequency ratio, suggesting that these samples are dependent on the viscous interaction. This split between water saturated samples and hydrocarbon saturated samples has been suggested to be related to the polarity of the fluids (Khazanehdrari and Sothcott, 2003). This, however, seems not to agree with the development seen for the high viscosity fluids which all are polar water/glycol mixtures. The undeprediction of the hydrocarbon saturated samples deviates from the premise of this study that the frame modulus should be corrected dependent on the magnitude of the kinematic viscosity of the saturating fluid relative to the kinematic viscosity of air. The constant level of the underprediction does raise the possibility of a competing effect.

The trends observed are also seen for the bulk moduli in Figure 5. For these moduli the effect is smaller compared to the absolute magnitude of the saturated moduli. The split between water based low viscosity fluids and hydrocarbons is not observed as clearly for this modulus. Care must be taken in evaluating the bulk moduli however since the shear moduli have been applied in the calculation. Any fluctuations on the shear modulus will have an affect the bulk modulus.

That the bulk modulus seems to be less affected than the shear modulus suggests that the effects observed might be associated with viscous shear coupling over the pores through the liquid. This would account for some of the deviations observed.

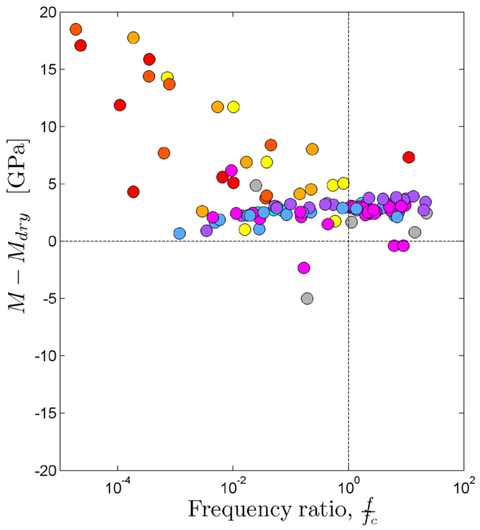

Figur 2: Comparison of saturated compressional modulus to the dry compressional modulus. These values are directly measured and no model have been applied. Points are colored with respect to kinematic viscosity. Specific legend can be seen in figure 3-5.

Conclusions

From the simple model applied in this study it can be concluded that it is indeed plausible that corrections should be applied to the dry moduli in order to achieve more fitting frame moduli. The correction could, however not yet be definitively established.

Downloaded 03/05/15 to 130.225.93.130. Redistribution subject to SEG license or copyright; see Terms of Use at http://library.seg.org/

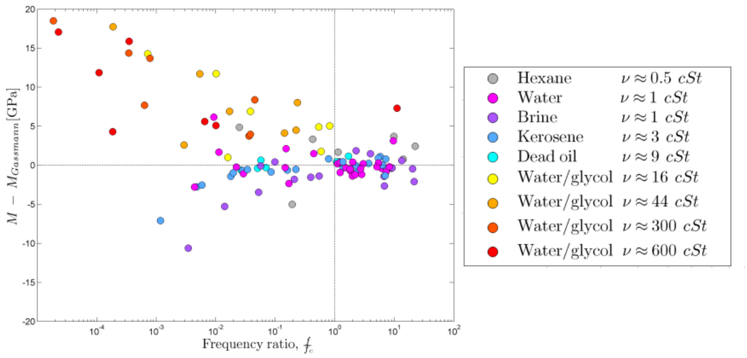

Figur 3: Deviation of compressional modulus compared to the values obtained by Gassmann.

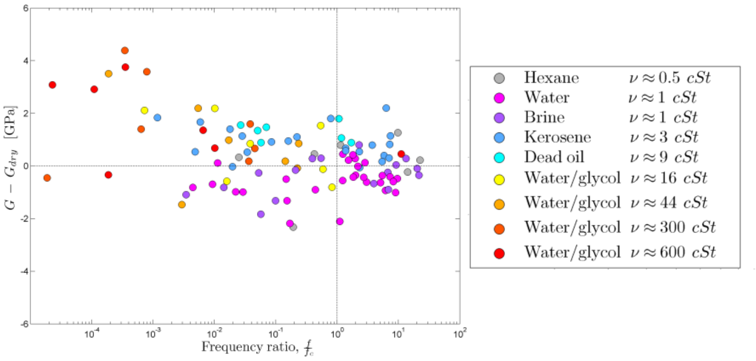

Figur 4: Deviation of shear modulus compared to the dry values expected by Gassmann.

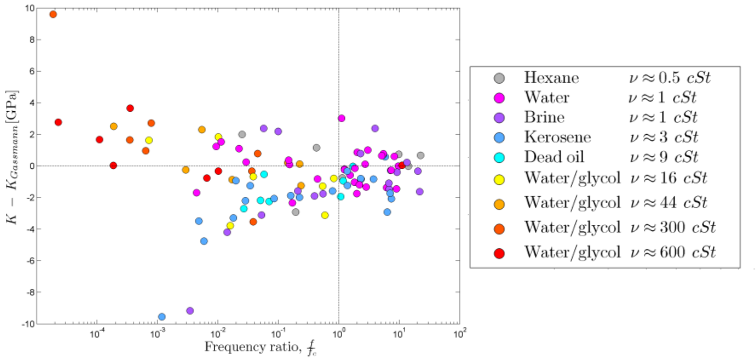

Figur 5: Deviation of the bulk modulus compared to the values obtained by Gassmann.

© 2011 SEG

Downloaded 03/05/15 to 130.225.93.130. Redistribution subject to SEG license or copyright; see Terms of Use at http://library.seg.org/

EDITED REFERENCES

Note: This reference list is a copy-edited version of the reference list submitted by the author. Reference lists for the 2011 SEG Technical Program Expanded Abstracts have been copy edited so that references provided with the online metadata for each paper will achieve a high degree of linking to cited sources that appear on the Web.

REFERENCES

Best, A. I., 1992, The prediction of the reservoir properties of sedimentary rocks from seismic measurements: Ph. D. thesis, University of Reading.

Biot, M. A., 1956a, Theory of propagation of elastic waves in a fluid-saturated porous solid. I. Low-frequency range: The Journal of the Acoustical Society of America, **28,** 168–178, doi:10.1121/1.1908239.

Biot, M. A., 1956b, Theory of propagation of elastic waves in a fluid-saturated porous solid. II. Higher frequency range: The Journal of the Acoustical Society of America, **28**, 179–191, doi:10.1121/1.1908241.

Fabricius, I. L., G. T. Bächle, and G. P. Eberli, 2010, Elastic moduli of dry and water-saturated carbonates - Effect of depositional texture, porosity and permeability: Geophysics, **75**, no. 3, N65–N78, doi:10.1190/1.3374690.

Gassmann, F., 1951, Über die Elastizität poröser Medien: Vierteljahresschrift der Naturforschenden Gesellschaft in Zürich, **96**, 1–23.

Khazanehdari, J., and C. McCann, 2005, Acoustic and petrophysical relationships in low-shale sandstone reservoir rocks: Geophysical Prospecting, **53**, 447–461, doi:10.1111/j.1365-2478.2005.00460.x.

Khazanehdari, J., and J. Sothcott, 2003, Variation in dynamic elastic shear modulus of sandstone upon fluid saturation and substitution: Geophysics, **68**, 472–481, doi:10.1190/1.1567215.

King, M. S., 1966, Wave velocities in rocks as a function of changes in overburden pressure and pore fluid saturants: Geophysics, **31**, 50–73, doi:10.1190/1.1439763.

Mavko, G., and D. Jizba, 1991, Estimating grain-scale fluid effects on velocity dispersion in rocks: Geophysics, **56**, 1940–1949, doi:10.1190/1.1443005.

Mavko, G., and D. Jizba, 1994, The relation between seismic P- and S-wave velocity dispersion in saturated rocks: Geophysics, **59**, 87–92, doi:10.1190/1.1443537.

Mortensen, J. F., F. Engstrøm, and I. Lind, 1998, The relation among porosity, permeability and specific surface of chalk from the Gorm field, Danish North Sea: SPE Reservoir Evaluation & Engineering, **1**, 245–251, doi:10.2118/31062-PA.

© 2011 SEG

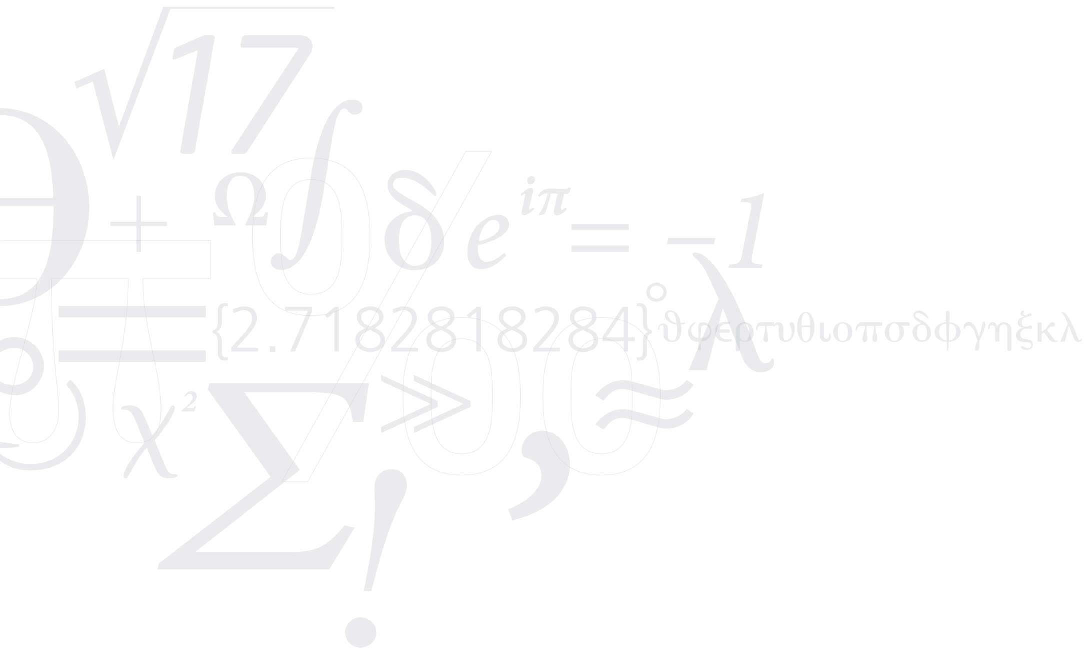
√17
Ω
δ
e^iπ = −1
{2.7182818284}
ϑφερτυθιοπσδφγηξκλ
λ
χ²
Σ
≫
≈
!